UNIVERSIDAD NACIONAL DEL LITORAL

Marco conceptual para el diseño inverso de metamateriales elásticos

Juan Manuel Podestá

FICH
FACULTAD DE INGENIERÍA
Y CIENCIAS HÍDRICAS

CIMEC
CENTRO DE INVESTIGACIÓN
DE MÉTODOS COMPUTACIONALES

INTEC
INSTITUTO DE DESARROLLO TECNOLÓGICO
PARA LA INDUSTRIA QUÍMICA

sinc(i)
INSTITUTO DE INVESTIGACIÓN EN
SEÑALES, SISTEMAS E
INTELIGENCIA COMPUTACIONAL

Tesis de Doctorado **2019**

UNIVERSIDAD NACIONAL DEL LITORAL

Facultad de Ingeniería y Ciencias Hídricas

Instituto de Desarrollo Tecnológico para la Industria Química

Marco conceptual para el diseño inverso de metamateriales elásticos

Juan Manuel Podestá

Tesis remitida al Comité Académico del Doctorado
como parte de los requisitos para la obtención
del grado de
DOCTOR EN INGENIERÍA
Mención Mecánica Computacional
de la
UNIVERSIDAD NACIONAL DEL LITORAL

2018

Comisión de Posgrado, Facultad de Ingeniería y Ciencias Hídricas, Ciudad Universitaria,
Paraje “El Pozo”, S3000, Santa Fe, Argentina.

UNIVERSIDAD NACIONAL DEL LITORAL

Facultad de Ingeniería y Ciencias Hídricas

Instituto de Desarrollo Tecnológico para la Industria Química

Marco conceptual para el diseño inverso de metamateriales elásticos

Juan Manuel Podestá

Lugar de trabajo:
CIMEC
Centro de Investigación de Métodos Computacionales
Facultad de Ingeniería y Ciencias Hídricas
Universidad Nacional del Litoral

Director:
Alfredo E. Huespe CONICET-CIMEC / Universidad Nacional del Litoral

Co-director:
Javier L. Mroginski CONICET / Universidad Nacional del Nordeste

Jurado Evaluador:
Dr. Victor Fachinotti CONICET-CIMEC / Universidad Nacional del Litoral
Dr. Adrián Cisilino CONICET-INTEMA / Universidad Nacional de Mar del Plata
Dr. Martín Idiart CONICET / Universidad Nacional de la Plata
Dr. Sebastián Giusti CONICET / Universidad Tecnológica Nacional Facultad Regional de Córdoba

2019

UNIVERSIDAD NACIONAL DEL LITORAL
Facultad de Ingeniería y Ciencias Hídricas

Santa Fe, 15 de Marzo de 2019.

Como miembros del Jurado Evaluador de la Tesis de Doctorado en Ingeniería titulada ***"Marco conceptual para el diseño inverso de metamateriales elásticos"***, desarrollada por el Ing. Juan Manuel PODESTÁ, en el marco de la Mención "Mecánica Computacional", certificamos que hemos evaluado la Tesis y recomendamos que sea aceptada como parte de los requisitos para la obtención del título de Doctor en Ingeniería.

La aprobación final de esta disertación estará condicionada a la presentación de dos copias encuadernadas de la versión final de la Tesis ante el Comité Académico del Doctorado en Ingeniería.

.....	.....
Dr. Adrián Cisilino	Dr. Sebastián Giusti
.....	.....
Dr. Martín Idiart (*)	Dr. Víctor Fachinotti

Santa Fe, 15 de Marzo de 2019

Certifico haber leído la Tesis, preparada bajo mi dirección en el marco de la Mención "Mecánica Computacional" y recomiendo que sea aceptada como parte de los requisitos para la obtención del título de Doctor en Ingeniería.

.....	.....
Dr. Javier Mroginski	Dr. Alfredo Huespe
Codirector de Tesis	Director de Tesis

(*) El Dr. Martín Idiart participó por videoconferencia.

Universidad Nacional del Litoral
Facultad de Ingeniería y Ciencias Hídricas

Secretaría de Posgrado

Ciudad Universitaria
C.C. 217
Ruta Nacional Nº 168 – Km. 472,4
(3000) Santa Fe
Tel: (54) (0342) 4575 229
Fax: (54) (0342) 4575 224
E-mail: posgrado@fich.unl.edu.ar

Dr. JOSE LUIS MACOR
SECRETARIO DE POSGRADO
Facultad de Ingeniería y Cs. Hídricas

Declaración legal del autor

Esta Tesis ha sido remitida como parte de los requisitos para la obtención del grado de Doctor ante la Universidad Nacional del Litoral y ha sido depositada en la Biblioteca de la Facultad de Ingeniería y Ciencias Hídricas para que esté disponible a sus lectores bajo las condiciones estipuladas por el Reglamento de la mencionada Biblioteca.

Citaciones breves de esta disertación son permitidas sin la necesidad de un permiso especial, en la suposición de que la fuente sea correctamente citada. Solicitudes de permiso para una citación extendida o para la reproducción de este manuscrito en un todo o en parte serán exigidas por el portador legal del derecho de propiedad intelectual de la misma.

Juan Manuel Podestá

Por vos Andrés.

Agradecimientos

En primer lugar, quiero agradecer a las instituciones que hicieron posible la realización de la presente Tesis; al Consejo Nacional de Investigaciones Científicas y Técnicas (CONICET), que me financió la beca de estudio de doctorado; a la Facultad de Ingeniería y Ciencias Hídricas (FICH-UNL), donde he realizado el doctorado, al Centro de Investigación de Métodos Computacionales (CIMEC) que me dio un lugar de trabajo.

No puedo dejar de agradecer a la Facultad de Ingeniería de la UNNE, y en particular al Departamento de Mecánica Aplicada, por la confianza depositada en mí para seguir una formación constante.

Deseo expresar mi profundo agradecimiento a mis directores de beca y Tesis, el Dr. Alfredo Huespe y el Dr. Javier Mroginski, por la libertad y el respeto a mis sugerencias e ideas y por el rigor científico con que han orientado las mismas. Pero principalmente agradezco el apoyo humano que me han brindado durante esta carrera.

Agradezco también a todos los compañeros del CIMEC, con quienes tengo el honor de compartir una gran pasión por nuestra profesión, pero también un gran vínculo de amistad.

Finalmente, nada de esto hubiera sido posible sin apoyo incondicional de mi esposa Miriam y de mis padres y hermanos.

Gracias a todos, ahora y siempre.

Resumen

En esta Tesis se describe un marco conceptual novedoso a ser aplicado en diseño inverso de materiales elásticos. El problema de diseño inverso se formula matemáticamente a través de un problema de optimización topológica. El marco conceptual provee herramientas para definir específicamente el espacio de variables del problema de optimización.

Las herramientas propuestas están basadas en un análisis de la conexión entre las simetrías geométricas que presentan las microarquitecturas periódicas y sus propiedades elásticas efectivas. Para este análisis se utilizan nociones de cristalografía. Son estudiados conceptos de redes de Bravais y grupos espaciales para entender la forma en que las simetrías de estos objetos pueden ser utilizadas en la metodología de diseño inverso.

Como complemento al marco conceptual propuesto, se implementa una base de datos de tensores homogeneizados mediante un análsis de distintos compuestos con microestructuras parametrizadas, apropiadas para el diseño de materiales con propiedades extremas.

El desempeño de las herramientas propuestas es evaluado mediante distintas aplicaciones numéricas. El primer ejemplo consiste en diseñar la microarquitectura del compuesto de una estructura elástica, de mínima flexibilidad y mínimo peso. Una segunda aplicación consta del diseño de metamateriales bidimensionales para camuflaje acústico. En ambos casos deben ser diseñados materiales pentamodales, con propiedades elásticas no convencionales caracterizados, por ejemplo, por un módulo de Poisson negativo o un módulo volumétrico anisotrópico. En el último ejemplo numérico se expone el diseño de un compuesto tridimensional periódico, de propiedades efectivas extremas.

Para resolver el problema de diseño inverso de la microarquitectura se adopta un enfoque de homogenización computacional y un algoritmo de optimización basado en derivada topológica y función *level-set*.

En los casos estudiados, la aplicación de los criterios propuestos da como resultado microarquitecturas alternativas a las reportadas en la bibliografía.

Abstract

An innovative conceptual framework addressed to solve the inverse elastic material design problem is described in this Thesis. The inverse design problem is formulated mathematically through a topological optimization problem.

The proposed conceptual framework provides a number of tools to specifically define the variable space of the optimization problem. These tools are based on the relation between the geometrical symmetry of the periodic microstructure and its elastic effective properties, which could be derived from crystallographic concepts. Notions involving Bravais lattices and spatial groups are studied to establish the relations that can be used in the inverse design methodology.

A further contribution of this Thesis consists of using a database of elastic homogenized tensors. This database has been built and used as an additional tool for the inverse design problem. These microstructures are conveniently chosen for helping the design of extreme materials.

Different applications of the conceptual framework are presented. The first example consists of the microarchitecture design of a composite for an elastic structure, having minimum compliance and weight. A second application is the design of a two-dimensional material for an acoustic cloaking. In both cases, pentamodal materials with exotic properties are demanded. The last numerical example is the design of a three-dimensional periodic composite, with extreme properties.

A topology optimization algorithm based on level set function and topological derivative are the mathematical tools taken for solving the inverse design problem.

For all these examples, the application of the proposed rules provides alternatives results to those reported in the bibliography.

Índice general

Índice de figuras

Índice de tablas

Capítulo 1

Introducción

Preliminares

En este trabajo de Tesis se presenta el desarrollo y aplicación de un marco conceptual para el diseño inverso de metamateriales periódicos elásticos. Dicho marco está fundamentado en un profundo análisis de la conexión entre las simetrías geométricas que presentan las microarquitecturas periódicas y sus propiedades elásticas efectivas. Asimismo, nociones de cristalografía, como redes de Bravais y grupos espaciales, son estudiadas para entender la forma en que las simetrías de estos objetos pueden ser utilizadas en la metodología de diseño inverso.

Un metamaterial es un material compuesto diseñado por el hombre con propiedades mecánicas no convencionales, que no pueden ser encontradas en la naturaleza (Zheng et al., 2014). Al tratarse de materiales diseñados para fines específicos, los metamateriales se caracterizan por microestructuras complejas con un elevado grado de detalle. Lo avances en tecnologías de impresión 3D abren un amplio rango de posibilidades para fabricar y producir estos compuestos.

En el contexto de esta Tesis, el diseño de metamateriales se plantea como un problema inverso mediante un enfoque de homogeneización computacional empleando técnicas de optimización topológica.

1.1. Optimización topológica utilizando homogeneización computacional

La optimización topológica consiste en encontrar la distribución de dos o mas materiales dentro de un dominio, tal que minimice cierta función costo y cumpla con restricciones impuestas. Típicamente, en problemas mecánicos, se busca minimizar la flexibilidad (maximizar rigidez) bajo una restricción de cantidad de material.

Particularmente, el diseño de materiales es abordado mediante optimización topológica a través de la siguiente idea: *Cualquier material es una estructura si se lo mira con un microscopio suficientemente potente* (Bendsoe y Sigmund, 2003). En este aspecto, la formulación introducida en Sigmund (1994, 1995), plantea una combinación de homogeneización numérica y optimización topológica. Sigmund llamó a esta formulación *problema de homogeneización inversa*.

En el libro de Bendsoe y Sigmund (2003) (ver también Sigmund y Maute (2013)) es posible encontrar excelentes descripciones de los distintos enfoques posibles para el problema de homogeneización inversa. Por ejemplo, en Huang et al. (2011) los autores resuelven el problema inverso utilizando un algoritmo de optimización estructural basado en evolución bidireccional (*Bidirectional Evolutionary Structural Optimization* - BESO). Otro ejemplo es el presentado por Andreassen et al. (2014), donde los autores realizan el diseño de metamateriales elásticos 3D utilizando el algoritmo de optimización *Solid Isotropic Material with Penalization* - *SIMP*. Existen muchos otros trabajos en la bibliografía que adoptan esta formulación, ver Coelho et al. (2016); Neves et al. (2000); Wang et al. (2014).

En el presente trabajo de Tesis, el diseño de metamateriales es abordado mendiante la mencionada formulación de homogeneización inversa propuesta por Sigmund. Sin embargo, la técnica utilizada para resolver dicho problema es la presentada en Amstutz y Andrä (2006). En este caso, los autores proponen la utilización de una función *level-set* y el uso del concepto de derivada topológica. Dicha técnica fue aplicada en contribuciones tales como diseño estructural sujeto a restricciones de tensión (Amstutz et al., 2012), diseño de materiales piezoeléctricos (Amigo et al., 2016) o diseño inverso de microestructuras (Amstutz et al., 2010). A continuación se presentan brevemente las distintas herramientas computacionales utilizadas en la presente Tesis para resolver el problema de homogeneización inversa.

1.1.1. Homogeneización de las propiedades efectivas

La obtención de propiedades efectivas se realiza por medio de homogeneización computacional. Se tienen en cuenta dos escalas de longitud características. En la escala macro (Fig.1.1 izquierda), la longitud característica ℓ es del mismo orden de magnitud de la estructura macro. La longitud de la escala micro ℓ_μ (Fig.1.1 derecha) es del mismo orden de magnitud que la longitud característica de la microarquitectura del material. Se asume que $\ell_\mu \ll \ell$. El compuesto, a nivel macro, es caracterizado por sus propiedades efectivas en cada punto $\mathbf{x}$ del dominio macro Ω. El dominio Ω_μ determina la microcelda donde el problema inverso es resuelto. Para la determinación del tensor elástico efectivo, $\mathbf{C}^h$[1], se aplican condiciones de borde periódicas en la microcelda y

[1]Los tensores de cuarto orden son representados por matrices $\mathbf{R}^{3\times3}$ utilizando la notación de Kelvin. En función de ello, los tensores de segundo orden simétricos son representados mediante $\boldsymbol{\varepsilon} = [\varepsilon_{11}, \varepsilon_{22}, \sqrt{2}\varepsilon_{12}]^T$ para deformaciones

se resuelve el problema mecánico elástico, mediante resolución por elementos finitos, para cada una de las deformaciones canónicas. Esto permite calcular las tensiones en la escala micro, que por un proceso de homogeneización de las mismas se determina el tensor elástico efectivo (ver de Souza Neto y Feijóo (2006); Guedes y Kikuchi (1990)).

Por otro lado, para el diseño de material se utiliza un compuesto periódico constituido por dos fases elásticas e isotrópicas, M_1 (fase rígida) y M_2 (fase flexible o vacío). Cada fase, M_1 y M_2, ocupa un subdominio, Ω_μ^1 y Ω_μ^2 respectivamente, (Fig.1.1-derecha). Se define la función

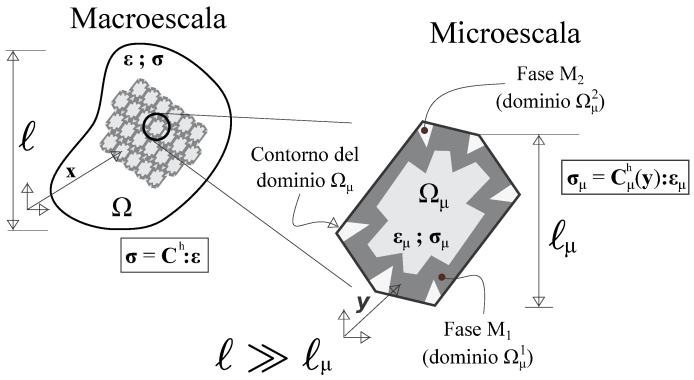

Figura 1.1: El diseño del material se realiza mendiante una técnica de homogenización inversa, formulada como un problema de optimización topológica, involucrando dos escalas de longitud características, ℓ en la macroescala y ℓ_μ en la microescala. La región Ω_μ se define como dominio de diseño para la optimización topológica.

característica $\chi(\mathbf{y})$, dentro del dominio Ω_μ, que determina la distribución de ambas fases en el dominio:

$$\chi(\mathbf{y}) = \begin{cases} 1 & \forall \mathbf{y} \in \Omega_\mu^1 \\ 0 & \forall \mathbf{y} \in \Omega_\mu^2 \end{cases} . \tag{1.1}$$

Resulta evidente que el tensor elástico homogeneizado, $\mathbf{C}^h$, depende de la distribución de las fases M_1 y M_2 en Ω_μ. Dicha dependencia se hace explícita mediante la notación $\mathbf{C}^h(\chi)$. Este tensor elástico homogeneizado puede obtenerse de la forma tradicional aplicando condiciones de borde periódicas.

1.1.2. Formulación del problema de homogeneización inversa

El objetivo del diseño inverso mediante homogeneización es obtener una microarquitectura que posea ciertas propiedades efectivas definidas de antemano. En el presente trabajo de Tesis, este problema es abordado mediante dos formulaciones estándar (Bendsoe y Sigmund, 2003):

$$\begin{aligned} &\min_{\chi} \ \|\mathbf{C}^h(\chi) - \hat{\mathbf{C}}\| \\ &\text{t.q.: } V^h(\chi) - V^{obj} = 0 \ , \end{aligned} \tag{1.2}$$

y $\boldsymbol{\sigma} = [\sigma_{11}, \sigma_{22}, \sqrt{2}\sigma_{12}]^T$ para tensiones. En adelante, se utilizará dicha representación matricial de Kelvin para los tensores de cuarto orden.

$$\begin{aligned} &\min_{\chi} \; V^h(\chi) \\ &\text{t.q.: } \|\mathbf{C}^h(\chi) - \hat{\mathbf{C}}\| = 0 \,, \end{aligned} \tag{1.3}$$

donde la variable de diseño es la función característica χ, $\mathbf{C}^h(\chi)$ es el tensor elástico efectivo de la microcelda, calculado según lo expuesto brevemente en la sub-Sección precedente, y $V^h(\chi) = \frac{1}{|\Omega_\mu|}\int_{\Omega_\mu} \chi \; d\Omega$ es la fracción volumen de fase rígida que tiene la microarquitectura. $\hat{\mathbf{C}}$ y V^{obj} representan, respectivamente, el tensor elástico objetivo y el volumen de fase rígida que se busca alcanzar mediante la topología diseñada. En la formulación 1.2 la función a minimizar consiste en la norma de la diferencia entre el tensor elástico efectivo y el tensor elástico objetivo de la microarquitectura, mientras que la cantidad de material rígido se impone mediante una restricción de igualdad. Por otro lado, en el caso 1.3 se busca minimizar la cantidad de material, mientras que la igualdad entre los tensores es una restricción.

1.1.3. Algoritmo de optimización topológica

Introduciendo en Ω_μ una función tipo *level-set* $\psi \in C^0(\Omega_\mu)$

$$\psi(\mathbf{y}) = \begin{cases} > 0 & \forall \mathbf{y} \in \Omega_\mu^1 \\ < 0 & \forall \mathbf{y} \in \Omega_\mu^2 \\ 0 & \text{en las interfases} \end{cases} , \tag{1.4}$$

y mediante una técnica de lagrangiano aumentado estándar (Lopes et al., 2015), el problema 1.2 se reescribe como:

$$\max_{\lambda} \min_{\psi} \mathcal{T}(\psi, \lambda), \tag{1.5}$$

siendo

$$\mathcal{T}(\psi, \lambda) = \|\mathbf{C}^h(\psi) - \hat{\mathbf{C}}\| + \lambda(V^h - V^{obj}) + \frac{\alpha}{2}\left(V^h - V^{obj}\right)^2, \tag{1.6}$$

donde λ es el multiplicador de Lagrange y α es el parámetro de penalidad[2].

El problema de minimización D.14 es resuelto con un algoritmo tipo *dirección de descenso*. La obtención de la dirección de descenso viene dada por la expresión

$$D_\psi \mathcal{T}(\psi, \lambda) = \frac{(\mathbf{C}^h - \hat{\mathbf{C}}) : D_\psi \mathbf{C}^h}{\|\mathbf{C}^h - \hat{\mathbf{C}}\|} + \lambda \mathbf{1} + \alpha V^h \mathbf{1}, \tag{1.7}$$

donde $D_\psi \mathbf{C}^h$ es la derivada topológica del tensor elástico homogeneizado y representa la sensibilidad del tensor de elasticidad al introducir una perturbación esférica en el dominio de diseño

[2]Para el problema 1.3 el desarrollo es similar y puede ser encontrado en los Anxeos.

Ω_μ. El desarrollo de $D_\psi \mathbf{C}^h$ para problemas en $\mathbb{R}^3$ se detalla en el Apéndice II del Anexo D, ver también Ammari et al. (2008) para un estudio más profundo. En cambio, para problemas en $\mathbb{R}^2$, $D_\psi \mathbf{C}^h$ se determina según los conceptos presentados en Amstutz et al. (2010).

En los Anexos A, B, C y D se encuentran detalles de implementación de tanto del presente algoritmo como del utilizado para resolver el problema 1.3.

1.2. Aportes al diseño inverso de metamateriales elásticos

En el desarrollo de la tesis, varios aspectos del problema de homogeneización inversa son abordados con el fin de aportar nuevos conceptos. En primer lugar, la adopción del dominio de diseño Ω_μ, o microcelda, constituye un problema poco estudiado en la bibliografía. Por ejemplo en Coelho et al. (2016) se presenta un análisis de la influencia de la forma de la microcelda sobre los resultados obtenidos. En Diaz y Benard (2003) se destaca cómo la elección de la forma del dominio puede influir positivamente en la ampliación de microarquitecturas posibles de alcanzar en el diseño. Sin embargo, la adopción de microceldas de forma cuadrada o cúbica, para $\mathbb{R}^2$ o $\mathbb{R}^3$ respectivamente, sigue siendo el criterio estándar, ver Amstutz et al. (2010); Andreassen et al. (2014). En problemas planos pueden encontrarse propuestas de microceldas con forma hexagonal, ver Giusti (2009), o más recientemente las aplicaciones presentadas en Watts (2014).

Otro punto analizado en esta Tesis es la influencia de la aplicación de restricciones geométricas, típicamente de simetría, que se imponen a la distribución de material dentro de la microcelda. En Sigmund (2000) y Andreassen et al. (2014) son presentados ejemplos donde la aplicación de ejes de simetría en la distribución interna de material favorece el alcance de microarquitecturas isotrópicas en problemas en $\mathbb{R}^2$ y $\mathbb{R}^3$.

En el presente trabajo se propone estudiar la clase de simetría del tensor elástico objetivo $\hat{\mathbf{C}}$ (Ting, 1996), y así determinar *a priori* características geométricas que debe cumplir el material a diseñar, aún antes de aplicar cualquier algoritmo de diseño inverso. Los distintos estudios presentados tienen como conclusión tres criterios fundamentales propuestos en esta Tesis:

i) Adoptar como **variable de diseño** la forma de la microcelda.

ii) Aplicar **restricciones geométricas** a la distribución de material dentro de la microcelda.

iii) Construcción de una **base de datos** que contenga tensores de elasticidad de compuestos cuya microestructura esté parametrizada. Esta base de datos es utilizada para definir la configuración inicial del problema de optimización.

Los criterios *i)* y *ii)* son función de la clase de simetría del tensor elástico objetivo. Sin embar-

go, en el primer punto, para definir de forma cerrada la relación de aspecto de las microceldas es preciso introducir información extra. Por ello es necesario incluir el criterio *iii)*. La mencionada base de datos se compone de tensores de elasticidad efectivos de un conjunto de topologías representativas. Esta información proporciona una configuración inicial adecuada para el algoritmo de optimización topológica, y además permite definir la esbeltez de la microcelda. La aplicación de estos criterios facilita el procedimiento de diseño inverso y garantiza el alcance de las propiedades de simetrías demandadas por el tensor elástico objetivo.

1.3. Organización del documento

La Tesis está organizada bajo el formato de *tesis por compilación*. Por lo tanto, en el cuerpo principal de la monografía sólo se presenta una descripción global y sucinta de la temática estudiada, mientras que los detalles de cada tema son direccionados a los trabajos presentados en los Anexos. Allí se podrán encontrar todos los desarrollos que han sido necesarios para alcanzar los resultados presentados en la monografía.

En el Capítulo 2 se presentan conceptos de cristalografía en los que se fundamenta el marco conceptual propuesto en esta Tesis.

En el Capítulo 3 se presenta un ejemplo de aplicación de diseño inverso en $\mathbb{R}^2$, aplicado a estructuras elásticas, mediante la realización de una optimización multiescala.

En el Capítulo 4 se presenta un segundo ejemplo de aplicación en $\mathbb{R}^2$, donde el objetivo es diseñar materiales componentes de camuflajes acústicos.

En el Capítulo 5 se exponen los primeros pasos para la generalización a problemas en $\mathbb{R}^3$. Además se presenta un test numérico en el que se diseña un material isotrópico de propiedades extremas.

Por último, el Capítulo 6 consiste en el desarrollo de las conclusiones generales. Además se realiza un recuento de las contribuciones científicas derivadas del trabajo realizado en la presente Tesis.

Anexos

En los Anexos se encuentran los artículos científicos en los que se fundamentan los temas expuestos en el cuerpo principal de la Tesis. Es importante aclarar que la disposición elegida no es cronológica, mas tiene como fin exponer primero los conceptos principales, para luego presentar las aplicaciones desarrolladas.

El desarrollo completo del marco conceptual se encuentra en el artículo correspondiente al Anexo A. Allí se realizan numerosas validaciones numéricas de las ideas presentadas. Los artícu-

los presentados en los Anexos B y C consisten en aplicaciones del marco conceptual a problemas específicos. En el Anexo D se presentan los conceptos para problemas en $\mathbb{R}^3$. Por último, en el Anexo E se expone la documentación correspondiente a la divulgación de las herramientas computacionales producidas en el marco de la Tesis.

Capítulo 2

Diseño inverso de materiales: Aplicación de conceptos de simetrías.

2.1. Introducción

La *simetría* es una propiedad muy común en la naturaleza. Se presenta en estructuras naturales como telas de araña, panales de abeja, cristales, organismos pluricelulares, etc. Por otro lado, en muchas disciplinas el uso de las simetrías es importante para definiciones más abstractas, como simetrías **C** (conservación de la carga) o simetrías **P** (conservación de la paridad) en el modelo estándar de la física.

La aplicación de simetrías en la resolución de problemas es siempre una ventaja. *"... si la simetría de un ente es conocida, es posible predecir algunas de sus propiedades mas importantes sin necesidad de recurrir a experimentos o cálculos profundos"*. (Powell, 2010). Es decir, un problema que tenga una propiedad de simetría, es un problema que puede ser simplificado.

La búsqueda de simetrías se ve motivada por la posibilidad de resolver un mismo problema con menor esfuerzo. En problemas numéricos, por ejemplo, todo dominio que es simétrico (condiciones de borde y cargas) puede ser caracterizado analizando solo una porción del mismo; en matemática todo tensor que posee simetrías puede ser expresado de manera simplificada.

El objetivo principal de este trabajo consiste en relacionar las simetrías observadas en la distribución geométrica espacial de las fases de un material con sus propiedades elásticas efectivas. Luego, explotar estas relaciones como herramientas que faciliten los procedimientos de diseño inverso en problemas de optimización topológica.

En el problema de diseño inverso, la microarquitectura (distribución geométrica de las fases) es desconocida de antemano. Sin embargo, mediante el tensor constitutivo elástico objetivo

$\hat{\mathbf{C}}$ (propiedad física efectiva), dato del problema, podemos buscar una caracterización inicial de aquella geometría, aún en etapas anteriores a la aplicación de un algoritmo de optimización topológica. Para perseguir este fin, se profundizará un aspecto poco explotado en la bibliografía: la evaluación de la forma del dominio de diseño Ω_μ en la escala micro, es decir, la forma que adopta la microcelda. Típicamente, las formas cuadradas o rectangulares para problemas en $\mathbb{R}^2$, o cúbicas para problemas en $\mathbb{R}^3$, son utilizadas como dominio de diseño estándar (ver Amstutz et al. (2010); Andreassen et al. (2014) para problemas inversos). Sin embargo, trabajos como Sigmund (2000) y Watts (2014) proponen microceldas de formas menos convencionales. Éstos ejemplos aportan una clara ventaja en la obtención de resultados alternativos, sin embargo los autores no fundamentan la razón de su elección.

La presente propuesta consiste en adoptar la forma de la microcelda como *incógnita* del problema de diseño inverso. Luego, resolver esa incógnita tomando en cuenta propiedades del tensor constitutivo elástico objetivo $\hat{\mathbf{C}}$ y, en función de dichas propiedades, imponer restricciones geométricas a la microarquitectura a diseñar.

Para un mejor seguimiento, se describen las secciones contenidas en el presente Capítulo: En la Sección 2.2 se exploran nociones de cristalografía, utilizadas en el desarrollo de los temas posteriores. En las Secciones 2.3 a 2.5 se desarrollan los fundamentos del marco conceptual propuesto en este trabajo de Tesis. Por último en la Sección 2.6 se detallan reglas de diseño, que constituyen la aplicación los conceptos presentados. Todo lo expuesto en el presente Capítulo se encuentra desarrollado en profundidad en el Anexo A.

2.2. Microarquitecturas periódicas y redes de Bravais

Sea un compuesto cuya microarquitectura es periódica y posee simetría de traslación. Esto es, la microarquitectura será invariante bajo traslaciones discretas a lo largo de las dos direcciones definidas por los vectores primitivos no proporcionales $\mathbf{a}_1$ y $\mathbf{a}_2$[1]. De este modo, la función característica χ_i para una i-ésima fase satisface:

$$\chi_i(\mathbf{x}+\mathbf{t}) = \chi_i(\mathbf{x}) \quad ; \quad \text{donde} \quad \mathbf{t} = \omega_1\mathbf{a}_1 + \omega_2\mathbf{a}_2 \tag{2.1}$$

y los valores $\omega_i \in \mathbb{Z}$ son coeficientes enteros cuyos valores identifican la magnitud de la traslación. De esta manera, con la expresión 2.1 es posible caracterizar una geometría periódica.

[1] En el presente capítulo se exponen conceptos y ejemplos para casos de dos dimensiones. Para tres dimensiones los conceptos son análogos y se encuentran desarrollados en el Anexo D

2.2.1. Red de Bravais subyacente en geometrías periódicas.

En geometría y cristalografía, una red de Bravais es un arreglo infinito de puntos discretos generados mediante un conjunto de traslaciones discretas y cuya estructura es invariante bajo ciertas operaciones de traslación. En el presente contexto, su importancia recae en el siguiente enunciado: *toda geometría periódica posee una red de Bravais subyacente y una base o patrón*[2].

El procedimiento para identificar la red de Bravais y el patrón en una geometría periódica puede verse en la Fig.2.1. La red y los vectores primitivos se identifican mediante la detección de puntos equivalentes (el ojo de cada pez, en el ejemplo). Una vez que la red de Bravais es caracterizada, tanto la celda unidad como el patrón (Figs. 2.1-b y -c) son fácilmente reconocibles. Se aprecia que los vectores primitivos $\mathbf{a}_i$ también son generadores de la red de Bravais. En función

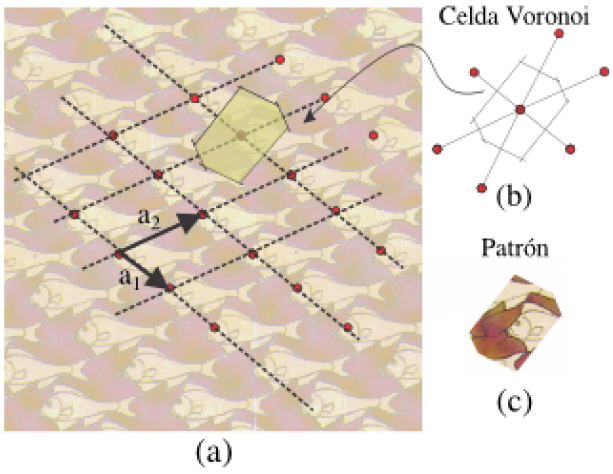

Figura 2.1: Determinación de la red de Bravais subyacente, vectores primitivos y celda unidad en una geometría periódica.

de los valores que tome la relación entre dichos vectores, se pueden distinguir cinco tipos de redes de Bravais en el plano, y se clasifican en Hexagonal (H), Cuadrada (S), Rectangular Primitiva (Rp), Rectangular Centrada (Rc) y Oblicua (O), ver Fig. 2.2 (Souvignier, 2016).

2.2.2. Celda unidad

Para una geometría periódica, la identificación de la red de Bravais subyacente es una herramienta esencial para la construcción de una celda unidad que sea generadora de dicha geometría. La construcción de una celda unidad no es única, y en la Fig.2.3 pueden verse algunos ejemplos para una geometría periódica que cuenta con una red de Bravais subyacente de simetría *rectangular centrada (Rc)*. Allí, todas las microceldas mostradas son celdas unidad, ya que son generadoras de la geometría. Sin embargo existen algunas diferencias: La celda m_1 es un ejemplo de la llamada

[2]Los términos motivo y patrón se usarán en referencia a la distribución geométrica dentro de la celda unidad, ya sea un motivo en imágenes como Fig. 2.1 o distribución de material en diseños presentados más adelante. En inglés también puede encontrarse el término *base*.

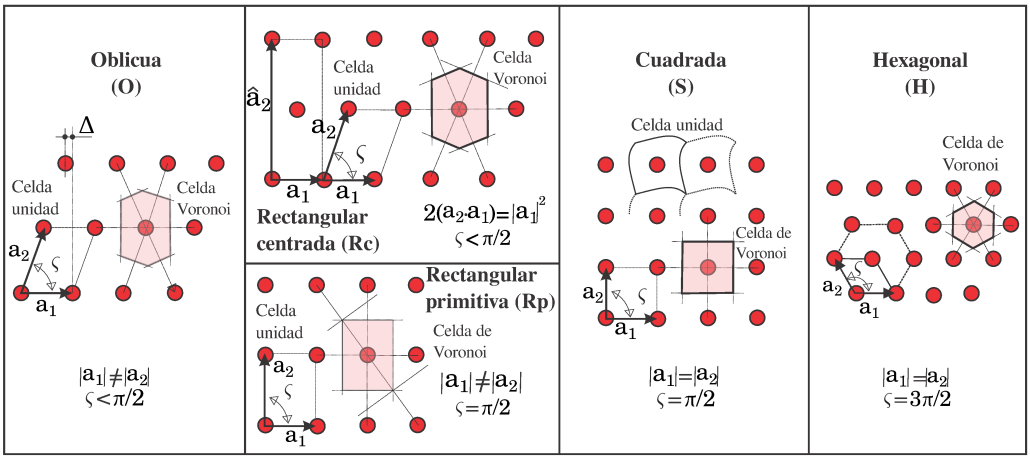

Figura 2.2: Detalle de los cinco tipos de redes de Bravais posibles en el plano.

celda unitaria convencional. En ella es fácil detectar los ejes de simetría vertical y horizontal de la red y del motivo, pero no posee la mínima área posible. Los casos m_2 y m_3 son *celdas unitarias primitivas*, poseen área mínima pero en general, de manera aislada, es difícil identificar en ellas las simetrías de la red de Bravais. El caso m_4 es la celda de Voronoi (también conocida como celda

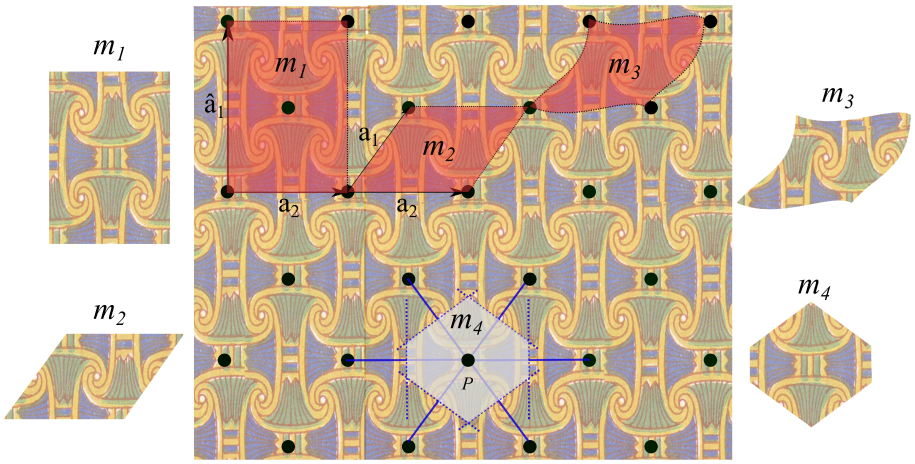

Figura 2.3: Diferentes celdas unidad para una geometría de Escher.

Wigner-Seitz). La misma tiene dos propiedades importantes en el contexto de este trabajo:

- Posee el volumen mínimo, es decir es una celda unidad primitiva.
- Tiene la misma simetría que la red de Bravais sobre la que es construida.

El dominio de dicha celda es determinado mediante el siguiente procedimiento: el punto P de la red es conectado con todos aquellos puntos cercanos (líneas azules) y se trazan líneas normales a estas conexiones (líneas de trazo) que pasan por el centro. El volumen más pequeño encerrado por estas líneas (superficie gris) constituye el dominio de la celda Voronoi. En la Fig. 2.2 puede apreciarse la construcción de las celdas para cada una de las cinco clases de red de Bravais en el

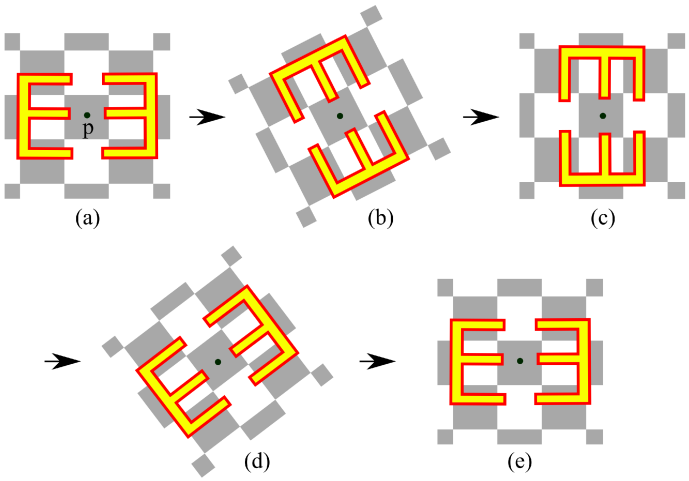

Figura 2.4: Aplicación de simetría de punto: Rotación de 180° alrededor del eje p normal al plano. Entre *(a)* se grafica la configuración inicial. Entre *(b)* y *(d)* se ve el proceso de rotación. Por último, en *(e)* se grafica la configuración final, que es idéntica a la inicial.

plano. La celda de Voronoi es adoptada como dominio de diseño del problema de homogeneización inversa.

2.2.3. Grupo puntual

Un *grupo puntual* es un conjunto de *simetrías de punto* que cumple con las condiciones de grupo, desde el punto de vista algebraico[3]. Una *simetría de punto* es una operación geométrica, sobre la red, con al menos un punto fijo, que deja invariante la geometría de la red. Un ejemplo es el caso de la Fig.2.4-a, a la cual se le aplica una rotación de 180° alrededor del eje p, normal al plano. La operación es aplicada (Fig.2.4-b,-c,-d) y el resultado es la misma geometría inicial Fig.2.4-e. En este caso, el eje p más el ángulo constituyen un *elemento de simetría*.

En el plano existen dos clases de transformaciones típicas con simetría de grupo puntual:

- Rotación alrededor de un eje normal al plano.
- Reflexión con respecto a un eje contenido en el plano.

Dadas las características de simetría translacional de las redes de Bravais, y considerando el teorema de restricción cristalográfica (Bamberg et al., 2003), sólo puede haber un número finito de grupos puntuales para cualquier tipo de red de Bravais. En el plano, los grupos puntuales para las redes son 10, y se encuentran enumerados en la Columna 2 de la Tabla 2.3. En la notación utilizada[4] el número es angulo de rotación, alrededor de un eje ortogonal al plano, que preser-

[3] *Grupo*: estructura algebraica formada por un conjunto no vacío dotado de una operación interna que combina cualquier par de elementos para componer un tercero, dentro del mismo conjunto y que satisface las propiedades asociativa, existencia de elemento neutro y simétrico

[4] Notación Internacional de Hermann-Mauguin, ver Souvignier (2016)

va inalterada la geometría de la red. Además, m y mm implican uno o dos sistemas de ejes de reflexión, respectivamente.

2.2.4. Grupo de Plano

Cuando se combina la simetría de punto con la simetría de traslación, aparece un elemento de simetría adicional, la *reflexión con deslizamiento*. Consiste en la existencia de una reflexión con respecto a un eje, seguida de una traslación a lo largo del mismo eje y de valor igual a la mitad de la distancia de periodicidad (Fig. 2.5).

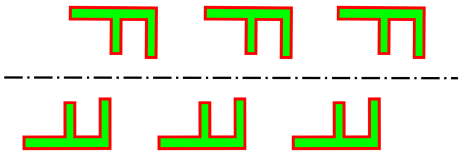

Figura 2.5: Simetría de reflexión con deslizamiento.

Un *grupo de plano* es un conjunto de elementos de simetría de punto más la simetría de traslación[5]. Como consecuencia, en el grupo de plano, hay que incluir las simetrías de reflexión con deslizamiento.

En dos dimensiones existen sólo 17 grupos de plano que caracterizan cualquier microestructura periódica (Bamberg et al., 2003). Ejemplos de todos los casos posibles se muestran en la Fig. 2.6. Es posible ver, para cada caso, la celda Voronoi de la red de Bravais subyacente de la estructura periódica para diferentes patrones. Además se aprecian los elementos de simetrías: Ejes de reflexión, simetrías de rotación de orden n y ejes de reflexión con deslizamiento.

Hasta aquí, un breve análisis de las propiedades de geometrías periódicas mediante la aplicación de conceptos estándar de cristalografía. Como conclusión podemos decir que, dada una geometría periódica, es posible conocer su clasificación: grupo puntual y grupo de plano. Dicha clasificación es función principalmente de los *elementos de simetría* con que la geometría periódica es compatible (ejes de simetría, ejes de rotación). Un desarrollo más profundo de estos conceptos puede encontrarse en el Anexo A.

[5] El *grupo de plano* también cumple las condiciones algebraicas de grupo.

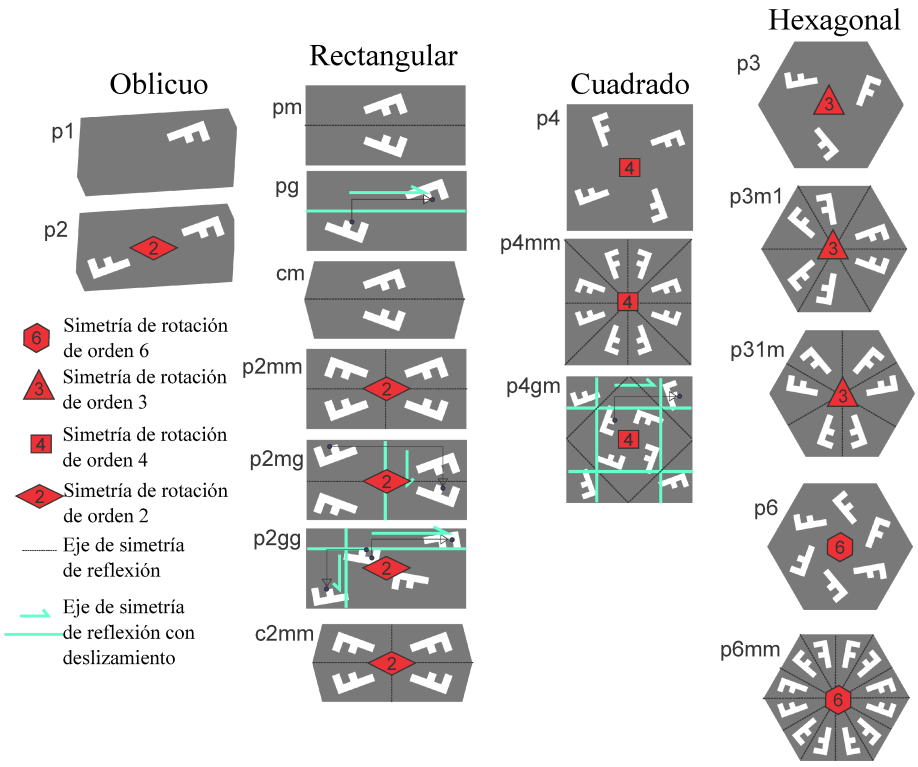

Figura 2.6: Detalle de las celdas Voronoi, con los 17 grupos de plano posibles en $\mathbb{R}^2$. Para cada caso se dibujan los elementos de simetría y el patrón. Los colores blanco y gris representan la distribución de fases en cada celda.

2.3. Clasificación de las *propiedades físicas* y su relación con las simetrías geométricas

2.3.1. Clasificación de los tensores de elasticidad en el plano

Es bien sabido que los tensores constitutivos elásticos pueden ser clasificados según el grupo puntual que los deja invariantes. En la Tabla 2.1 se detallan ejemplos de tensores de transformación correspondientes a cada grupo puntual, también puede verse un ejemplo de geometría para cada caso. Cada tensor de transformación corresponde a una operación de simetría de punto. Partiendo de un tensor elástico *general* (6 coeficientes independientes), y aplicando al mismo diversas operaciones de simetría de punto, se puede demostrar que, en el plano, surgen sólo cuatro tipos de tensores elásticos. Sea un tensor de elasticidad

$$\mathbf{C}^A = \begin{pmatrix} C^A_{1111} & C^A_{1122} & C^A_{1112} \\ C^A_{1122} & C^A_{2222} & C^A_{2212} \\ C^A_{1112} & C^A_{2212} & C^A_{1212} \end{pmatrix}, \tag{2.2}$$

escrito en notación de Voigt. Al tensor $\mathbf{C}^A$ se le aplica una trasformación m, correspondiente a un eje de simetría. El tensor de transformación $\mathbf{Q}$ será el correspondiente al grupo puntual m (fila 3

Tabla 2.1: *Columna 1*: Clases de simetría de los tensores constitutivos en elasticidad plana, expresadas coordenadas naturales. El ángulo de rotación entre $\mathbf{C}$ y $\mathbf{C}_N$ es considerado también una variable independiente del tensor; *Columna 2*: Cada grupo puntual que en el plano cumple con la restricción cristalográfica (Bamberg et al., 2003) (Notación de Hermann-Mauguin); *Columna 3*: Ejemplo de tensores de transformación de 2do orden; *Columna 4*: Ejemplo de una distribución geométrica compatible con el grupo puntual.

Clase de tensor de elasticidad	Grupo puntual	Ejemplos de tensores de transformación	Geometría compatible
$Z2 = \begin{pmatrix} * & * & * \\ & * & * \\ & & * \end{pmatrix}$	1	$\begin{pmatrix} 1 & 0 \\ 0 & 1 \end{pmatrix}$	
	2	$\begin{pmatrix} -1 & 0 \\ 0 & -1 \end{pmatrix}$	
$D2 = \begin{pmatrix} * & * & 0 \\ & * & 0 \\ & & * \end{pmatrix}$	m	$\begin{pmatrix} 1 & 0 \\ 0 & -1 \end{pmatrix}$	
	2mm	$\begin{pmatrix} -1 & 0 \\ 0 & -1 \end{pmatrix}, \begin{pmatrix} 1 & 0 \\ 0 & -1 \end{pmatrix}, \begin{pmatrix} -1 & 0 \\ 0 & 1 \end{pmatrix}$	
$D4 = \begin{pmatrix} * & * & 0 \\ & * & 0 \\ & & * \end{pmatrix}$	4	$\begin{pmatrix} 0 & -1 \\ 1 & 0 \end{pmatrix}$	
	4mm	$\begin{pmatrix} 0 & -1 \\ 1 & 0 \end{pmatrix}, \begin{pmatrix} 1 & 0 \\ 0 & -1 \end{pmatrix}, \begin{pmatrix} -1 & 0 \\ 0 & 1 \end{pmatrix}$	
$O(2) = \begin{pmatrix} * & * & 0 \\ & * & 0 \\ & & \otimes \end{pmatrix}$	3	$\begin{pmatrix} cos(2\pi/3) & -sen(2\pi/3) \\ sen(2\pi/3) & cos(2\pi/3) \end{pmatrix}$	
	3m	$\begin{pmatrix} cos(2\pi/3) & -sen(2\pi/3) \\ sen(2\pi/3) & cos(2\pi/3) \end{pmatrix}, \begin{pmatrix} 1 & 0 \\ 0 & -1 \end{pmatrix}$	
	6	$\begin{pmatrix} cos(\pi/3) & -sen(\pi/3) \\ sen(\pi/3) & cos(\pi/3) \end{pmatrix}$	
	6mm	$\begin{pmatrix} cos(\pi/3) & -sen(\pi/3) \\ sen(\pi/3) & cos(\pi/3) \end{pmatrix}, \begin{pmatrix} 1 & 0 \\ 0 & -1 \end{pmatrix}, \begin{pmatrix} -1 & 0 \\ 0 & 1 \end{pmatrix}$	

de la Tabla 2.1). La transformación toma la siguiente forma en notación indicial:

$$C^B_{ijkl} = Q_{im}Q_{jn}Q_{kp}Q_{lq}C^A_{mnpq}. \tag{2.3}$$

Desarrollando la Ec.2.3 se obtienen las identidades que debe cumplir cada componente de tensor para reflejar la simetría de un grupo puntual m. Por ejemplo, la componente C^B_{1111} se determina según la siguiente expresión:

$$C^B_{1111} = Q_{11}Q_{11}Q_{11}Q_{11}C^A_{1111} + Q_{12}Q_{12}Q_{12}Q_{12}C^A_{2222} + Q_{11}Q_{11}Q_{11}Q_{12}C^A_{1112}... \tag{2.4}$$

Para este caso sencillo, es fácil ver que cualquier término para Q_{ab} con $a \neq b$ será nulo, por lo tanto se debe cumplir que $C^B_{1111} = C^A_{1111}$. Todas las identidades a cumplir serán:

$$\begin{aligned}
C^B_{1111} &= C^A_{1111} \\
C^B_{2222} &= C^A_{2222} \\
C^B_{1122} &= C^A_{1122} \\
C^B_{1212} &= C^A_{1212} \\
C^B_{1112} &= -C^A_{1112} = 0 \\
C^B_{2212} &= -C^A_{2212} = 0
\end{aligned} \tag{2.5a}$$

Es decir:

$$\mathbf{C}^B = \begin{pmatrix} C^B_{1111} & C^B_{1122} & 0 \\ C^B_{1122} & C^B_{2222} & 0 \\ 0 & 0 & C^B_{1212} \end{pmatrix} = \begin{pmatrix} C^A_{1111} & C^A_{1122} & 0 \\ C^A_{1122} & C^A_{2222} & 0 \\ 0 & 0 & C^A_{1212} \end{pmatrix} = \mathbf{C}^A \tag{2.6}$$

Entonces, el tensor que cumpla con esta identidad refleja la simetría geométrica del grupo puntual m. Este procedimiento puede verse desarrollado en Ting (1996) y en Newnham (2005). Para tensores de elasticidad en 2 dimensiones, la clasificación, de menor a mayor clase de simetría es: Anisotrópico (Z_2), Ortotrópico (D_2), Tetragonal (D_4) e Isotrópico $(O(2))$. En la Tabla A.1 se detalla la relación entre coeficientes para las distintas clases de simetrías del tensor elástico. Los números entre paréntesis indican la cantidad de coeficientes independientes que definen en cada caso al tensor.

El mencionado criterio de clasificación impone, implícitamente, un sistema de coordenadas alineado con los planos de simetrías de los grupos puntuales, que en el contexto de esta Tesis es llamado sistema de *coordenadas naturales* (ver Auffray y Ropars (2016) y Anexo B). En adelante

Tabla 2.2: Clases de simetría de los tensores constitutivos en elasticidad plana, expresadas coordenadas naturales, $\mathbf{C}_N$: $O(2)$ para tensores isotrópicos, D_4 para tensores tetragonales, D_2 para tensores ortotrópicos y Z_2 para tensores totalmente anisotrópicos. Entre paréntesis se detalla el número de coeficientes independientes para cada caso. El ángulo de rotación entre $\mathbf{C}$ y $\mathbf{C}_N$ es considerado también una variable independiente del tensor.

Clasificación de los tensores de elasticidad			
$O(2)$ (2)	D_4 (4)	D_2 (5)	Z_2 (6)
$\begin{pmatrix} C_1 & C_2 & 0 \\ C_2 & C_1 & 0 \\ 0 & 0 & (C_1 - C_2) \end{pmatrix}$	$\begin{pmatrix} C_1 & C_2 & 0 \\ C_2 & C_1 & 0 \\ 0 & 0 & C_3 \end{pmatrix}$	$\begin{pmatrix} C_1 & C_2 & 0 \\ C_2 & C_4 & 0 \\ 0 & 0 & C_3 \end{pmatrix}$	$\begin{pmatrix} C_1 & C_2 & C_5 \\ C_2 & C_1 & -C_5 \\ C_5 & -C_5 & C_3 \end{pmatrix}$

se utiliza la notación $\mathbf{C}_N$ para indicar que un tensor elástico se encuentra expresado matricialmente en coordenadas naturales.

Veamos un ejemplo sencillo de similitudes entre propiedades físicas y las simetrías geométricas. Sea la geometría $\mathcal{G}$ de la Fig. 2.7 y su tensor elástico efectivo representado en notación de

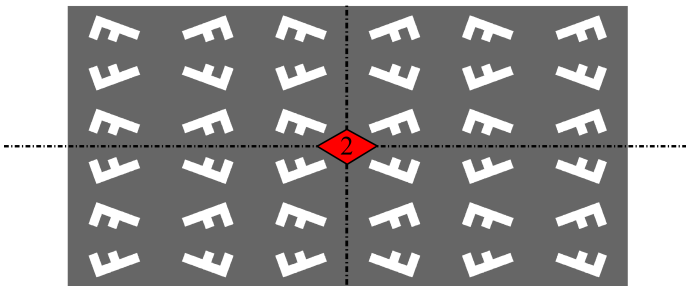

Figura 2.7: Geometría $\mathcal{G}$.

Voigt en la Ec.2.7.

$$\mathbf{C}^{\mathcal{G}} = \begin{pmatrix} 1.0000 & 0.1929 & 0.0000 \\ 0.1929 & 0.7839 & 0.0000 \\ 0.0000 & 0.0000 & 0.3692 \end{pmatrix}. \tag{2.7}$$

Es posible ver que la geometría se mantiene invariante ante un eje de reflexión horizontal, un eje de reflexión vertical y una rotación de magnitud π. Esto corresponde a un grupo puntual $2mm$. Entonces, al aplicar a $\mathbf{C}^{\mathcal{G}}$ los tensores de transformación adecuados (fila 6 de la Tabla 2.1), el mismo se mantendrá invariante.

2.3.2. Relación entre propiedades físicas y simetrías geométricas

Lo mostrado en el ejemplo es un caso particular del teorema de Neumann:

Los elementos de simetría de cualquier propiedad física (óptica, magnética, térmica, mecánica) de un cristal deben incluir los elementos de simetría del grupo puntual del cristal, (Nye, 2006).

El teorema de Neumann expresa una implicancia unidireccional: la simetría geométrica implica una simetría física igual (idéntico grupo puntual) o más alta (con más elementos de simetría).

En el ejemplo anterior, estos conceptos se interpretan de la siguiente manera (ver Tabla A.1): si la microarquitectura corresponde a un grupo de plano *p2mm*, cuyo grupo puntual es un *2mm*, se puede afirmar que su tensor elástico efectivo tiene, al menos, una clase de simetría D_2. En el Anexo A se presentan validaciones numéricas de estas relaciones para los 17 casos de grupos de plano.

2.4. Tabla resumen de las relaciones entre *propiedades físicas* y *propiedades geométricas*

Los conceptos desarrollados se encuentran resumidos en la Tabla 2.3. Allí se detalla la relación entre las cuatro clases de simetrías de los tensores, los grupos puntuales, grupos de plano y las redes de Bravais que corresponden a cada clase de simetría elástica.

Tabla 2.3: Las clases de simetrías elásticas (Columna 1) se determinan a través del grupo puntual (Columna 2). Además, cada uno de los diecisiete grupos de planos (Columna 3), corresponden a un grupo puntual. Adicionalmente, cada grupo de plano es compatible con varias redes de Bravais (Columna 4).

Clase de simetría elástica	Grupo puntual	Grupo de plano	Redes de Bravais y celdas Voronoi compatibles.				
			Oblicua (O)	Rectangular primitiva (Rp)	Rectangular centrada (Rc)	Cuadrada (S)	Hexagonal (H)
Z_2	1	p1	⬣	▬	⬣	■	⬣
	2	p2					
D_2	m	pm		▬		■	
		pg					
		cm			⬣	◆	⬣
	2mm	p2mm		▬		■	
		p2mg					
		p2gg					
		c2mm			⬣	◆	⬣
D_4	4	p4				■	
	4mm	p4mm					
		p4gm					
$O(2)$	3	p3					
	3m	p3m1					
		p31m					⬣
	6	p6					
	6mm	p6mm					

La forma de aplicación de las relaciones expresadas en la Tabla 2.3 puede verse en el siguiente ejemplo: Sea un tensor $\hat{\mathbf{C}}^{D_2}$ (con simetría D_2), del cual se quiere diseñar su microarquitectura. Si como dominio de diseño Ω_μ (microcelda) se adopta una celda Voronoi construida sobre una red de Bravais Rp, y ademas se impone simetría (distribución espacial de fases) que satisfaga un grupo plano pm (por ejemplo, con un eje de simetría horizontal) en el interior de Ω_μ, es posible garantizar que el tensor constitutivo efectivo de la microcelda tendra simetría D_2.

Los procedimientos de diseño de microarquitecturas, que están basados (y que son concordantes) con los resultados descritos en la Tabla 2.3, constituyen el fundamento principal del aporte de esta tesis. Las relaciones que se pueden extraer de la información contenida en dicha Tabla, permiten imponer restricciones geométricas al problema de optimización, de forma tal de garantizar la clase de simetría que caracteriza al tensor elástico objetivo. Esas restricciones son:

- **Forma de la microcelda**.
- **Simetrías** del grupo plano que gobierna la distribución de material.

A estas restricciones se suman otros conceptos que serán desarrollados a continuación.

2.5. Construcción de una base de datos en función de redes de Bravais

Es importante resaltar que la relación de lados en los casos de celdas de redes O, Rc y Rp no es un parámetro que dependa exclusivamente de la clase de simetría del tensor. En el ejemplo del tensor $\hat{\mathbf{C}}^{D_2}$ no es conocida *a priori* la relación de lados que requiere la red de Bravais. Por ello, para evitar una elección arbitraria, se desarrolló una base de datos de tensores elásticos efectivos sobre la cual se definen las microceldas a utilizar en la optimización.

2.5.1. Parametrización de las Redes de Bravais

Parametrizar las redes de Bravais implica parametrizar la celda que se vaya a utilizar como dominio de diseño. En este caso serán las celdas Voronoi. Como fue expuesto en la Ec.(2.1), una red de Bravais en $\mathbb{R}^2$ puede ser caracterizada por dos vectores primitivos $\mathbf{a}_1$ y $\mathbf{a}_2$. En adelante utilizaremos la siguiente parametrización:

$$\omega = \|\mathbf{a}_2\|/\|\mathbf{a}_1\| \ , \tag{2.8}$$

$$\varsigma = \arccos\left[(\mathbf{a}_2 \cdot \mathbf{a}_1)/(\|\mathbf{a}_2\|\|\mathbf{a}_1\|)\right] \ , \tag{2.9}$$

donde cada par de valores (ω, ς) define una red de Bravais. En la Fig.2.8-a se muestra un dominio acotado (zona gris) de los parámetros (ω, ς). Es fácil probar que el rango (ω, ς) contenido en dicho dominio acotado representa la totalidad de redes de Bravais posibles en el plano. En la Fig.2.8-b se esquematizan las celdas Voronoi para distintos sectores del dominio acotado de la red de Bravais.

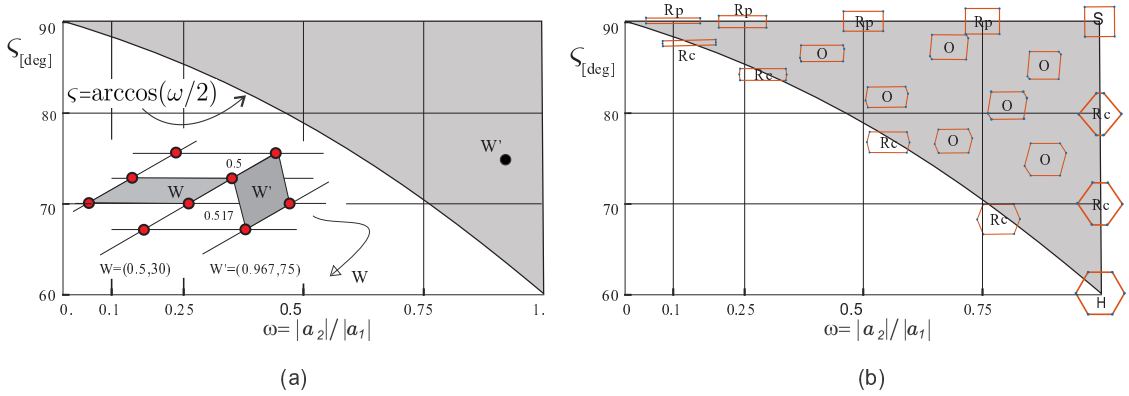

Figura 2.8: Espacio $\mathbb{R}^2$ de los parámetros (ω, ς) que caracterizan la red de Bravais. a) La zona gris corresponde al dominio reducido. Todo punto fuera de dicho dominio (W) representa una red de Bravais que puede ser obtenida mediante un punto interior del dominio (W'). b) Representación esquemática de celdas Wigner-Seitz para distintos puntos (ω, ς): O (oblicua), Rc (rectangular centrada), Rp (rectangular primitiva), S (cuadrada) y H (hexagonal).

Se aprecia que todas las celdas posibles para los casos de redes O se encuentran dentro del dominio. Las celdas de redes Rc se construyen con puntos ubicados sobre el lado vertical ($\omega = 1$) y la curva inferior ($\varsigma = arccos(\omega/2)$). El lado superior ($\varsigma = 90$) corresponde a redes Rp. Y por último los vértices superior ($\varsigma = 90, \omega = 1$) e inferior ($\varsigma = 60, \omega = 1$), corresponden a redes S y redes H, respectivamente.

2.5.2. Construcción de una base de datos

La base de datos se genera de forma *off-line*, mediante la resolución de un amplio rango de ejemplos parametrizados. Para el cálculo se utiliza un muestreo de microceldas, las cuales varían tanto en su forma externa, como en distribución interna de material. A continuación una breve descripción de los parámetros que identifican cada entrada de la base de datos:

- **Forma de la microcelda**. Mediante la variación del par (ω, ς) dentro del dominio acotado, Fig.2.8.

- **Distribución de material dentro del dominio**, Figs.2.9-a y 2.9-b. Se trabaja con los casos mas simples de distribución de material: El patrón de la Fig. 2.9-a corresponde a barras de igual sección distribuidas en todo el borde de la celda. El patrón de la Fig.2.9-b contiene re-entrancias en los vértices, con el fin de alcanzar comportamientos similares al de materiales auxéticos (Kolken y Zadpoor, 2017; Lakes, 1987).

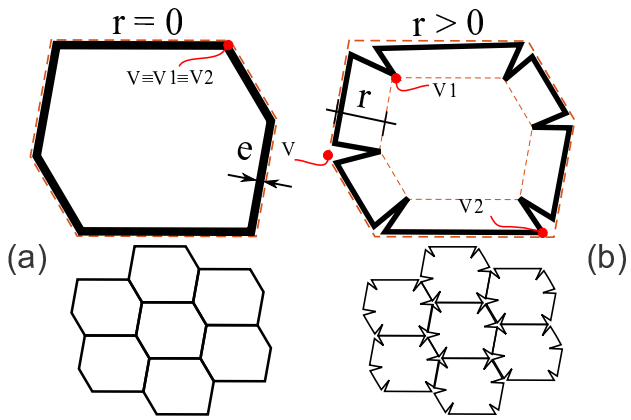

Figura 2.9: Distribución de material en microceldas parametrizadas. *a)* Barras de igual espesor e distribuidas en el borde de la microcelda. *b)* Los vértices $V1$ no coinciden con los vértices de la microcelda. Existe un desplazamiento de los $V1$ hacia el interior de la microcelda. Con esta topología se busca lograr compuestos con módulo de Poisson negativo. Debajo de cada microcelda se aprecia la microarquitectura ensamblada.

- **Fracción de volumen de material sólido** f. Este parámetro determina el espesor e de las barras.

Finalmente, todos los tensores elásticos homogeneizados contenidos en la base de datos pueden ser caracterizados por cuatro parámetros: ω y ς definen la forma de la celda Voronoi, f define la fracción de volumen de sólido y P define el patrón *a* o *b*. Cada caso contenido en la base de datos es identificado con la notación $\mathbf{C}^h_{db}(\omega, \varsigma, f, P)$. Luego de definido el tensor elástico objetivo $\hat{\mathbf{C}}_N$, se realiza una búsqueda en la base de datos mediante la resolución de un problema de minimización discreto:

$$\zeta = \arg\left\{ \min_{\zeta} \|\mathbf{C}^h_{db}(\zeta) - \frac{1}{E_1}\hat{\mathbf{C}}_N\| \right\}, \tag{2.10}$$

donde $\zeta := \{\omega, \varsigma, P, f\}$, y el factor que escala el tensor elástico objetivo, E_1, es el módulo de Young de la fase rígida a utilizar en el diseño. La búsqueda del tensor elástico $\mathbf{C}^h_{db}(\zeta)$ se realiza dentro del conjunto de tensores elásticos que poseen la misma simetría que el tensor elástico objetivo $\hat{\mathbf{C}}_N$. La solución de esta búsqueda arroja dos datos: *i)* la relación de lados de la microcelda, para los casos O, Rc y Rp; y *ii)* la distribución inicial de material para el problema de optimización topológica.

2.6. Reglas de diseño para algoritmos de optimización topológica

En base a los conceptos presentados, se proponen cuatro reglas empíricas para facilitar el proceso de diseño inverso de materiales periódicos mediante optimización topológica:

$\Re_1$ El problema de optimización se resuelve en coordenadas naturales. En las formulaciones de problemas de optimización presentadas en el Capítulo 1, Ecs. 1.2 y 1.3 se reemplaza $\hat{\mathbf{C}}$ por

$\hat{\mathbf{C}}_N$. El tensor $\hat{\mathbf{C}}_N$ es obtenido mediante lo propuesto por Auffray y Ropars (2016), cuyo algoritmo se detalla en el Anexo B.

$\Re_2$ En función de la clase de simetría a la que pertenezca el tensor objetivo $\hat{\mathbf{C}}_N$, mediante la Tabla 2.3 se adopta la celda Voronoi a utilizar como dominio de diseño Ω_μ.

$\Re_3$ La relación de aspecto de la celda unidad se puede determinar mediante la búsqueda definida en la Ec. (2.10). La relación de aspecto es variable en los casos de celdas de redes oblicuas, rectangular centradas y rectangular primitivas (Fig. 2.2).

$\Re_4$ Los ejes de simetría a imponer a la topología interior (Columna 3, Tabla 2.3) se eligen en función de la clase de simetría a la que pertenezca el tensor objetivo $\hat{\mathbf{C}}_N$.

Las reglas $\Re_1$, $\Re_2$ y $\Re_3$ constituyen un pre-proceso de la optimización topológica. En cambio la regla $\Re_4$ consiste en una restricción geométrica a imponer durante el proceso de optimización topológica. En los próximos Capítulos se presentan aplicaciones de estas reglas en distintos problemas.

En el Anexo A las definiciones dadas en el presente Capítulo son desarrolladas con mayor profundidad. Además son presentados distintos ejemplos de validación numérica y de aplicación, utilizando distintos algoritmos como derivada topológica y SIMP. Además, la implementación del procedimiento de diseño fue puesta a disposición a la comunidad científica mediante un repositorio de acceso libre. En el Anexo E se encuentra la documentación correspondiente para el uso de dichas herramientas computacionales.

2.6.1. Procedimiento de aplicación de la regla de diseño $\Re_4$

La regla de diseño $\Re_4$ consiste en imponer una simetría de grupo de plano a la topología de una microarquitectura en el marco del algoritmo de optimización topológica. Para ello, al final de cada iteración, la variable de diseño es actualizada de forma tal de satisfacer los requerimientos de simetría del grupo de plano a imponer. El procedimiento se detalla a continuación, ejemplificado mediante un dominio cuadrado discretizado con elementos finitos cuadrados, Fig.2.10.

Previo al inicio de la optimización:

a1 Se determina el conjunto de puntos del dominio espacial relacionados entre sí según las operaciones de simetría del grupo espacial. En el ejemplo de la Fig. 2.10 se tiene el conjunto de elementos *master*, $\mathbf{M} = \{e : 1..8\}$, y el conjunto de elementos *slave*, $\mathbf{S} = \{e : 9..16\}$. En dicho ejemplo, la relación se da: $M1 - S10$, $M2 - S9$, $M3 - S12$,... etc.

Luego de iniciado el proceso de optimización, en cada iteración se procede de la siguiente manera:

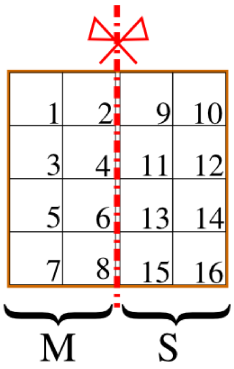

Figura 2.10: Ejemplo simplificado de una discretización de elementos finitos, donde se definen elementos *master* $\mathbf{M} = \{e : 1..8\}$, y elementos *slave* $\mathbf{M} = \{e : 9..16\}$, según una operación de simetría (eje de reflexión vertical)

b1 Se calculan las sensibilidades en cada elemento.

b2 Se calcula el promedio de las sensibilidades entre los elementos relacionados a través de las operaciones de simetría (punto *a1*).

b3 Se actualizan las variables de diseño, solo para el dominio *master*, mediante la actualización correspondiente al algoritmo de minimización.

b4 En los puntos *slave* se copian los valores actualizados de los puntos *master*.

Capítulo 3

Diseño de metamateriales para estructuras elásticas

3.1. Introducción

El objetivo de este Capítulo es presentar un procedimiento de optimización multiescala débilmente acoplado, para el diseño de metamateriales para estructuras elásticas de dos dimensiones.

En la macroescala se busca optimizar las componentes del tensor elástico efectivo $\mathbf{C}(\mathbf{x})$ en cada punto $\mathbf{x}$ del dominio macro del problema, para satisfacer un criterio de optimización dado. Luego, en la microescala se plantea la optimización topológica de la microestructura relacionada con el tensor elástico efectivo, para cada punto $\mathbf{x}$ de la escala macro. Para este último caso se utilizan las técnicas presentadas en el Capítulo 1 y las reglas de diseño introducidas en el Capítulo 2. El Anexo B se exponen con mayor detalle los conceptos y resultados del presente Capítulo.

3.2. Optimización Libre de Material

En el marco de la optimización estructural, la técnica de diseño estructural denominada Optimización Libre de Material (*Free Material Optimization* - FMO, ver Bendsøe et al. (1994), Zowe et al. (1997)) ha tomado gran interés en los últimos años. Mediante esta herramienta se obtiene la distribución óptima de las propiedades efectivas del material dentro de un dominio macro Ω. Esto es, se resuelve un problema de optimización donde las variables de diseño son las componentes del tensor constitutivo elástico $\mathbf{C}$ en cada punto $\mathbf{x}$ del dominio Ω. En la optimización en la escala macro son tenidas en cuenta restricciones de manufacturabilidad, para luego, en una escala micro, realizar el diseño de la microarquitectura en cada punto $\mathbf{x}$.

La formulación de FMO utilizada en el presente trabajo de Tesis, es la siguiente:

$$\min_{\mathbf{u}\in\mathcal{V}^{eq},(\hat{\mathbf{C}})_{ijkl}} \int_{\Omega} \mathrm{tr}\,(\hat{\mathbf{C}})\, dV \tag{3.1a}$$

$$\text{tal que:} \quad \sum_{k=1}^{n_{load}} w_k \left\langle \mathbf{f}_k, \mathbf{u}_k \right\rangle \leq \bar{f_u}\ , \tag{3.1b}$$

$$\underline{\rho} \leq\ \mathrm{tr}\,(\hat{\mathbf{C}}) \leq \bar{\rho}\ ,\ , \tag{3.1c}$$

$$\hat{\mathbf{C}} \succeq 0, \tag{3.1d}$$

donde el término $\mathrm{tr}\,(\hat{\mathbf{C}})$ es la traza del tensor constitutivo elástico en cada punto. Las variables de diseño del problema son los desplazamientos $\mathbf{u}$ y las componentes del tensor elástico $(\hat{\mathbf{C}})_{ijkl}$ en cada punto $\mathbf{x}$. $\mathcal{V}^{eq}$ es el espacio de desplazamientos admisibles que determinan campos de deformación y de tensión que están en equilibrio con las fuerzas externas $\mathbf{f}_k$. El problema se resuelve en el dominio de diseño Ω.

En la restricción 3.1b se impone una cota superior a la flexibilidad de la estructura, mediante un peso w_k aplicado a cada estado de cargas n_{load}. En 3.1c se plantean restricciones de cota inferior $\underline{\rho}$ y superior $\bar{\rho}$ para la traza $\mathrm{tr}\,(\hat{\mathbf{C}})$. La cota inferior es requerida para evitar singularidades en la solución del equilibrio estructural, mientras que el valor superior es determinado según el mayor autovalor del tensor elástico isotrópico del material del cual estará compuesta la fase resistente M_1 de la microestructura (Schury, 2013). Por último, en 3.1d se restringe al tensor elástico $\hat{\mathbf{C}}$ a ser semidefinido positivo.

La solución del problema 3.1 da como resultado la distribución espacial óptima de las propiedades efectivas, representadas con $\hat{\mathbf{C}}(\mathbf{x})$, para cada punto $\mathbf{x}$ del dominio Ω. Sin embargo, para que estos resultados sean apropiados para el método de diseño propuesto en la presente Tesis, es necesario aplicar un trabajo de postproceso. El fundamento del postproceso es explicado en las siguientes subsecciones. Detalles sobre la implementación de la formulación 3.1 pueden ser encontrados en el Anexo B.

Dominio reducido Ω^{red}

La solución del problema de FMO, Ec.3.1, arroja sectores de Ω donde los tensores $\hat{\mathbf{C}}(\mathbf{x})$ poseen un valor de traza muy bajo. Esto se traduce en microceldas con un contenido de fase rígida casi nulo cuando se diseña la microarquitectura. Es viable considerar que dichos sectores no contribuyen de manera significativa a la estructura macro. Por ende, en una primer solución de FMO, estos sectores son identificados y removidos, generando así un dominio de diseño Ω^{red} para una segunda etapa.

Materiales pentamodales y restricción de manufacturabilidad

Es sabido que mediante el FMO se obtienen materiales pentamodales, como respuesta al problema de mínimo peso y mínima flexibilidad (Bendsøe et al., 1994). Un material pentamodal es un metamaterial que tiene un modo de deformación rígida y en el resto de las direcciones es fácilmente deformable, ver Milton y Cherkaev (1995). Esto se traduce en un tensor efectivo elástico con sólo un autovalor no-nulo. Para casos en dos dimensiones, estos materiales tienen un modo de deformación rígida y dos modos de deformación flexible[1]. El tensor de elasticidad de un material pentamodal puede ser caracterizando de la siguiente forma:

$$\mathbf{C} = \mathbf{S} \otimes \mathbf{S}, \tag{3.2}$$

donde $\mathbf{S}$ es un tensor de segundo orden simétrico, $\otimes$ representa un producto tensorial. En función de lo expresado en 3.2, para cualquier deformación $\boldsymbol{\varepsilon}$, la tensión $\boldsymbol{\sigma}$ se calcula como:

$$\boldsymbol{\sigma} = \mathbf{C} : \boldsymbol{\varepsilon} = (\mathbf{S} : \boldsymbol{\varepsilon})\mathbf{S} = -p\mathbf{S} \ , \tag{3.3}$$

donde

$$p = -(\mathbf{S} : \boldsymbol{\varepsilon}) \tag{3.4}$$

es un escalar que representa una pseudo-presión. En la Ec.3.3, el símbolo $(:)$ representa la traza del producto tensorial. En función de la Ec.3.3, es notorio que materiales bimodales solo pueden soportar tensiones proporcionales a $\mathbf{S}$, siendo p un factor de proporcionalidad.

Por otro lado, el diseño de estos metamateriales, caracterizados por autovalores nulos, es difícil de llevar a cabo. Por ello, para facilitar el diseño de su microarquitectura, se impone la restricción de manufacturabilidad propuesta por Schury (2013), mediante la introducción del siguiente cambio en la restricción 3.1d:

$$(\hat{\mathbf{C}} - \Phi\mathbf{I}) \succeq 0. \tag{3.5}$$

Mediante esta restricción, el mínimo autovalor de $\hat{\mathbf{C}}$ será mayor o igual al escalar Φ, lo cual facilita el diseño inverso.

Clases de simetrías de los tensores elásticos.

La formulación de FMO presentada no restringe las posibles simetrías de los tensores $\hat{\mathbf{C}}(\mathbf{x})$. Es decir, las componentes $(\hat{\mathbf{C}})_{ijkl}$ son totalmente independientes y por ende, en los puntos del

[1] Estrictamente, en dos dimensiones, estos materiales se llamarían bimodales, pero a fines prácticos se usará el término pentamodal para ambos casos, dos y tres dimensiones

dominio, pueden obtenerse tensores de cualquiera de las cuatro clases de simetrías detalladas en la Tabla 2.3 (Capítulo 2). La determinación de la clase de simetría es necesaria para aplicar a la optimización topológica las reglas de diseño propuestas en esta Tesis (ver Sección 2.6). Para este fin, el procedimiento propuesto por Auffray y Ropars (2016) fue implementado como parte del postproceso de FMO. Mediante dicho procedimiento es posible determinar su expresión en coordenadas naturales y su clase de simetría. Su descripción puede verse en el Anexo B.

3.3. Secuencia de optimización multiescala.

La secuencia de diseño consiste en realizar una doble optimización, primero en la macroescala y luego en la microescala. Se parte de un dominio macroscópico Ω donde se quiere diseñar una estructura sometida a cierto estado de cargas. Luego, para dicha estructura se diseña la microarquitectura del material en cada punto $\mathbf{x}$ de Ω. El procedimiento se compone de tres etapas y son explicadas a continuación:

Etapa i) **Macroescala - Primer problema de FMO:** Se resuelve el problema planteado en la Ec.3.1, en un dominio macroscópico Ω, Fig.B.3-a. Como solución se obtiene la distribución óptima de las propiedades efectivas en cada punto $\mathbf{x}$, siendo $\hat{\mathbf{C}}$ definido positivo para todo $\mathbf{x}$, Fig.B.3-b. Luego, considerando que valores bajos de la $tr(\hat{\mathbf{C}})$ representan sectores con material escaso o casi nulo, los subdominions de Ω que satisfacen la condición

$$tr(\hat{\mathbf{C}}) < \epsilon E_1 \tag{3.6}$$

son removidos del dominio de diseño del problema macro[2]. De esta manera se obtiene un nuevo dominio Ω^{red} igual o más pequeño que el original.

Etapa ii) **Macroescala - Segundo problema de FMO:** Sobre el dominio Ω^{red}, Fig.B.3-c, se resuelve nuevamente el problema FMO. Pero en este caso la restricción de la Ec.3.1d es reemplazada por la Ec.3.5. Como resultado de este segundo problema de FMO se obtiene una nueva distribución del tensor elástico $\mathbf{C}^*$ en cada punto $\mathbf{x}$ del dominio Ω^{red}. Este campo de tensores elásticos óptimos $\mathbf{C}^*$ es el que se adopta como tensor elástico objetivo en el diseño de la microarquitectura, en cada punto $\mathbf{x}$[3].

Etapa iii) **Microescala - Diseño inverso:** Por último, en cada punto $\mathbf{x}$ del dominio Ω^{red} se busca una microarquitectura cuyo tensor efectivo $\mathbf{C}^h$ sea lo mas cercano posible al tensor elástico

[2]El parámetro ϵ ($0 < \epsilon \ll 0$) es un valor empíricamente adoptado. El parámetro E_1 es el módulo de Young de la fase rígida de la microescala.

[3]La obtención del campo $\mathbf{C}^*$ se realiza mediante un procedimiento, cuyas precisiones es posible encontrar en el Anexo B, Secciones 3.2.2 y 3.3.

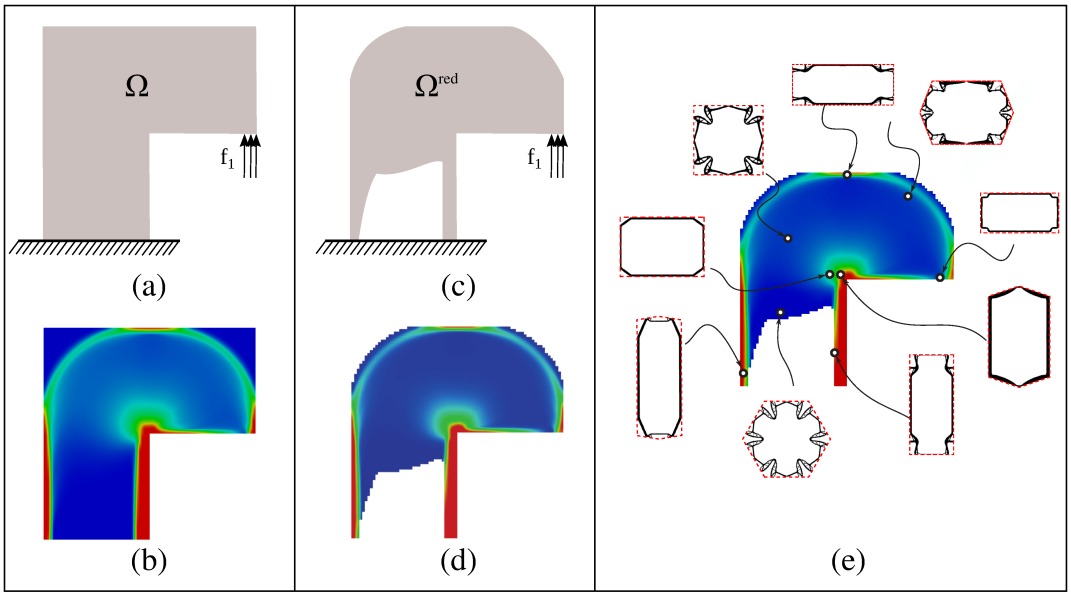

Figura 3.1: Secuencia de optimización multiescala: a) Dominio de diseño Ω para el primer problema de FMO, b) distribución de la traza de los tensores elásticos efectivos, c) dominio de diseño Ω^{red} para el segundo problema de FMO, d) distribución de la traza de los tensores elásticos efectivos en la segunda etapa, e) diseño de la microarquitectura para cada punto del dominio Ω^{red}.

objetivo $\mathbf{C}^*$, Fig.B.3-e. La microarquitectura es diseñanda mediante las técnicas presentadas en el Capítulo 1 y aplicando las reglas de diseño propuestas en la Sección 2.

3.4. Resultados y discusión

3.4.1. Aplicación de la técnica FMO - *Etapas i)* y *ii)*

En la Fig.B.3 se presenta la secuencia de resultados de FMO para una viga L empotrada en su base y con carga en el extremo del voladizo. En las Figs.B.3-a y B.3-c se aprecian los dominios para las etapas *i)* y *ii)*, respectivamente, de la secuencia de diseño. En las Figs.B.3-b y B.3-d se expone, para cada caso, la distribución final de la traza del tensor elástico efectivo en cada punto del dominio.

En el Anexo B se presenta una profundización de estos resultados y también otros ejemplos típicos de problemas de diseño estructural.

3.4.2. Diseño de la microarquitectura - *Etapa iii)*

Para el diseño de la microarquitectura se plantea el siguiente problema de minimización:

$$\begin{aligned} &\min_{\chi} \int_{\Omega_\mu} \chi \, d\Omega \\ &\text{such that: } \|\mathbf{C}_N^h(\chi) - \mathbf{C}_N^*\| = 0 \, . \end{aligned} \tag{3.7}$$

En el Anexo B se dan detalles de la implementación del algoritmo para resolver este problema. Las reglas de diseño introducidas en la Sección 2.6 fueron utilizadas de la siguiente manera:

- $\Re_1$*:* Mediante la aplicación del algoritmo de Auffray, el tensor objetivo $\mathbf{C}^*$ es expresado en coordenadas naturales, $\mathbf{C}^*_N$.
- $\Re_2 \& \Re_3$*:* Se definen la forma y las dimensiones de la celda unidad a utilizar para el diseño, a la vez que es determinada la configuración inicial del problema de optimización, mediante el uso de la base de datos, ver Ec. 2.5.2.
- $\Re_4$*:* Se eligen las restricciones geométricas a imponer a la optimización topológica, es decir los ejes de simetría en el dominio de diseño Ω_μ.

Resultados

En la Fig.3.2 se aprecian algunas microarquitecturas diseñadas. Las celdas unidad son graficadas de tal forma que la dirección horizontal coincide con una dirección de la base normal del tensor homogeneizado. En la misma figura se grafican, para cada caso, la microarquitectura ensamblada y orientada según ejes globales cartesianos del problema macro. En la Fig.3.3 se aprecia la comparación de algunos casos diseñados (Columna 3) con sus respectivas configuraciones iniciales (Columna 2). En la primer columa se detalla la clase de simetría del tensor objetivo correspondiente. En la tabla 3.1 se muestran las componentes del tensor objetivo $\mathbf{C}^*_N$, el tensor inicial de la base de datos $\mathbf{C}^h_{db}$ y el tensor obtenido $\mathbf{C}^h_N$ en algunos de los sectores mencionados. Cabe remarcar que, aún cuando el valor de la configuración inicial $\mathbf{C}^h_{db}$ es cercana al objetivo, el algoritmo de optimización mejora notablemente los resultados sin realizar cambios bruscos de la distribución inicial de material.

3.5. Conclusiones

En este Capítulo se presenta un procedimiento de diseño con enfoque multiescala, acoplando las técnicas de FMO y optimización de topología mediante derivada topológica. Se presentan resultados del diseño de microarquitecturas elásticas, llevados a cabo mediante uso de las reglas de diseño propuestas en la Sección 2.6.

La formulación débilmente acoplada del problema de optimización multiescala no es un aporte en sí mismo, dado que existen casos en la bibliografía que trabajan de esta manera (Schury, 2013). Sin embargo, en la secuencia de diseño se proponen conceptos novedosos, como la reducción del domino de diseño en FMO. Otro concepto importante es la resolución del problema de diseño

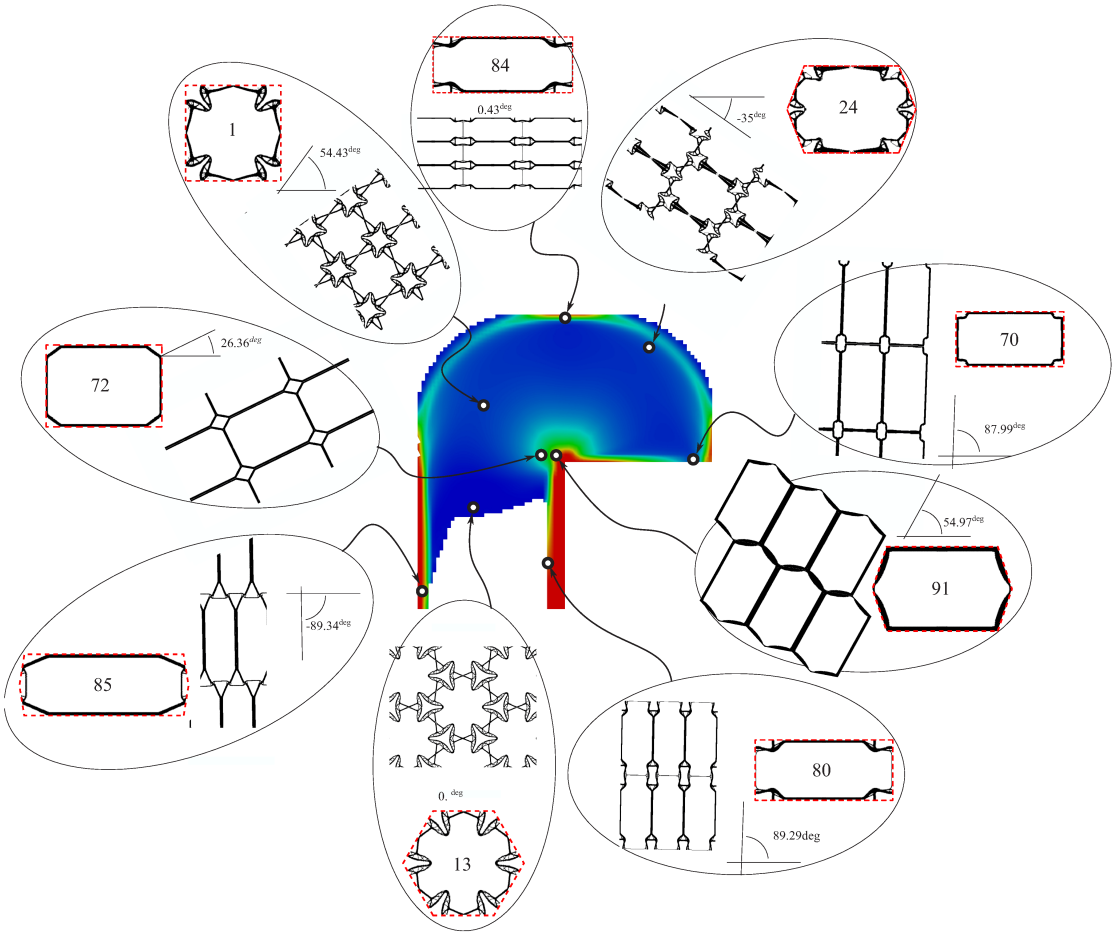

Figura 3.2: Microarquitecturas diseñadas en varios sectores de la viga L. La dirección horizontal en cada microcelda coincide con una dirección de la base normal del tensor homogeneizado. Se grafican además el ensamble de las microceldas, orientadas según ejes cartesianos del problema macro.

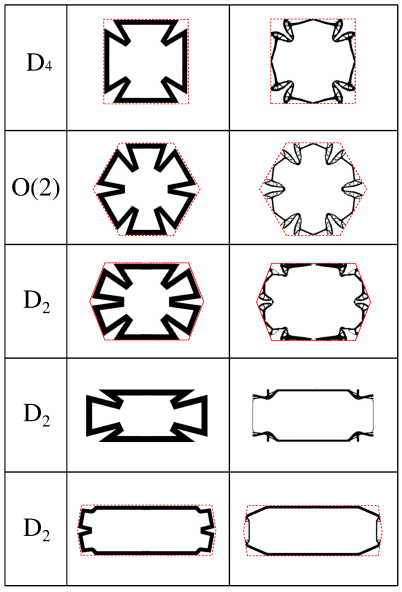

Figura 3.3: Detalle de la topología final en algunos casos (Columna 3), en comparación con la solución inicial obtenida de la base de datos (Columna 3). En la primer columna se detalla la clase de simetría en cada caso.

Tabla 3.1: Resultados de la optimización topológica. $\mathbf{C}^*$ tensor elástico objetivo, $\mathbf{C}^h_{db}$ tensor elástico homogeneizado de la configuración inicial (base de datos), $\mathbf{C}^h_N$ tensor elástico homogeneizado de la configuración solución del problema de optimización (los valores son multiplicados por un factor 1000 ($E_0 = 1.MPa$). En la última columna se detalla la fracción de volumen de la rígida.

Sector		C_{1111}	C_{2222}	C_{1212}	C_{2212}	C_{1112}	C_{1122}	Frac. de Vol.
1	$\mathbf{C}^h_{db}$	7.93	7.93	0.94	0	0	-1.79	0.30
1	$\mathbf{C}^h_N$	7.19	7.19	1.85	0	0	-3.12	0.17
1	$\mathbf{C}^*$	7.07	7.07	2.00	0	0	-3.07	-
13	$\mathbf{C}^h_{db}$	4.04	4.04	1.90	0	0	0.24	0.35
13	$\mathbf{C}^h_N$	4.04	4.04	2.01	0	0	0.02	0.14
13	$\mathbf{C}^*$	4.04	4.03	2.00	0	0	0.01	-
24	$\mathbf{C}^h_{db}$	13.73	3.09	1.94	0	0	-0.96	0.40
24	$\mathbf{C}^h_N$	13.22	4.29	1.57	0	0	-1.80	0.15
24	$\mathbf{C}^*$	14.03	4.35	2.00	0	0	-1.85	-
72	$\mathbf{C}^h_{db}$	48.11	15.27	0.12	0	0	18.55	0.12
72	$\mathbf{C}^h_N$	47.35	13.73	0.07	0	0	20.79	0.10
72	$\mathbf{C}^*$	48.38	14.03	2.00	0	0	21.09	-
80	$\mathbf{C}^h_{db}$	82.81	2.08	2.37	0	0	-2.21	0.40
80	$\mathbf{C}^h_N$	80.15	3.43	0.02	0	0	-0.46	0.12
80	$\mathbf{C}^*$	82.43	4.00	2.00	0	0	-0.37	-
84	$\mathbf{C}^h_{db}$	91.52	1.64	2.20	0	0	-2.29	0.40
84	$\mathbf{C}^h_N$	89.69	3.19	0.02	0	0	-0.18	0.12
84	$\mathbf{C}^*$	91.79	4.00	2.00	0	0	-0.14	-
91	$\mathbf{C}^h_{db}$	57.25	50.52	0.86	0	0	38.57	0.18
91	$\mathbf{C}^h_N$	60.84	36.03	0.76	0	0	40.68	0.17
91	$\mathbf{C}^*$	60.39	35.61	2.00	0	0	42.16	-

inverso por homogeneización en coordenadas naturales. Este último concepto ha sido generalizado en la regla de diseño $\Re_1$ (Sección 2.6). Su aplicación resulta en la obtención de microarquitecturas simples, e inclusive se presentan resultados alternativos a los habituales en la bibliografía.

En el Anexo B se presentan importantes análisis sobre los resultados tanto de la optimización en la macro como en la microescala. Aspectos como distribución de clases de simetrías, obtención de materiales auxéticos, etc., son destacados en dicho Anexo.

Capítulo 4

Diseño de metamateriales para camuflaje acústico

4.1. Materiales pentamodales para dispositivos de camuflajes acústicos

En el presente Capítulo se expone la aplicación de las reglas de diseño propuestas en el Capítulo 2 para el diseño de materiales pentamodales aplicados a camuflajes acústicos.

Un camuflaje acústico es un material cuya propiedad consiste en volver *invisible*, de las ondas de sonido, al objeto que camufla. Por ejemplo, sea un fluido contenido un dominio infinito $\mathcal{B}$ (Fig.4.1-a), con un sistema de coordenadas polares (θ, r). En dicho dominio se encuentra un objeto cilíndrico $\mathcal{C}$ que es interceptado por una onda plana $\mathcal{W}$ que se desplaza de izquierda a derecha, Fig.4.1-b. El objeto $\mathcal{C}$ actuará como perturbación en el medio causando una dispersión de ondas, Fig.4.1-c.

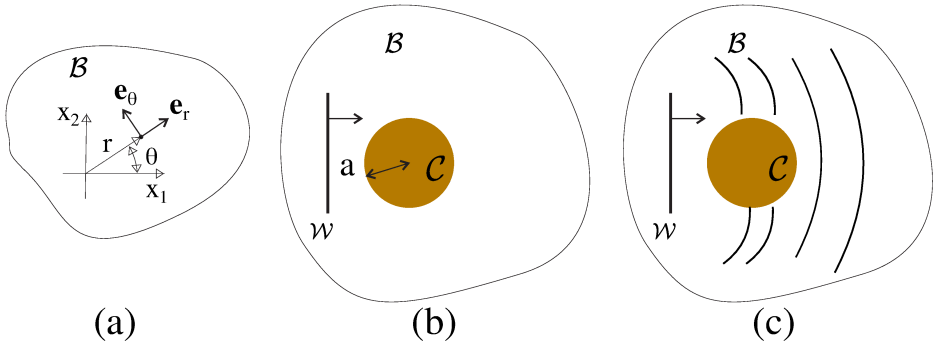

Figura 4.1: (a) sistema de coordenadas polares en un medio $\mathcal{B}$; (b) objeto cilíndrico embebido en el fluido $\mathcal{B}$; (c) dispersión de la onda $\mathcal{W}$.

El camuflaje acústico consiste en un material que ocupa el dominio Ω, y cuyo propósito es manipular el paso de la onda de tal manera que, fuera del dominio Ω, la onda no sufre dispersión

(Fig.4.2-a y -b).

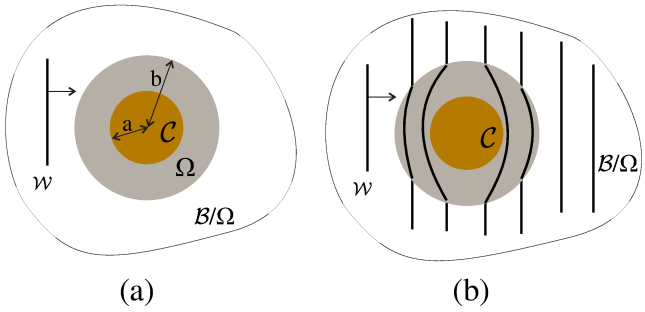

Figura 4.2: (a) objeto cilíndrico camuflado; (b) onda no perturbada en el dominio $\mathcal{B}/\Omega$.

Según lo propuesto por Norris (2008), un material para camuflaje acústico puede ser conseguido mediante un método de transformación de coordenadas, donde las propiedades del camuflaje copian los coeficientes geométricos de una transformación espacial singular, ver también Pendry et al. (2006). Según Norris, los materiales basados en dicha transformación pueden ser clasificados en dos tipos: materiales que requieren masa inercial anisotrópica (ver Cheng et al. (2008)) y materiales con módulo volumétrico anisotrópico. Este último caso puede ser conseguido mediante materiales pentamodales.

En el presente Capítulo se expone el uso de las reglas de diseño propuestas para la obtención de un camuflaje acústico mediante el diseño de materiales pentamodales de módulo volumétrico anisotrópico. Lo aquí expuesto puede verse desarrollado en detalle en el Anexo C.

4.2. Descripción del problema resuelto

El problema consiste en el diseño de un camuflaje de espesor $b - a$, para un cilindro sólido $\mathcal{C}$, de diámetro a, inmerso en el fluido $\mathcal{B}$, con el fin de atenuar la dispersión de una onda acústica $\mathcal{W}$ al impactar sobre dicho cilindro (ver Fig.4.2). El fluido en $\mathcal{B}$ es caracterizado por un módulo volumétrico κ_0 y una densidad ρ_0, y la relación entre los radios del camuflaje y el cilindro es $b = 2a$. En este caso, se utilizan materiales pentamodales propuestos por Norris (2008) cuyo módulo volumétrico será anisotrópico. Según lo discutido en la Sección 3.2 el tensor elástico objetivo para materiales pentamodales puede ser expresado de la siguiente manera:

$$\hat{\mathbf{C}} = \kappa^{\star}\mathbf{S} \otimes \mathbf{S}, \tag{4.1}$$

donde $\kappa^{\star}$ es un pseudo módulo volumétrico, el tensor $\mathbf{S}$

$$\mathbf{S} = \sqrt{\frac{\kappa_r}{\kappa^{\star}}}(\mathbf{e}_r \otimes \mathbf{e}_r) + \sqrt{\frac{\kappa_\theta}{\kappa^{\star}}}(\mathbf{e}_\theta \otimes \mathbf{e}_\theta), \tag{4.2}$$

$\mathbf{e}_r$ y $\mathbf{e}_\theta$ son los vectores unitarios en sentido radial y circunferencial, ver Fig.4.1-a, κ_r y κ_θ son los módulos volumétricos en dirección radial y circunferencial, respectivamente. En la expresión 4.3 se detalla la forma final del tensor elástico objetivo:

$$\hat{\mathbf{C}} = \begin{pmatrix} \kappa_r & \sqrt{\kappa_r \kappa_\theta} & 0 \\ \sqrt{\kappa_r \kappa_\theta} & \kappa_\theta & 0 \\ 0 & 0 & 0 \end{pmatrix}. \tag{4.3}$$

La determinación de las propiedades materiales κ_r y κ_θ se realiza mediante una función de mapeo entre el dominio real Ω y el que se quiere lograr mediante el camuflaje, Ω^m, ver Fig.4.3. La función lineal (línea roja de trazo) representa el caso en que no hubiera camuflaje. Si se busca un camuflaje perfecto, la función de mapeo debería ser la curva azul. Sin embargo, esto es difícil de alcanzar dado que serían necesarios en el material módulos volumétricos y densidades excesivamente grandes. Por ello en la función de mapeo se introduce el parámetro δ, el cual vuelve viable el diseño de un camuflaje con módulos volumétricos razonables, a costo de perder eficiencia. En este caso, algunas posibles funciones de mapeo se representan en líneas verdes. En Gokhale et al. (2012) los autores proponen la función de mapeo detallada en la Ec.4.4 (línea roja en la Fig.4.3(b)), mediante la cual es posible asegurar que la anisotropía del módulo volumétrico del camuflaje será mínima:

$$f_{_G}(r) = \begin{cases} \left(\frac{b^2-a\delta}{b^2-a^2} r - \frac{a-\delta}{b^2-a^2} b^2 \frac{a}{r}\right); & a \le r \le b \\ r; & r \ge b, \end{cases} \tag{4.4}$$

donde r es la coordenada radial (ver Fig.4.1-a). El uso del mapeo $f_{_G}(r)$ contribuye enormemente a la facilidad del diseño de la microarquitectura del material. En el Anexo C (Sección 2.1) es presentado en detalle el mencionado análisis.

Las propiedades materiales se determinan mediante las siguientes expresiones:

$$\kappa_r = \kappa_o \frac{1}{f'_{_G}(r)} \left(\frac{f_{_G}(r)}{r}\right) \quad , \quad \kappa_\theta = \kappa_o f'_{_G}(r) \left(\frac{r}{f_{_G}(r)}\right), \tag{4.5}$$

$$\boldsymbol{\rho}^\star = \hat{\rho}\mathbb{I} \qquad , \qquad \hat{\rho} = \rho_o f'_{_G}(r) \left(\frac{f_{_G}(r)}{r}\right). \tag{4.6}$$

Aquí, κ_o es el módulo volumétrico del medio, ρ_o la densidad del medio, $\boldsymbol{\rho}^\star$ la densidad de masa inercial y $\mathbb{I}$ el tensor unitario. Las propiedades elásticas del camuflaje, para cada punto r/a del dominio Ω, se presentan en la Fig.4.4. Todos los coeficientes están normalizados por las propiedades

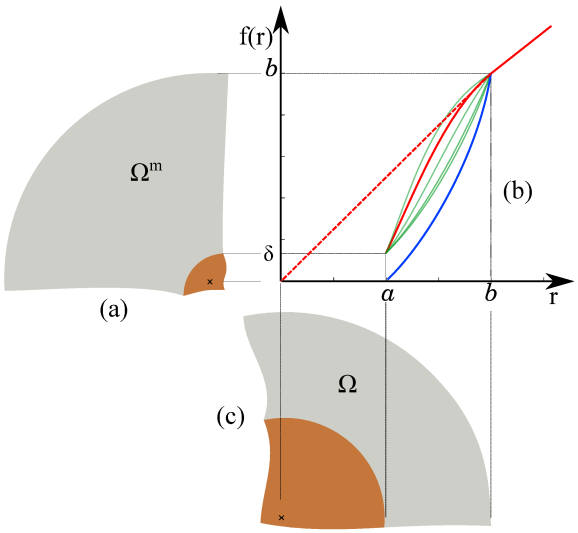

Figura 4.3: *(a)* dominio Ω^m luego de realizado el mapeo, *(b)* distintos casos de función de mapeo $f(r)$, *(c)* dominio real Ω.

materiales del fluido.

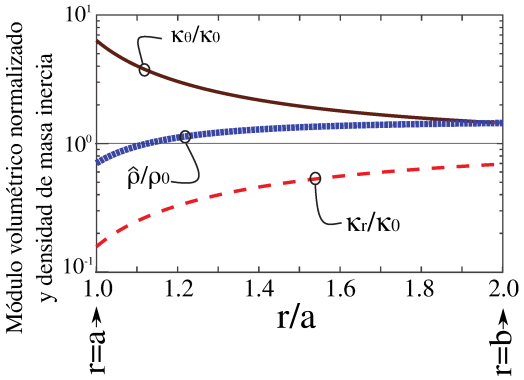

Figura 4.4: Propiedades materiales del camuflaje, normalizadas por las propiedades materiales del fluído. Las propiedades del camuflaje fueron obtenidas mediante el procedimiento de transformación de coordenadas detallado en el Anexo C.

4.3. Diseño de la microarquitectura

Para el diseño del camuflaje, el dominio Ω es discretizado en sentido radial en 20 sub-capas de igual espesor. Por cada sub-capa es diseñada su correspondiente microarquitectura, utilizando aluminio para la fase rígida, siendo sus parámetros $\kappa_{Al} = 70.GPa$, $G_{Al} = 25.5GPa$ y $\rho_{Al} = 2700.Kg/m^3$. Para la fase blanda se asume un polímero flexible caracterizado por un material isotrópico cuyo módulo elástico contrasta con el aluminio en un factor de $\gamma = 1.e-5$ (ver Ashby (2005)). Se adopta un valor de $\delta = 0.333$.

Para el problema de optimización topológica se utiliza la formulación D.14 y se aplican las

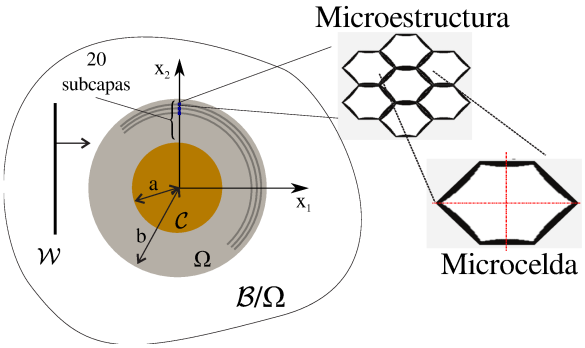

Figura 4.5: División por sub-capas del dispositivo de camuflaje.

reglas de diseño presentadas en la Sección 2.6[1]. Al utilizar la expresión 4.3 para la determinación de los tensores objetivo, la aplicación de las reglas $\Re_1$ y $\Re_2$ es directa. Además, es posible inferir que todos los tensores se encuentran en coordenadas naturales y poseen una simetría D_2. Dada esta simetría, de lo presentado en la regla $\Re_3$ se desprende que la forma de microcelda mas apropiada se obtiene mediante una red de Bravais que cumpla con una de las siguientes relaciones del dominio acotado (ver 2.8):

$$0 < \omega < 1, \quad \varsigma = 90^{\circ} \tag{4.7a}$$

$$\varsigma = arc\,cos(\omega/2) \tag{4.7b}$$

$$\omega = 1, \quad 60^{\circ} < \varsigma < 90^{\circ} \tag{4.7c}$$

Sin embargo, en este caso, la relación de aspecto fue determinada mendiante un análisis de sensibilidad de la forma de la microcelda sobre la solución del problema inverso, presentado en la siguiente Subsección. Por último, con respecto a la regla $\Re_4$, la simetría aplicada sobre las microceldas es una $c2mm$ (ejes vertical y horizontal en la microcelda de la Fig.4.5).

4.3.1. Forma de la microcelda

La relación de aspecto fue determinada mediante un análisis de sensibilidad de la forma de la microcelda sobre la solución del problema inverso. En decir, el problema de optimización topológica D.14 se resuelve para una sub-capa y utilizando distintas formas de la microcelda, variando según el parámetro geométrico η, definido en la Fig.4.6. El tensor objetivo utilizado es el correspondiente a la sub-capa 15, Ec.4.8, y las distintas microceldas utilizadas se muestran en la

[1]Detalles de formulación e implementación del problema son desarrollados en el Anexo C

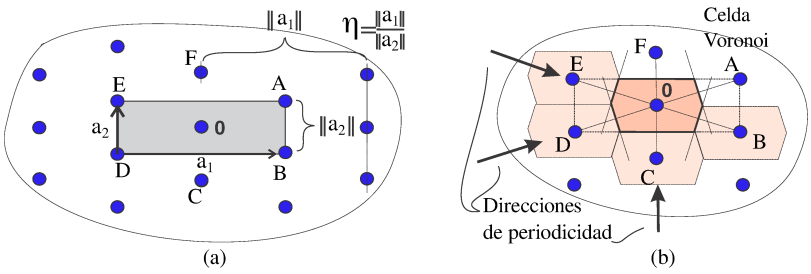

Figura 4.6: Definición del parámetro geométrico η (a) y celda de Voronoi análoga (b).

Fig.4.7.

$$\hat{\mathbf{C}}^{l15} = \begin{pmatrix} 5.893 & 2.250 & 0 \\ 2.250 & 0.859 & 0 \\ 0 & 0 & 0 \end{pmatrix} . \tag{4.8}$$

La variación de η entre $\sqrt{3}$ y 7 corresponde a un recorrido de la curva inferior 4.7b del dominio acotado, Fig.2.8.

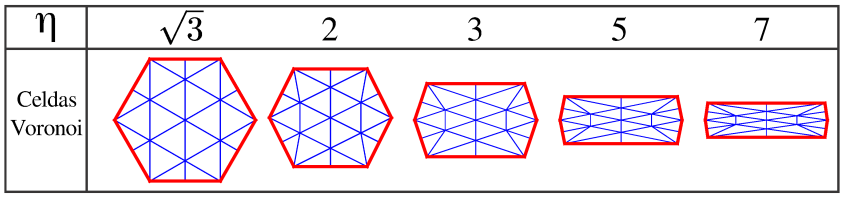

Figura 4.7: Celda Voronoi para distintos valores de η.

Resultados

En la Fig.4.8 son representados distintos resultados en función de η. En la Fig.4.8-a se grafica la función costo $\mathcal{J}$ del problema de optimización topológica D.14. En la Fig.4.8-b se tiene la componente C_{33} del tensor elástico efectivo. Por último, en la Fig.4.8-c se tiene la densidad de masa inercial efectiva ρ^{OT} de la microcarquitectura obtenida. Se aprecia que valores de η en el rango $3 \leq \eta \leq 5$ proporcionan una función costo $\mathcal{J}$ mínima en comparación con otros valores. El mismo rango arroja los menores valores de la componente C_{33}^{hom}. Recordar que cuanto más cercana a cero la componente C_{33}^{hom}, mejor será el desempeño del dispositivo de camuflaje, ver Norris (2008).

En base a estos resultados se formuló de forma empírica el siguiente criterio para la adopción de la forma de la microcelda:

$$\eta = \sqrt{3}\left(1 + 0.2\frac{\hat{C}_{11} - \hat{C}_{22}}{\hat{C}_{22}}\right) . \tag{4.9}$$

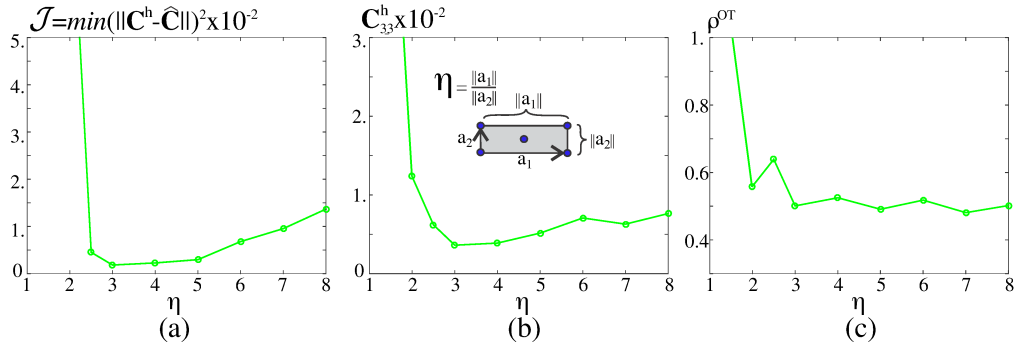

Figura 4.8: Resultados obtenidos mediante el análisis de sensibilidad de la forma de la microcelda sobre la solución del problema inverso. Las celdas Voronoi son caracterizadas con el mismo parámetro η: a) valor obtenido de la función costo $\mathcal{J}$ para el problema de optimización topológica D.14, b) coeficiente de corte C_{33} del tensor elástico efectivo obtenido, c) densidad de masa inercial obtenida ρ^{OT}.

Donde $\hat{C}_{11}$ y $\hat{C}_{22}$ son coeficientes correspondientes al tensor elástico objetivo. De esta manera, mediante la expresión 4.9 se determina la relación de aspecto de las microceldas para diseñar las 20 sub-capas del camuflaje. El presente análisis de sensibilidad puede verse desarrollado en profundidad en el Anexo C, Sección 4.3.

4.4. Resultados del dispositivo de camuflaje acústico diseñado

En la Fig.4.9 se grafican las microarquitecturas diseñadas para las sub-capas 1, 5, 10, 15 y 20. En la segunda columna se aprecia un detalle de los elementos estructurales del compuesto. Por último, en la tercer columna se detallan: el tensor elástico homogeneizado $\mathbf{C}^h$ y la densidad ρ^{OT}, obtenidos de mediante la optimización; y además el tensor elástico $\hat{\mathbf{C}}$ y densidad $\hat{\rho}$, ambos objetivos del problema de optimización topológica. Para cada una de las soluciones de las 20 sub-capas diseñadas, la densidad de masa obtenida es menor a la densidad objetivo, dada según los requerimientos de Norris.

Por otro lado, en la Fig.4.10 se grafican las propiedades efectivas κ_r^h, κ_θ^h y C_{33}^h para las 20 capas diseñandas, obtenidas mediante la resolución del problema de optimización topológica. Para cada sub-capa se tiene un valor de η obtenido según la expresión 4.9, el cual define la forma de la microcelda.

4.4.1. Desempeño del dispositivo diseñado

El desempeño del camuflaje diseñado se evalúa mediante la medición cuantitativa de la dispersión del campo de ondas, con una onda plana incidente sobre el cilindro camuflado en un medio fluido infinito. Dado que el camuflaje ha sido diseñado con un parámetro $\delta = 0.333$, la dispersión debería ser equivalente al caso de una onda incidente sobre un cilindro sin camuflaje de radio $r = 0.333a$.

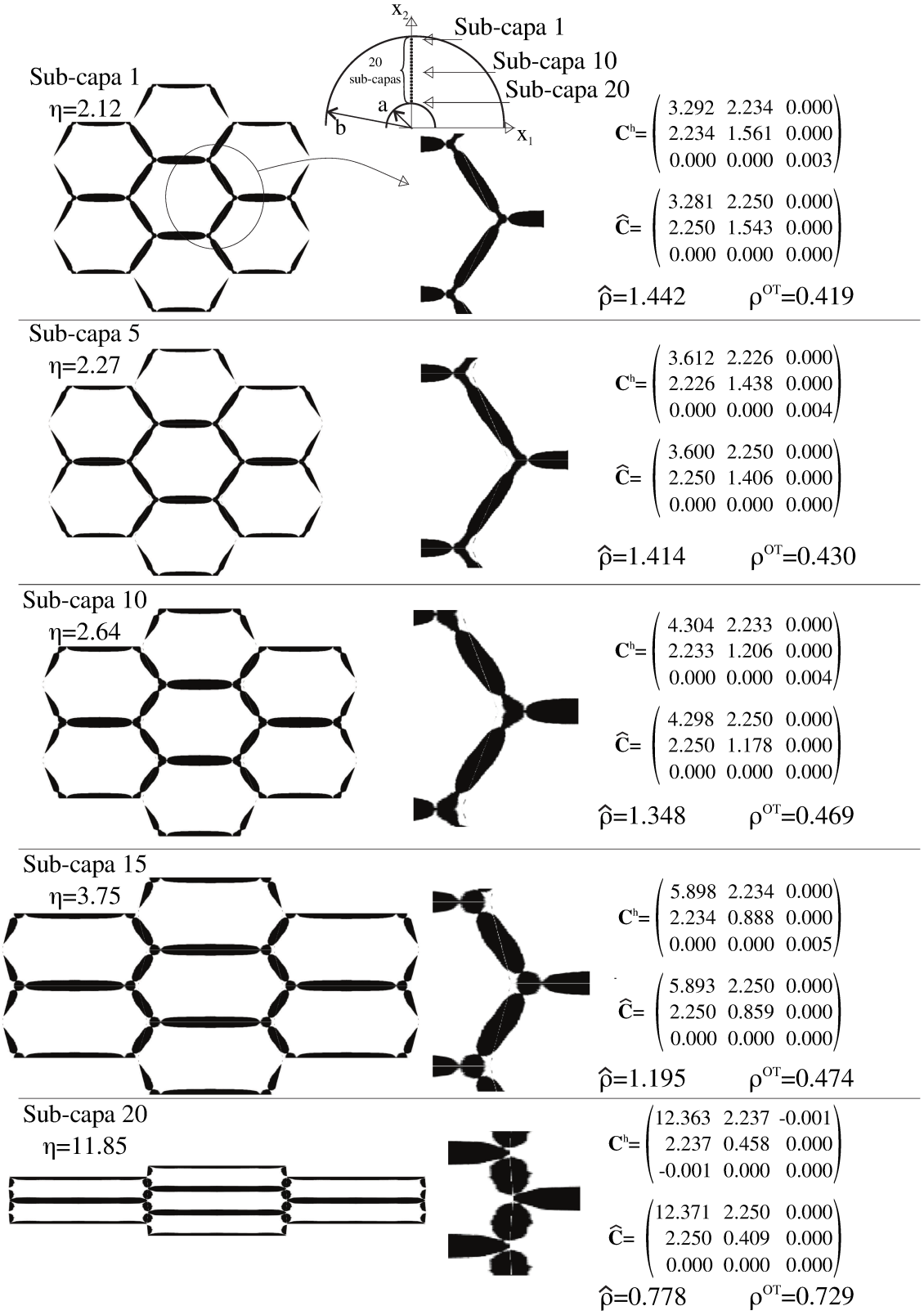

Figura 4.9: Soluciones obtenidas para distintas sub-capas del dispositivo de camuflaje acústico. En cada fila, $\mathbf{C}^h$ es el tensor elástico homogeneizado y ρ^{OT} la densidad en cada microcelda, ambos solución del problema de optimización. $\hat{\mathbf{C}}$ y $\hat{\rho}$ son el tensor elástico objetivo y la densidad objetivo, respectivamente, ambos obtenidos mediante el análisis de Norris.

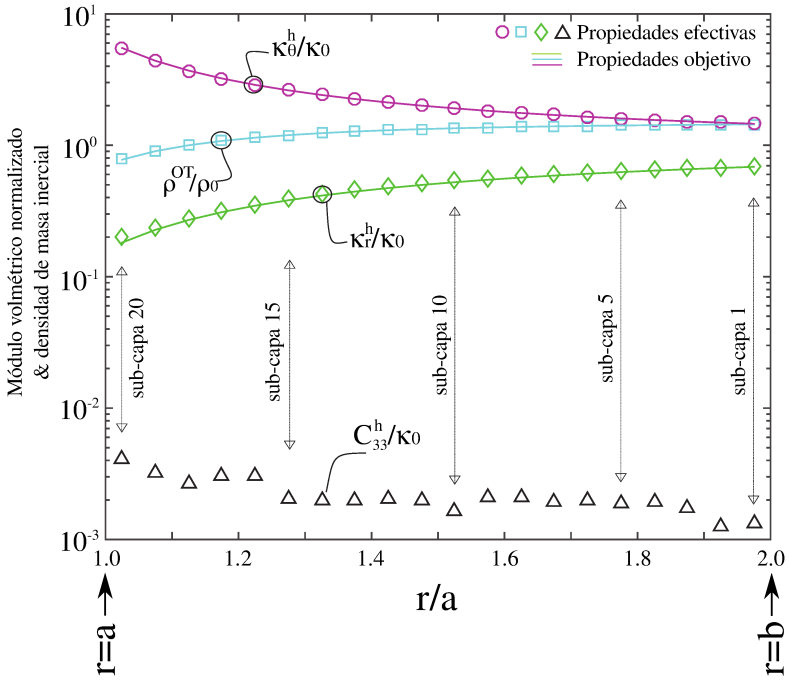

Figura 4.10: Propiedades efectivas de las 20 sub-capas, obtenidas mediante el algoritmo de optimización topológica. Los valores obtenidos de módulo volumétrico en ambas direcciones (κ^h_r y κ^h_θ), la densidad (ρ^h) y el módulo de corte (C^h_{33}) se grafican normalizados mediante símbolos. Las curvas en líneas continuas representan los valores objetivo.

El test consiste en el modelado del camuflaje con 20 sub-capas perfectamente conectadas, de material base elástico cuyas propiedades son idénticas a las propiedades efectivas de los materiales diseñados. Los detalles y resultados de este análisis pueden ser encontrados en el Anexo C, Sección 5.

4.5. Conclusiones

Los resultados muestran la viabilidad de aplicación de las técnicas de optimización propuestas en el Capítulo 2 para el diseño de dispositivos de camuflaje acústico utilizando materiales pentamodales. Para alcanzar las microarquitecturas diseñadas fue estrictamente necesario el uso de los conceptos propuestos en el procedimiento 2.6, principalmente la aplicación del la reglas de diseño $\Re_2$, es decir, uso de la celda de Voronoi para la selección de una forma de microcelda apropiada. Por otro lado, el análisis de sensibilidad presentado es una buena opción como alternativa a la regla de diseño $\Re_3$.

En los casos aquí abordados, el uso de microceldas de formas convencionales, como cuadradas o rectangulares, no ha dado resultados satisfactorios. Notar, por ejemplo, que en el análisis de sensibilidad, valores de $\eta > 5$, otorgan microceldas con forma cercana a la rectangular, y los resultados obtenidos con las mismas no son buenos.

Mediante los resultados obtenidos para el rango $3 < \eta < 5$, es posible concluir que existe mas

de una microarquitectura solución al problema inverso, en este caso para el diseño del dispositivo de camuflaje acústico.

En el Anexo C se pueden encontrar un desarrollo mas detallado de las conclusiones aquí expuestas.

Capítulo 5

Diseño inverso de compuestos elásticos en tres dimensiones

5.1. Introducción

En este Capítulo se expone una breve introducción de los conceptos de *simetrías geométricas* y *simetrías físicas* para el espacio $\mathbb{R}^3$. Sin necesidad de incurrir en definiciones ya tratadas, lo expuesto en el Capítulo 2 es análogo para el caso $\mathbb{R}^3$, y un análisis exhaustivo puede encontrarse en el Anexo D. Nuevamente, se utiliza el concepto de *grupo puntual* como nexo para relacionar las clases simetrías de los tensores (*propiedad física*) con la forma de la microcelda y la distribución interna de material (*propiedad geométrica*).

5.2. Simetrías en el espacio $\mathbb{R}^3$: Celda unidad, grupo puntual y grupo de espacio

El concepto de celda Voronoi (o Wigner-Seitz) es válido también en tres dimensiones. Su construcción en este caso es similar (Fig.5.1): luego de unir el punto P con los puntos cercanos, estas uniones son cortadas en su punto medio por planos normales. El mínimo volumen encerrado por dichos planos constituye la celda unidad. En este caso la celda Voronoi conserva las mismas propiedades detalladas en la Sección 2.2.2. En $\mathbb{R}^3$ existen 14 redes de Bravais posibles[1]. Los *grupos puntuales* son 32, y los *grupos de espacio*[2] son 230. Todas estas relaciones, presentadas en la Tabla D.1, permiten utilizar las reglas $\Re_1$, $\Re_2$ y $\Re_4$ en algoritmos de optimización topológica, de la misma forma en que se aplican para problemas en $\mathbb{R}^2$.

[1] En la Tabla 5 del Anexo D se pueden ver los esquemas de cada red.
[2] Antes *grupos de plano*.

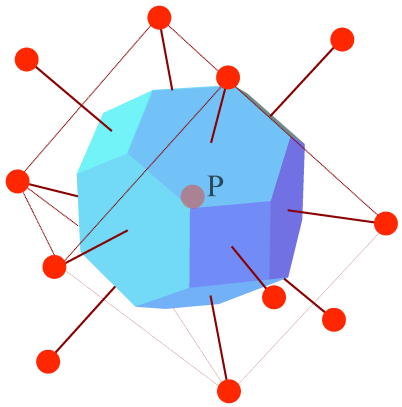

Figura 5.1: Construcción de la celda Voronoi sobre una red de Bravais en $\mathbb{R}^3$.

Tabla 5.1: Elementos de simetría (grupo puntual y grupo espacial) para cada clase de simetría de tensor elástico. En la primer columna, se utiliza la siguiente notación: "$*$" una componente no necesariamente nula; "$* - *$" componentes iguales; "$* - \bar{*}$" dos componentes iguales y de signo contrario; "$\otimes$" el módulo de corte es igual a $(C_{11} - C_{12})$ (ver Ting (1996)). La última columna indica la cantidad de redes de Bravais que son compatibles con los grupos de punto en cada caso.

Tensor elástico	Grupo puntual	Grupo espacial	Red de Bravais
Triclínico	1,$\bar{1}$	2	1
Monoclínico	2,m,2/m	13	2
Ortotrópico	222,mm2, mmm	59	4
Tetragonal	4,$\bar{4}$,4/m, 442,4mm, $\bar{4}$2m,4/mmm	68	2
Trigonal	3,$\bar{3}$, 32,3m, $\bar{3}$m	7	1
Hexagonal	6,$\bar{6}$, 6/m,622, 6mm,$\bar{6}$m2, 6/mmm	27	1
Cúbico	23,m$\bar{3}$, 432,$\bar{4}$3m, m$\bar{3}$m	36	3
Total	32	230	14

5.3. Diseño de un compuesto isotrópico extremo

Se presenta el diseño de una microarquitectura compuesta por un material rígido y vacío. Las propiedades de la fase rígida consisten en módulo volumétrico $\kappa^1 = 1.669[GPa]$ y módulo de corte $G^1 = 0.3571[GPa]$. El vacío es numéricamente simulado adoptando un factor de contraste $\gamma = 1e-5$[3] y la fracción volumétrica de la fase sólida es $f = 0.338$.

El problema atacado consiste en diseñar un metamaterial isotrópico con máximos valores efectivos de módulo volumétrico y módulo de corte, $\hat{\kappa}$ y $\hat{G}$ respectivamente. Los valores teóricos máximos fueron propuestos por Hashin y Shtrikman (1963). Dichos valores se determinan en función de las propiedades elásticas del material base. Para este caso, los valores límites son $\hat{\kappa} = 0.1699[GPa]$ y $\hat{G} = 0.0789[GPa]$. En notación de Kelvin, el tensor isotrópico elástico, objetivo de la optimización, viene dado por:

$$\hat{\mathbf{C}} = \begin{pmatrix} \hat{\kappa}+\frac{4}{3}\hat{G} & \hat{\kappa}-\frac{2}{3}\hat{G} & \hat{\kappa}-\frac{2}{3}\hat{G} & 0 & 0 & 0 \\ & \hat{\kappa}+\frac{4}{3}\hat{G} & \hat{\kappa}-\frac{2}{3}\hat{G} & 0 & 0 & 0 \\ & & \hat{\kappa}+\frac{4}{3}\hat{G} & 0 & 0 & 0 \\ & & & 2\hat{G} & 0 & 0 \\ & sim. & & & 2\hat{G} & 0 \\ & & & & & 2\hat{G} \end{pmatrix} \tag{5.1}$$

Aplicación de reglas de diseño: isotropía en $\mathbb{R}^3$

En el diseño de metamateriales es de particular interés alcanzar topologías de microestructuras, cuyo comportamiento efectivo sea isotrópico. En el plano es posible garantizar la obtención de propiedades isotrópicas en una microarquitectura, sólo con seguir las reglas $\Re_1$, $\Re_2$ y $\Re_4$ (ver Tabla 2.3, fila correspondiente a $O(2)$). En $\mathbb{R}^3$, en cambio, no existe ningún *grupo espacial* que garantice la existencia de un compuesto periódico cuyas propiedades efectivas sean isotrópicas, como puede verse en la Tabla D.1. Por ello, para abordar el diseño de un material isotrópico en $\mathbb{R}^3$, la propuesta de este trabajo consiste en usar celdas Voronoi correspondientes a la clase de simetría más alta posible, en este caso la *simetría cúbica*. De esta manera, evaluar el grado de

[3] Relación entre el módulo elástico de pseudo-vacío y el módulo de la fase rígida

Tabla 5.2: Propiedades de la simetría cúbica. Compatibilidad entre grupos puntuales y grupos espaciales. Las redes de Bravais compatibles son: primitiva (SC), cúbica de cara centrada (FCC) y cúbica de cuerpo centrado (BCC). Se dibujan las celdas Voronoi para las tres redes de Bravais.

Tensor de elasticidad	Grupo puntual	Grupo espacial		
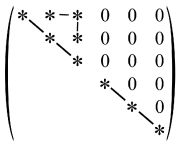	23	P23, P2_13	F23	I23, I2_13
	m$\bar{3}$	Pm$\bar{3}$, Pn$\bar{3}$, Pa$\bar{3}$	Fm$\bar{3}$, Fd$\bar{3}$	I$\bar{3}$, Ia$\bar{3}$
	432	P432, P4_232, P4_332, P4_132	F432, F4_132	I432, I4_132
	$\bar{4}$3m	P$\bar{4}$3m, P$\bar{4}$3n	F$\bar{4}$3m, F$\bar{4}$3c	I$\bar{4}$3m, I$\bar{4}$3d
	m$\bar{3}$m	**Pm$\bar{3}$m**, Pn$\bar{3}$n, Pm$\bar{3}$n, Pn$\bar{3}$m	**Fm$\bar{3}$m**, Fm$\bar{3}$c, Fd$\bar{3}$m, Fd$\bar{3}$c	**Im$\bar{3}$m**, Ia$\bar{3}$d
Redes de Bravais compatibles				
Celda Voronoi				

isotropía logrado en las propiedades efectivas para cada celda de Voronoi, y además estudiar las topologías obtenidas en cada caso.

Dado que en la expresión 5.1 el tensor objetivo se encuentra en ejes naturales, se cumple la condición impuesta por la regla $\Re_1$. Con respecto a la regla de diseño $\Re_2$, las celdas de Voronoi posibles son tres y se encuentran detalladas, junto con algunas propiedades de simetrías, en la Tabla 5.2. Allí se muestran las tres redes de Bravais compatibles con la simetría cúbica: primitiva, caras centradas y cuerpo centrado, cuya notación es SC, FCC y BCC respectivamente (según sus nombres en inglés). Dado que las celdas de Voronoi elegidas no presentan variación en su relación de aspecto, no es necesaria la aplicación de la regla de diseño $\Re_3$. Por otro lado, no fueron aplicados ejes o planos de simetría a la distribución de material dentro de la microcelda, lo que, según la regla de diseño $\Re_4$, implica no garantizar ninguna simetría en la microarquitectura. Por último, las configuraciones iniciales utilizadas son las siguientes:

- *i)* Microcelda con un vacío esférico en su centro, de tal manera que la fracción de volumen inicial de la fase rígida sea $25\,\%$ aproximadamente.
- *ii)* Configuración tipo celular, donde el material ocupa las caras de la microcelda con un espesor constante.
- *iii)* Configuración de barras de igual sección ubicadas en las aristas de la microcelda.

Cabe destacar que estas configuraciones pertenecen al grupo espacial $Pm\bar{3}m$ para la celda SP, $Fm\bar{3}m$ para la celda FCC y $Im\bar{3}m$ para la celda BCC. Estos grupos espaciales comparten el grupo de punto $m\bar{3}m$ con la simetría cúbica, ver Tabla 5.2.

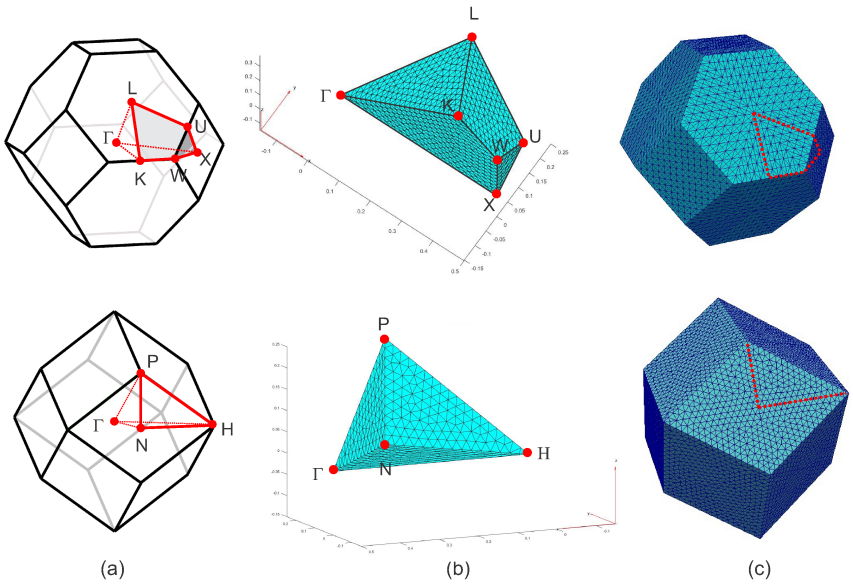

Figura 5.2: Mallas de elementos finitos de las celdas Voronoi (celdas BCC y FCC). a) Volumen generador. El punto central de la celda Voronoi es Γ; L es el punto central de la cara hexagonal; X el punto central de la cara cuadrada contigua a la hexagonal; K es el punto medio del borde que une dos caras hexagonales; U es el punto medio que une las caras hexagonales y cuadradas. b) Malla del volumen generador para cada caso. c) Malla de la microcelda completa, obtenida a partir del volumen generador, mediante la aplicación de trasnformaciones geométricas sucesivas

5.3.1. Construcción de las celdas unidad mediante elementos finitos

Para resolver el problema de elementos finitos, se utilizaron tetraedros lineales. Para la construcción de la celda Voronoi solo se malló un *volumen generador*[4] (ver Fig.5.2-b). Luego, sobre la malla parcial generada se aplican una serie operaciones de simetría (reflexiones y rotaciones) para obtener finalmente la celda Voronoi completa. Esta técnica provee una malla con simetrías que preservan la más alta simetría de punto de la correspondiente celda Voronoi. De esta forma es mucho más sencillo imponer simetrías geométricas como restricción al problema de optimización topológica.

5.3.2. Medición del grado de anisotropía

Se introduce un indicador para medir cuán anisotrópicas son las propiedades efectivas obtenidas. Dado un tensor elástico cualquiera $\mathbf{C}^h$, se define un tensor isotrópico elástico de comparación (Ver Meille y Garboczi (2001)) de la siguiente manera:

$$C_{11}^{iso} = \frac{1}{5}(C_{11}^h + C_{22}^h + C_{33}^h) + \frac{2}{15}(C_{12}^h + C_{13}^h + C_{23}^h) + \frac{4}{15}(C_{44}^h + C_{55}^h + C_{66}^h), \tag{5.2}$$

$$G^{iso} = \frac{1}{15}(C_{11}^h + C_{22}^h + C_{33}^h) - (C_{12}^h + C_{13}^h + C_{23}^h) + 3(C_{44}^h + C_{55}^h + C_{66}^h), \tag{5.3}$$

$$\kappa^{iso} = C_{11}^{iso} - \frac{4}{3}G^{iso}, \tag{5.4}$$

[4]También llamado *unidad asimétrica*, ver Souvignier (2016).

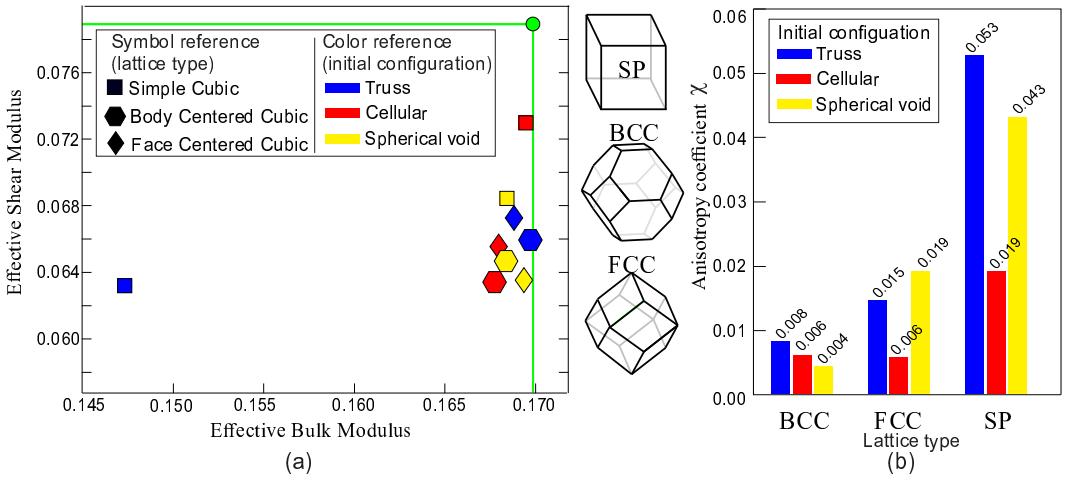

Figura 5.3: a) Espacio $\hat{\kappa}$ vs. $hatG$: En líneas verdes se representan los límites de Hashin-Strikman, en el mismo se disponen los resultados obtenidos con las celdas primitiva (SP), cara centrada (FFC) y cuerpo centrado (BCC). b) Coeficiente de anisotropía χ obtenido según forma de microcelda y solución inicial.

y utilizando los valores de G^{iso} y κ^{iso} se construye el tensor de comparación $\mathbf{C}^{iso}$ mediante la definición (5.1). Por último se define el coeficiente de anisotropía:

$$\chi = \|\mathbf{C}^h - \mathbf{C}^{iso}\|_{Fro} \tag{5.5}$$

el cual es mas cercano a cero cuanto mas isotrópico sea $\mathbf{C}^h$.

5.4. Resultados y discusión

En la Fig.5.3-a se grafican los resultados en el espacio κ vs. G, puestos en comparación con los límites superiores de Hashin-Strikman, graficados en líneas verdes. Los distintos símbolos detallan los tipos de celda unidad utilizados y la topología inicial. En la Fig.5.3-b se grafican los coeficientes de anisotropía alcanzados en los distintos tests. Queda claro que la celda unidad BCC provee microarquitecturas que tienden a ser mas isotrópicas que las demás celdas unidad, independientemente de la configuración inicial adoptada. Algunos resultados de distribución de material pueden verse en la Fig.5.4, graficándose la celda unidad completa (*b), d) y f)*) y la celda unidad con un corte en el plano medio (*a), c) y e)*). Se aprecian patrones de distribución de material altamente simétricos, mas allá de no haber aplicado ninguna restricción de simetría geométrica. Por último en la Tabla 5.3 se detallan las componentes del tensor elástico objetivo, en comparación con las componentes de los tensores efectivos obtenidos en los casos de celdas unidad SC, BCC y FCC, con topología inicial *ii)* tipo celular. En todos los casos la fracción de volumen de fase sólida es $f = 0.338$.

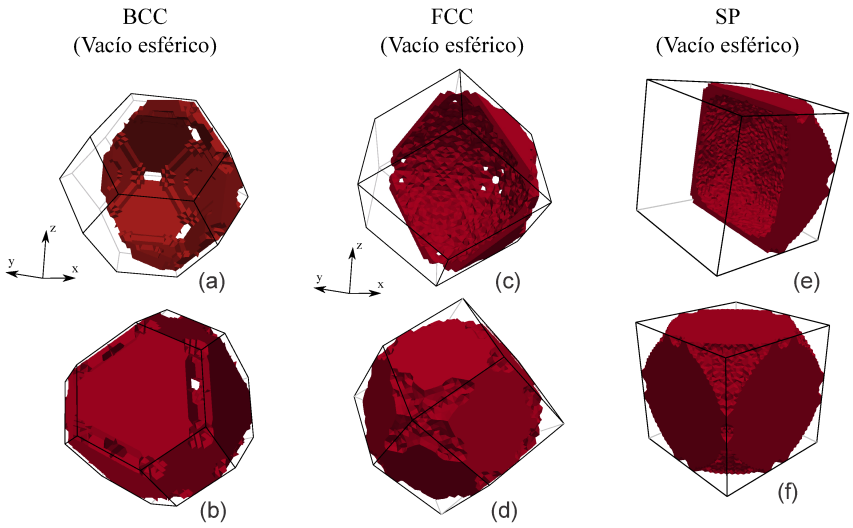

Figura 5.4: A) Resultados obtenidos en el diseño: Celda BCC, a) con un corte en el plano medio, b) celda completa; Celda FCC, c) con un corte en el plano medio, d) celda completa; Celda SP, e) con un corte en el plano medio, f) celda completa;

Tabla 5.3: Tensores elásticos efectivos: *Fila 2)* Tensor elástico objetivo de la optimización, *Filas 3 a 5)* Tensores elásticos obtenidos mediante el proceso de diseño, con distintas formas de microceldas.

	C_{11}	C_{22}	C_{33}	C_{44}	C_{55}	C_{66}	C_{12}	C_{13}	C_{23}
Tensor elástico objetivo $\hat{\mathbf{C}}$	0.2750	0.2750	0.2750	0.1578	0.1578	0.1578	0.1172	0.1172	0.1172
Celda SP	0.2732	0.2732	0.2732	0.1398	0.1394	0.1392	0.1177	0.1177	0.1179
Celda BCC	0.2559	0.2571	0.2552	0.1272	0.1274	0.1276	0.1246	0.1243	0.1244
Celda FCC	0.2570	0.2572	0.2569	0.1286	0.1274	0.1284	0.1242	0.1239	0.1241

5.5. Conclusiones

Se presentó la aplicación de las reglas de diseño al problema de diseño inverso de materiales elásticos isotrópicos en $\mathbb{R}^3$. Al proponer formas de microceldas no convencionales se logra una amplitud del espectro de soluciones posibles. Además, el grado de anisotropía obtenido con celdas BCC es satisfactorio e inclusive sustancialmente menor al caso convencional de microcelda de forma cúbica. Esto es independiente de la configuración inicial dada al algoritmo de optimización en los casos presentados.

Con respecto a la distribución de material en el interior de las microceldas, en este caso no se imponen ejes o planos de simetría. Sin embargo, la técnica propuesta de generación de malla de la celda Voronoi a partir de un volumen generador facilitaría una posible imposición de dichas restricciones geométricas.

Capítulo 6

Conclusiones

6.1. Contribuciones

En esta Tesis se presenta un *marco conceptual* para facilitar el diseño inverso de metamateriales elásticos con enfoque multiescala. Dicho marco ofrece cuatro reglas desarrolladas a partir de un análisis exhaustivo de conceptos de cristalografía para geometrías periódicas. De allí se desprenden propiedades de simetrías que permiten relacionar las geometrías periódicas con propiedades físicas y su caracterización matemática, en este caso el tensor constitutivo elástico. Dichas propiedades permiten formular cuatro reglas de diseño que son acopladas a algoritmos de optimización inversa. Como resultado, se garantiza que la topología diseñada cumpla de manera estricta con las propiedades de simetrías requeridas por el tensor elástico objetivo.

De las mencionadas reglas se desprende el uso de microceldas de formas no convencionales, basadas en redes de Bravais y celdas Voronoi. Desde el punto de vista topológico, el uso de estas microceldas facilita la obtención de un amplio rango de microarquitecturas posibles, que serían difícilmente alcanzables mediante microceldas típicas en la literatura.

Como parte de estas reglas, se presenta una base de datos de tensores homogeneizados, cuyo fin es determinar de forma no arbitraria la forma de la microcelda, ademas de otorgar al proceso de diseño una solución inicial cercana al objetivo buscado. Las familias de topologías presentadas en la base de datos son pocas y simples. Sin embargo, la forma de construcción de la base de datos constituye un aporte conceptual, dado que la generación de las microceldas está estrictamente relacionada con todas las propiedades efectivas que un tensor elástico puede tener.

Como aplicación de las reglas propuestas, se presenta la solución de problemas de diseño inverso en $\mathbb{R}^2$, aplicando un algoritmo de optimización basado en derivada topológica. En primer lugar se presenta la solución de problemas de diseño de estructuras elásticas, con un enfoque de optimización multiescala débilmente acoplado. Para un problema mecánico dado, la Optimiza-

ción Libre de Material da como resultado la distribución espacial de material y sus propiedades efectivas óptimas. Un segundo problema abordado consiste en el diseño de materiales para camuflaje acústico. En ambos problemas las propiedades objetivo describen materiales con propiedades extremas, como materiales auxéticos, materiales altamente anisotrópicos o con módulo de corte nulo, etc. La aplicación de las reglas propuestas fue fundamental para alcanzar satisfactoriamente las propiedades objetivo.

También se presenta un estudio, desde el punto de vista cristalográfico, de compuestos periódicos en $\mathbb{R}^3$. Esto permite desarrollar herramientas conceptuales para poder utilizar las reglas de diseño en problemas de tres dimensiones. Como aplicación numérica, se presenta el diseño un material isotrópico con propiedades extremas, mediante el uso de distintos dominios de diseño no convencionales. Se logran niveles de anisotropía bajos. Por último se presenta un algoritmo de generación de microceldas 3D construidas en base a los conceptos de redes de Bravais y celdas Voronor. La generación de la malla se basa en volúmenes generadores. De esta manera, la generación sistemática de la microcelda facilita la aplicación de simetrías geométricas y la implementación de distribución inicial de material.

6.1.1. Resumen de contribuciones presentadas en esta Tesis

- Resolución de diseño inverso mediante optimización topológica en coordenadas naturales del tensor objetivo.

- Parametrización en $\mathbb{R}^2$ de redes de Bravais y celdas unidad Voronoi para uso de microceldas de formas no convencionales en problemas multiescala.

- Construcción de una base de datos de tensores homogeneizados en $\mathbb{R}^2$, con cuatro variables de entrada: dos parámetros de red de Bravais, fracción de volumen de material rígido y distribución interna de material.

- Definición del conjunto de simetrías admisibles y posibles para obtener las simetrías requeridas por el tensor elástico objetivo.

- Formulación de un procedimiento de optimización multiescala débilmente acoplado *Optimización Libre de Material-Derivada Topológica*.

- Procedimiento para generación de celdas unidad Voronoi para problemas en $\mathbb{R}^3$, contemplando las más altas simetrías geométricas.

6.2. Publicaciones científicas derivadas

A continuación se listan las contribuciones científicas derivadas directa o indirectamente de los estudios y desarrollos abordados durante la presente Tesis.

6.2.1. Publicaciones en revistas

1. J.M. Podestá, C. Méndez, S. Toro, A.E. Huespe. *Making use of Symmetries in the 3D Elastic Inverse Homogenization Problem*. International Journal for Multiscale Computational Engineering. *En revisión*

2. J.M. Podestá, C. Méndez, S. Toro, A.E. Huespe. *Symmetry considerations for topology design in the elastic inverse homogenization problem*. Journal of the Mechanics and Physics of Solids. *En revisión.*

3. C. Méndez, J.M. Podestá, O. Lloberas-Valls, S. Toro, A.E. Huespe, J. Oliver. *Material design of elastic structures using Voronoi cells*. International Journal for Numerical Methods in Engineering. DOI: 10.1002/nme.5804

4. C. Méndez, J.M. Podestá, O. Lloberas-Valls, S. Toro, A.E. Huespe, J. Oliver. *Computational material design for acoustic cloaking*. International Journal for Numerical Methods in Engineering. DOI: 10.1002/nme.5560

5. S. Toro, P.J. Sánchez, J.M. Podestá, P.J. Blanco, A.E. Huespe, R.A. Feijóo. *Cohesive surface model for fracture based on a two-scale formulation: computational implementation aspects*. Computational Mechanics. DOI: 10.1007/s00466-016-1306-y

6.2.2. Divulgación de herramientas computacionales

Con el fin de facilitar la reproducción de los resultados obtenidos en este trabajo mediante reglas de diseño presentadas en la Sección 2.6, se puso a disposición el algoritmo realizado en un repositorio de acceso público, en el cual contiene:

- Algoritmo de obtención de la clase de simetría y expresión en coordenadas naturales de un tensor elástico arbitrario de estado plano.

- Base de datos de tensores homogeneizados para problemas en estado plano.

- Algoritmo de generación de base de datos para geometrías parametrizadas para el usuario.

6.2.3. Publicaciones y presentaciones en congresos

1. C. Méndez, J.M. Podestá, S. Toro, A.E. Huespe, J, Oliver. *Uso de simetrías en la homogenización inversa de un problema elástico.* MECOM 2018. Tucuman, Argentina.

2. J.M. Podestá, C. Méndez, S. Toro, A.E. Huespe *Materials inverse design in 3D problems using elastic symmetry properties.* MECOM 2018. Tucuman, Argentina.

3. J.M. Podestá, C. Méndez, S. Toro, A.E. Huespe, J, Oliver. *Computational optimization tools for material design of elastic problems using inverse homogenization.* EngOpt 2018. Lisboa, Portugal.

4. C. Méndez, J.M. Podestá, S. Toro, A.E. Huespe, J, Oliver. *Making use of Symmetries in the Elastic Inverse Homogenization Problem.* WCCM 2018. New York, EEUU.

5. C. Méndez, J.M. Podestá, A.E. Huespe, S. Toro, J, Oliver. *Offline pre-processing in micro-architecture design of composites.*, ECCOMAS 2018. Glasgow, U.K..

6. J.M. Podestá, C. Méndez, A.E. Huespe. *Diseño computacional jerárquico de materiales para estructuras elástica*. ENIEF 2017. La Plata, Argentina.

7. C. Méndez, A.E. Huespe, J.M. Podestá, J. Oliver. *Computational material design for acoustic cloaking.* European Congress on Computational Methods in Applied Sciences and Engineering 2016. Creta, Grecia.

8. C. Méndez, A.E. Huespe, J.M. Podestá, Pablo Sanchez, J. Oliver. *Diseño de materiales para camuflaje acústico usando derivada topológica.* ENIEF 2016. Córdoba, Argentina.

9. J.M. Podestá, A.E. Huespe, C. Méndez. *Diseño computacional de metamateriales ultrarígios y ultralivianos.* ENIEF 2016. Córdoba, Argentina.

10. S. Toro, P. Sanchez, P.J. Blanco, J.M. Podestá, A.E. Huespe. *New developments in multiscale formulations for material failure*. Euromech 2015. Eindhoven, Países Bajos.

11. S. Toro, P. Sanchez, J.M. Podestá, A.E. Huespe. *Modelado de falla de material tipo hormigón mediante formulaciones multiescala.* ENIEF 2014. Bariloche, Argentina.

Bibliografía

Amigo R., Giusti S., Novotny A., Silva E., y Sokolowski J. Optimum design of flextensional piezoelectric actuators into two spatial dimensions. *SIAM Journal on Control and Optimization*, 54(2):760–789, 2016.

Ammari H., Calmon P., y Iakovleva E. Direct elastic imaging of a small inclusion. *SIAM Journal on Imaging Sciences*, 1(2):169–187, 2008.

Amstutz S. y Andrä H. A new algorithm for topology optimization using a level-set method. *Journal of Computational Physics*, 216(2):573–588, 2006.

Amstutz S., Giusti S., Novotny A., y de Souza Neto E. Topological derivative for multi-scale linear elasticity models applied to the synthesis of microstructures. *International Journal for Numerical Methods in Engineering*, 84(6):733–756, 2010.

Amstutz S., Novotny A., y de Souza Neto E. Topological derivative-based topology optimization of structures subject to drucker–prager stress constraints. *Computer Methods in Applied Mechanics and Engineering*, 233:123–136, 2012.

Andreassen E., Lazarov B., y Sigmund O. Design of manufacturable 3d extremal elastic microstructure. *Mechanics of Materials*, 69(1):1–10, 2014.

Ashby M. *Materials selection in mechanical design*. Elsevier, Butterworth-Heinemann, 3rd. edición, 2005.

Auffray N. y Ropars P. Invariant-based reconstruction of bidimensional elasticity tensors. *International Journal of Solids and Structures*, 87:183–193, 2016.

Bamberg J., Cairns G., y Kilminster D. The crystallographic restriction, permutations, and goldbach's conjecture. *The American mathematical monthly*, 110(3):202–209, 2003.

Bendsøe M., Guedes J., Haber R., Pedersen P., y Taylor J. An analytical model to predict optimal material properties in the context of optimal structural design. *Journal of Applied Mechanics*, 61(4):930–937, 1994.

Bendsoe M. y Sigmund O. *Topology optimization: theory, methods, and applications*. Springer Science & Business Media, 2003.

Cheng Y., Yang F., Xu J., y Liu X. A multilayer structured acoustic cloak with homogeneous isotropic materials. *Applied Physics Letters*, 92(15):151913, 2008.

Coelho P., Amiano L., Guedes J., y Rodrigues H. Scale-size effects analysis of optimal periodic material microstructures designed by the inverse homogenization method. *Computers & Structures*, 174:21–32, 2016.

de Souza Neto E. y Feijóo R. Variational foundation on multi-scale constitutive models of solids: small and large strain kinematical formulation. *LNCC Research & Development Report No 16*, 16, 2006.

Diaz A. y Benard A. Designing materials with prescribed elastic properties using polygonal cells. *International Journal for Numerical Methods in Engineering*, 57(3):301–314, 2003.

Giusti S. *Análise de sensibilidade topológica em modelos constitutivos multiescalas*. Tesis de

Doctorado, Laboratório Nacional de Computaçao Científica, LNCC, Brasil, 2009.

Gokhale N., Cipolla J., y Norris A. Special transformations for pentamode acoustic cloaking. *The Journal of the Acoustical Society of America*, 132(4):2932–2941, 2012.

Guedes J. y Kikuchi N. Preprocessing and postprocessing for materials based on the homogenization method with adaptive finite element methods. *Computer methods in applied mechanics and engineering*, 83(2):143–198, 1990.

Hashin Z. y Shtrikman S. A variational approach to the theory of the elastic behaviour of multiphase materials. *Journal of the Mechanics and Physics of Solids*, 11(2):127–140, 1963.

Huang X., Radman A., y Xie Y. Topological design of microstructures of cellular materials for maximum bulk or shear modulus. *Computational Materials Science*, 50(6):1861–1870, 2011.

Kolken H. y Zadpoor A. Auxetic mechanical metamaterials. *RSC Advances*, 7(9):5111–5129, 2017.

Lakes R. Foam structures with a negative poisson's ratio. *Science*, 235:1038–1041, 1987.

Lopes C., dos Santos R., y Novotny A. Topological derivative-based topology optimization of structures subject to multiple load-cases. *Latin American Journal of Solids and Structures*, 12(5):834–860, 2015.

Meille S. y Garboczi E. Linear elastic properties of 2d and 3d models of porous materials made from elongated objects. *Modelling and Simulation in Materials Science and Engineering*, 9(5):371, 2001.

Milton G. y Cherkaev A. Which elasticity tensors are realizable? *Journal of engineering materials and technology*, 117(4):483–493, 1995.

Neves M., Rodrigues H., y Guedes J.M. Optimal design of periodic linear elastic microstructures. *Computers & Structures*, 76(1-3):421–429, 2000.

Newnham R.E. *Properties of materials: anisotropy, symmetry, structure*. Oxford University Press on Demand, 2005.

Norris A. Acoustic cloaking theory. En *Proceedings of the Royal Society of London A: Mathematical, Physical and Engineering Sciences*, volumen 464, páginas 2411–2434. 2008.

Nye J. *Physical Properties of Crystals: Theri representation be tensors and matrices*, volumen 146. Clarendon Press- Oxford, 2006.

Pendry J., Schurig D., y Smith D. Controlling electromagnetic fields. *science*, 312(5781):1780–1782, 2006.

Powell R.C. Tensor properties of crystals. En *Symmetry, Group Theory, and the Physical Properties of Crystals*, páginas 55–78. Springer, 2010.

Schury F. *Two-scale material design-From theory to practice*. Tesis de Doctorado, Friedrich-

Alexander-Universitat Erlangen-Nurnberg, 2013.

Sigmund O. Materials with prescribed constitutive parameters: an inverse homogenization problem. *International Journal of Solids and Structures*, 31(17):2313–2329, 1994.

Sigmund O. Tailoring materials with prescribed elastic properties. *Mechanics of Materials*, 20(4):351–368, 1995.

Sigmund O. A new class of extremal composites. *Journal of the Mechanics and Physics of Solids*, 48(2):397–428, 2000.

Sigmund O. y Maute K. Topology optimization approaches. *Structural and Multidisciplinary Optimization*, 48(6):1031–1055, 2013.

Souvignier B. A general introduction to space groups. *International Tables for Crystallography*, A:22–41, 2016. Chapter:1.3.

Ting T. *Anisotropic elasticity: theory and applications*. 45. Oxford University Press, 1996.

Wang Y., Luo Z., Zhang N., y Kang Z. Topological shape optimization of microstructural metamaterials using a level set method. *Computational Materials Science*, 87:178–186, 2014.

Watts S. *Design of meta-materials with novel thermoelastic properties*. Tesis de Doctorado, University of Illinois at Urbana-Champaign, 2014.

Zheng X., Lee H., Weisgraber T., Shusteff M., DeOtte J., Kuntz E.D.J., Biener M., Ge Q., Jackson J., et al. Ultralight, ultrastiff mechanical metamaterials. *Science*, 344(6190):1373–1377, 2014.

Zowe J., Kočvara M., y Bendsøe M. Free material optimization via mathematical programming. *Mathematical programming*, 79(1):445–466, 1997.

Anexos

En el presente apartado se exponen los principales artículos que contienen la totalidad del trabajo desarrollado para esta Tesis. La disposición elegida no es cronológica, pero tiene como fin ordenar primero los conceptos principales, para luego presentar las aplicaciones desarrolladas.

Los artículos se listan a continuación:

Anexo **A** J.M. Podestá, C. Méndez, S. Toro, A.E. Huespe. *Symmetry considerations for topology design in the elastic inverse homogenization problem.* Journal of the Mechanics and Physics of Solids. DOI: 10.1016/j.jmps.2019.03.018.

Anexo **B** J.M. Podestá, C. Méndez, S. Toro, A.E. Huespe. *Material design of elastic structures using Voronoi cells.* International Journal for Numerical Methods in Engineering. DOI: 10.1002/nme.5804

Anexo **C** C. Méndez, J.M. Podestá, O. Lloberas-Valls, S. Toro, A.E. Huespe, J. Oliver. *Computational material design for acoustic cloaking.* International Journal for Numerical Methods in Engineering. DOI: 10.1002/nme.5560

Anexo **D** C. Méndez, J.M. Podestá, S. Toro, A.E. Huespe, J. Oliver. *Making use of Symmetries in the 3D Elastic Inverse Homogenization Problem.* International Journal for Multiscale Computational Engineering. DOI: 10.1615/IntJMultCompEng.2019029111.

Además, se presenta la documentación guía para el usuario del código de Base de Datos:

Anexo **E** J.M. Podestá, S. Toro, C. Méndez, A.E. Huespe. *Homogenized elasticity tensor database of periodic composites with microarchitectures displaying symmetric topologies.* Mendeley Data repositories. 10.17632/7kgf9xnrhb.1

El tesista declara haber participado activamente en el desarrollo de los nuevos conceptos aportados y llevado a cabo los experimentos numéricos necesarios para alcanzar los resultados que se exponen. Estas tareas fueron realizadas bajo la dirección del Dr. Alfredo Huespe y del Dr. Javier Mroginski, y en conjunto con los co-autores de cada artículo. Las sugerencias, revisiones y comentarios de los Dres. Huespe y Mroginski han sido una contribución importante para lograr la alta calidad de artículos presentados.

Los abajo firmantes avalan esta declaración.

Aval del Director de Tesis

Dr. Alfredo E. Huespe

Aval del Co-Director de Tesis

Dr. Javier L. Mroginski

Anexo A

Symmetry considerations for topology design in the elastic inverse homogenization problem

El artículo presentado a continuación ha sido publicado en la revista **"Journal of the Mechanics and Physics of Solids"**.

J.M. Podestá, C. Méndez, S. Toro, A.E. Huespe, *"Symmetry considerations for topology design in the elastic inverse homogenization problem"*, DOI: 10.1016/j.jmps.2019.03.018.

Symmetry considerations for topology design in the elastic inverse homogenization problem

J.M. Podestá[1], C. Méndez[1], S. Toro[1], A.E. Huespe[1,2,3][1]

[1]CIMEC-UNL-CONICET, Predio Conicet "Dr Alberto Cassano", CP 3000 Santa Fe, Argentina

[2]Centre Internacional de Metodes Numerics en Enyinyeria (CIMNE),Campus Nord UPC.

[3]E.T.S d'Enginyers de Camins, Canals i Ports, Technical University of Catalonia (Barcelona Tech)

Campus Nord UPC, Mòdul C-1, c/ Jordi Girona 1-3, 08034, Barcelona, Spain

Keywords: metamaterial design; elastic symmetry; topology optimization; inverse homogenization; tailored elastic properties.

Abstract

An analysis of the symmetries characterizing the micro-architecture topologies and the elastic material properties is performed. The goal is to elucidate a systematic procedure that facilitates the design of elastic metamaterial with a prescribed target elasticity tensor via inverse homogenization methodologies. This systematic procedure, which is defined through a set of rules, is based on the relationship established between the elasticity tensor symmetries and the symmetry displayed by the micro-architecture topology.

Following this procedure, it can be guaranteed that the designed composites, with the attained micro-structures, have effective elasticity tensors that possess the same or higher symmetries than those shown by the target elasticity tensors. Furthermore, the micro-architectures designed through this technique display simple topologies.

Both properties that are supplied by the procedure, i.e., the accomplishment of the required symmetry of the composite homogenized elasticity tensor combined with the topology simplicity,

[1]Corresponding author. E-mail address: ahuespe@cimec.unl.edu.ar (A.E. Huespe).

are assessed through numerical simulations of several micro-architecture design problems. They are designed by formulating the inverse homogenization problem as a topology optimization problem which is solved with two different standard algorithms. The proposed procedure and the conclusions here obtained do not depend on the algorithm adopted for solving this problem.

1. Introduction

The goal of the inverse homogenization problem addressed in this work is the micro-architecture design of a two-phase periodic elastic composite whose effective elasticity tensor $\mathbf{C}^h$ is identical to a target elasticity tensor $\hat{\mathbf{C}}$. In this context, a systematic procedure for restricting the search space of variables that are meaningful in this problem is described.

An approach to solve the mentioned inverse homogenization problem has been reported in the past by formulating it as a topology optimization problem, see for instance the landmark works by Sigmund (Sigmund (1994) and Sigmund (1995)) who has coined the name inverse homogenization to this kind of problem. See also the reference book by Bendsoe y Sigmund (2003) and the bibliography cited therein related to this topic. According to this approach, the topology optimization problem is formulated by choosing a design domain, Ω_μ, assumed as a base cell of the composite, which is also used to compute its overall elastic properties. The algorithm solving the topology optimization problem tests different distributions of given hard and soft materials to satisfy a proposed optimality condition, see for example the methodologies proposed by Huang et al. (2013), Amstutz et al. (2010), Ferrer et al. (2016), and Paulino et al. (2009) where the design of graded micro-architectures has been addressed.

The selection of the cell Ω_μ is a decision that has to be taken by the designer and is a particular aspect of the inverse problem that we want to highlight in this work. There are several issues related to this choice. For example, Coelho et al. (2016) investigate the cell size influence on the designed topology.

Also, Diaz. y Benard (2003) mention that the shape of the design domain plays an important role in widening the range of attainable micro-architectures with unusual properties. This has been the case for developing new classes of extreme material micro-structures by using rectangular unit cells and certain material distribution symmetries, see the cases studied in Sigmund (2000). The relationship between tensor symmetry and unit cell shape has already been discussed by Barbarosie et al. (2017) and Lukkassen et al. (2003). These authors exploit the symmetry of the material configuration within the unit cell to get a less expensive computation of the effective material properties. But, in these cases, the morphological symmetries have not been used to facilitate the search of a topology satisfying the inverse homogenization problem requirement.

In this work, we make an exhaustive analysis of the information associated with the target elasticity tensor. This information could be used to make easier the inverse design procedure. In particular, we aim to study the elasticity tensor symmetry and its connection with the base cell geometry and the material configuration within this cell. Then, based on this analysis, we introduce a set of guidelines, which can be taken as a protocol to guarantee the accomplishment of the required elastic symmetry.

To reach this goal, arguments taken from crystallography are employed. Typically, each crystal is associated with a point group through its Bravais lattice and its motif. This association helps to determine the crystal system, as well as, the symmetry of any effective material property, according to Neumann's principle (Nye (2006)). See the discussion about the connection between material and physical symmetries reported by Zheng y Boehler (1994).

In a complete parallelism, a Bravais lattice and a motif can be assigned to each periodic material configuration. Therefore, by following the same arguments to that given in crystallography, the material micro-architecture can be classified by possessing one of the seventeen plane groups with a given point group. Also, in this case, the point group of the material configuration geometry is connected with the effective elasticity tensor symmetry class. Hence, when this notion is applied to the inverse homogenization problem, the plane group characterization of the micro-structure could give a hint for distributing the material within the design domain such that the effective properties of the composite display a similar or higher symmetry than that shown by the target elasticity tensor. This is the principal line of argument taken by this work.

Another aspect related to the choice of the design domain has to be remarked. The symmetry properties of the target elasticity tensor give useful information to select the base cell shape between a family of cells. However, the slenderness of the adopted cell, taken from one particular family, should be defined by introducing more information. We propose to build a database storing effective elasticity tensors of composites with a set of representative and simple topologies. Then, the stored information in this database is used to choose the cell slenderness, as well as, to provide an initial configuration to solve the topology optimization algorithm.

A brief description of this paper is given as follows. Initially, we analyze the point and plane groups properties of different crystal systems in two-dimensions, as well as the point groups of the Bravais lattices associated with these crystals. We perform an exhaustive analysis of the full set of possible symmetries that can display a periodic crystal.

Next, we define a criterion to build the database. Based on this database and the symmetry notions previously discussed, in Section 4 we present the procedure through a series of rules that facilitates the inverse homogenization process.

The influence of these rules on the topology design process are assessed in Section 5 by means of a set of numerical simulations. We solve some representative inverse homogenization problems with techniques that follow the proposed rules and the solutions are compared with those obtained using conventional approaches that do not follow these rules.

1.1. Inverse material design as a topology optimization problem

Material design via inverse homogenization refers to the problem of finding the micro-architecture configuration of a composite whose effective elasticity tensor is identical to a target elasticity tensor. This problem involves two characteristic scale lengths; the macro-scale length, ℓ, which is of the same order of magnitude as that of the structure size, and the micro-scale length, ℓ_μ, which is of the same order of magnitude as that of the material micro-architecture characteristic length. We assume that $\ell_\mu \ll \ell$. The effective elasticity tensor is defined at the macro-scale level, such as sketched in Figure D.1, and the material design is performed at the scale ℓ_μ.

Material design via inverse homogenization has been formulated as a topology optimization problem in a given design domain and we follow a similar formulation in this paper.

Let us consider a structure whose material is a periodic composite constituted by two isotropic elastic phases M_1 and M_2. We take a basic micro-cell of this material identified by Ω_μ. In this micro-cell, phases M_1 and M_2 occupy the domains Ω_μ^1 and Ω_μ^2, respectively, see Figure D.1.

The characteristic function $\chi(\mathbf{y})$ in Ω_μ identifies the positions where the phase M_1 is placed and is defined by:

$$\chi(\mathbf{y}) = \begin{cases} 0 & \forall \mathbf{y} \in \Omega_\mu^2 \\ \\ 1 & \forall \mathbf{y} \in \Omega_\mu^1 \end{cases} . \tag{A.1}$$

Evidently, the homogenized elasticity tensor of the composite, $\mathbf{C}^h$, depends on the geometrical configuration of the phases M_1 and M_2 in Ω_μ. This dependence is made explicit by introducing the notation $\mathbf{C}^h(\chi)$. This tensor can be evaluated in Ω_μ by enforcing periodic boundary conditions in displacements fluctuations. Then, standard computational techniques based on finite elements (Bendsøe y Kikuchi (1988), Feyel y Chaboche (2000)) or Fast Fourier Transform (Michel et al. (1999)) can be used to get this goal.

Next, we formulate the micro-architecture inverse design problem as a topology optimization problem expressed as follows: given the design domain Ω_μ and the target effective elasticity tensor

$\hat{\mathbf{C}}$, find the characteristic function χ satisfying:

$$\begin{aligned} &\min_{\chi} \frac{1}{|\Omega_\mu|} \int_{\Omega_\mu} \chi \, d\Omega \\ &\text{such that: } \|\mathbf{C}^h(\chi) - \hat{\mathbf{C}}\| = 0 \ . \end{aligned} \tag{A.2}$$

The cost function represents the stiff phase volume fraction. In particular, considering that the soft phase is void, the problem (A.2) identifies a minimum weight problem.

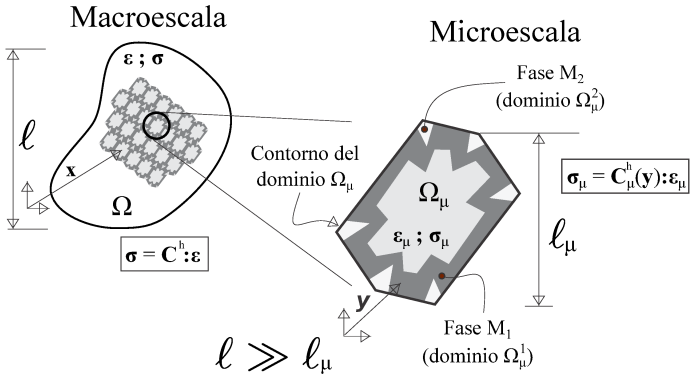

Figura A.1: The material design is carried out by solving an inverse homogenization technique formulated as a topology optimization problem which involves two characteristic scale lengths. The micro-cell Ω_μ is used as the design domain for the topology optimization problem. The symbols $\boldsymbol{\sigma}$ and $\boldsymbol{\varepsilon}$ represent the macro-stress and macro-strain tensors, respectively.

There are several implicit variables in the problem (A.2). One of particular interest here is the design domain, Ω_μ, where this problem is posed. The shape of this domain is a variable that should be fixed in advance; it results from a decision taken by the designer. Also, the enforcing of periodic boundary conditions along pre-established directions to find the effective properties of the composite, $\mathbf{C}^h$, is a decision taken in advance by arguing that the micro-architecture is periodic along these directions. Due to this arguments, the full material architecture must result from a spatial replica, by tessellation, of the cell Ω_μ.

We remark that both decisions play an important role to govern the complexity of the attained micro-architecture topology.

2. Effective elastic symmetry inherited from the micro-architecture configuration

Effective elastic properties of composites constituted by two isotropic phases show different classes of symmetries. These symmetries are a result of the micro-structure geometry, due to the spatial distribution of phases.

In this Section, by resorting to a complete parallelism with crystallography, we analyze the

connection between the overall elastic properties and the micro-structure geometry, from the common perspective involving the symmetry properties.

First, we categorize the periodic material micro-architectures according to their point groups. To reach this goal, we identify the underlying Bravais lattice, the motif and the crystal system of the material configuration. This classification involves only the geometrical features of the composite. See the book of Sólyom (2007) for additional information about this topic. Then, the elastic symmetry classes of these composites are briefly discussed and presented. Finally, we close this Section by discussing the connection between physical and material configuration symmetries stated in terms of Neumann's principle.

Point group symmetry

An isometric transformation imposed on the material configuration, which leaves invariant its spatial distribution, is a symmetry operation. The composition of successive symmetry operations is also a symmetry operation for that material configuration. So, from an algebraic point of view, this set of transformations constitutes a group. One simple operation of this group is a symmetry element.

First, we consider a restricted set of symmetry transformations which leaves a point of the material fixed. In this case, the symmetry elements are the rotations around a fixed axis (orthogonal to the plane of analysis), reflections across straight lines intersecting the fixed point and inversion in the fixed point. The last one can be ignored as it corresponds to a rotation through an angle of π[rad]. The element of the group denoted n is a rotation through an angle $2\pi/n$ [rad] and the element denoted m is a reflection through a plane.

Now, consider the groups that contain mirror lines and rotations. Any line obtained from a mirror line via a rotation with the angle $2\pi/n$ [rad], around the $n-$fold axis, is also a mirror line. Then:

- for n odd, the angular separation of the n mirror lines obtained in this way is π/n [rad]. Thus, the group has $2n$ symmetry elements, n rotations and n reflection planes, and is denoted by nm;

- for n even, rotations of a mirror line will yield only $n/2$ different mirror lines whose angular separation is $2\pi/n$ [rad]. Nevertheless, in this case, there must exist another set of mirror lines, i.e., the angle bisectors of the previously obtained lines. This is so because the composition of a reflection, in a mirror line, and a rotation through $2\pi/n$ [rad] is equivalent to a reflection in a mirror line that makes an angle π/n with the original mirror line. Therefore, there are two independent sets of mirror lines. This is expressed by the notation nmm of

such groups.

Considering the material distribution in the space, we can identify all the isometric transformation with fixed point leaving invariant this distribution. The set of all the symmetry elements of a given material is called its *point group*.

2.1. Materials with periodic micro-architecture

Let us consider materials having periodic micro-architectures with a given translational symmetry. The micro-architecture is invariant under discrete translations along two directions defined by the non-proportional primitive vectors $\mathbf{a}_1$ and $\mathbf{a}_2$. The translation of the material along directions that result from integer multiples of $\mathbf{a}_1$ and $\mathbf{a}_2$ takes the material into itself. Therefore, the characteristic function χ_i, for a given i-th phase, satisfies

$$\chi_i(\mathbf{x}+\mathbf{t}) = \chi_i(\mathbf{x}) \quad ; \quad \text{where} \quad \mathbf{t} = \omega_1\mathbf{a}_1 + \omega_2\mathbf{a}_2 \tag{A.3}$$

and the scaling factors ω_1 and ω_2 are two arbitrary integers.

Underlying Bravais lattices of a periodic pattern

Every periodic configuration of material possesses an underlying Bravais lattice and a motif. The procedure to identify the underlying lattice of a periodic structure and its motif is indicated in the artistic wallpapers reproduced in Figure A.2. The lattice and the primitive vectors are found by identifying the equivalent set of points of the material periodic array. For example, equivalent sets of points are the eyes of the fishes in Figure A.2-a and the red points in Figure A.2-b. Once the Bravais lattice is characterized, the unit cells can be easily recognized. The motif is the material configuration pattern within a unit cell.

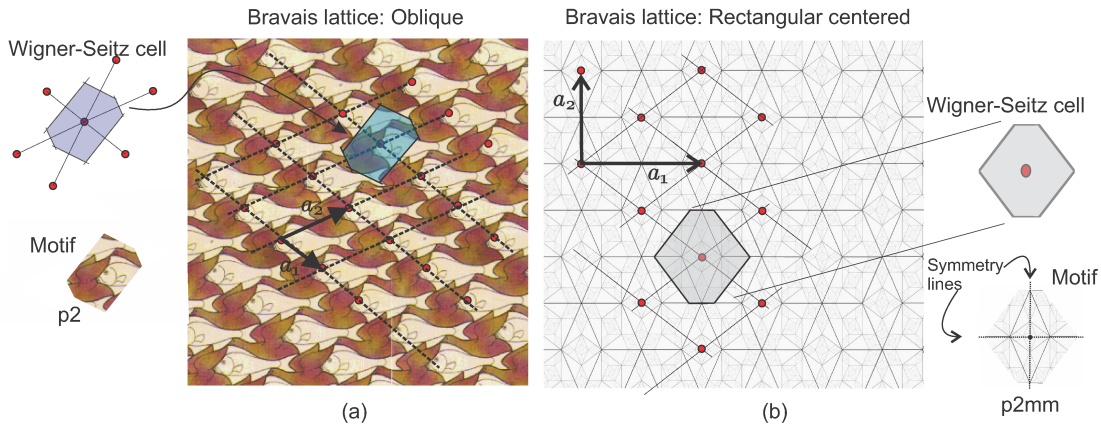

Figura A.2: Identification of the underlying Bravais lattices, primitive vectors, Weigner-Seitz (Voronoi) cells and plane groups of artistic wallpapers by: (a) Escher; b) Geometrical draw.

According to the angle that the primitive vectors $\mathbf{a}_1$ and $\mathbf{a}_2$ form and the ratio between their magnitudes, only five different types of Bravais lattices can be identified. They are depicted in Figure A.3 and are called: Hexagonal, Square, Rectangular primitive, Rectangular centered and Oblique.

Lattice point group

Due to the characteristic translational symmetry of Bravais lattices, and considering the crystallographic restriction theorem, there can only be a finite number of point groups for the five types of lattices. They are n-fold angles of symmetries, where $n \in \{2, 3, 4, 6\}$, with one or two systems of symmetry lines. Then, the only possible point groups that Bravais lattices can have are the following four types: 2, $2mm$, $4mm$, $6mm$. In this notation[2], the number identifies the n-fold angle of rotational symmetry and m and mm means one or two mirror line systems. A mirror line system is the set of reflection lines which are obtained by the n-fold rotation of one mirror line.

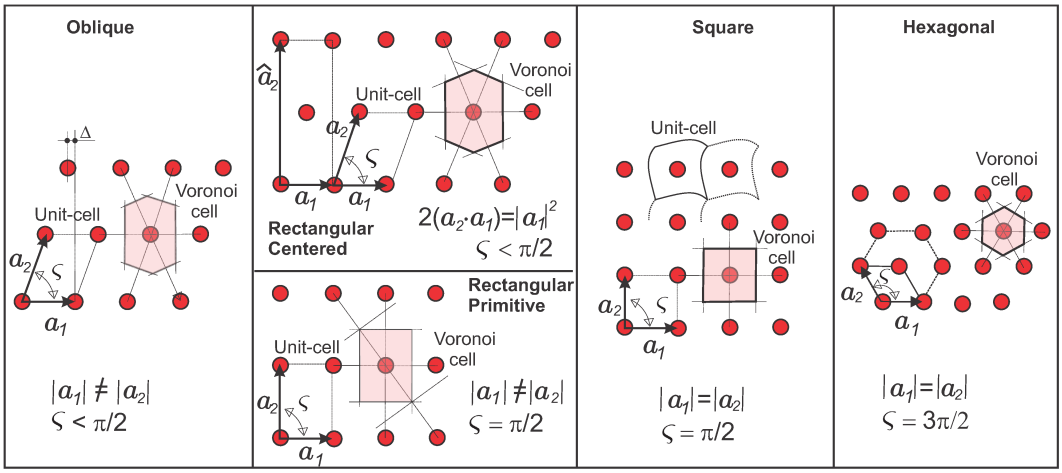

Figura A.3: The five Bravais lattice types in the plane.

All the symmetry elements with a fixed point of the five types of plane lattices are shown in Figure A.4. The fixed point can be any one of the lattice atoms. Therefore, the respective point group of each lattice can also be identified. They are shown in the same Figure.

The *lattice system* is formed by collecting the lattice types sharing similar point groups. So, due to the fact that the Rectangular primitive and the Rectangular centered lattices share the same point group, $2mm$, they are grouped into one lattice system identified as the Rectangular lattice systems. Therefore, the four lattice systems are Oblique, Rectangular, Square and Hexagonal.

A Bravais lattice is the tessellation of a repetitive pattern, i.e., the juxtaposition of a given domain by the translation along the primitive directions. The domains with the repetitive patterns which have the smallest areas are the unit cells of the lattice, such as shown in Figure A.4. In

[2]We use the International or Hermann-Mauguin notation, see Souvignier (2016).

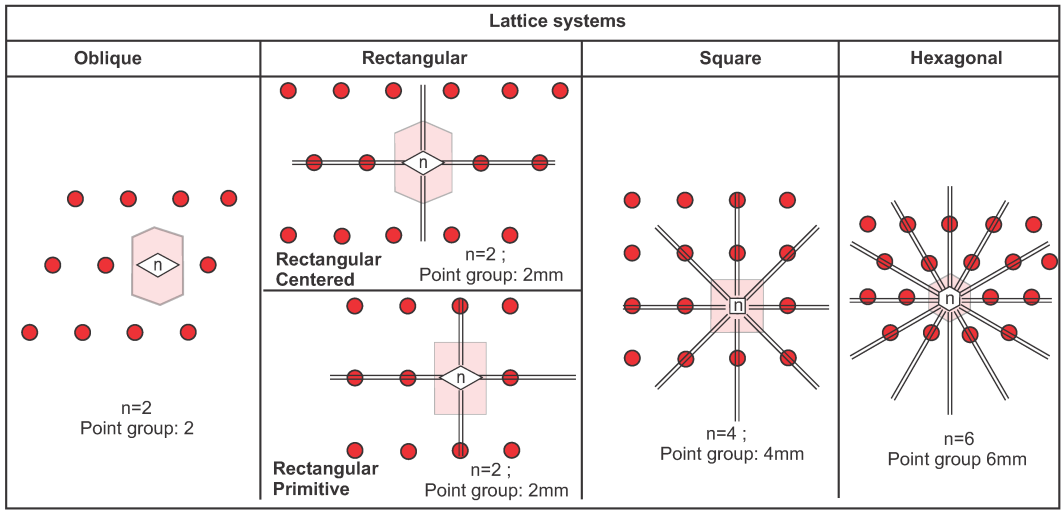

Figura A.4: Rotational and reflection symmetries of Bravais lattices. Mirror planes (reflection symmetries) are depicted with two parallel lines; rotational symmetries are identified with the rotation angle $2\pi/n$ around an axis perpendicular to the plane. Parameters n and the lattice point groups are depicted. Voronoi cells have the same point groups as that shown by the associated lattices, i.e., they preserve the symmetries of the lattices. According to the lattice point group, there are four Bravais lattice systems: Oblique (2), Rectangular (2mm), Square (4mm) and Hexagonal (6mm). The Rectangular system has two subsystems: centered and primitive.

particular, we focus on the Weigner-Seitz[3] (or Voronoi) unit-cell of the Bravais lattice.

Remark: the Weigner-Seitz cell and the associated lattice have the same point group. This statement is graphically observed in Figure A.4.

Parametrization of Bravais lattices

All Bravais lattices can be characterized through the following two parameters:

$$\omega = \|\mathbf{a}_2\|/\|\mathbf{a}_1\| \; ; \tag{A.4}$$

$$\varsigma = \arccos\left[(\mathbf{a}_2 \cdot \mathbf{a}_1)/(\|\mathbf{a}_2\|\|\mathbf{a}_1\|)\right] \; . \tag{A.5}$$

Each pair of values ω, ς defines a Bravais lattice. It can be easily proven that the range of parameters ω, ς identifying the full set of Bravais lattices is limited to the points displayed in gray in Figure A.5-a. We refer to this region as the reduced domain of parameters. In fact, due to the symmetry properties of these lattices, the points that are outside this reduced domain characterize lattices which can always be parametrized with points in the reduced domain.

Figure A.5-b depicts the Voronoi cells of the Bravais lattices in several points on the reduced domain (ω, ς). Note that Oblique Bravais lattices are only represented by points in the interior of the reduced domain, while Rectangular, Square and Hexagonal lattices are only represented by points on its boundary.

[3]The Weigner-Seitz cell of a lattice is the domain centered in a lattice atom and comprising all the spatial points that are closer to the central atom than to any other atom of the lattice.

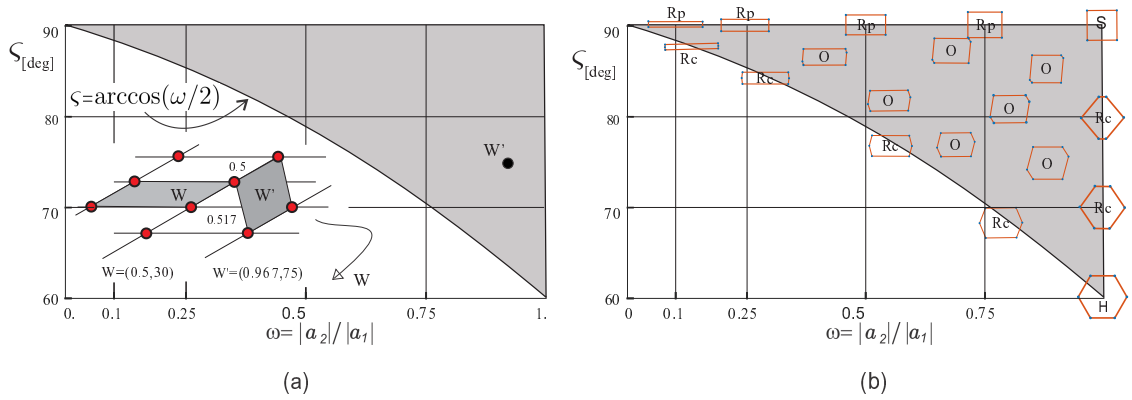

Figura A.5: Space of parameters (ω, ς) characterizing the Bravais lattices. a) The gray region is the reduced domain. Points outside of the reduced domain (W) identify lattices that can be parameterized with equivalent points in the reduced domain (W'). b) Voronoi cells of lattices characterized by different parameters (ω, ς): O (Oblique), Rc (Rectangular centered), Rp (Rectangular primitive), S (Square) and H (Hexagonal).

Plane groups

The material configuration, or crystal motif, can be defined by identifying a unit cell. When the motif is taken into account, an additional symmetry element, the *glide reflection*, has to be contemplated. It consists of a geometrical reflection, through a mirror line, followed by a translation, parallel to the same line. The translation distance is half of the periodicity distance, or unit cell size, parallel to the mirror line.

A plane group is the set of symmetry elements, including glide reflection, which identifies a wallpaper[4]. Here, we use the word *wallpaper* to denote a specific configuration of the material distribution of a periodic composite. Therefore, every wallpaper has an underlying Bravais Lattice and a motif that defines a plane group.

Similar to Bravais Lattice point groups, there are only a finite number of plane groups identifying all possible wallpapers. After introducing the motif and the glide reflection symmetries, the number of plane groups is seventeen. All of them are shown in Figure A.6, where we depict the Voronoi cells of the underlying lattices with different motifs and the symmetry elements characterizing each plane group: reflection symmetry lines, the n-fold angle of rotational symmetry and the glide lines.

These plane groups are denoted by the letters p or c which indicates that the underlying lattice is either primitive or centered. The existence of one or two glide reflection lines are identified with the letters g and gg, respectively. And, similar to the notation of point groups, the number identifies the n-fold angle of rotational symmetry, and the letters m and mm indicates if there are one or two mirror line systems, respectively.

The Bravais lattice symmetry of the wallpaper may be broken when the motif has a lower

[4]The words wallpaper and plane crystal have an identical meaning in this work.

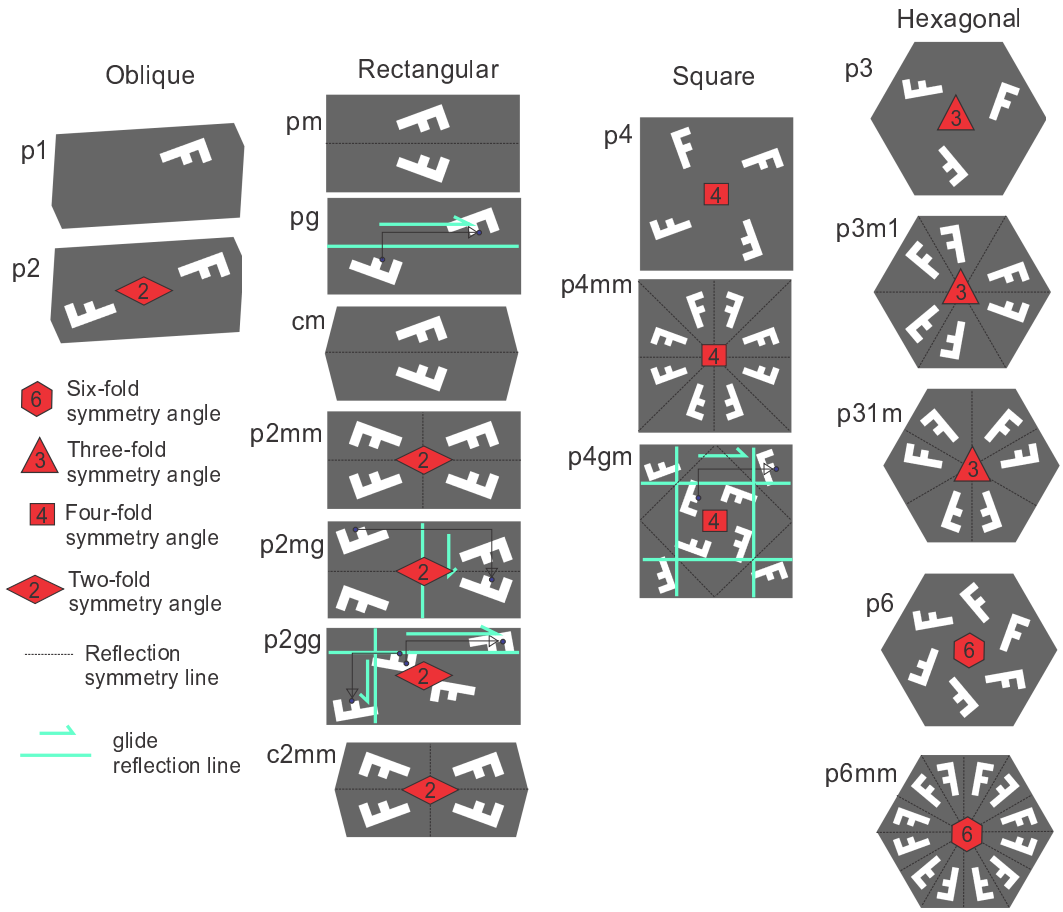

Figura A.6: Voroni cells of crystals with the seventeen plane groups in 2D. The symmetry elements of each crystal, i.e. the Voronoi cell and the motif, are shown. Gray and white colors in the wallpapers represent the distribution of the composite phases.

symmetry than that of the underlying lattice. Therefore, the wallpaper symmetry group is a subgroup of that characterizing the underlying lattice. According to this property, we next establish the relationship that assigns one point group to each one of the seventeen plane groups that represent arbitrary wallpapers and motifs. This relationship is shown in Table A.2. Each plane group in the fourth column is associated (in the same line) with one point group in the third column. Note that wallpapers with plane group pg has a point group m. This relationship comes from the fact that performing a mirror symmetry of a crystal with symmetry pg results in the same crystal with a translation of half of the unit cell size parallel to the glide line. Therefore, by considering an infinite crystal, both crystals, the original one and the reflected and translated one, are indistinguishable when the effective material properties are evaluated. A similar conclusion can be given to wallpapers with plane group $p2mg$, $p2gg$ and $p4gm$ by changing the g symmetry operation by a mirror symmetry operation m.

From these comments, there are only ten point groups characterizing the full set of wallpapers. They are depicted in Table A.2, third column, and are : 1, 2, m, $2mm$, 4, $4mm$, 3, $3mm$, 6 and $6mm$.

The system of crystals: the crystals are next classified by their point group symmetry. We identify all crystals which have a given point group. This identification is shown in Table A.2, see also Landwehr (2011). Note that each crystal is composed of an underlying lattice, shown in column 5, and a motif having the symmetry given by the plane group in column 4. For example, crystals which lattices are Rectangular or Square and their plane groups are $p2mm$, $p2mg$, $p2gg$ and $c2mm$ have a point group $2mm$. Also, observe that a crystal with hexagonal lattice and plane group $p1$ has the point group 1.

Once this relationship has been established, the *systems of crystals* can be defined as follows. A crystal system is the collection of crystals sharing the same point groups with an identical set of compatible lattices. Using this criterion, we can classify the crystals into four systems: Oblique, Rectangular, Square and Hexagonal[5].

Again, as an example, the crystals having point groups m and $2mm$ are compatible with the same lattices, and therefore, they belong to the Rectangular crystal system.

2.2. Elasticity tensor structures according with their symmetries

The symmetry of the overall elastic properties of heterogeneous materials are well established and are classified according to their point group, such as described in the work of Ting (1996), see

[5]In plane crystals, there is a one-to-one relationship between the lattice systems and the crystal systems. However, when the same classification is extended to three-dimensions, this one-to-one relationship is not preserved.

Elasticity tensors $\mathbf{C}_N$			
$O(2)$ (2)	D_4 (4)	D_2 (5)	Z_2 (6)
$\begin{bmatrix} c_1 & c_2 & 0 \\ c_2 & c_1 & 0 \\ 0 & 0 & (c_1-c_2) \end{bmatrix}$	$\begin{bmatrix} c_1 & c_2 & 0 \\ c_2 & c_1 & 0 \\ 0 & 0 & c_3 \end{bmatrix}$	$\begin{bmatrix} c_1 & c_2 & 0 \\ c_2 & c_4 & 0 \\ 0 & 0 & c_3 \end{bmatrix}$	$\begin{bmatrix} c_1 & c_2 & c_5 \\ c_2 & c_4 & -c_5 \\ c_5 & -c_5 & c_3 \end{bmatrix}$

Tabla A.1: a) Symmetry classes in plane elasticity. Structure of the elasticity tensors, $\mathbf{C}_N$, expressed in the Normal coordinates (material axis): $O(2)$ for Isotropic, D_4 for Tetragonal, D_2 for Orthotropic and Z_2 for fully Anisotropic materials. The total numbers of elastic coefficients $c_1, c_2, ...$ defining the elasticity tensors are shown in parenthesis for each symmetry class. The rotation angle transforming $\mathbf{C}$ into $\mathbf{C}_N$ is also considered as an additional coefficient of the elasticity tensor.

also Nye (2006).

The methodology followed by Ting to classify the elasticity tensor structures with comparable symmetries, a very conventional procedure in solid mechanics, consists of applying isometric transformations, compatible with a given point group, to the elasticity tensor. Then, the elastic tensor coefficients have to satisfy the necessary invariance conditions derived from these transformations.

In plane elasticity, this methodology determines four different elastic symmetry classes. They are denoted $O(2)$ for Isotropic, D_4 for Tetragonal, D_2 for Orthotropic and Z_2 for fully Anisotropic materials. From higher to lower symmetry classes, they are: $O(2) \subset D_4 \subset D_2 \subset Z_2$. Furthermore, the point group with lower symmetry that is compatible with each one of these classes is: 3 for $O(2)$, 4 for D_4, m for D_2, and 1 for Z_2, respectively. This association between the four elastic classes and the point groups is shown in Table A.2 (Ting (1996)).

The criterion followed to find the four classes of elastic symmetries implicitly introduces a coordinate system which is aligned with the symmetry planes of the point group. This coordinate system is called here as the Normal coordinate system. We use the notation $\mathbf{C}_N$ to indicate that the elasticity tensor is described in this coordinate system.

The Table A.1 displays the elasticity tensor coefficients of $\mathbf{C}_N$ for the four elastic symmetry classes[6]. The numbers in parenthesis indicate the quantity of independent elastic coefficients that define the elasticity tensors.

Considering an arbitrary elasticity tensor $\mathbf{C}$ described in the Cartesian coordinate system, Auffray et al. Auffray y Ropars (2016) describe an algorithm to determine its elastic symmetry class as well as to computes the rotation angle transforming $\mathbf{C}$ into its normal form $\mathbf{C}_N$. See also the Appendix in the paper by Podestá et al. (2018a).

[6]Here, the elasticity tensor $\mathbf{C}_N$ is described as a matrix in Kelvin's notation. The stress and strain vectors in Kelvin's notations are given by: $[\sigma_{ss}; \sigma_{nn}; \sqrt{2}\sigma_{sn}]^T$ and $[\varepsilon_{ss}; \varepsilon_{nn}; \sqrt{2}\varepsilon_{sn}]^T$, respectively, where s and n are the Natural coordinates. Therefore, the components of the matrix $\mathbf{C}_N$ are the corresponding elastic coefficients that are defined in accordance with the notation of these vectors.

Elastic symmetry class	Crystal system	Point group	Plane group	Compatible Bravais lattice and Wigner-Seitz unit cell				
				Oblique	Rectangular primitive	Rectangular centered	Square	Hexa
Z2	oblique	1	p1	⬣	▬	⬣	■	⬣
		2	p2					
D2	rectangular	m	pm		▬		■	
			pg					
			cm			⬣	◆	⬣
		2mm	p2mm		▬		■	
			p2mg					
			p2gg					
			c2mm			⬣	◆	⬣
D4	square	4	p4				■	
		4mm	p4mm					
			p4gm					
O(2)	hexagonal	3	p3					
		3m	p3m1					
			p31m					⬣
		6	p6					
		6mm	p6mm					

Tabla A.2: Elastic symmetry classes (column 1) are determined by the point group (column 3) of the crystal system (column 2). Also, each one of the seventeen plane groups (column 4), depicted in Tables A.3 and A.4, corresponds to a point group. Additionally, each plane group is compatible with several Bravais lattices (column 5). The symmetries (number of symmetry elements) increase from top to bottom. The higher symmetry is in the bottom of the Table.

2.3. Neumann's principle

The connection existing between the symmetry elements of the micro-architecture geometry and the symmetry elements of the overall elasticity tensor can be stated with a fundamental postulate of the crystal physics known as Neumann's principle.

This principle states that *"the symmetry elements of any effective physical property (optical, magnetic, thermal, mechanical properties) of a crystal must include the symmetry elements of the point group of the crystal"*, see Nye (2006).

According to this principle, the relation between the point group and the elastic symmetry class is recognized in Table A.2 between the first and third column. Note that, in the elastic case we are considering, identical lines of the Table relates an elastic class (column 1) with a crystal system (column 2).

This principle is confirmed by the computed results presented in Tables A.3 and A.4. In these Tables, the effective elasticity tensors of seventeen composites depicted in column 1 are shown. The micro-architectures of these composites show different plane groups. The Voronoi cells of these micro-architectures are shown in Figure A.6 and their plane groups are displayed in column 2 of the Tables A.3 and A.4. The related point group to each plane group is presented in column 3 of the same Tables.

The computed effective elasticity tensors in Normal coordinates[7] are denoted by $\mathbf{C}_N^h$ and are presented in Column 5 of Tables A.3 and A.4. In the same column, the angle between Cartesian and Normal coordinates are only shown for those cases where both coordinate systems are not coincident. According to the expressions of $\mathbf{C}_N^h$ in the Tables, and comparing with Table A.1, we can identify their elastic symmetry class which are depicted in column 4. Also, and according to the same characterization of the elastic symmetry, the point groups of the effective elasticity tensors, $\mathbf{C}_N^h$, are compatible with the symmetry anticipated by Neumann's principle and the information given in Table A.2. Finally, it is noted that the Normal axes coincide with the Cartesian ones when one of the symmetry axes of the plane group is parallel to one Cartesian axis.

Remark: Neumann's principle does not state that the symmetry elements of a physical property *must be the same* as the corresponding ones to the crystal point group. Very often, the physical properties may possess higher symmetry than the crystal point group. For example, some periodic materials with square unit-cells and motifs having a plane group $p1$, with a point group 1, may have an isotropic effective elasticity. Examples of this feature are the micro-structures displayed in Figure 1 of reference Andreassen et al. (2014) having a plane group $p2mg$, with a point group

[7] The composites are constituted by a stiff material, displayed in gray color, and void displayed in white color. The elasticity tensor is normalized with an adequate Young's modulus of the stiff material to attain a coefficient C_{11} with value 1 in all cases. The Poisson's ratio of the stiff material is 0.3.

$2mm$, and an isotropic effective elasticity tensor. See also Figure A.11 below, case S_{pm}, instance 2.

As a remarkable consequence of this principle, a procedure based on the following premise is developed: *given the number of parameters characterizing the elastic response, or similarly, the symmetry class of the target elasticity tensor, we design the micro-structure by appealing to Voronoi cells and plane groups guaranteeing the attainment of effective properties having the same or higher symmetries to those of the target tensor*.

3. Database of elasticity tensors

An additional ingredient introduced in the present inverse design methodology is the use of a database containing homogenized elasticity tensors. This database is built off-line by sampling a spectrum of periodic composite materials.

The homogenized elasticity tensors stored in the database are computed from composites with a stiff phase and void. Their micro-structures are identified with the Bravais lattices parameters (ω, ς) which are defined by expressions (A.4) and (A.5). The motifs are determined by a set of hard material bars. These bars are distributed into the Voronoi cell of the lattice by following two patterns P, denoted P_A and P_B.

The pattern P_A consists of a set of bars placed on the boundaries of the cell such as shown in Figure A.7-a. Pattern P_B is similar to P_A but with a re-entrant architecture of bars in the vertices of the Voronoi cells, such as shown in Figure A.7-b. The geometry of pattern P_B is defined with the relative position of points $V1$, $V2$ and the size r respect to the cell size. Patterns P_A and P_B are arbitrarily chosen. However, pattern P_A is a simple topology with a lattice-type micro-architecture. This type of micro-architecture has attracted enormous interest in last years, see for example Rashed et al. (2016) and Wang et al. (2018). Also, the pattern P_B is a lattice-type micro-architecture that is introduced to obtain elastic properties with negative Poisson's ratios (Kolken y Zadpoor (2017), Jiang y Li (2018)). The bar thickness e in both patterns P_A and P_B defines the volume fraction f of the composite.

In this way, the database contains homogenized elasticity tensors $\mathbf{C}^h_{db}$ of materials whose micro-structures are defined by four parameters ω, ς, P and f. Therefore, each element of the database is identified through its dependence with these parameters, $\mathbf{C}^h_{db}(\omega, \varsigma, P, f)$. The range of parameters $(\omega, \varsigma, P, f)$ that is utilized to compute the database are the following:

- The first two parameters, ω and ς, are varied such that the parametrized reduced domain of Figure A.5-a is swept by defining a regular mesh of 6283 sampling points which cover the

Assemblage	Plane group	Point group	Elastic Symmetry class	C_N^h and angle
	p1	1	Z_2	$\begin{bmatrix} 1.0000 & 0.2604 & -0.0027 \\ 0.2604 & 0.8797 & 0.0027 \\ -0.0027 & 0.0027 & 0.6126 \end{bmatrix}$ $ang = 10.0835°$
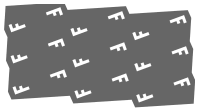	p2	2	Z_2	$\begin{bmatrix} 1.0000 & 0.2269 & 0.0187 \\ 0.2269 & 0.7257 & -0.0187 \\ 0.0187 & -0.0187 & 0.5638 \end{bmatrix}$ $ang = 9.0361°$
	pm	m	D_2	$\begin{bmatrix} 1.0000 & 0.2468 & 0.0000 \\ 0.2468 & 0.9530 & 0.0000 \\ 0.0000 & 0.0000 & 0.4584 \end{bmatrix}$
	pg	m	D_2	$\begin{bmatrix} 1.0000 & 0.2349 & 0.0000 \\ 0.2349 & 0.7311 & 0.0000 \\ 0.0000 & 0.0000 & 0.5930 \end{bmatrix}$
	cm	m	D_2	$\begin{bmatrix} 1.0000 & 0.2450 & 0.0000 \\ 0.2450 & 0.9495 & 0.0000 \\ 0.0000 & 0.0000 & 0.4545 \end{bmatrix}$
	p2mm	2mm	D_2	$\begin{bmatrix} 1.0000 & 0.1929 & 0.0000 \\ 0.1929 & 0.7839 & 0.0000 \\ 0.0000 & 0.0000 & 0.3692 \end{bmatrix}$
	p2mg	2mm	D_2	$\begin{bmatrix} 1.0000 & 0.2166 & 0.0000 \\ 0.2166 & 0.8250 & 0.0000 \\ 0.0000 & 0.0000 & 0.4226 \end{bmatrix}$
	p2gg	2mm	D_2	$\begin{bmatrix} 1.0000 & 0.2248 & 0.0000 \\ 0.2248 & 0.5645 & 0.0000 \\ 0.0000 & 0.0000 & 0.5736 \end{bmatrix}$
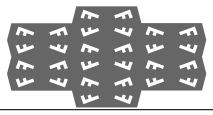	c2mm	2mm	D_2	$\begin{bmatrix} 1.0000 & 0.1893 & 0.0000 \\ 0.1893 & 0.7667 & 0.0000 \\ 0.0000 & 0.0000 & 0.3653 \end{bmatrix}$

Tabla A.3: Column 1 depicts the microstructure of the composites resulting from the assemblage of the Voronoi cells in Figure A.6. These assemblages show the seventeen types of paper groups. Columns 2 and 3 depict the point and plane groups, respectively, of the assemblages. The column 5 presents the homogenized elasticity tensors in Natural coordinates, $\mathbf{C}_N^h$, and the rotation angle from Cartesian to Natural coordinates, of the composites in column 1. These homogenized tensors have the symmetry classes depicted in column 4.

Assemblage	Plane group	Point group	Elastic Symmetry class	C_N^h and angle
	p4	4	D_4	$\begin{bmatrix} 1.0000 & 0.2378 & 0.0000 \\ 0.2378 & 1.0000 & 0.0000 \\ 0.0000 & 0.0000 & 0.6594 \end{bmatrix}$ $ang = -80.0970°$
	p4mm	4mm	D_4	$\begin{bmatrix} 1.0000 & 0.2803 & 0.0000 \\ 0.2803 & 1.0000 & 0.0000 \\ 0.0000 & 0.0000 & 0.6515 \end{bmatrix}$
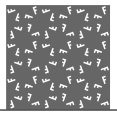	p4gm	4mm	D_4	$\begin{bmatrix} 1.0000 & 0.2444 & 0.0000 \\ 0.2444 & 1.0000 & 0.0000 \\ 0.0000 & 0.0000 & 0.6972 \end{bmatrix}$
	p3	3	$O(2)$	$\begin{bmatrix} 1.0000 & 0.2784 & 0.0000 \\ 0.2784 & 1.0000 & 0.0000 \\ 0.0000 & 0.0000 & 0.7216 \end{bmatrix}$
	p3m1	3m	$O(2)$	$\begin{bmatrix} 1.0000 & 0.2991 & 0.0000 \\ 0.2991 & 1.0000 & 0.0000 \\ 0.0000 & 0.0000 & 0.7009 \end{bmatrix}$
	p31m	3m	$O(2)$	$\begin{bmatrix} 1.0000 & 0.3016 & 0.0000 \\ 0.3016 & 1.0000 & 0.0000 \\ 0.0000 & 0.0000 & 0.6984 \end{bmatrix}$
	p6	6	$O(2)$	$\begin{bmatrix} 1.0000 & 0.2068 & 0.0000 \\ 0.2068 & 1.0000 & 0.0000 \\ 0.0000 & 0.0000 & 0.7932 \end{bmatrix}$
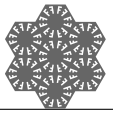	p6mm	6mm	$O(2)$	$\begin{bmatrix} 1.0000 & 0.3401 & 0.0000 \\ 0.3401 & 1.0000 & 0.0000 \\ 0.0000 & 0.0000 & 0.6599 \end{bmatrix}$

Tabla A.4: (Continuation of Table A.3).

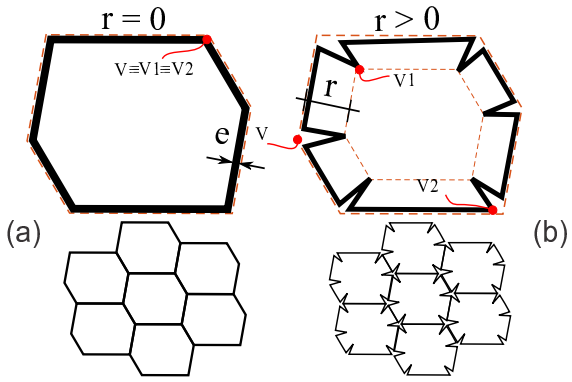

Figura A.7: Two-parametrized topologies used for the database construction. Patterns: a) P_A, and b) P_B.

full reduced space.

- Several volume fractions f varying from $f = 0.005$ to $f = 0.8$. The volume fraction is given in term of the thickness e of the bars.

- The variable P takes the values, P_A and P_B.

The stiff material properties utilized to build the database are defined with a normalized Young's modulus $E = 1.GPa$ and Poisson's ratio $\nu = 0.3$.

Partial results of this database have been presented in Podestá et al. (2018a). From that work, it can be observed that auxetic materials are captured with the micro-architectures characterized by the pattern P_B.

Remark: The information stored in the database, of the order of 10^5 elasticity tensors, is utilized to provide a hint for selecting, from a predefined Bravais lattice system, the Voronoi cell used as the design domain of the topology optimization problem, see item (3) of the next Section 4. The database information is managed as follows:

- Once the target elasticity tensor $\hat{\mathbf{C}}_N$ and its point group is known, we search the parameters, ζ, of the database entry whose elasticity tensor $\mathbf{C}^h_{db}(\zeta)$ satisfies the solution of the problem:

$$\zeta = \arg\left\{ \min_{\zeta} \|\mathbf{C}^h_{db}(\zeta) - \frac{1}{E_1}\hat{\mathbf{C}}_N\| \right\}; \qquad \text{where } \zeta := \{\omega, \varsigma, P, f\}, \tag{A.6}$$

  with the parameters (ω, ς) restricted to the region characterizing Bravais lattices with identical point group to that of the target tensor. Regions in the plane (ω, ς) with the related point groups are shown in Figure A.5-b. The factor E_1 scaling the target elasticity tensor is the Young's modulus of the composite stiff phase to be designed.

- Furthermore, the micro-architecture associated with the solution of problem (A.6) could be taken as the initial configuration for the iterative topology optimization algorithm.

The database of homogenized elasticity tensors, the software to compute the entries of the database for the parameter set ζ and the software to attain the solution of the problem (A.6) are freely available in the Mendeley dataset repository, see Podestá et al. (2018b). All the codes are written in Matlab.

4. A systematic procedure for tailoring elastic composites through inverse homogenization technique

Based on the symmetry properties of the target elasticity tensors, the discussion given in Section 2 and taking into account the elasticity tensor database, four heuristic rules are introduced to facilitate and enlarge the possible set of configurations obtained with the inverse homogenization design problem. These rules define a systematic procedure that can be adopted by the designer and are established as follows.

1) The topology optimization problem (A.2) is solved in the Normal basis of the target tensor. It means that the tensor $\hat{\mathbf{C}}$ is replaced by $\hat{\mathbf{C}}_N$ in the formulation (A.2).

2) Voronoi cells of Bravais lattices, whose point groups are compatible with the point groups of the target tensors, are chosen as the design domain Ω_μ. The relationship between the point groups of both entities, lattice and elasticity tensor, are shown in Table A.2. Entities sharing the same point group in the Table are displayed in identical lines. For example, for a target tensor having D_2 symmetry, the compatible cells are those associated with R_p or R_c Bravais lattices, such as rectangles or irregular hexagons are shown in Figure A.4. In this case, note that square and regular hexagonal cells are also compatible.

3) The slenderness of the cell, i.e., the aspect ratio between the larger and shorter size of the cell, can be determined through the database entries and the criterion defined by expression (A.6). Typically, this slenderness ratio should be defined in the Voronoi cells of Oblique, R_c and R_p lattices.

4) The symmetry displaying the material distribution within the Voronoi cell is decided in accordance with symmetry properties of the target elasticity tensor. The material configuration symmetry defines the micro-architecture plane group. Then, this configuration should be compatible with the target elasticity tensor point group. The compatibility relationships between plane groups and elasticity tensor point groups are presented in Table A.2; the entries displayed in the first and the fourth columns of the same line are compatible. Thus, recalling the previous example, i.e., a target tensor having D_2 symmetry, the compatible

plane groups are pm, pg, cm, $p2mm$, $p2mg$, $p2gg$ or $c2mm$. Our experience is that several configurations, with compatible plane groups, have to be tested and solved. In some cases, improved designs are attained by enforcing the higher compatible symmetry, though, this is not a general rule.

To apply the last rule, the symmetries of the material configuration compatible with the plane group can only be enforced if the topology optimization problem is solved in the Normal basis of $\hat{\mathbf{C}}$, such as mentioned in the first rule. In this basis, the symmetry planes of the plane groups are coincident with the symmetry axes of the Voronoi cells, such as shown in Figure A.6. Note also that the cost of the finite element analysis for computing the homogenized elasticity tensor, in the topology optimization problem, can significantly be reduced after introducing the symmetries compatible with the plane group. This issue has been addressed by Barbarosie et al. (2017) and Lukkassen et al. (2003).

5. Numerical assessments

Some micro-structures designed via a topology optimization problem that follows the systematic procedure previously described are analyzed and compared with micro-structures obtained with alternative conventional procedures without enforcing those rules. The effects that several design variables have on the attained solutions are assessed, such as:

i) Different types of design domains. The tested cell shapes are square, rectangles with different aspect ratios and regular or irregular hexagons. Additionally, the enforcement of different plane groups is also tested.

ii) Voronoi cells with symmetry axes arbitrarily placed or aligned with the Normal bases are tested.

iii) Different material configurations are taken as the starting points of the topology optimization algorithm.

The objective is to compare the solutions obtained in those different situations.

5.1. Designing an extreme isotropic material with minimum Poisson's ratio

The target material, whose micro-structure is designed in this test, is a biphasic isotropic composite with the minimum Poisson's ratio that is estimated using the Cherkaev y Gibiansky (1993) bounds for this kind of composite. The properties of the composite components and the volume

fraction of the hard material are chosen such that the Cherkaev et al.'s bounds estimate an elasticity tensor with negative Poisson's ratio, which makes this test more challenging.

Due to the interesting properties of auxetic materials, their micro-architecture designs have been profusely studied in the literature, such as mentioned in the review by Ren et al. (2018). Only to cite a few works closely related to the present contribution, the paper of Larsen et al. (1997) describes the micro-architecture design of auxetic composites using topology optimization tools, particularly the SIMP technique. This paper also shows the manufacture of such composites and their experimental testing. More recently, and using a similar development, Andreassen et al. (2014) have reported the designs of 3D micro-architectures with negative Poisson's ratios and describe their manufacture attainability. Also, the work by Jiang y Li (2018) gives a survey of this topic, as well as a discussion about the fabrication of auxetic materials. An interesting analysis of three typical micro-architecture topologies, re-entrant, chiral and rotating, that can be used for designing auxetic materials has been reported in the work by Kolken y Zadpoor (2017), while a family of lattice-like metamaterials, with macroscopic effective Poisson's ratio arbitrarily close to the stability limit -1, has been studied by Sigmund (1995) and more recently by Cabras y Brun (2014). Finally, the initial contributions on auxetic materials of Lakes and Evans and co-workers in the 80's and 90's must be here mentioned, see for example Evans y Alderson (2000) and reference cited therein.

Studied case

An isotropic composite constituted by two phases M_1 and M_2 is assumed. Material M_1 has a bulk modulus[8] $K_1 = 5/7[GPa]$ and shear modulus $G_1 = 5/13[GPa]$. Material M_2 has a bulk modulus $K_2 = K_1/200[GPa]$ and shear modulus $G_2 = G_1/200[GPa]$. The volume fraction of M_1 is $f_1 = 0.5$. Plane strain hypothesis is considered.

According to the Cherkaev et al.'s analysis, the effective moduli of an isotropic composite constituted by M_1 and M_2 is bounded below and above with the curves plotted in Figure A.8-a, where $\hat{K}$ and $\hat{G}$ are the effective bulk and shear moduli of the composite, respectively. Taking into account these bounds, the minimum possible Poisson's ratio for such composites [9] is attained at the point satisfying:

$$\text{mín}\ \frac{\hat{K} - \hat{G}}{\hat{K} + \hat{G}}\ , \tag{A.7}$$

with $\hat{K}$ and $\hat{G}$ bounded by the domain specified by the Cherkaev et al.'s analysis. This point should be on the curve ABC. The Poisson's ratios of points on that curve are plot in Figure A.8-b. The

[8]The plane strain bulk modulus K is given by $K = \kappa + G/3$, where κ and G are the conventional bulk and shear moduli of the three-dimensional theory.

[9]The effective Poisson's ratio of plane elasticity theory if given by: $\hat{\nu}^* = (\hat{K} - \hat{G})/(\hat{K} + \hat{G})$.

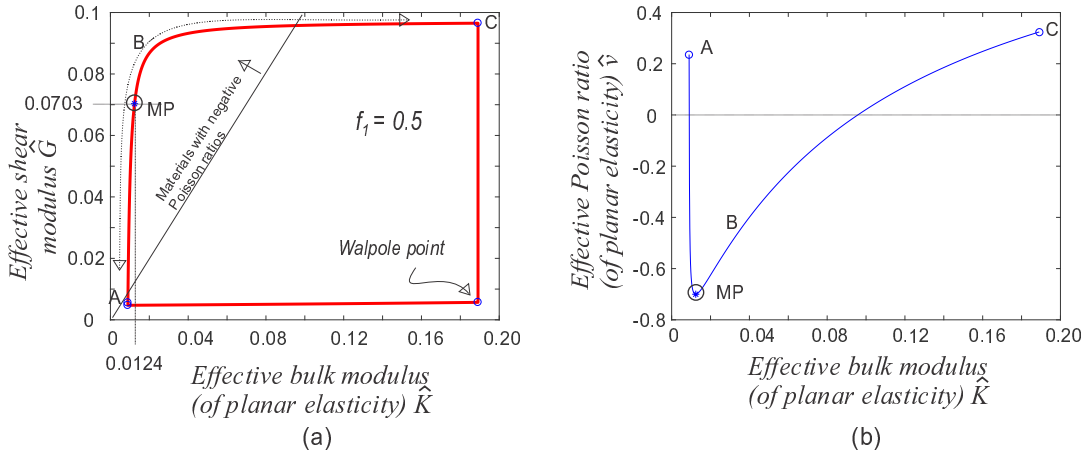

Figura A.8: a) Bounds of effective properties for a two-phase isotropic composite according to Cherkaev et al. Properties of phases M_1 and M_2 are $K_1 = 5/7$; $K_2 = K_1/200$; $G_1 = 5/13$; $G_2 = G_1/200$ (units of moduli in GPa). Volume fraction of phase M_1 is $f_1 = 0.5$. Iso-lines of $\hat{\nu}^*$ with values 0, -0.25 and -0.5 are shown. b) Poisson's ratios of isotropic composites whose effective properties are characterized by the points on the curve ABC in a).

point MP with coordinates $(\hat{K}, \hat{G}) = (0.012404, 0.070334)$ is the one satisfying (A.7) with the minimum Poisson's ratio $\hat{\nu}^* = -0.7002$. Then, the effective elasticity tensor that is related to the MP point results:

$$\hat{\mathbf{C}}_N = \begin{bmatrix} 0.082739 & -0.057930 & 0 \\ -0.057930 & 0.082739 & 0 \\ 0 & 0 & 0.140669 \end{bmatrix}, \tag{A.8}$$

which is taken as the target elasticity tensor to formulate the topology optimization problem. Note that this tensor is isotropic, and therefore, it is given in the Normal coordinates.

The topology optimization algorithm

The volume fraction constraint ($f_1 = 0.5$) is satisfied in the present case by redefining the objective function of the optimization problem (A.2) as follows

$$\min_{\chi} \left(\frac{1}{|\Omega_\mu|} \int_{\Omega_\mu} \chi \, d\Omega - f_1 \right)^2 .$$

Problem (A.2) with the above objective function is solved with a topology optimization technique that uses the concepts of topological derivative and level-set function, similar to the procedure explained in the Amstutz's works, see Amstutz y Andrä (2006) and Amstutz et al. (2010). A brief summary of this technique is given in Appendix 6.

Also, considering that the target tensor $\hat{\mathbf{C}}_N$ may not be attainable, the convergence of the algorithm is reached when the following conditions are satisfied: i) the error in the normalized

constraint $\|\mathbf{C}^h - \hat{\mathbf{C}}\|/\|\hat{\mathbf{C}}\|$ has stabilized to a value less than $tol_C = 0.4$, and ii) the criterion (D.24) of the Appendix 6 has stabilized to a value greater than $1 - tol_\psi$ with $tol_\psi = 0.1$. Stabilization in both values means that they do not substantially change during the last 10 iterations.

To facilitate the comparative analysis in these cases, the topology optimization algorithm forces solutions with material configurations displaying only one length scale. Therefore, the isotropic homogeneous phases are spatially distributed in such a way that their finest width is limited below by a size of the order of the micro-cell size. Under this condition, typical layered sub-microstructures are topologies not admitted. This criterion is imposed on the topology optimization algorithm through a conventional Helmoltz's type spatial filter that is described by equation (D.25) in Appendix 6, see additional details in Lazarov y Sigmund (2011) and Wang et al. (2011) for local length scale control. The filter size r_{ls} is constant and identical in all computed cases.

Voronoi cells, symmetries and stiff phase configurations for initializing the topology optimization algorithm

Considering that the target composite is isotropic, and following the procedure proposed in Section 4 and Table A.2, the design domain of the topology optimization problem could be taken as a regular hexagon. Also, the material distribution could be compatible with the plane groups $p3$, $p3m1$, $p31m$, $p6$ or $p6mm$. These choices guarantee the isotropy of the designed material. Particularly in this Section, we test the Hexagonal cell with $p1$, $p3$ and $p6$ plane groups. We additionally test a square cell enforcing symmetries consistent with $p1$ and pm plane groups.

The five tested cases are identified as follows: H_{p1}, H_{p3} and H_{p6} refer to hexagonal cells with plane groups $p1$, $p3$ and $p6$, respectively. S_{p1} and S_{pm} refer to square cells with plane groups $p1$ and pm, respectively. In the cases with $p1$ and pm plane groups, the isotropy of the designed material is not guaranteed.

In order to attain a representative response of the computational procedure, ten instances of each one of these five tested cases are solved with the iterative topology optimization algorithm. So, they are a total of 50 designs. All of them are initialized with random distributions of the stiff phase satisfying the condition $f_1 = 0.5$. Note that the item (3) of Section 4 is not brought into play for solving these cases.

Numerical results

The effective moduli of the 50 solved micro-architectures are depicted in the space defined by the effective shear modulus and effective bulk modulus shown in Figure A.9-a. The Cherkaev et al.'s bounds and the MP point are also depicted in the plot. In the cases H_{p1}, S_{p1} and S_{pm}, where

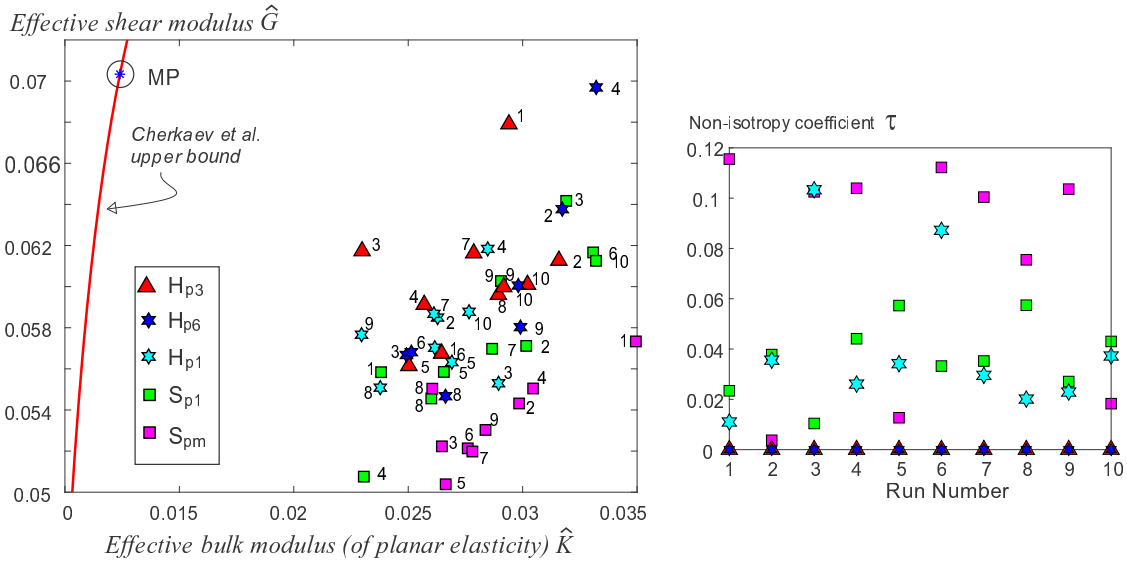

Figura A.9: Micro-structure design of a composite with negative Poisson's ratio. Three design cases denoted H_{p1}, H_{p3} and H_{p6} are solved with hexagonal cells and $p1$, $p3$ and $p6$ plane groups. Two cases with square cells denoted S_{p1} and S_{pm} are solved with $p1$ and pm plane groups. Ten instance of each one of the five cases have been solved. a) Solutions plotted in the space of the effective bulk and shear moduli. Diferent instances of each plane group are identified with a run number. The iso-lines of effective Poisson's ratios of plane elasticity theory $\hat{\nu}^* = -0.25, -0.35, -0.45$ and -0.5 are shown; b) non-isotropy coefficients that correspond to the complete set of solutions.

isotropy cannot be guaranteed, the parameters $\hat{K}$ and $\hat{G}$ are computed using the expression (A.11) below. In Figure A.9, five different symbols identify the five cases, while the numbers (from 1 to 10) beside the symbols identify the corresponding instances of each case.

We remark that all of the 50 designs have been solved with the same filter to avoid micro-structure solutions displaying subscales.

The isotropy of $\mathbf{C}^h$ can be estimated through the non-isotropy coefficient τ that measures its distance to the space of isotropic tensors (see Coelho et al. (2016)):

$$\tau = \frac{\|\mathbf{C}^h - \mathbf{C}^{iso}\|}{\|\mathbf{C}^h\|} \tag{A.9}$$

where $\mathbf{C}^{iso}$ is considered as a projection of $\mathbf{C}^h$ onto the space of isotropic tensors and is computed with the formula:

$$\mathbf{C}^{iso} = \begin{bmatrix} K^{iso} + G^{iso} & K^{iso} - G^{iso} & 0 \\ K^{iso} - G^{iso} & K^{iso} + G^{iso} & 0 \\ 0 & 0 & 2G^{iso} \end{bmatrix}, \tag{A.10}$$

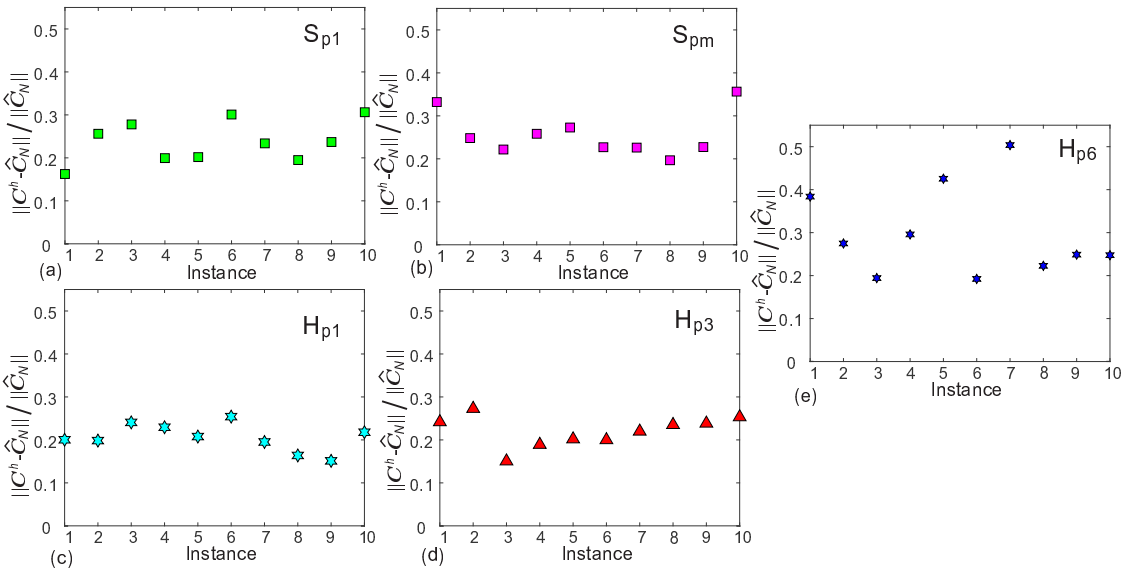

Figura A.10: Normalized errors to satisfy the constraint $\|\mathbf{C}^h - \hat{\mathbf{C}}_N\|$. Plane groups: a) S_{p1}; b) S_{pm}; c)H_{p1}, d) H_{p3}, e) H_{p6}.

where

$$K^{iso} = \frac{1}{8}(3C^h_{11} + 3C^h_{22} + 2C^h_{12} + 2C^h_{33}) - G^{iso} \ ,$$
$$G^{iso} = \frac{1}{8}(C^h_{11} + C^h_{22} - 2C^h_{12} + 2C^h_{33}) \ . \tag{A.11}$$

Expressions (A.11) have been taken from Meille y Garboczi (2001).

The so-defined non-isotropy coefficient τ has been computed for the complete set of solutions. Figure A.9-b plots these coefficients. These results confirm that the solutions obtained with the $p3$ and $p6$ plane groups are exactly isotropic ($\tau = 0$)[10].

Figure A.10 presents the errors of the solutions to satisfy the constraint condition of the problem (A.2). Each sub-Figure display the normalized distance between the target elasticity tensor $\hat{\mathbf{C}}_N$ and the homogenized elasticity tensor $\mathbf{C}^h$ of each micro-architecture design case. Note that this distance is not necessarily equal to the distance between the point MP and each solution point displayed in Figure A.9-a. For example, compare in both Figures the results of instances 2 and 8 with plane group S_{pm}. Figure A.10-b displays that the error for instance 8 is lower than the error for instance 2. However, the contrary effect is observed in Figure A.9-a. This result comes from the fact that Figure A.10 disregards the isotropy property of the obtained homogenized elasticity tensors.

Figure A.11 displays some designed micro-structures. The plot of Figure A.9-a is repeated in Figure A.11 but only including the instances whose micro-structure are shown in this Figure.

[10]Computational homogenization of solutions obtained with $p3$ and $p6$ plane groups and using unit cell finite element meshes that preserve the symmetry $p3$ or $p6$ provides a value τ being exactly zero to the machine precision.

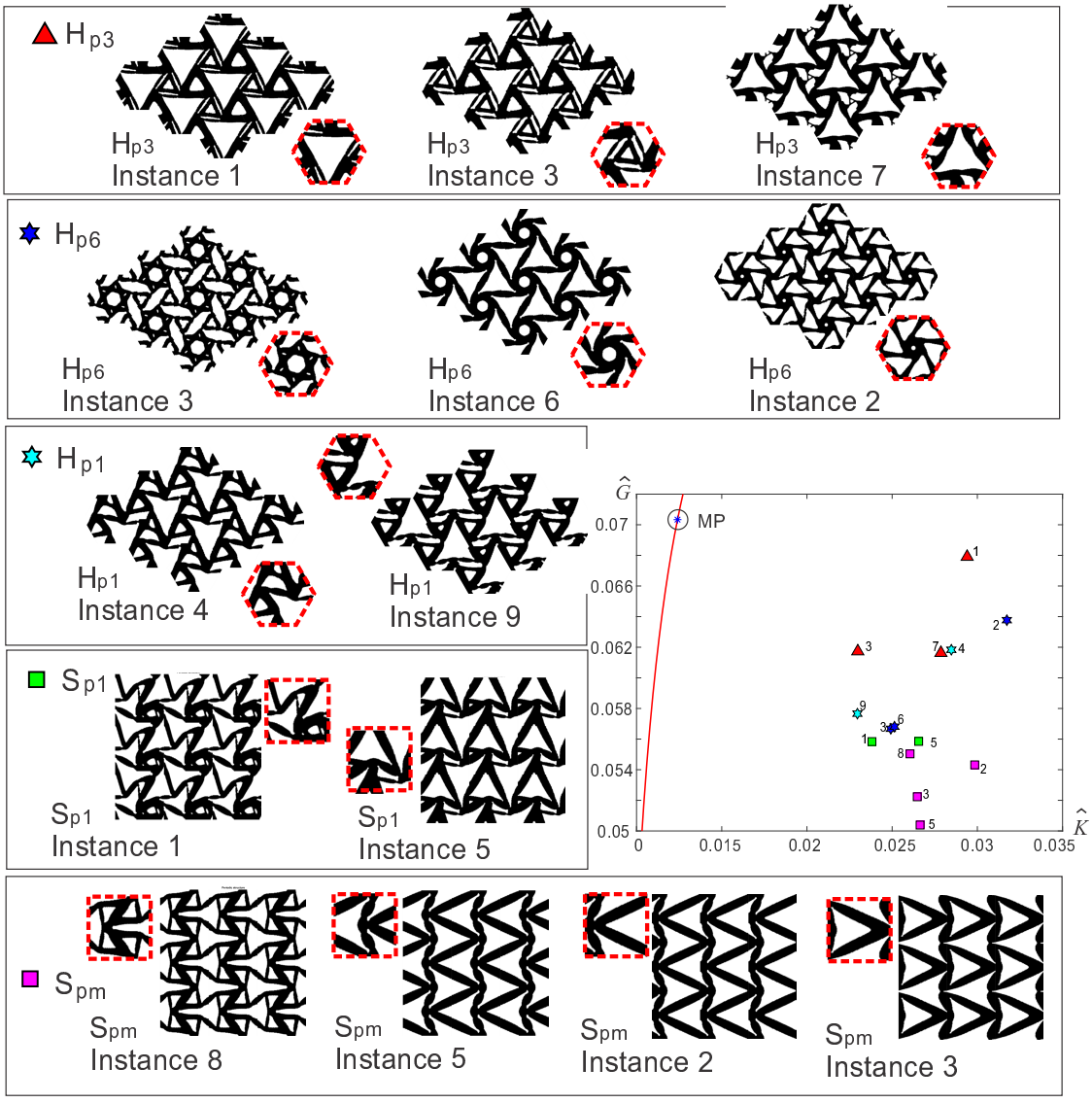

Figura A.11: Several instances of the designed micro-structures of a composite with negative Poisson's ratio. plane groups H_{p1}, H_{p3}, H_{p6}, S_{p1} and S_{pm}. Composites with phases M_1 and M_2 and properties given by: $K_1 = 5/7$; $K_2 = K_1/200$; $G_1 = 5/13$; $G_2 = G_1/200$ (units of moduli in GPa). The volume fraction of phase M_1 is $f_1 = 0.5$.

Discussion of results

From the analysis of the solutions obtained in these tests, it can be drawn some observations:

- Solutions obtained by enforcing the H_{p3} plane group are the closer ones to the MP-point. This conclusion is attained with the distances computed with the metric induced by (A.9)–(A.11). Solutions with H_{p3} plane group have intermediate material configuration symmetries, between H_{p1} and H_{p6} plane groups. Alternatively, the farther solutions with hexagons have been obtained by enforcing the higher symmetry, i.e., H_{p6} plane group. However, this result cannot be taken as a general conclusion. As a counterexample, we remind the case of the composite designed to attain the Walpole point, see Sigmund (2000). In this case, it has been shown that enforcing the H_{p6mm} plane group, instead of H_{p3}, provides better solutions, see Méndez et al. (2017).

- The double bar mechanisms depicted in Figure A.11, case H_{p3} instances 1 and 3, may suggest for auxetic materials a similar observation to that reported by Sigmund (2000), in the sense that better structures are obtained by splitting individual bars into "multiply laminated bars". In fact, Sigmund proposed a very general class of optimal stiffness microstructures based on this principle which achieves the maximum energy bounds. Even when, we cannot guarantee this conclusion in the present study, this important aspect of auxetic material designs with isotropic properties deserves additional research by repeating the design process with finer grids to generate a sequence of solutions tending to the theoretical value.

- Chiral materials (Kolken y Zadpoor (2017),Jiang y Li (2018)) appear to be the micro-architecture topologies attained when enforcing the H_{p6} plane group. This type of architecture can be observed in instances 6 and, though less clearly, in instances 2 and 3. Also, there can be observed a tendency for capturing chirality in the solution S_{p1}, instance 1.

- The attainment of isotropy with H_{p1}, S_{p1} and S_{pm} plane groups lies purely on the effectiveness of the topology optimization algorithm. Some solutions of S_{pm} plane group show micro-structures whose effective responses are closely isotropic. However, this is not the general response for these plane groups.

- Solutions obtained with S_{pm} plane group, instances 2 and 5, display a similar micro-architecture to the one previously reported in the literature, see Larsen et al. (1997) and Andreassen et al. (2014). As can be observed in Figure A.9-b and ignoring a small error, both particular instances (2 and 5) display isotropic effective elastic responses, agreeing, therefore, with the reported results in Andreassen et al. (2014).

- Micro-architecture configurations with higher symmetries appear to be more easily parametrized.

- Solutions obtained by enforcing the S_{p1} plane group indicate a preference to attain topologies with higher symmetries, compatible with the S_{pm} plane group. An identical conclusion can be drawn for the solutions obtained by enforcing the H_{p1} plane group; these topologies have a preference to attain symmetries compatible with the H_{p3} plane group. It is particularly observed that the solutions of instance 2, 5 and 8, of the case S_{pm}, present a vertical glide plane. Therefore, these micro-structures result with a S_{p2mg} plane group which is a higher symmetry than the one originally imposed.

- It is also important to remark that the number of optimal topologies in the design problem decreases by enforcing higher symmetries. For example, non-centered or flipped topologies in the base cell can be avoided by enforcing that the symmetry lines cross the central point of the cell.

5.2. Micro-structure designs of materials with D_2 symmetry

Elasticity tensors with D_2 symmetry and positive Poisson's ratios are taken for assessing the topologies that are obtained with the procedure of Section 4.

Studied cases

Two composite micro-structure designs are assessed. These composites are denoted by I and II, and their effective elasticity tensors in Cartesian coordinates are:

$$\hat{\mathbf{C}}^{I} = \begin{bmatrix} 0.0392 & 0.0578 & -0.0385 \\ 0.0578 & 0.1050 & -0.0931 \\ -0.0385 & -0.0931 & 0.1100 \end{bmatrix} \quad ; \quad \hat{\mathbf{C}}^{II} = \begin{bmatrix} 0.0364 & 0.0462 & 0.0211 \\ 0.0462 & 0.0785 & 0.0631 \\ 0.0211 & 0.0631 & 0.0846 \end{bmatrix} . \tag{A.12}$$

The same tensors in Normal coordinates, denoted $\hat{\mathbf{C}}^{I}_{N}$ and $\hat{\mathbf{C}}^{II}_{N}$, are expressed by:

$$\hat{\mathbf{C}}^{I}_{N} = \begin{bmatrix} 0.2254 & 0.0031 & 0. \\ 0.0031 & 0.0281 & 0. \\ 0. & 0. & 0.0006 \end{bmatrix} \quad ; \quad \hat{\mathbf{C}}^{II}_{N} = \begin{bmatrix} 0.1624 & 0.0043 & 0. \\ 0.0043 & 0.0363 & 0. \\ 0. & 0. & 0.0008 \end{bmatrix} \tag{A.13}$$

being that the rotation angles between the Cartesian and the Normal bases are $\theta_I = -\arctan(\sqrt{2})$ and $\theta_{II} = \arctan(\sqrt{2})$ for materials I and II, respectively.

The composites are constituted of a stiff phase M_1 and void. Young's modulus and Poisson's ratio of the stiff phase are $E_1 = 1.[GPa]$ and $\nu = 0.3$, respectively. The plane stress hypothesis is assumed.

The topology optimization algorithm.

A density-based topology optimization technique combined with the Solid Isotropic Material with Penalization (SIMP) interpolation formulation (Bendsoe y Sigmund (2003)) is adopted in this Section for solving the problem (A.2). The resulting formulation is iteratively solved with the IPOPT interior point primal-dual algorithm, see Wächter y Biegler (2006) and the bibliography cited therein. The coupling of these procedures has been analyzed by Rojas-Labanda et al. (2017). Therefore, in Appendix 6, we sketch a brief description of this approach remarking the filters that are used to solve these cases.

Algorithm parameters: Similar to the previous examples, we use a density filter that forces the optimum solution to display a material topology with only one length scale and a Heaviside projection filter to alleviate the issue related to the presence of gray material.

The density filter described in Appendix 6, uses a value $R = \alpha L$, where L is the cell size and α (with $0 < \alpha \leq 1$) is the adimensional parameter scaling the filter radius. We adopt $\alpha = 0.01$. The gray material presence is diminished by using the Heaviside filter described in Appendix 6, also discussed in Wang et al. (2011). The parameter β handles the Heaviside filter. An external loop of the IPOPT algorithm increases the β-parameter according to the sequence $\{0, 1, 2, 4, 8, ...\}$. Finite element meshes with 40000 elements are used; SIMP density exponent $p = 3.5$.

All the solutions satisfy the normalized constraint of the problem (A.2) with the tight tolerance ($tol = 1.e-4$) defined in the IPOPT algorithm.

Performance assessment of the design procedure

Micro-structures designed by enforcing the rules 1 and 4

Squares cells are used and the IPOPT algorithm is initialized with two different configurations: a stiff material density randomly distributed or uniformly distributed (with initial density $\rho = 0.5$). Additionally, two procedures are followed to solve four topology optimization problems:

i) The first procedure performs the inverse design of composites I and II with the target tensors $\hat{\mathbf{C}}^I$ and $\hat{\mathbf{C}}^{II}$ in Cartesian coordinates without imposing symmetries.

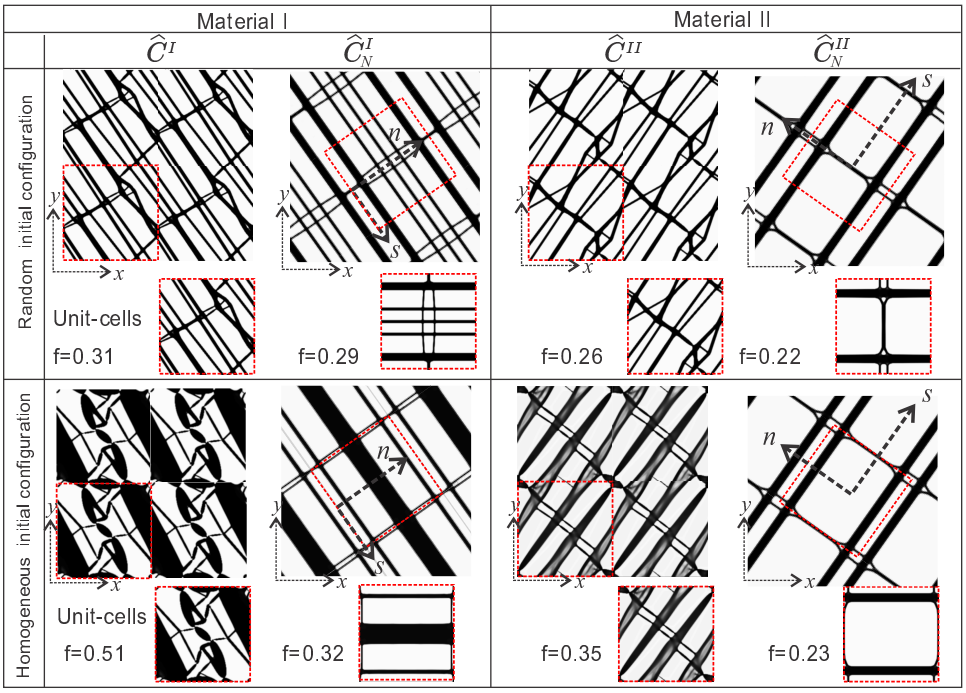

Figura A.12: Four examples of micro-architecture designs. Target tensors are: $\hat{\mathbf{C}}^I$ and $\hat{\mathbf{C}}^I_N$ for material I; $\hat{\mathbf{C}}^{II}$ and $\hat{\mathbf{C}}^{II}_N$ for material II. Pictures correspond to the assembled micro-architectures in a direction agreeing with the Cartesian basis. Unit cells and volume fractions are also shown.

ii) In the second procedure, tensors $\hat{\mathbf{C}}^I$ and $\hat{\mathbf{C}}^{II}$ are first rotated to Normal coordinates. Therefore, the inverse designs are performed with the target tensors $\hat{\mathbf{C}}^I_N$ and $\hat{\mathbf{C}}^{II}_N$ and the Voronoi cells are aligned with their Normal basis. Furthermore, a symmetric material distribution consistent with a $p2mm$ plane group is imposed on the SIMP methodology. The horizontal and vertical central lines of the cells are symmetry lines. In summary, the micro-structure design is performed according to the two rules 1 and 4 describe in Section 4.

The solutions of these four cases, with the two initial configurations, are compared in Figure A.12. We observe that the solutions, whose cells are aligned with the Normal basis of the target tensors and with the imposed symmetry being consistent with a $p2mm$ plane group (second and fourth column of the Figure), display simpler topologies. These solutions are similar to laminates which can be easily parametrized. Alternatively, the micro-architectures designed with the elasticity tensor in the original Cartesian basis display more complex topologies which result as a consequence of using square cells and periodic boundary conditions not aligned with the symmetry lines of the materials.

It is additionally noted that the solutions in Figure A.12 are not very sensitive to the initial configuration taken to start the IPOPT algorithm. Even when this conclusion will be partially relativized in the following numerical tests, it is in the same line with observations reported in the literature, see Rojas-Labanda et al. (2017).

Micro-structures designed by enforcing the four rules

The same composites I and II, with target elasticity tensor $\hat{\mathbf{C}}^I$ and $\hat{\mathbf{C}}^{II}$, are next designed by following the full set of rules described in Section 4. The Voronoi cells compatible with a target elasticity displaying D_2 symmetry corresponds to R_p or R_c Bravais lattices. The cell slendernesses, i.e., the aspect ratio between the larger and shorter size of the cells, are assessed through the database and the criterion defined by expression (A.6). The shape of the cells for material I and II determined with this criterion are the rectangular cells, compatible with R_p Bravais lattices, shown in Figure A.13-a. Furthermore, an adequate plane group determining the material distribution geometry would be one of the seven plane groups denoted in Table A.2 by pm, pg, cm, $p2mm$, $p2mg$, $p2gg$ or $c2mm$. In particular, we choose the plane group $p2mm$.

Figure A.13-b depicts the topologies computed with this procedure. The effect of taking an initial configuration given by the database (topologies shown in the third column of these results) is evaluated by comparing the micro-architectures solved with different initial configurations, a stiff material density randomly distributed or uniformly distributed (with density $\rho = 0.5$), such as shown in the first and second columns.

It can be seen that the final micro-architecture, obtained with the initial configuration taken from the database, is the simpler one constituted by bars of (almost) uniform thickness, but different length ratios. The bar lengths typically agree with the cell slenderness.

Figure A.14 show the micro-architectures of material I and II that have been obtained by using SIMP with the initial configuration taken from the database.

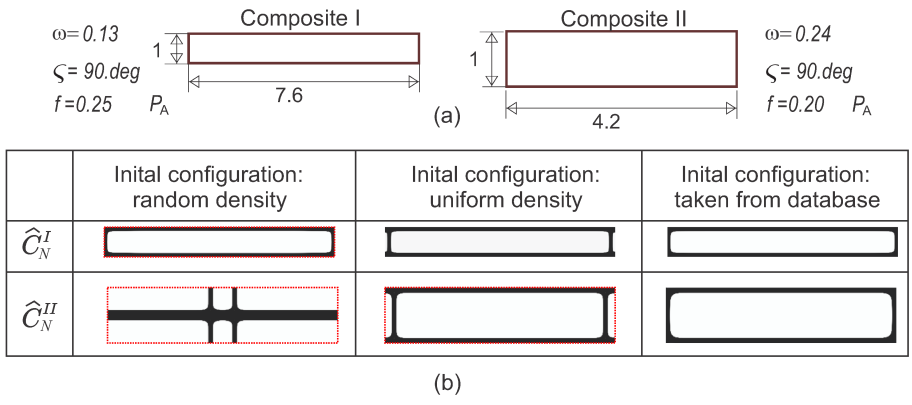

Figura A.13: Micro-structure designs of composites I and II. The topology optimization problem uses the four rules of Section 4. a) Voronoi cells determined with criterion (A.6); b) Unit-cell solutions of the topology optimization algorithm by adopting three different initial material configurations.

Discussion of results

The obtained solutions show that enforcing periodic boundary condition along directions not aligned with the Normal basis may be the cause of attaining micro-structures with complex topolo-

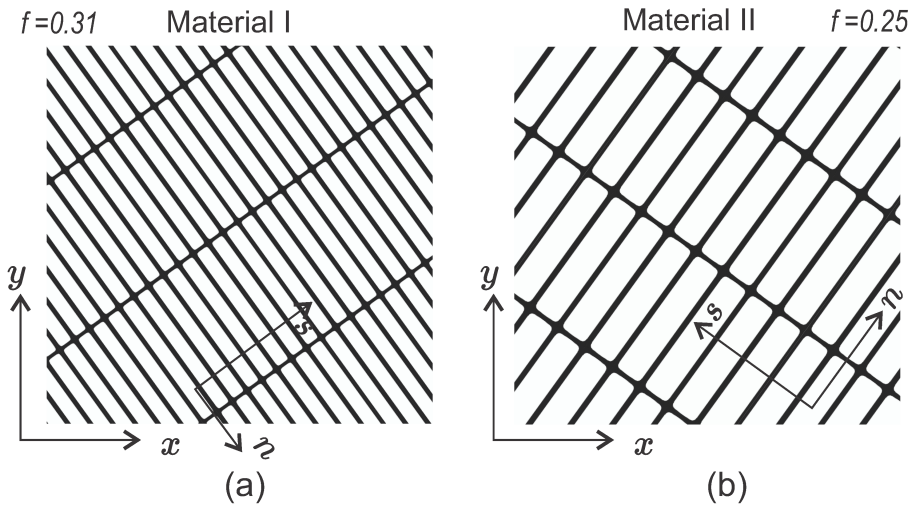

Figura A.14: Micro-structure asasamblages of the composites I and II. The topology optimization problem uses the four rules of Section 4. Initial configurations are taken from the database. The resulting volume fractions are $f = 0.31$ and $f = 0.25$ for composites I and II, respectively.

gies if compared with solutions obtained by following the first rule of the procedure here proposed. Even simpler topologies can be attained when the initial configuration of the iterative algorithm are taken from the database. Nevertheless, a simple configuration may not be the global optimum solution of the problem.

In a similar way, the sensitivity of the attained material configuration with different design domains is evidenced in these tests. Notably, the aspect ratios of the cells also play an important role in obtaining different topology types.

5.3. Pentamode material design

According to Norris (2008), pentamode materials are useful for constructing acoustic cloaking devices. A Pentamode material is a class of extremal material having five easy (compliant) modes of deformation in a three-dimensional space, and having only one non-easy (hard) mode of deformation[11]. The elasticity tensor of this material has one non-null eigenvalue and five null eigenvalues (hence the name of pentamode given to this class of material). In 1995, Milton y Cherkaev (1995) have coined the name of pentamode materials in the context of linear elasticity. In the same year, Sigmund (1995) has independently introduced it in the context of inverse homogenization problems.

Pentamode materials are a special class of linear anisotropic elastic solids. They can be characterized through elasticity tensors represented by:

[11] In the following, we preserve the name of pentamode material for plane (two-dimensional) problems. Removing the third dimension and the out-of-plane field components, the elasticity tensor has only three eigenvalues. Particularizing the same concept of pentamode material, two of these eigenvalues are related to compliant modes of deformation and only one is related to a hard mode. Strictly, this material should be called bi-mode material. Additional discussion about bi-mode materials can be found in Podestá et al. (2018a).

$$\mathbf{C}^* = \kappa^* \mathbf{S} \otimes \mathbf{S}; \tag{A.14}$$

where κ^* is a pseudo-bulk modulus with the dimensions of stress and $\mathbf{S}$ is an adimensional symmetric second order tensor with norm not necessarily equal to one. As usual, the symbol $\otimes$ denotes the tensorial product.

The micro-structure design of a pentamode material proposed for constructing an acoustic cloaking device is here studied.

The goal of this assessment is to show that different design domains Ω_μ provide markedly dissimilar solutions of the topology optimization algorithm and that the solution obtained with the systematic procedure of Section 4 display the simpler topologies.

Studied cases

Norris (2008) has reported that an acoustic cloaking device can be realized by designing a layered graded pentamode material whose effective elastic properties can be determined with the analytical results presented by Gokhale et al. (2012).

The design and realization of the idealized layer have been addressed in a number of works. In particular, the reported solution by Méndez et al. (2017) divides the layer into 20 sub-layers whose micro-structures are then determined by means of an inverse homogenization design. The layered composite is constituted of aluminum, with a bulk modulus $\kappa_{Al} = 70.GPa$ and shear modulus $G_{Al} = 25.5GPa$, and a flexible polymer foam characterized by an isotropic material whose elastic modulus has a contrast factor $\gamma = 0.00001$ times the elastic modulus of the aluminum.

Sub-layer number 15 of the acoustic cloaking device described in Méndez et al. is chosen to perform this study. Here, we only consider a partial aspect of the total layer design for the mentioned device, i.e., the micro-architecture design is only addressed without enforcing the required density constraint.

For this sub-layer in particular, the target elastic properties are characterized by the elasticity tensor described in Normal coordinates as follows:

$$\hat{\mathbf{C}}_N = \begin{bmatrix} 5.893 & 2.250 & 0. \\ 2.250 & 0.8590 & 0. \\ 0. & 0. & 0. \end{bmatrix} . \tag{A.15}$$

This tensor corresponds to a pentamode material with D_2 symmetry. The composite is designed to copy these elastic properties.

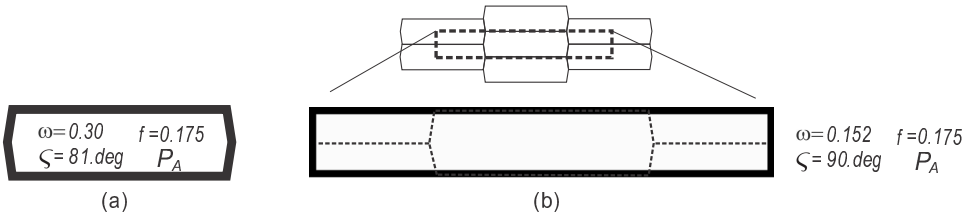

Figura A.15: Pentamode material design. a) Hexagonal cell taken from the database using the criteria (A.6). b) Rectangular cell being compatible with the Bravais lattice whose Voronoi cell is the hexagonal cell in picture a).

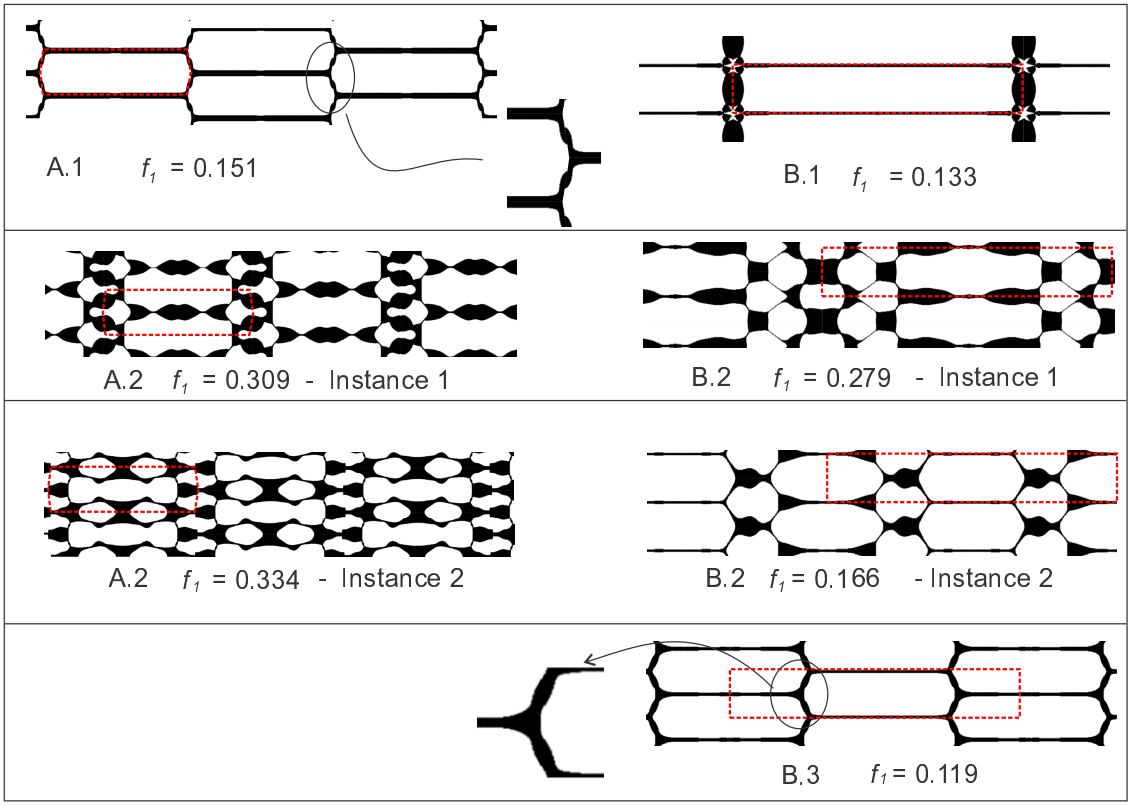

Figura A.16: Pentamode material designs. Topologies attained with sub-cases A1, A.2 and B. The volume fraction of each case is f_1.

Topology optimization algorithm

The level-set algorithm presented in the previous sub-Section is used in this case to solve problem (A.2). Similar to the technique adopted in the previous examples, we use a spatial filter to avoid topology designs with multiple length scales.

Obtained results

First, we remark that it has not been possible to attain acceptable results with square cells and the adopted mesh resolution. Therefore, the analysis is restricted to rectangular and hexagonal cells (R_p or R_c Bravais lattices)which are compatible with the D_2 symmetry of the target tensor. Furthermore, the solved topologies are enforced to satisfy the $p2mm$ plane group.

Case A: The hexagonal cell shown in Figure A.15-a has been determined with the criterion (A.6).

The resulting parameters are: $\omega = 0.3$, $\varsigma = 81.deg$, pattern P_A and $f = 0.175$. Taking a domain of analysis defined by this hexagonal cell, we test two sub-cases, A1 and A.2, which are defined with different initial stiff phase configurations, as follows.

A.1 The initial stiff phase configuration is the one given by the solution of problem (A.6), such as shown in Figure A.15-a.

A.2 The initial configuration consists of a random stiff phase distribution. Five different instances of this sub-case are solved.

Case B: the rectangular cell shown in Figure A.15-b is taken as the design domain. This cell with parameters $\omega = 0.1517$, $\varsigma = 90.deg$ can reproduce a similar micro-structure as that given by the hexagonal cell of the case A. The three sub-cases are solved with the following initial conditions:

B.1 stiff bars are disposed in the boundary of the cell;

B.2 a random distribution of stiff phase. Five instances are solved with initial random configurations.

B.3 stiff bars are disposed in a hexagonal array. This hexagonal array is the same as that of the initial configuration of Case A.1, but here, it is projected onto the rectangular cell such as shown in Figure A.15-b.

The topologies obtained in all these cases are shown in Figure A.16.

Figure A.17 plots the relative errors $\|\mathbf{C}^h - \hat{\mathbf{C}}\|/\|\hat{\mathbf{C}}\|$ for all the tested cases solved with the Level-set algorithm. The solution with the lower error is computed under the following conditions: the hexagonal cell and the initial configuration are taken from the database, and the algorithm is run without the filter. In the remaining cases, the filter penalizes the solutions to attain effective elasticity tensors closer to the target one. In any case, it is notable that the hexagonal cell provides more accurate solutions if compared with those obtained, in comparable circumstances, with the rectangular cell.

6. Conclusions

The associations presented in Tables A.2, A.3, A.4 and Figure A.6 constitute the fundamental ingredients introduced in this paper to connect the symmetries characterizing the material configurations and the physical properties. They also constitute the basic components to identify an adequate micro-architecture design procedure of composites whose effective properties fulfill a given elastic response.

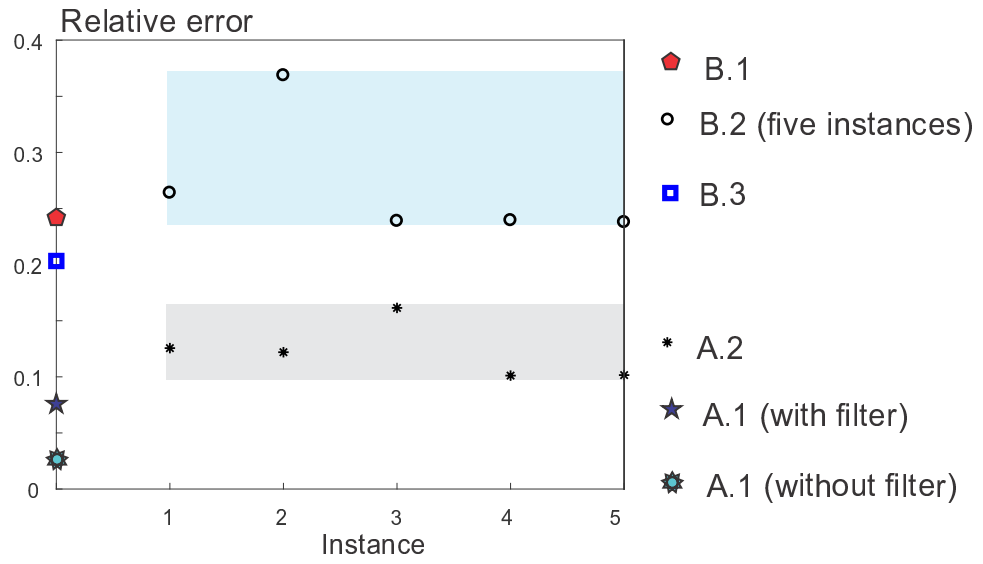

Figura A.17: Pentamode material design. Relative errors $\|\mathbf{C}^h - \hat{\mathbf{C}}\|/\|\hat{\mathbf{C}}\|$ computed for the solutions obtained with the Level-set algorithm.

Based on these notions, four rules have been proposed in this work. These rules define a systematic procedure that can be followed to facilitate the micro-structure design carried out by means of an inverse homogenization technique.

Through a number of numerical assessments, it has been shown that the conventional square cells, adopted as the design domain for the inverse homogenization techniques formulated as a topology optimization problem, are not adequate to obtain simple micro-architecture configurations in general situations. Instead, appropriate cells and plane groups, identifying the material configuration symmetry within the cell, can alternatively be chosen to guarantee the attainment of composites with simple topologies and effective elastic responses displaying identical symmetries to the target ones. These conclusions are independent of which topology optimization algorithm is taken to solve the inverse homogenization problem.

An observation here remarked is that the proposed rules could be extended to inverse homogenization techniques involving 3D elastic material designs. The generalization of the concepts involving crystal physics and the related symmetries in 3D could provide some hints to conceive base cells for more general domain designs in 3D problems.

Acknowledgments

The authors acknowledge the financial support from CONICET and ANPCyT (grants PIP 2013-2015 631 and PICT 2014-3372 and 2016-2673).

Appendix A1: Solving the topology optimization problem with Topological Derivate Algorithm

The topology optimization problem (A.2) can be solved by introducing a smooth level set-funtion, $\psi \in C^0(\Omega_\mu)$, satisfying

$$\psi(\mathbf{y}) = \begin{cases} < 0 & \forall \mathbf{y} \in \Omega_\mu^2 \\ > 0 & \forall \mathbf{y} \in \Omega_\mu^1 \\ 0 & \text{in the interfaces} \end{cases}, \tag{A.16}$$

and utilizing an augmented Lagrangian technique, see Lopes et al. (2015). In this case, the problem is rewritten as follows

$$\max_{\lambda} \min_{\psi} \mathcal{T}(\psi, \lambda), \tag{A.17}$$

with:

$$\mathcal{T}(\psi, \lambda) = \int_{\Omega_\mu} \chi(\psi)\, d\Omega + \lambda(\|\mathbf{C}^h(\psi) - \hat{\mathbf{C}}\|) + \frac{\alpha}{2}(\|\mathbf{C}^h(\psi) - \hat{\mathbf{C}}\|)^2 \tag{A.18}$$

where λ is the Lagrange multiplier and α is the penalty parameter of the augmented term.

The algorithm for solving the problem (D.14) utilizes two nested loops. In an internal loop, the objective function $\mathcal{T}$ is minimized by holding fixed λ and α. This loop, with index denoted k, consists of a level-set function-based iteration. While an external loop, with index denoted l, modifies iteratively λ.

The minimum of $\mathcal{T}$ in the internal loop is searched with a descent direction algorithm. For problem (D.14), the topological derivative used to estimate the descent direction is given by

$$D_\psi \mathcal{T}(\psi, \lambda) = 1 - \left(\left(\lambda - \alpha \|\mathbf{C}^h - \hat{\mathbf{C}}\| \right) \frac{(\mathbf{C}^h - \hat{\mathbf{C}}) : D_\psi \mathbf{C}^h}{\|\mathbf{C}^h - \hat{\mathbf{C}}\|} \right) \tag{A.19}$$

where $D_\psi \mathbf{C}^h$ is the topological derivative of the homogenized elasticity tensor, see Amstutz et al. (2010) for an additional description of this term. Then, we define the function :

$$g(\mathbf{y}) = \begin{cases} -(D_\psi \mathcal{T}) & if : \psi < 0 \\ +(D_\psi \mathcal{T}) & if : \psi > 0 \end{cases}, \tag{A.20}$$

The updating formula for ψ, at the $(k+1)$-th internal loop, is defined by

$$\psi^{k+1} = \psi^k + \tau g, \tag{A.21}$$

with the scaling factor τ being determined by means of a line search technique.

In the $(l+1)$-th external loop, the Lagrange multiplier λ is updated using the Uzawa algorithm

$$\lambda^{l+1} = \text{máx}(0, \lambda^l + \alpha\|\mathbf{C}^h - \hat{\mathbf{C}}\|). \tag{A.22}$$

The penalty parameter α is hold fixed during the full process.

A local optimality criterion of problem (D.14), see Amstutz (2011), is given by the condition

$$D_\psi \mathcal{T} > 0 \quad ; \quad \forall \mathbf{y} \in \Omega_\mu \tag{A.23}$$

which can be implemented by verifying the inequality

$$\left[\frac{\int_{\Omega_\mu} g\psi \, dV}{\|g\|_{L^2}\|\psi\|_{L^2}}\right] > (1 - tol_\psi) \; ; \tag{A.24}$$

combined with

$$\|\mathbf{C}^h - \hat{\mathbf{C}}\| < tol_C \; ; \tag{A.25}$$

Additionally, a Helmoltz-type filter taken from Lazarov y Sigmund (2011) is implemented. The smooth level set function $\tilde{\psi}$ in each iteration $(k+1)$-iteration is computed by solving the field equation:

$$r_{ls}^2 \nabla^2 \tilde{\psi}^{k+1} + \tilde{\psi}^{k+1} = \psi^{k+1} \tag{A.26}$$

with homogeneous boundary conditions $d(\tilde{\psi}^{k+1})/d\mathbf{n} = 0$ on the boundary of Ω_μ. The filter measure r_{ls} defines the minimum length scale in the topology optimization problem.

Appendix A2: Solving the topology optimization problem with SIMP

The SIMP technique reported in Bendsoe y Sigmund (2003) is here adopted. In this technique, the design domain Ω_μ is subdivided using a finite element mesh, and each element e is assigned a density ρ^e. This density represents the presence of soft or stiff materials (zero density for soft phase, unit density for stiff phase) by defining a non-linear interpolation of the elasticity tensors,

$\mathbf{C}_2$ for soft and $\mathbf{C}_1$ for stiff phases, as follows:

$$\mathbf{C}^e(\rho^e) = \mathbf{C}_2 + (\rho^e)^p(\mathbf{C}_1 - \mathbf{C}_2) \ . \tag{A.27}$$

This is a smooth transition of elastic properties with density varying in the interval $0 \leq \rho^e \leq 1$. The intermediate densities ($0 < \rho^e < 1$) are penalized by defining the power law of ρ with exponent $p > 1$.

Given the distribution of densities in Ω_μ and the interpolated elasticity tensors (A.27), the homogenized elasticity tensor, $\mathbf{C}^h$ can be computed through standard procedures. This notation: $\mathbf{C}^h(\rho)$, remarks the dependence of $\mathbf{C}^h$ with the spatial distribution of the so-defined densities.

A2.1. Topology optimization problem

The inverse homogenization technique can be formulated as follows:

$$\begin{aligned} &\min_{\rho} \int_{\Omega_\mu} \rho \, d\Omega \ , \\ &\qquad \text{such that: } \|\mathbf{C}^h(\rho) - \hat{\mathbf{C}}\| = 0 \ . \end{aligned} \tag{A.28}$$

A2.2. Density filter

The density filter taken from Lazarov y Sigmund (2011) is also implemented in the context of the SIMP methodology. The density of an element ρ^e is taken as being the weighted average of the design variables of the neighbor finite elements. The neighborhood is defined as a circle in 2D with the radius R. Then, the application of a density filter leads to the variables $\overline{\rho}^e$:

$$\overline{\rho}^e = \frac{\sum_{i=1}^{Q} w_i^e \, \Omega_i \, \rho_i}{\sum_{i=1}^{Q} r_i^e \, \rho_i} \tag{A.29}$$

where Q is the number of elements in the neighborhood of element e defined by R, r_i^e is the distance from element i to elements e, Ω_i is the volume of element i, w_i^e is a weighting factor defined as:

$$w_i^e = max(0, R - r_i^e)$$

A2.3. Volume preserving Heaviside filter

The filtered variables $\overline{\rho}^e$ are further transformed into element densities $\hat{\overline{\rho}}^e$ by means of an additional Heaviside filter: values smaller than a threshold value g are projected to 0; values larger than η are projected to 1. In this work it is used a Volume preserving Heaviside filter (Xu et al.

(2010)).

$$\hat{\overline{\rho}}^e = \begin{cases} \eta[e^{-\beta(1-\overline{\rho}^e/\eta)} - (1-\overline{\rho}^e/\eta)e^{-\beta}] & 0 \leq \overline{\rho}^e \leq \eta \\ (1-\eta)[1 - e^{-\beta(\overline{\rho}^e-\eta)/(1-\eta)} & , \\ +(\overline{\rho}^e - \eta)e^{-\beta}/(1-\eta) & \eta < \overline{\rho}^e \leq 1 \end{cases} \tag{A.30}$$

where β is a parameter taken as $\beta \geq 1$. When the Heaviside filter is applied in each iteration, the volume fraction is preserved by satisfying the following equation:

$$\sum_{i=1}^{N} \rho_i \, \Omega_i = \sum_{i=1}^{N} \hat{\overline{\rho}}_i(\eta) \, \Omega_i \; . \tag{A.31}$$

where, the left-hand side is the volume before the filtering, and the right-hand side is the volume after applying the filter. This equation is satisfied by adjusting the parameter η with a bisection iterative method. The number of elements is N.

Finally, the objective function and the homogenized elasticity tensor $\mathbf{C}^h$ in problem (A.28) are computed with the filtered density $\hat{\overline{\rho}}^e$.

A2.4. Procedure for imposing the plane group symmetry on the micro-architecture topology

The design variable are updated at the end of each iteration of the topology optimization algorithm to satisfy the symmetry requirement specified by the plane group. For the level set methodology, the design variable update is computed according to the following sequence of operations. Initially, the set of points of the spatial domain related through the space group symmetry operations are found. One node of this set is chosen as the master one, and the remaining are the slave ones. At each iteration: 1) calculate element sensitivities and project to nodes; 2) compute the averaging of sensitivities corresponding to nodes that are linked through the symmetry operations, 3) using equation (A.20), update the level-set variable only for the master nodes and 4) copy the value of the master node level-set variable to all the slave nodes. For the SIMP methodology, the updating procedure is the following: 1) calculate sensitivities for all elements; 2) identifying "master elements" or design variables, 3) compute the averaging of sensitivities that are linked through the symmetry operations, 4) solve the optimization update only for the reduced set of master elements, 5) copy the master design variable value to the linked elements.

Bibliografía

Amstutz S. Analysis of a level set method for topology optimization. *Optimization Methods and Software*, 26(4-5):555–573, 2011.

Amstutz S. y Andrä H. A new algorithm for topology optimization using a level-set method. *Journal of Computational Physics*, 216(2):573–588, 2006.

Amstutz S., Giusti S., Novotny A., y de Souza Neto E. Topological derivative for multi-scale linear elasticity models applied to the synthesis of microstructures. *International Journal for Numerical Methods in Engineering*, 84(6):733–756, 2010.

Andreassen E., Lazarov B., y Sigmund O. Design of manufacturable 3d extremal elastic microstructure. *Mechanics of Materials*, 69(1):1–10, 2014.

Auffray N. y Ropars P. Invariant-based reconstruction of bidimensional elasticity tensors. *International Journal of Solids and Structures*, 87:183–193, 2016.

Barbarosie C., Tortorelli D., y Watts S. On domain symmetry and its use in homogenization. *Computer Methods in Applied Mechanics and Engineering*, 320:1–45, 2017.

Bendsøe M. y Kikuchi N. Generating optimal topologies in structural design using a homogenization method. *Computer methods in applied mechanics and engineering*, 71(2):197–224, 1988.

Bendsoe M. y Sigmund O. *Topology optimization: theory, methods, and applications*. Springer Science & Business Media, 2003.

Cabras L. y Brun M. Auxetic two-dimensional lattices with poisson's ratio arbitrarily close to-1. En *Proceedings of the Royal Society of London A: Mathematical, Physical and Engineering Sciences*, volumen 470, páginas 1–23. 2014.

Cherkaev A. y Gibiansky L. Coupled estimates for the bulk and shear moduli of a two-dimensional isotropic elastic composite. *Journal of the Mechanics and Physics of Solids*, 41(5):937–980, 1993.

Coelho P., Amiano L., Guedes J., y Rodrigues H. Scale-size effects analysis of optimal periodic material microstructures designed by the inverse homogenization method. *Computers & Structures*, 174:21–32, 2016.

Diaz. A. y Benard A. Designing materials with prescribed elastic properties using polygonal cells. *International Journal for Numerical Methods in Engineering*, 57(3):301–314, 2003.

Evans K. y Alderson A. Auxetic materials: functional materials and structures from lateral thinking! *Advanced materials*, 12(9):617–628, 2000.

Ferrer A., Oliver J., Cante J., y Lloberas-Valls O. Vademecum-based approach to multi-scale topological material design. *Advanced Modeling and Simulation in Engineering Sciences*, 3(1):23,

2016.

Feyel F. y Chaboche J. Fe2 multiscale approach for modelling the elastoviscoplastic behaviour of long fibre sic/ti composite materials. *Computer methods in applied mechanics and engineering*, 183(3-4):309–330, 2000.

Gokhale N., Cipolla J., y Norris A. Special transformations for pentamode acoustic cloaking. *The Journal of the Acoustical Society of America*, 132(4):2932–2941, 2012.

Huang X., Zhou S., Xie Y., y Li Q. Topology optimization of microstructures of cellular materials and composites for macrostructures. *Computational Materials Science*, 67:397–407, 2013.

Jiang Y. y Li Y. 3d printed auxetic mechanical metamaterial with chiral cells and re-entrant cores. *Scientific reports*, 8(1):2397, 2018.

Kolken H. y Zadpoor A. Auxetic mechanical metamaterials. *RSC Advances*, 7(9):5111–5129, 2017.

Landwehr K. Visual discrimination of the 17 plane symmetry groups. *Symmetry*, 3(2):207–219, 2011.

Larsen U., Signund O., y Bouwsta S. Design and fabrication of compliant micromechanisms and structures with negative poisson's ratio. *Journal of Microelectromechanical Systems*, 6(2):99–106, 1997.

Lazarov B. y Sigmund O. Filters in topology optimization based on helmholtz-type differential equations. *Int. J. Numer. Meth. Engng*, 86:765–781, 2011.

Lopes C., dos Santos R., y Novotny A. Topological derivative-based topology optimization of structures subject to multiple load-cases. *Latin American Journal of Solids and Structures*, 12(5):834–860, 2015.

Lukkassen D., Meidell A., y Vigdergauz S. On the elastic deformation of symmetric periodic structures. *The Quarterly Journal of Mechanics and Applied Mathematics*, 56(3):441–454, 2003.

Meille S. y Garboczi E. Linear elastic properties of 2d and 3d models of porous materials made from elongated objects. *Modelling and Simulation in Materials Science and Engineering*, 9(5):371, 2001.

Méndez C., Podestá J., Lloberas-Valls O., Toro S., Huespe A., y Oliver J. Computational material design for acoustic cloaking. *International Journal for Numerical Methods in Engineering*, 2017.

Michel J., Moulinec H., y Suquet P. Effective properties of composite materials with periodic microstructure: a computational approach. *Computer methods in applied mechanics and engineering*, 172(1-4):109–143, 1999.

Milton G. y Cherkaev A. Which elasticity tensors are realizable? *Journal of engineering materials and technology*, 117(4):483–493, 1995.

Norris A. Acoustic cloaking theory. En *Proceedings of the Royal Society of London A: Mathematical, Physical and Engineering Sciences*, volumen 464, páginas 2411–2434. 2008.

Nye J. *Physical Properties of Crystals: Theri representation be tensors and matrices*, volumen 146. Clarendon Press- Oxford, 2006.

Paulino G.H., Silva E., y Le C.H. Optimal design of periodic functionally graded composites with prescribed properties. *Structural and Multidisciplinary Optimization*, 38(5):469–489, 2009.

Podestá J., Méndez C., Toro S., Huespe A., y Oliver J. Material design of elastic structures using voronoi cells. *International Journal for Numerical Methods in Engineering*, 2018a.

Podestá J., Toro S., Méndez C., y Huespe. Homogenized elasticity tensor database of periodic composites with microarchitectures displaying symmetric topologies. 2018b. Dataset available from Mendeley, http://dx.doi.org/10.17632/7kgf9xnrhb.1.

Rashed M., Ashraf M., Mines R., y Hazell P. Metallic microlattice materials: A current state of the art on manufacturing, mechanical properties and applications. *Materials & Design*, 95:518–533, 2016.

Ren X., Das R., Tran P., Ngo T., y Xie Y. Auxetic metamaterials and structures: A review. *Smart Materials and Structures*, 2018.

Rojas-Labanda S., Sigmund O., y Stolpe M. A short numerical study on the optimization methods influence on topology optimization. *Structural and Multidisciplinary Optimization*, 56(6):1603–1612, 2017.

Sigmund O. Materials with prescribed constitutive parameters: an inverse homogenization problem. *International Journal of Solids and Structures*, 31(17):2313–2329, 1994.

Sigmund O. Tailoring materials with prescribed elastic properties. *Mechanics of Materials*, 20(4):351–368, 1995.

Sigmund O. A new class of extremal composites. *Journal of the Mechanics and Physics of Solids*, 48(2):397–428, 2000.

Sólyom J. *Fundamentals of the Physics of Solids: Volume 1: Structure and Dynamics*, volumen 1. Springer Science & Business Media, 2007.

Souvignier B. A general introduction to space groups. *International Tables for Crystallography*, A:22–41, 2016. Chapter:1.3.

Ting T. *Anisotropic elasticity: theory and applications*. 45. Oxford University Press, 1996.

Wächter A. y Biegler L. On the implementation of a primal-dual interior point filter line search algorithm for large-scale nonlinear programming. *Mathematical Programming*, 106(1):25–57,

2006.

Wang F., Lazarov B., y Sigmund O. On projection methods, convergence and robust formulations in topology optimization. *Structural and Multidisciplinary Optimization*, 43(6):767–784, 2011.

Wang Y., Zhang L., Daynes S., Zhang H., Feih S., y Wang M. Design of graded lattice structure with optimized mesostructures for additive manufacturing. *Materials & Design*, 2018.

Xu S., Cai Y., y Cheng G. Volume preserving nonlinear density filter based on heaviside functions. *Structural and Multidisciplinary Optimization*, 41(4):495–505, 2010.

Zheng Q. y Boehler J. The description, classification, and reality of material and physical symmetries. *Acta Mechanica*, 102(1-4):73–89, 1994.

Anexo B

Material design of elastic structures using Voronoi cells

El artículo presentado a continuación ha sido publicado en la revista **International Journal for Numerical Methods in Engineering**.

J.M. Podestá, C. Méndez, S. Toro, A.E. Huespe, *"Material design of elastic structures using Voronoi cells"*, **"International Journal for Numerical Methods in Engineering"**, DOI: 10.1002/nme.5804

Material design of elastic structures using Voronoi cells

J.M. Podestá[1], C. Méndez[2], S. Toro[1], A.E. Huespe[1,3][1], J. Oliver[3,4]

[1]CIMEC-UNL-CONICET, Predio Conicet "Dr Alberto Cassano", CP 3000 Santa Fe, Argentina

[2]CIMNE-Latinoamérica, Iturraspe 785, CP 3000, Santa Fe, Argentina

[3]Centre Internacional de Metodes Numerics en Enyinyeria (CIMNE),Campus Nord UPC.

[4]E.T.S d'Enginyers de Camins, Canals i Ports, Technical University of Catalonia (Barcelona Tech)

Campus Nord UPC, Mòdul C-1, c/ Jordi Girona 1-3, 08034, Barcelona, Spain

Keywords: inverse material design; two-scale material design; Free Material Optimization (FMO); micro-architecture topology optimization; Topology Optimization Problem (TOP)

Abstract

New tools for the design of metamaterials with periodic micro-architectures are presented.

Initially, a two-scale material design approach is adopted. At the structure scale, the material effective properties and their spatial distribution are obtained through a Free Material Optimization (FMO) technique. At the micro-structure scale, the material micro-architecture is designed by appealing to a Topology Optimization Problem (TOP). The TOP is based on the topological derivative and the level set function.

The new proposed tools are used to facilitate the search of the optimal micro-architecture configuration. They consist of the following:

i) a procedure to choose an adequate shape of the unit-cell domain where the TOP is formulated. Shapes of Voronoi-cells associated with Bravais lattices are adopted.

ii) a procedure to choose an initial material distribution within the Voronoi cell being utilized as the initial configuration for the iterative topology optimization algorithm.

[1]Corresponding author. E-mail address: ahuespe@intec.unl.edu.ar (A.E. Huespe).

Symbols for elasticity tensors

$\mathbf{C}$: Generic effective fourth order symmetric elasticity tensor expressed in Cartesian coordinates.

$\mathbf{C}_N$: Generic effective elasticity tensor expressed in normal form (see sub-Section 2.2 and Appendix 6).

$\hat{\mathbf{C}}$: Effective elasticity tensor solution of the FMO problems expressed in Cartesian coordinates (Section 3).

$\hat{\mathbf{C}}_N$: Effective elasticity tensor solution of the FMO problems expressed in normal form (sub-Section 3.3).

$\mathbf{C}^*$: Effective elasticity tensor being the average of $\hat{\mathbf{C}}_N$ in a given body sector (sub-Section 3.3).

$\mathbf{C}^h$: Homogenized elasticity tensor evaluated with a micro-cell (using a computational homogenization technique, Section 4) expressed in Cartesian coordinates.

$\mathbf{C}^h_N$: Tensor $\mathbf{C}^h$ expressed in normal form.

$\mathbf{C}^h_{db}$: Homogenized tensor constituting the database (sub-Section 5.2) expressed in normal form.

$\mathbf{C}_\mu$: Micro-scale elasticity tensor (Section 4).

1. Introduction

In the early 1990's, after the seminal papers of Bendsøe and coauthors (Bendsøe et al. (1994)–Bendsøe et al. (1995)), the contribution of Ringertz (1993) and the book of Bendsøe (1995), the Free Material Optimization (FMO) methodology has become a well-established technique in the mechanical structural optimization community. This methodology seeks, in a given spatial domain, the optimal distribution of material and its effective properties using the objective of minimum material resource or minimum compliance.

The most specific aspect of this structural optimization methodology is that the minimum of the objective function is sought by assuming a free parametrization of the material elastic tensor. Hence, it is sometime called Design by Free Parametrization of Material. Such as mentioned in the Section 3.4 of the book Sigmund y Maute (2013), the so-formulated optimization problem is general enough and *"...encompasses the design of structural materials in a broad sense, predicting*

optimal structural topologies and shapes associated with the optimum distribution of the optimized material".

In the following years, the mathematical basis and new numerical algorithms for the FMO technique have been developed. In fact, some formulations of FMO can be written as convex optimization problems which satisfy the criterion for guaranteeing uniqueness of the solution, as shown by Zowe et al. (1997) and Kočvara et al. (2008). Additionally, Kočvara and coauthors have developed optimized algorithms mainly based on non-linear semi-definite programming procedures for solving very large FMO problems, see Kočvara et al. (2008) and Stingl et al. (2009). Furthermore, efficient primal-dual interior point methods for large-scale problems have been proposed and studied more recently by Weldeyesus y Stolpe (2015).

Intrinsically associated with the FMO methodology is the inverse problem of the material micro-architecture design. In this case, the goal is to find a heterogeneous composite whose effective properties are similar to those required by the FMO solution. Important contributions to reach this objective have also been proposed in the 1990's, particularly in the papers of Sigmund (Sigmund (1994b) and Sigmund (2000)), who has solved the inverse material design problem using a topology optimization procedure. In this sense, the density-based SIMP (Solid Isotropic Material with Penalization) method has proved to be a very effective tool for solving this kind of inverse problem.

A FMO technique jointly with inverse material design, as a global two-scale material design methodology, can be utilized as a weakly coupled procedure between the involved scales. First, a FMO technique is employed to compute the effective material properties at the large scale, i.e. at the structure length scale identified as the macro-scale, followed by a technique for designing the micro-structure of the heterogeneous composite. Such two-scale technique and variants were worked out by several authors and particularly utilized by Schury et al. (2012). Interestingly, this type of two-scale technique does not only provide an optimal material distribution at the macro-scale, but also the requested computational cost is accessible even for attacking 3D problems.

There is, however, an inherent difficulty associated with this two-scale methodology which is caused by the one-way coupling between scales. In fact, it is not possible to add well-founded mathematical constraints to the FMO formulation in order to guarantee the micro-structure attainability. Such as mentioned by Allaire in his book, Allaire (2012), from the mechanical point of view, this issue is similar to answer the question on how to characterize the range of the effective properties obtained from a two-phase composite by varying its micro-structure. In this context, the micro-structure variation is understood as changing either the void fractions, the distributions of the constituent phases or their elastic properties. From the mathematical point of view, this issue

corresponds to finding the G-closure of the set of effective elastic properties obtained from composites with all possible micro-structures, see also Cherkaev (2012). Milton y Cherkaev (1995) have studied this problem and have determined that any positive definite tensor may be attained using sequential laminates under the condition that a stiff enough material exists. However, positive definite tensor bounds guaranteeing this property with less stringent conditions to that required by the Cherkaev and Milton analysis do not exist; for example when the stiffness of the composite phases have an upper finite limit. Therefore, this problem is an open issue at the present time.

More recently, there have been intents of including additional manufacture constraints to the FMO problem, such as described in Schury (2013). These constraints not only force a gradual spatial change of the effective material properties, but also they restrict the set of FMO solutions by avoiding the use of extreme materials at the cost of obtaining suboptimal solutions.

From this perspective, additional contributions could be expected by developing new procedures that help designing micro-architectures with a wide spectrum of attainable effective elasticity tensors. In this paper we emphasize this specific issue of the problem.

On the one hand, we adopt a FMO technique at the macro-scale to determine the material distribution and its effective elastic properties. On the other hand, we employee a topology optimization technique to solve the inverse micro-structure design problem. The technique adopted at the micro-scale is similar to the procedure explained in the Amstutz's works and uses the concepts of topological derivative and level-set function, see Amstutz y Andrä (2006) and Amstutz et al. (2010). These two techniques are now well-established in the literature, and therefore, no new contributions on these procedures are revealed in this paper.

Instead, the essential contribution here aims to describe two new tools that aid to explore and design a range of periodic material micro-architectures. The principal ideas supporting these contributions are summarized as follows:

i) The first tool is addressed to define the shape of the unit-cell domain where the micro-structure material inverse design problem is posed. Our numerical experience shows that adequate cell shapes increase the range of elasticity tensors that can be attained through simple micro-architecture topologies. In this sense, it should be noted that certain topologies may be hidden when only conventional square or rectangular cells subjected to periodic boundary conditions are taken.

   The objective that we pursue here is to use a cell shape matching a unit-cell shape of the designed periodic material. So, by using the symmetry of the effective material properties, we conjecture that the stiff material of the composite is periodically distributed by following a pattern which can be assimilated to a Bravais lattice having the same class of symmetry as

that of the target elasticity tensor. Then, the adopted cell for the topological design problem is a Voronoi cell of this Bravais lattice.

Although the use of polygonal cells for the material inverse design was analyzed in the past by Diaz. y Benard (2003), to the best of our knowledge, the use of Voronoi cells applied to topological design has not been previously considered in the literature.

ii) The second of these tools provides a procedure to choose an adequate stiff phase distribution within the Voronoi-cell. This configuration is then utilized as the starting point for the topology optimization algorithm determining the final cell configuration.

A brief description of this paper is the following: the two-scale approach for the material micro-architecture design is briefly revisited in Section 2. Then, the taxonomy of the elastic materials obtained with the structural optimization technique is explored. This classification is utilized for the posterior development of the relevant topics in this paper.

Section 3 gives an overview of two FMO problems that are sequentially solved. Results in terms of extreme materials are analyzed in the same Section.

In Section 4, the adopted methodology for the micro-structure design is first presented. Then, Section 5 describes the new tools above mentioned.

In the last Section of the paper, we expose the conclusions. Two Appendices are finally added. The first Appendix describes the FMO discrete formulation and the algorithm to solve this problem. The second Appendix deals with issues related to symmetry properties of elastic materials. Also, the algorithm to compute the symmetry class and the normal form of an arbitrary elasticity tensor is there briefly exposed.

2. Overview of the two-scale based approach

In this work, the approach taken for the optimal material design of a plane elastic structure involves two length scales. The macro-scale length ℓ is of the same order of magnitude as that of the structure size, as shown in Figure B.1. The micro-scale length ℓ_μ is of the same order of magnitude as that of the material micro-architecture characteristic length. We assume that $\ell_\mu \ll \ell$.

The macro-scale spatial domain is denoted Ω. It identifies the region where the structure is analyzed and where the optimal distribution of the graduated homogenized material is sought. The material at this scale is characterized by its effective properties, and its optimal distribution is sought by means of a FMO technique.

The material micro-architecture design is defined as an inverse problem after the optimal elastic effective properties at the macro-scale point are known. This inverse problem is solved with a

topology optimization technique. The domain Ω_μ denotes the cell where the material is designed. The goal is to find the material distribution within this cell such that the homogenized elasticity tensor, $\mathbf{C}^h$, matches a target effective elasticity tensor provided by the FMO technique.

The vector $\mathbf{x}$, as shown in Figure B.1, denotes the spatial position of a point at the macro-scale. Also, the vector $\mathbf{y}$ identifies the spatial position of a point at the micro-scale.

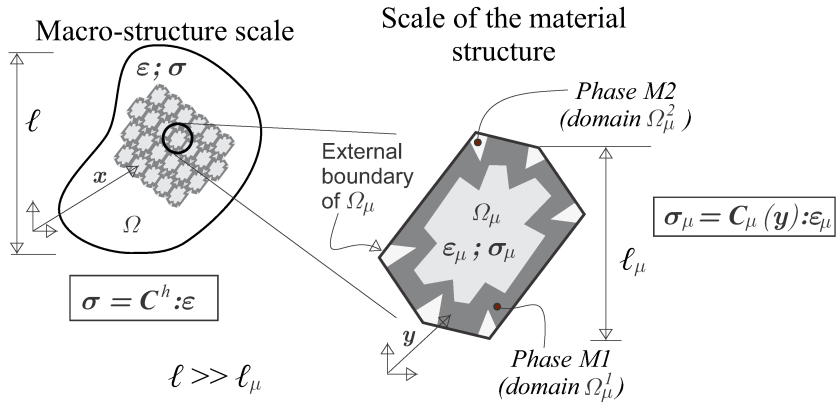

Figura B.1: Two-scale material design. Notation and entities involved in the analysis. Macro-scale domain Ω and micro-cell Ω_μ.

Macro-stress and macro-strains are denoted $\boldsymbol{\sigma}$ and $\boldsymbol{\varepsilon}$, respectively. The same entities at the micro-scale are denoted $\boldsymbol{\sigma}_\mu$ and $\boldsymbol{\varepsilon}_\mu$. The key material property in this work is the homogenized elasticity tensor $\mathbf{C}^h$ at every point $\mathbf{x}$ in Ω. This tensor is computed through a conventional homogenization technique. The elasticity tensors of the component phases at the micro-scale are identified with the symbol $\mathbf{C}_\mu$.

It is convenient to remind the standard concepts of unit-cell and Representative Volume Element (RVE) utilized for computing effective elastic properties of periodic materials. A unit-cell in 2-D problems is the smallest area representing the overall behavior of the heterogeneous material, which, with all possible translation along the primitive vectors, fills the full plane without overlapping. Unit-cells have not arbitrary shapes, but they should be adapted in accordance with the periodic material micro-structure. Then, conventional periodic boundary conditions are a good choice for computing the homogenized properties utilizing these cells.

Arbitrary cell shapes, not matching unit-cell shapes, only represent the overall behavior of the material if they satisfy the condition of being RVEs. This situation occurs even forcing periodic boundary conditions. In this sense, for a given micro-structure, the RVE size should be much larger than the unit-cell size; its domain should comprise several unit-cells.

An additional important point to be also reminded here refers to Voronoi-cells. Periodically structured materials, such as crystals with their atomic arrangement represented through Bravais lattices, have one particular unit-cell whose geometry preserves the symmetry of the underlying

lattice. This unit-cell is identified as the Voronoi-cell of the Bravais lattice.

2.1. Sequence of optimization problems

The two-scale material design procedure is performed in three successive stages.

i) Initially, the FMO problem discussed in Section 3 is solved in the spatial region Ω. This domain is chosen with a predefined geometry. The problem solution provides a graded distribution of effective properties given by the effective elasticity tensor $\hat{\mathbf{C}} \in \mathbb{S}^+$ in Ω, where $\mathbb{S}^+$ is the symmetric positive definite fourth order tensor set. Then, considering that $\mathrm{tr}\,(\hat{\mathbf{C}})$ in the FMO formulation represents the pointwise material resource, the sub-domains of Ω satisfying the condition

$$\mathrm{tr}\,(\hat{\mathbf{C}}) < \epsilon E_0 \tag{B.1}$$

are removed, and the original domain results in a smaller domain Ω^{red}. The parameter ϵ is a small value ($\epsilon \ll 1$), empirically adopted. The parameter E_0 is a reference Young's modulus, typically the modulus of the stiff phase of the designed composite.

Therefore, after the graded material has been defined in the complete domain through the FMO methodology, the heuristic condition (B.1) removes the sub-domains where the demanded material resource is low. A similar result can also be obtained using a more formal mathematical tool based on the topology optimization algorithm described in Giusti et al. (2016). Note that the topologies of Ω^{red} and Ω may be different.

ii) A second FMO problem is solved in the domain Ω^{red} by imposing the additional constraint,

$$(\hat{\mathbf{C}} - \delta\mathbf{1}) \in \mathbb{S}^+. \tag{B.2}$$

The scalar $\delta > 0$ is a small parameter ensuring that all the elasticity tensor eigenvalues are non-null. This constraint has been proposed by Schury (2013) as a manufacture restriction.

Even when constraint (B.2) generates sub-optimal solutions, it facilitates the micro-structure design because it fixes lower bounds to the material properties. The effects of this constraint on the material design process are additionally discussed in sub-Section 3.2.

The solution of the second FMO problem provides the graded distribution of elasticity tensors, $\hat{\mathbf{C}}$, in Ω^{red}. Then, a target elasticity tensor, $\mathbf{C}^*$, representative of $\hat{\mathbf{C}}$ in a given sector of Ω^{red} is defined. The tensor $\mathbf{C}^*$ is utilized to design the material micro-structure in that sector. Sub-Section 3.3 describes the criteria defining these sectors and how $\mathbf{C}^*$ is computed.

iii) Finally, in a third stage, the micro-structure is designed using a topology optimization technique explained in Section 4. The design of the micro-structure is performed with $\mathbf{C}^*$ as the target tensor.

The new tools for material design proposed in this paper are utilized in the third stage.

2.2. Charaterization of linear elastic materials for optimal structures

Two remarkable features of linear elastic materials arising as the FMO problem solution are their symmetry and stability properties. In this sub-Section, we revisit both concepts because they are utilized to predict the shape and orientation of the cell Ω_μ.

Bi-mode and uni-mode unstable materials

Bi and uni-mode materials are special sub-classes of materials which frequently appear as solutions of optimal structural problems with design criterion related to minimal compliance or minimal material volume. In particular, bi-mode materials always arise as the optimal FMO solutions of structures subjected to a unique load system, see Bendsøe et al. (1994). But, even considering problems with multiple independent load systems (Bendsøe et al. (1995)), it is possible that optimal solutions would require bi or uni-mode materials in restricted regions of the structure. Both kinds of materials are particularly relevant in this work and analyzed in this Section.

Bi-mode materials are unstable materials having two easy (compliant) modes of deformation in a two-dimensional space and only one non-easy (hard) mode of deformation. Alternatively, uni-mode materials have one easy (compliant) mode of deformation and two non-easy (hard) modes of deformation. The elasticity tensors of bi and uni-mode materials have two and one null-eigenvalues, respectively. Hence, the names bi or uni-mode are given to these classes of materials.

Milton y Cherkaev (1995) have coined these names in the context of linear elasticity, see also Milton (2002) where additional properties of these materials are analyzed.

Bi and uni-mode materials are special classes of linear anisotropic elastic solids. They are characterized by elasticity tensors [2]

$$\mathbf{C} = \sum_{i=1}^{n_m} \mathbf{S}_i \otimes \mathbf{S}_i \quad , \tag{B.3}$$

where $\mathbf{S}_i$ are symmetric second order tensors, $n_m = 1$ for bi-mode and $n_m = 2$ for uni-mode materials, respectively. For uni-mode materials, $\mathbf{S}_1$ and $\mathbf{S}_2$ are orthogonal tensors. As usual, the

[2] Fourth order tensors are represented by matrices $\mathbf{R}^{3\times3}$ using the conventional Kelvin's notation. Consistent with this notation, symmetric second order tensors are represented by $\boldsymbol{\varepsilon} = [\varepsilon_{11}, \varepsilon_{22}, \sqrt{2}\varepsilon_{12}]^T$ for strains and $\boldsymbol{\sigma} = [\sigma_{11}, \sigma_{22}, \sqrt{2}\sigma_{12}]^T$ for stresses. From now on, we will indistinctly identify a fourth order tensor by its matrix representation.

symbol $\otimes$ denotes the tensorial product. In the plane (x_1, x_2), the eigenvector associated with the non-null eigenvalue in bi-mode materials is $\mathbf{S}_1/\|\mathbf{S}_1\|$.

Considering (B.3), for any strain $\boldsymbol{\varepsilon}$, the stresses $\boldsymbol{\sigma}$ result

$$\boldsymbol{\sigma} = \mathbf{C} : \boldsymbol{\varepsilon} = (\mathbf{S}_1 : \boldsymbol{\varepsilon})\mathbf{S}_1 = -p\mathbf{S}_1 \ , \tag{B.4}$$

where

$$p = -(\mathbf{S}_1 : \boldsymbol{\varepsilon}) \tag{B.5}$$

is a pseudo-pressure scalar term. In (B.4), the trace of the tensorial product is denoted by the symbol $(:)$.

In accordance with (B.4), bi-mode materials can only support stresses proportional to $\mathbf{S}_1$, with the proportionality factor given by pseudo-pressures. Therefore, this material collapses when subjected to a different stress state.

Material symmetry

Symmetry classes of elastic materials are well established in the literature, see for example Ting (1996). In Appendix 6 we define the four symmetry classes for plane elasticity tensors and summarize the algorithm to compute them. The same algorithm also computes the rotation angle transforming an arbitrary elasticity tensor $\mathbf{C}$, expressed in the Cartesian coordinate system, to its normal form $\mathbf{C}_N$[3].

Figure B.2 sketches the diagram of set inclusions for the four symmetry classes. Elements of these sets are elasticity tensors. We denote $O(2)$ for isotropic, D_4 for tetragonal, D_2 for orthotropic and Z_2 for anisotropic symmetries, respectively. From higher to lower symmetry classes, they are: $O(2) \subset D_4 \subset D_2 \subset Z_2$. In the Figure, the number of coefficients characterizing a generic elasticity tensor of the corresponding symmetry class is depicted in parenthesis.

Bi and uni-mode material sets are also included in the diagram. It can be seen the relationship between the stability properties of these materials, i.e. the number of null eigenvalues, and the symmetry class to which they can belong to. It is remarked that bi or uni-mode materials with isotropic symmetry, $O(2)$, as well as bi-mode materials with tetragonal symmetry, D_4, have elasticity tensors $\mathbf{C}_N$ being proportional to those displayed in the Figure B.2. They are characterized by only one parameter C_0. Optimal structure solutions demanding bi-mode materials have been reported by Bendsøe et al. (1994), see also Pedersen (1989).

Orthotropic bi-mode materials have elasticity tensors with the normal form also shown in

[3]Elasticity tensors in normal axis are denoted with subindex N. The directions of the normal axes for a generic elasticity tensor $\mathbf{C}$ are computed with the algorithm of Auffray et al. described in Appendix 6.

Figure B.2. They are characterized by only two parameters. It is important to remark that a bi-mode isotropic material has an in-plane Poisson ratio $\nu = (C_N)_{1122}/(C_N)_{1111} = 1$. On the other hand, a tetragonal bi-mode material has a ratio: $(C_N)_{1122}/(C_N)_{1111} = -1$.

Important additional observations about this topic are:

i) bi-mode materials cannot be fully anisotropic (Z_2),

ii) bi and uni-mode materials are characterized with fewer parameters than those required by generic tensors in the corresponding symmetry class.

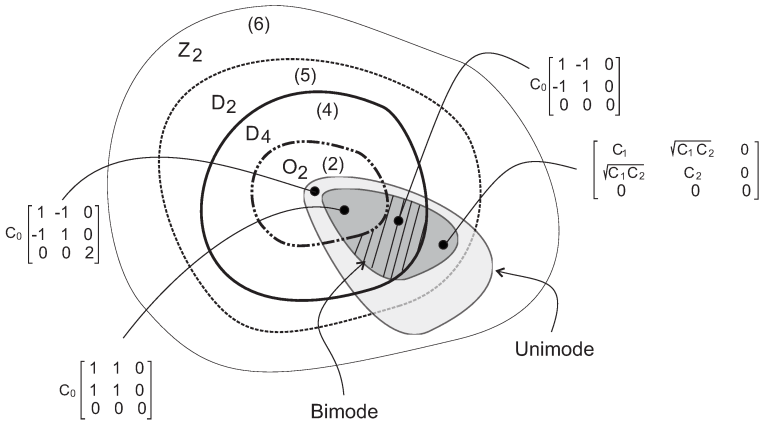

Figura B.2: Diagram of symmetry class set for plane elasticity tensors. Symmetry classes are denoted $O(2)$ for isotropic, D_4 for tetragonal, D_2 for orthotropic and Z_2 for fully anisotropic materials. The number of elastic coefficients defining the elasticity tensors in each class is shown in parenthesis. Bi and uni-mode material sets are also depicted. C_0, C_1 and C_2 are material parameters.

3. Free Material Optimization at the macro-scale

Free Material Optimization (FMO) is a useful technique for obtaining the optimal distribution of material and effective elastic properties in a given spatial domain such that this material configuration satisfies a determined structural requirement. In the present context, the optimization criterion refers to minimum material resource and the structural requirement refers to the attainment of a limit compliance for a given external force.

3.1. Problem setting

Let us consider the equilibrium problem of an elastic body in Ω subjected to an external load $\mathbf{f}$. The space of displacement fields $\mathbf{u}$ in equilibrium with the external forces, $\mathcal{V}^{eq}$, is:

$$\mathcal{V}^{eq} := \{\mathbf{u} \quad | \quad \int_{\Omega} \nabla^s \mathbf{v} : \hat{\mathbf{C}} : \nabla^s \mathbf{u} \, dV - \langle \mathbf{f}, \mathbf{v} \rangle = 0 \quad \forall \mathbf{v} \in \mathcal{V}\}; \tag{B.6}$$

where the equilibrium condition is expressed through the conventional virtual work equation, with $\mathcal{V}$ being the space of admissible virtual displacements and $\hat{\mathbf{C}}$ being the elasticity tensor.

In the present FMO formulation, the optimization problem consists of minimizing the structural material resource

$$\begin{aligned} &\min_{\hat{\mathbf{C}}\in\mathbb{S}^{+},\mathbf{u}\in\mathcal{V}^{eq}} \int_{\Omega} \mathrm{tr}\,(\hat{\mathbf{C}})\; dV \\ &\text{such that:} \quad \langle \mathbf{f}, \mathbf{u}\rangle \leq \bar{f}_u \;, \\ &\qquad\qquad \underline{\rho} \leq \mathrm{tr}\,(\hat{\mathbf{C}}) \leq \bar{\rho}\;, \end{aligned} \tag{B.7}$$

where the term $\mathrm{tr}\,(\hat{\mathbf{C}})$ represents the pointwise material resource and the design variables are the displacement field $\mathbf{u}$ and the elasticity tensor $\hat{\mathbf{C}}$. Also, $\mathbb{S}^{+}$ is the space of symmetric positive semi-definite fourth order tensors, $\underline{\rho}$ and $\bar{\rho}$ are the lower and upper bounds imposed to the material resource, respectively. The lower bound $\underline{\rho}$ is a solvability condition imposed to avoid singularities in the structural equilibrium solution. Also, the upper bound $\bar{\rho}$ is a manufacturability condition that is chosen by considering the higher eigenvalue of the matrix representing the isotropic elasticity tensor of the stiff phase. This eigenvalue is proportional to the Young's modulus, E_0, of the composite stiff phase. Then we take

$$\bar{\rho} = \beta E_0 \;, \tag{B.8}$$

with $\beta < 3$ being an adimensional factor related to the volume fraction of the stiff phase. An empirical rule in material design indicates that the lower the parameter β, the easier is to find extreme materials with complex mechanism-like micro-structures. In (B.7), the upper bound for the structural compliance, $\bar{f}_u$, is taken as the compliance computed with the structure constituted by a homogeneously distributed elastic material in Ω, with an elasticity tensor given by $(\beta/3)E_0\mathbf{1}$, where $\mathbf{1}$ is the identity fourth order tensor.

The optimal solution of problem (B.7) gives: *i)* the spatial distribution of $\hat{\mathbf{C}}$, *ii)* the symmetry class to which the material belongs to and *iii)* the magnitude of the elastic coefficients.

In structural optimization problems involving several independent load systems, the constraint (B.7)-b is replaced by

$$\sum_{k=1}^{n_{load}} w_k \,\langle \mathbf{f}_k, \mathbf{u}_k\rangle \leq \bar{f}_u; \tag{B.9}$$

where n_{load} is the number of load cases. The k-th load system is defined by the external force $\mathbf{f}_k$ and $\mathbf{u}_k$ is the associated displacement of the equilibrium solution, w_k (with $w_k \geq 0$ and $\sum_{k=1}^{n_{load}} w_k = 1$) is a factor weighting each load system. and $\bar{f}_u$ is an upper limit for the weighted average of the compliance.

In Appendix 6, we summarize the discretization technique utilized to solve the present FMO formulation and give some details about the algorithm utilized to solve it.

3.2. Discussion of results obtained with the FMO technique

Discussions of the results obtained with the FMO technique are mainly addressed to analyze the stability, symmetry classes, and additional features of the optimal material properties. This analysis provides basic guidelines for taking adequate decisions in the posterior stage of micro-structure inverse design.

As an empirical rule in the present discussion, we keep in mind that material demanding high effective shear stiffness jointly with effective in-plane Poisson ratio tending to -1, requires the design of complex micro-structures.

First FMO problem

Four conventional structural optimization tests reported in the literature are presented. They are sketched in the first column of Figure B.3 and are: *i)* L-shaped plate, *ii)* cantilever beam, *iii)* plate subjected to bending loads, all of them subjected to only one load system, f_1. The test *iv)*, is a plate subjected to three independent load systems, f_1, f_2 and f_3.

Second to fourth columns of Figure B.3, as well as Figure B.4, display the results of the four tests obtained with the FMO methodology and $\beta = 0.1$ (see equation (B.8)). These Figures show the color maps of the optimal distribution of the following fields:

- **Trace of the normalized elasticity tensors**, $\mathrm{tr}\,(\hat{\mathbf{C}}/E_0)$, ranging from 0.1 to 6×10^{-5}. The material in regions with low values of this field can be removed.

- **Material symmetry classes**. In the tests subjected to only one load system (*i* to *iii*), the optimal materials determined with the FMO problem are bi-mode materials with symmetries D_4 or D_2. In general, materials with isotropic symmetry $O(2)$ are not observed.

  For the plate subjected to three independent load systems, the optimal solution gives materials with three non-null eigenvalues, compare Figure B.3 and Figure B.4. In this case, it is also interesting to observe large regions displaying uni-mode materials with full anisotropy (Z_2), as well as, extended regions with bi-mode materials.

- **Ratio** $(\hat{C}_N)_{1122}/(\hat{C}_N)_{1111}$. The material symmetry classes of optimum solutions computed in tests *i-iii*, display rather extended regions with tetragonal (D_4) symmetry meaning that $(\hat{C}_N)_{1111} = C_{2222}$. Therefore, in accordance with the comments remarked in sub-Section

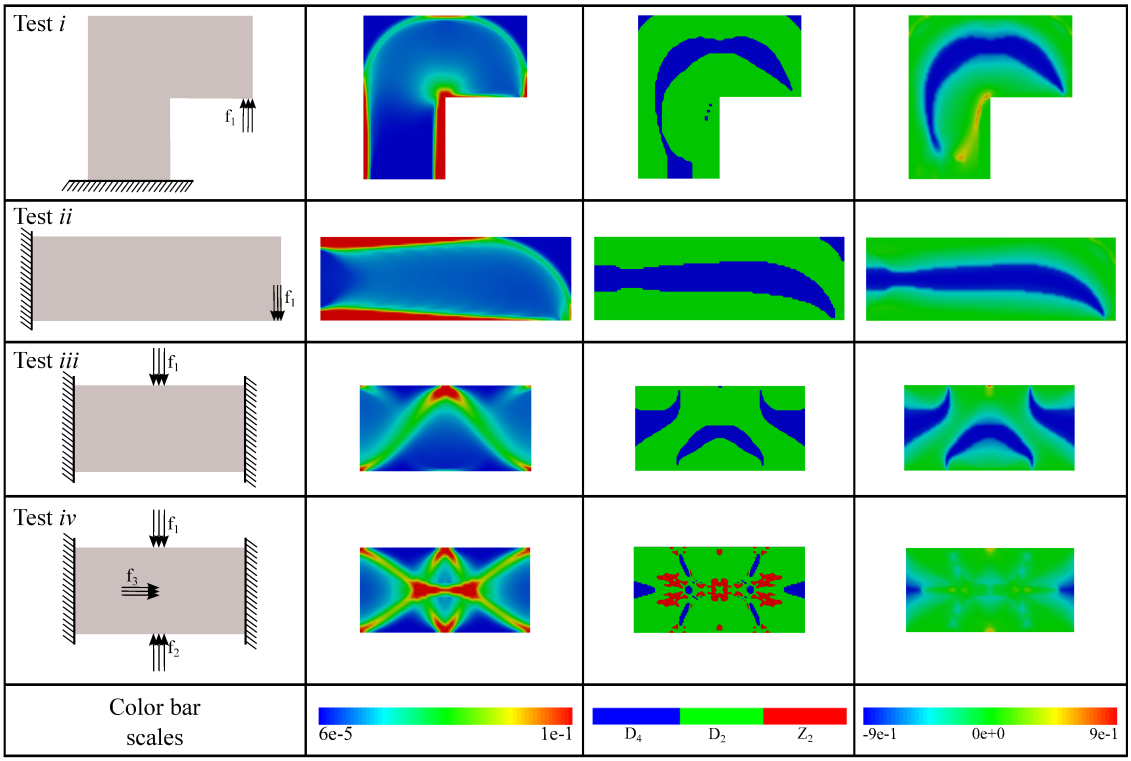

Figura B.3: FMO results. *First column:* test description; *second column:* elastic tensor trace; *third column:* symmetry classes; *fourth column:* ratio $(\hat{C}_N)_{1122}/(\hat{C}_N)_{1111}$. The condition $(\hat{C}_N)_{1122}/(\hat{C}_N)_{1111} < 0$ defines the regions where the optimal solution requires auxetic materials (zones in blue).

2.2, the bi-mode materials in these regions should necessarily have an in-plane Poisson ratio of value $(\hat{C}_N)_{1122}/(\hat{C}_N)_{1111} = -1$.

A further analysis of the ratio $(\hat{C}_N)_{1122}/(\hat{C}_N)_{1111}$ in tests (*i* to *iii*) shows that the optimal solutions in large part of the structures demand auxetic materials. Roughly speaking, auxetic materials with ratios close to $(\hat{C}_N)_{1122}/(\hat{C}_N)_{1111} \approx -1$ requires the design of more complex micro-structure with mechanism-like topologies.

- **Smallest non-null eigenvalues of** $\hat{\mathbf{C}}/E_0$. Solutions corresponding to only one load system (tests *i* to *iii*) display two eigenvalues equal to zero in the complete structural domain indicating that a bimodal material is the optimal solution, such as reported by Bendsøe et al. (1994). Then, the only one non-null eigenvalue is identical to the map of $\mathrm{tr}\,(\hat{\mathbf{C}}/E_0)$. We recall from equation (B.3) that bi-mode material properties have symmetry axes aligned with the principal stress and strain directions.

  In Figure B.4, we show the distribution of the three elasticity tensor eigenvalues obtained as result of the test *iv*. Zones with three non-null eigenvalues can be observed. However, there still exist regions with one and two close to zero eigenvalues.

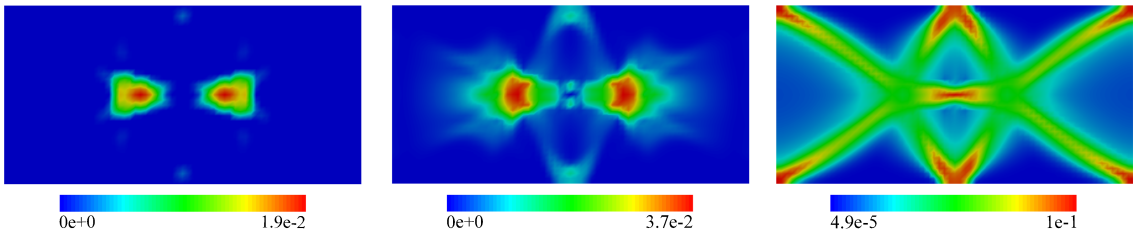

Figura B.4: Eigenvalues of the three load test. Left to right: from smallest to largest eigenvalues.

Second FMO problem

Next, we analyze the results obtained with the second FMO problem with the addition of constraint (B.2) for the L-plate test. This problem is solved in the reduced domain Ω^{red} that results after adopting a tolerance $\epsilon = 0.015$ in expression (B.1). The so-reduced domain Ω^{red} is depicted in Figure B.5-a.

We start the analysis by studying first the sensitivity of results respects to the parameters δ and β introduced in expressions (B.2) and (B.8), respectively. Let us consider the role played by parameter δ:

- On the one hand, δ is utilized to suppress solutions yielding extreme materials. This effect is notoriously shown in the FMO solutions for problems with only one load system. In these cases, we have already seen that the resulting elasticity tensors of the first FMO problem corresponds to bi-mode materials with symmetries D_2 and D_4. Then, the addition of constraint (B.2) fixes a lower bound for the shear modulus, since $(\hat{C}_N)_{1212} \geq \delta/2$. Also, it fixes an upper bound for the ratio $\left|(\hat{C}_N)_{1122}/(\hat{C}_N)_{1111}\right|$. In fact, being $(\hat{C}_N)_{1111} \geq (\hat{C}_N)_{2222} \geq \delta$, it results

$$\left|\frac{(\hat{C}_N)_{1122}}{(\hat{C}_N)_{1111}}\right| \leq \sqrt{\left(\frac{(\hat{C}_N)_{2222}}{(\hat{C}_N)_{1111}} - \frac{\delta}{(\hat{C}_N)_{1111}}\right)\left(1 - \frac{\delta}{(\hat{C}_N)_{1111}}\right)} \leq 1. \tag{B.10}$$

- On the other hand, by comparing with the original FMO problem, the constraint (B.2) produces sub-optimal solutions. The larger the value δ the higher the optimal cost function value.

Both effects are confirmed by analyzing the results shown in Table B.1. This Table displays the optimal cost functions obtained with different values of δ. In the same Table, we also show the corresponding lower and upper values of $(\hat{C}_N)_{1122}/(\hat{C}_N)_{1111}$ in Ω^{red}. We can see that, as δ gets larger, the optimal cost function increases and the extremal values of the field $|(\hat{C}_N)_{1122}/(\hat{C}_N)_{1111}|$ are closer to zero.

Also, in order to understand the connection between the parameters β and δ, it should be kept

Tabla B.1: L-plate test solved with the second FMO problem, $\beta = 0.1$ and different values of parameters δ.

δ/E_0	mín $\int_{\Omega^{red}}$ tr $(\hat{\mathbf{C}}/E_0)dV$	mín $\left(\frac{(\hat{C}_N)_{1122}}{(\hat{C}_N)_{1111}}\right)$	máx $\left(\frac{(\hat{C}_N)_{1122}}{(\hat{C}_N)_{1111}}\right)$
0.	1.89e2	-1.00	1.00
0.020	2.27e2	-0.76	0.95
0.025	2.37e2	-0.71	0.93
0.033	2.52e2	-0.64	0.92
0.040	2.62e2	-0.52	0.65

in mind that designing complex materials could be facilitated by taking smaller volume fractions of the stiff phase, or similarly, smaller values of β, see the discussion about this issue in Sigmund (1994a). So, the parameters δ and β have to be adjusted after an adequate trade-off between optimality and manufacturability requirements.

Finally, the parameter ϵ, defining the size of the domain Ω^{red}, is related to δ, in the sense that it should be taken $\epsilon < \delta/E_0$. However, this parameter plays a less important role in the second FMO problem.

Result obtained with the second FMO problem

Figure B.5-b displays the field $\text{tr}\,(\hat{\mathbf{C}}/E_0)$ on the domain Ω^{red} of the L-plate problem, only one load system, obtained with $\delta = E_0/25$ and $\beta = 0.1$.

Figure B.5-c and d show the color maps of the optimum material symmetry classes and their ratio $(\hat{C}_N)_{1122}/(\hat{C}_N)_{1111}$. The distribution, as well as the maximum and minimum values, are slightly different from that obtained with the original FMO problem on Ω depicted in Figure B.3. Notably in this case, the range of values $(\hat{C}_N)_{1122}/(\hat{C}_N)_{1111}$ are limited to $-0.52 < (\hat{C}_N)_{1122}/(\hat{C}_N)_{1111} < 0.65$, which is a much narrow interval to that displayed by the original FMO solution ranging between $-1 \leq (\hat{C}_N)_{1122}/(\hat{C}_N)_{1111} \leq 1$, see Figure B.3. Also, in accordance with the constraint (B.2), the smallest eigenvalue of the elasticity tensor is δ.

3.3. Domain partition criterion for material design

Once solved the second FMO problem, the structure domain Ω^{red} is partitioned into disjoint sectors with similar effective material properties. The criterion to define this partition is next discussed.

Given the fields: $\text{tr}\,(\hat{\mathbf{C}}/E_0)$ and $(\hat{C}_N)_{1122}/(\hat{C}_N)_{1111}$, we take the intervals defined by their extreme values:

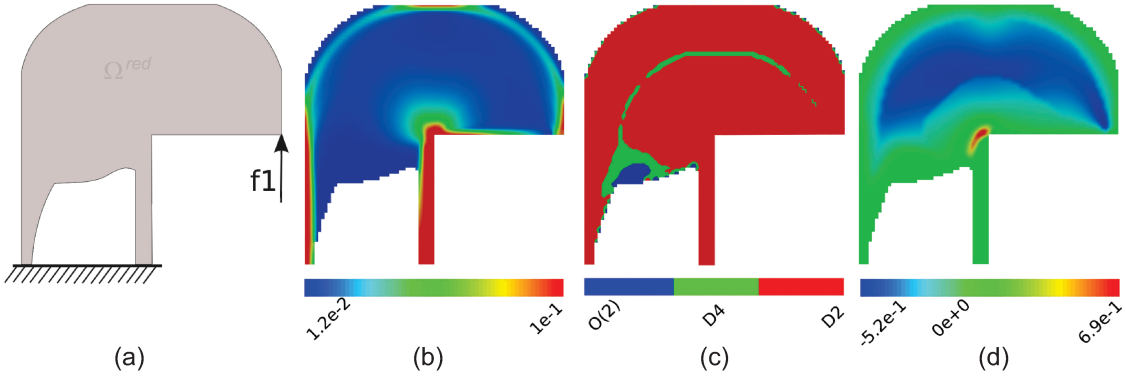

Figura B.5: L-plate test solved with the second FMO problem. a) Reduced domain Ω^{red} after adopting $\delta = E_0/25$. b) Trace of the elasticity tensor ($\mathrm{tr}\,(\hat{\mathbf{C}}/E_0)$); c) material symmetry classes; d) ratio $(\hat{C}_N)_{1122}/(\hat{C}_N)_{1111}$

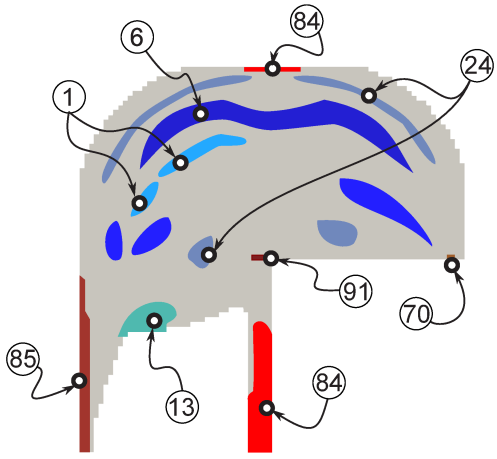

Figura B.6: Domain partition criterion for the material micro-structure design, $N_{tr} = N_{Poi} = 13$, $N_{sym} = 3$, and $n_s = 91$. Only a small number of sectors Ω_i^{red} (with $i = 1, 6, 13, 24, 70, 84, 85, 91$), defined by similar effective elastic properties are identified in colors.

a) $\mathcal{I}_{tr} := [\text{mín}(\,\text{tr}\,(\hat{\mathbf{C}}/E_0)); \text{máx}(\,\text{tr}\,(\hat{\mathbf{C}}/E_0))]$,

b) $\mathcal{I}_{Poi} := [\text{mín}\left(\frac{(\hat{C}_N)_{1122}}{(\hat{C}_N)_{1111}}\right); \text{máx}\left(\frac{(\hat{C}_N)_{1122}}{(\hat{C}_N)_{1111}}\right)]$.

and divide them in N_{tr} and N_{Poi} proportional sub-intervals, respectively. Also, we take the N_{sym} different symmetry classes of the elasticity tensors found in the FMO solution. With these sub-intervals and classes of symmetries, we can define $N_{tr} \times N_{poi} \times N_{sym}$ sets of elastic properties sharing similar values. Then, it can be defined a natural map relating the $N_{tr} \times N_{poi} \times N_{sym}$ sets of elastic properties to sectors in Ω^{red} whose points have effective elastic properties lying within the range of the associated sets, with similar elastic properties: $\text{tr}\,(\hat{\mathbf{C}}/E_0)$, $(\hat{C}_N)_{1122}/(\hat{C}_N)_{1111}$ and symmetry class. Then, these sectors are denoted Ω_i^{red} with $i = 1, ..., n_s$ and n_s is the number of sectors satisfying $n_s \leq N_{tr} \times N_{poi} \times N_{sym}$.

For the L-plate test and taking $N_{tr} = N_{poi} = 13$ and $N_{sym} = 3$, it results $n_s = 91$. Some of these sectors are identified in Figure B.6.

Finally, for every sector, a representative elasticity tensors $\mathbf{C}_i^*$ can be computed as the average

$$\mathbf{C}_i^* = \frac{1}{\left|\Omega_i^{red}\right|} \int_{\Omega_i^{red}} \hat{\mathbf{C}}_N dV \; ; \qquad \forall i = 1, ..., n_s \qquad . \tag{B.11}$$

where $\left|\Omega_i^{red}\right|$ is the area of the corresponding i-th sector.

The tensor[4] $\mathbf{C}^*$ is taken as the target tensor to design the micro-structure using the algorithm described in the following Section.

4. Micro-architecture design

Let us consider a two-phase composite constituted by a periodic distribution of a stiff phase M1 and a soft phase M2. Figure B.7 represents the micro-cell of the periodic composite. We seek the distribution of phases M1 and M2 within the micro-cell such that the homogenized elasticity tensor $\mathbf{C}_N^h$[5], of this composite material, is identical to the target elasticity tensor $\mathbf{C}^*$ derived from the treatment given to the FMO problem solution in the previous Section.

This goal is reached by using an inverse design technique that is formulated as a Topology Optimization Problem (TOP). The TOP is solved in a predefined micro-domain Ω_μ with the algorithm proposed by Amstutz y Andrä (2006) and Amstutz et al. (2010), see also Lopes et al. (2015) and Méndez et al. (2017) where the authors of the present paper use this technique for metamaterial design in acoustic applications.

[4] In the following development, sub-index i identifying the sector of Ω_i^{red} is dropped out of the notation.
[5] The micro-structure design is performed in the normal basis.

The TOP uses a computational technique for evaluating the homogenized elasticity tensor $\mathbf{C}_N^h$, the topological derivative concept of the homogenized elasticity tensor and a function describing the distribution of phases in the micro-cell. The zero-level set of this function represents the interfaces within the cell.

In this work, we only remark some aspects of the TOP which have been particularly adapted for solving the present inverse design problem. They are: the TOP cost function, the imposed constraints and the augmented Lagrangian technique to solve it. Other more conventional aspects of the topology optimization algorithm, such as the topological derivative expression, are not addressed here because they have been extensively treated in the above-referenced literature.

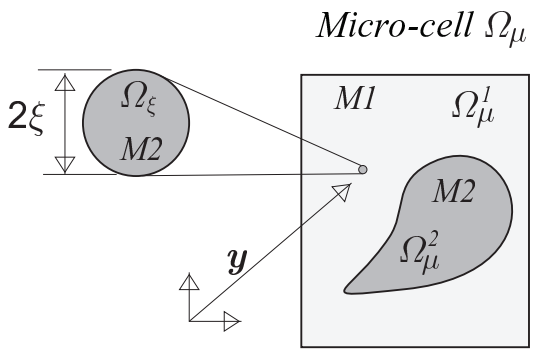

Figura B.7: Original micro-cell problem with a material distribution perturbation consisting of introducing a ball Ω_ξ of soft phase within the stiff phase. The radius of the infinitesimal ball is ξ.

4.1. Inverse material design as a TOP

Let us consider a micro-cell, Ω_μ, of the periodic composite constituted by isotropic elastic phases M1 and M2 occupying the domains Ω_μ^1 and Ω_μ^2, respectively. See Figure B.7. The corresponding elastic tensors of both phases are $\mathbf{C}_\mu^2 = \gamma \mathbf{C}_\mu^1$ with γ being a contrast factor. The characteristic and contrast functions in Ω_μ are defined by

$$\chi(\mathbf{y}) = \begin{cases} 0 & \forall \mathbf{y} \in \Omega_\mu^2 \\ \\ 1 & \forall \mathbf{y} \in \Omega_\mu^1 \end{cases} \quad ; \quad \rho(\mathbf{y}) = \begin{cases} \gamma & if : \chi = 0 \\ \\ 1 & if : \chi = 1 \end{cases} , \tag{B.12}$$

respectively. Evidently, the homogenized elasticity tensor $\mathbf{C}^h$ of the composite depends on the way in which phases M1 and M2 are distributed in Ω_μ. This dependence is made explicit by introducing the notation $\mathbf{C}^h(\chi)$.

Next, we redefine the micro-architecture inverse design problem as a topology optimization problem expressed as follows: given the target effective elasticity tensor $\mathbf{C}^*$, find the characteristic

function χ satisfying

$$\begin{aligned} &\min_{\chi} \int_{\Omega_\mu} \chi \, d\Omega \\ &\text{such that: } \|\mathbf{C}_N^h(\chi) - \mathbf{C}^*\| = 0 \, . \end{aligned} \tag{B.13}$$

The cost function represents the stiff phase volume fraction. In particular, considering that the soft phase is void, the problem (B.13) identifies a minimum weight problem.

4.2. Algorithm for solving the TOP

The TOP (B.13) can be solved by introducing a level set-funtion $\psi \in C^0(\Omega_\mu)$ defined by

$$\psi(\mathbf{y}) = \begin{cases} < 0 & \forall \mathbf{y} \in \Omega_\mu^2 \\ > 0 & \forall \mathbf{y} \in \Omega_\mu^1 \\ 0 & \text{in the interfaces} \end{cases} , \tag{B.14}$$

and utilizing an augmented Lagrangian technique. In this case, the problem is rewritten as follows

$$\max_{\lambda} \min_{\psi} \mathcal{T}(\psi, \lambda), \tag{B.15}$$

with:

$$\mathcal{T}(\psi, \lambda) = \int_{\Omega_\mu} \chi(\psi) \, d\Omega + \lambda(\|\mathbf{C}_N^h(\psi) - \mathbf{C}^*\|) + \frac{\alpha}{2}(\|\mathbf{C}_N^h(\psi) - \mathbf{C}^*\|)^2 \tag{B.16}$$

where λ is the the constraint Lagrange multiplier and α is the augmented term penalty parameter.

The algorithm for solving the problem (B.15) utilizes two nested loops. In an internal loop, the objective function $\mathcal{T}$ is minimized by holding fixed λ and α. This loop, with index denoted k, consists of a level-set function-based iteration. While, an external loop, with index denoted l, modifies iteratively λ.

The minimum of $\mathcal{T}$ in the internal loop is searched with a descent direction algorithm. For problem (B.15), the topological derivative is given by

$$D_\psi \mathcal{T}(\psi, \lambda) = 1 - \left(\left(\lambda - \alpha \|\mathbf{C}_N^h - \mathbf{C}^*\| \right) \frac{D_\psi \mathbf{C}^h}{\|\mathbf{C}_N^h - \mathbf{C}^*\|} \right) \tag{B.17}$$

where $D_\psi \mathbf{C}^h$ is the topological derivative of the homogenized elasticity tensor, see Amstutz et al.

(2010) for an additional description of this term. Then, we define the function :

$$g(\mathbf{y}) = \begin{cases} -(D_\psi \mathcal{T}) & if : \psi < 0 \\ \\ +(D_\psi \mathcal{T}) & if : \psi > 0 \end{cases}, \tag{B.18}$$

The updating formula for ψ, at the $(k+1)$-th internal loop, is defined by

$$\psi^{k+1} = \psi^k + \tau g, \tag{B.19}$$

with the scaling factor τ being determined by means of a line search technique.

In the $(l+1)$-th external loop, the Lagrange multiplier λ is updated using the Uzawa algorithm

$$\lambda^{l+1} = \text{máx}(0, \lambda^l + \alpha \|\mathbf{C}_N^h - \mathbf{C}^*\|). \tag{B.20}$$

The penalty parameter α is held fixed during the full process.

A local optimality criterion of problem (B.15), see Amstutz (2011), is given by the condition

$$D_\psi \mathcal{T} > 0 \quad ; \quad \forall \mathbf{y} \in \Omega_\mu \tag{B.21}$$

which can be implemented by verifying the equality

$$\arccos \left[\frac{\int_{\Omega_\mu} g\psi \, dV}{\|g\|_{L^2} \|\psi\|_{L^2}} \right] = 0. \tag{B.22}$$

5. Methodology for searching the optimal micro-structure

Leaving aside the issue related to existence of solutions[6], finding one solution of problem (B.15) may be difficult, especially when extreme materials are designed. The search of a solution with the algorithm described in sub-Section 4.2 is facilitated by following two procedures that are summarized in sub-Section 5.1 and 5.2.

5.1. Selection of the micro-cell shape Ω_μ

The shape of the domain Ω_μ is an implicit variable utilized in the inverse design problem (B.13) that should be defined in advance. Considering that problem (B.13) searches for an optimal periodic micro-structure, this variable plays a major role to find an adequate material micro-architecture adjusting the target elasticity.

[6] As previously mentioned, this issue can be mitigated through the handling of the parameter δ in equation (B.2).

A good decision is to choose Ω_μ coinciding with the shape of a micro-structure unit-cell. However, in view that the periodic micro-structure is unknown at the moment of solving the inverse design problem, we conjecture that the periodic micro-cell Ω_μ coincides with the shape of the Voronoi Cell of a Bravais lattice related to a crystal which elasticity tensor has the same symmetry as that displayed by the target tensor $\mathbf{C}^*$.

In Figure B.8, we show the only five different Bravais lattices in 2D and their associated symmetry classes. A Bravais lattice is fully described with the primitive vectors $\mathbf{a}_1$ and $\mathbf{a}_2$. Therefore, Bravais lattices could be described with two parameters, the ratio $\omega = \|\mathbf{a}_2\|/\|\mathbf{a}_1\|$ and the angle $\varsigma = \arccos[(\mathbf{a}_2 \cdot \mathbf{a}_1)/(\|\mathbf{a}_2\|\|\mathbf{a}_1\|)]$. Additional information about this topic can be found in the book Ashcroft y Mermin (1976).

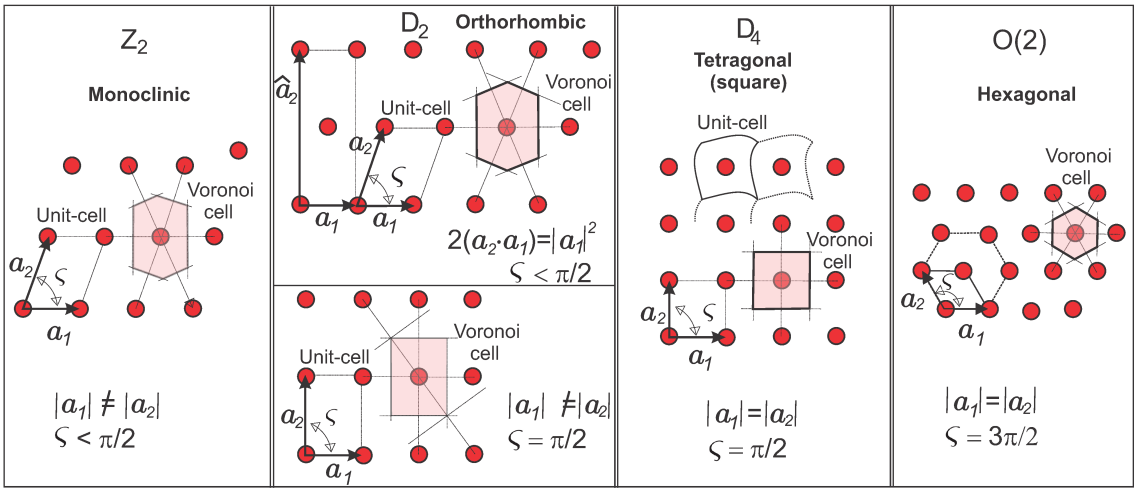

Figura B.8: Bravais lattices and Voronoi cells (Wigner–Seitz cells) for the material symmetry classes in plane problems. There are only five Bravais lattices in two dimensions, see Kittel (2005).

Also, in the same Figure, it can be observed that several unit-cells are associated with a given Bravais lattice, see for instance the unit-cells of the lattice with D_4 symmetry.

From all possible unit-cells, our interest lies in the Voronoi cells (Weigner-Seitz cells) also depicted in the Figure. Voronoi-cell shapes preserve the symmetry of the underlying lattice. Observing the lattice with D_4 symmetry, horizontal and vertical directions are axes of symmetry for the lattice, however, they are not symmetry axes for all the unit-cells. Instead, the Voronoi-cell is symmetric respect to both axes, as well as to rotations of $\pm 90.deg$.

What is more important for the topology optimization problem is that distributing the material within a Voronoi-cell with certain spatial symmetry, prescribed according to each type of lattice, it can be guaranteed that the symmetry of the underlying lattice is preserved for the homogenized elasticity tensor. So, following this criterion, we force the material distribution defined by the level-set function in the iterative algorithm of sub-Section 4.2 to satisfy the rotational or reflection symmetries displayed in Figure B.9.

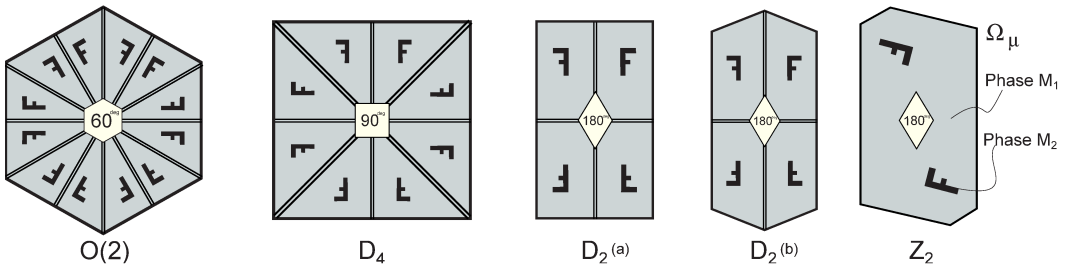

Figura B.9: Voronoi-cell of a two-phase composite material. Planes and angles of symmetry utilized in the topology optimization algorithm for material distribution. The central symbol indicates the rotation angle preserving the symmetry. Reflection planes are symbolized with double segments.

Figure B.10-a displays the plane ω, ς in R^2, where each pair ω, ς define a Bravais lattice. In gray, we show a bounded space of points with coordinates (ω, ς) defining the full set of all possible Bravais lattices. This reduced space is found by applying symmetry conditions to Bravais lattices. Notice, for example, that the lattice represented in the Figure B.10-b by the point denoted W', with coordinates $(0.967, 75.deg)$, is the same lattice as that represented by the point denoted W with coordinates $(0.5, 30.deg)$.

Figure B.10-c shows, in the same bounded space, the Voronoi cells associated with different points and the corresponding symmetry classes of these lattices. So, in the case that the target elasticity tensor $\mathbf{C}^*$ has symmetry D_2 or D_4, as it generally happens in FMO problem solutions with only one load system, it should be sufficient to restrict the search of the Ω_μ shape to some of the Voronoi-cells represented by the set of parameter ω, ς lying along the boundary of the gray region.

One additional criterion to determine which point (ω, ς) of this set is the most convenient one, is described in the following sub-Section.

5.2. Additional criteria to choose the micro-cell shape and the initial material configuration in Ω_μ

The criteria for choosing a particular Voronoi-cell of the space (ω, ς), as well as an adequate distribution of material within this cell which can be taken as the initial configuration for the iterative algorithm solving the problem (B.13), are summarily explained here. A full description of this procedure is given in Podestá et al. (2017).

Initially, an off-line computation of several homogenized elasticity tensors is performed. These results are used to build a database of homogenized elastic tensors.

The homogenized elastic tensors stored in the data base are the results of several micro-cells with varying shapes and material configurations, such as described in the following items:

- Voronoi-cells with lattice parameters ω and ς sweeping the entire range of values depicted

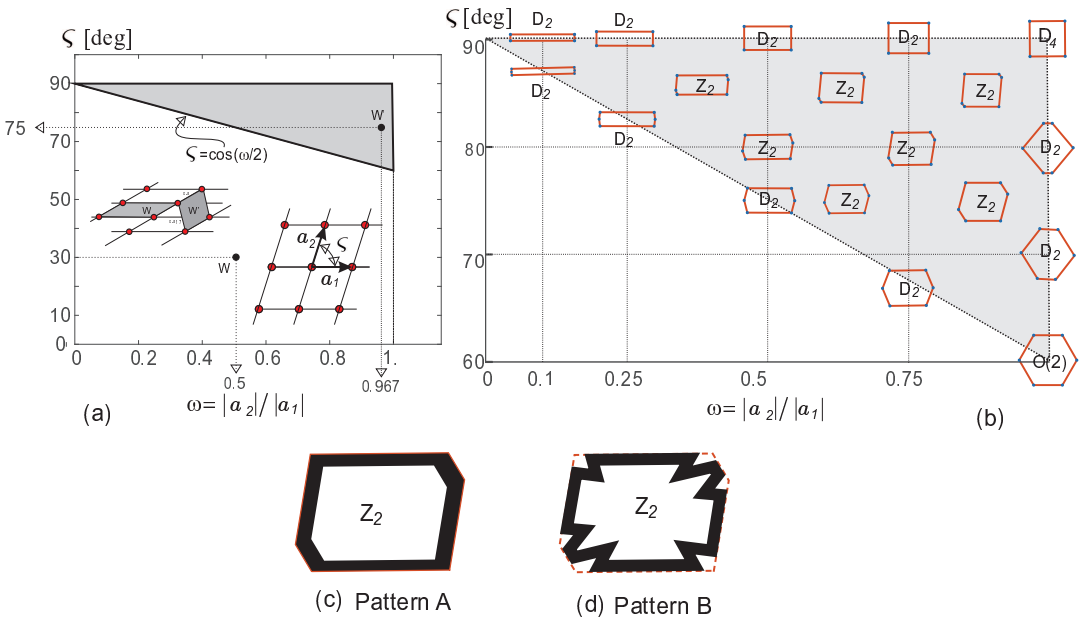

Figura B.10: Space of parameters ω, ς and micro-cell shapes. a) Bounded space of parameters ω, ς identifying the complete set of Bravais lattices; one Bravais lattice can be represented by two different points, W' and W, in the space ω, ς; b) Voronoi cells and symmetry classes; c) and d) material distribution patterns A and B for determining the map $\mathbf{C}^h_{db}(\omega, \varsigma, f, P)$

in gray in Figure B.10-a;

- two material configurations denoted pattern A and B in Figure B.10d-e. The material configuration of pattern A corresponds to equal thickness bars of solid material placed on the boundaries of the cells. The pattern B also corresponds to equal thickness bars placed on the boundaries of the cells but with a re-entrant configuration.

- several volume fractions f of solid material. This parameter f determines the bar thickness in each case.

Therefore, all computed homogenized elasticity tensors in the database can be characterized by four parameters: ω and ς, defining the Voronoi-cell shape, the solid volume fraction f and P defining the "Pattern" A or B. We identify each database entry with the notation $\mathbf{C}^h_{db}(\omega, \varsigma, f, P)$.

We recall that auxetic materials can be built with re-entrant configurations of bars, see Kolken y Zadpoor (2017). A profuse literature about honeycomb re-entrant auxetic materials exists, see for example Fu et al. (2016) and references cited therein. The fact of capturing materials with negative ratios $(C^h_{db})_{1122}/(C^h_{db})_{1111}$ is the reason why we include pattern B in the database.

The database is built with a bar material having a normalized Young's modulus[7] $E = 1.$ and Poisson ratio $\nu = 0.3$. Several values of f are used. We take approximately $6e3$ points to sweep

[7]For all configurations displayed in this study, where the soft phase is void, the homogenized elasticity tensor is proportional to Young's modulus of the stiff phase.

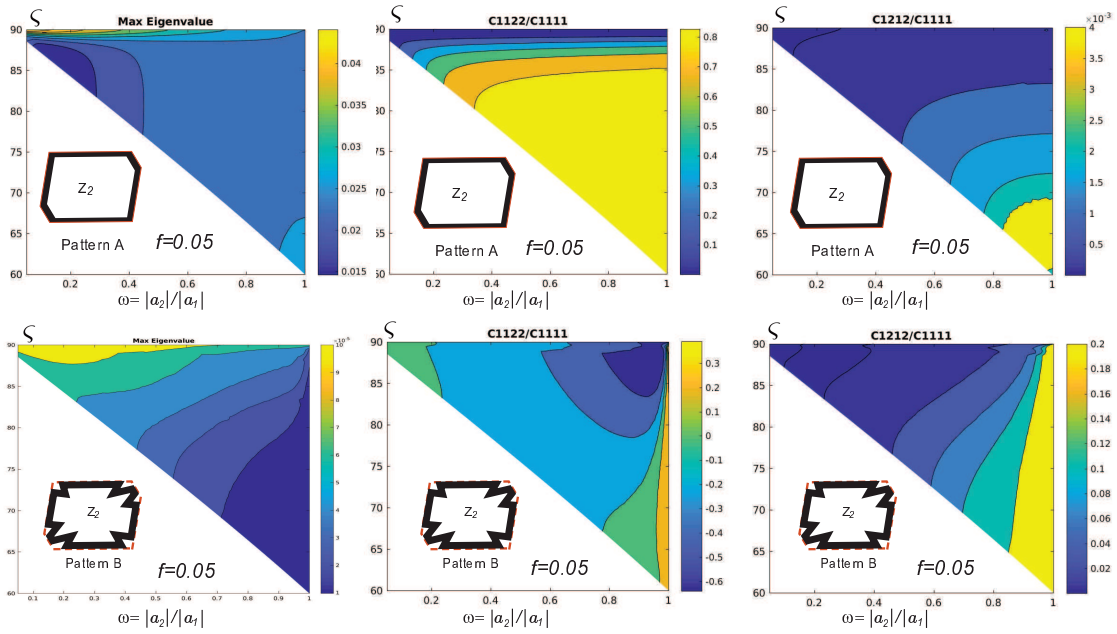

Figura B.11: Maps of homogenized elastic properties of Voronoi cells parameterized with ω and ς, stiff material is distributed according to the patterns A and B and volume fraction of the stiff phase is $f = 0.05$.

the reduced domain in the plane (ω,ς). Therefore, the database stores more than $1e5$ homogenized elasticity tensors.

Partial results of this database corresponding to the patterns A, B and $f = 0.05$ are depicted in Figure B.11. These colored maps show in column: a) the maximum eigenvalue of the homogenized elasticity tensors, b) the ratios $(C^h_{db})_{1122}/(C^h_{db})_{1111}$ and c) the normalized shear stiffness $(C^h_{db})_{1212}/(C^h_{db})_{1111}$. As expected, the ratio $(C^h_{db})_{1122}/(C^h_{db})_{1111}$ of pattern B shows a large region of parameters ω, ς defining auxetic micro-architectures. The maximum eigenvalue gives an idea of the maximum stiffness displayed by the respective configuration. Also, note the connection between the ratio $(C^h_{db})_{1122}/(C^h_{db})_{1111}$ and the shear stiffness for different configurations.

With this database, the most adequate micro-cell shape and material distribution is adopted by using the criterion

$$\zeta = \arg\left\{ \min_{\mathbf{C}^h_{db}} \|\mathbf{C}^h_{db}(\zeta) - \mathbf{C}^*\| \right\}; \qquad \text{where } \zeta := \{\omega, \varsigma, f, P\}, \tag{B.23}$$

which defines the instance of the database that is closer to the target elasticity tensor. The search of the minimum in (B.23) is restricted to the set of parameters (ω, ς) whose lattices have the same symmetry as $\mathbf{C}^*$.

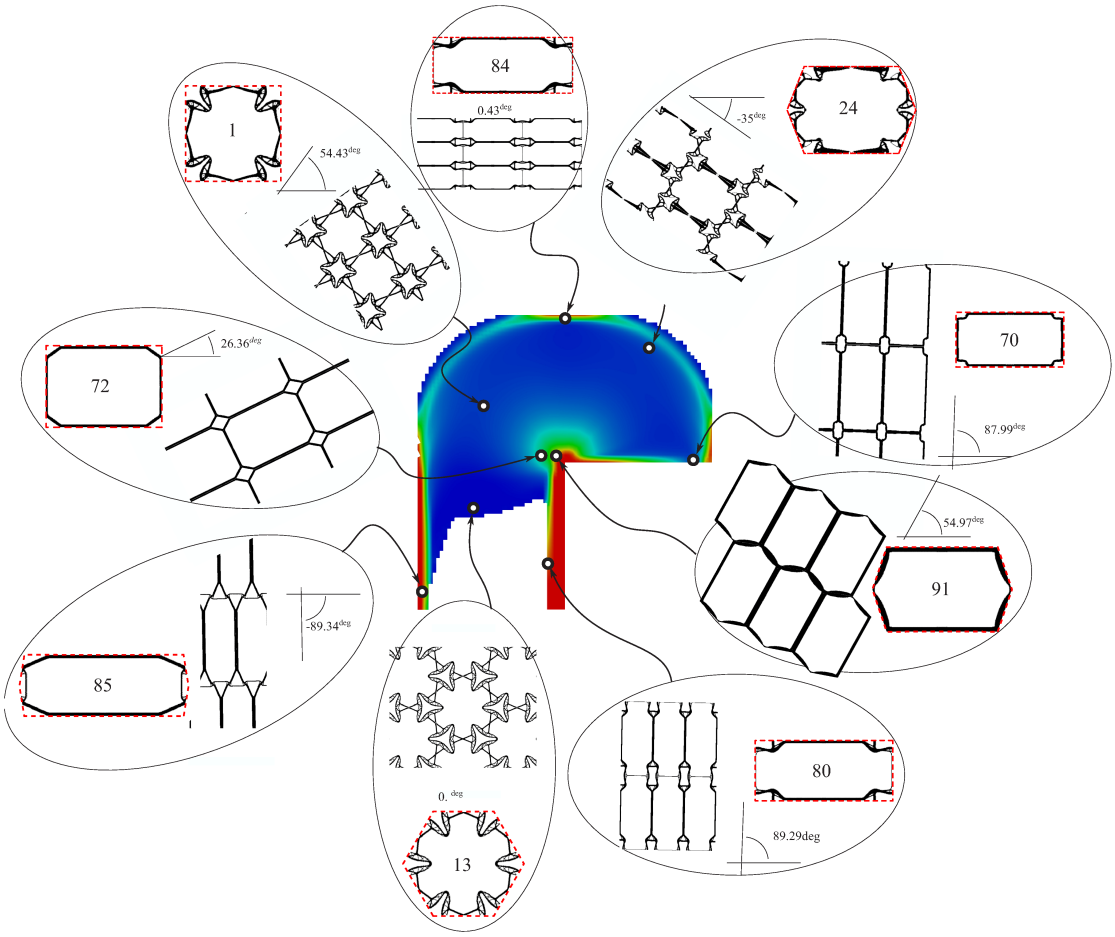

Figura B.12: Computed micro-cells for several sectors of the L-panel test. The Cartesian basis of the micro-cells coincides with the normal basis. Assembled micro-cells are rotated to the physical directions in each sector.

5.3. Results

L-panel with one load system

Figure B.12 shows the micro-structures computed with the explained design methodology. The results correspond to nine sectors of the L-panel denoted 1, 13, 24, 70, 72, 80, 84, 85 and 91, respectively. The unit-cells computed for these sectors are depicted such that the horizontal direction coincides with one of the homogenized tensor normal bases. In the same Figure, an assembly of several cells is also shown but rotated to the global Cartesian directions. The angle $-\theta$ transforms the normal basis direction to the global Cartesian one. Therefore, θ transforms $\hat{\mathbf{C}}$ into $\hat{\mathbf{C}}_N$, recalling that $\hat{\mathbf{C}}_N$ is used to compute equation (B.11). This angle θ is determined for every point of the L-panel.

Figure B.13 compares the micro-cells gathered from the database and those obtained as solution of the TOP. The micro-cells depicted in the Figure correspond to the Sectors $1, 13, 24, 80$ and 85. Micro-cells gathered from the database, using the procedure (B.23), are adopted as the initial configuration for the iterative topology optimization algorithm. Their homogenized elasti-

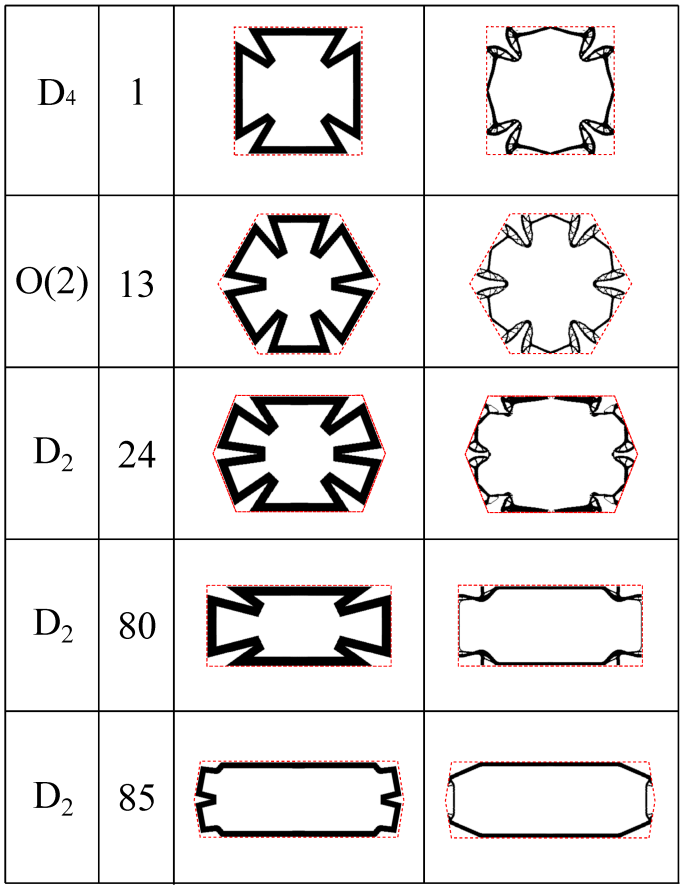

Figura B.13: L-panel test, micro-structure design with the TOP. First column reveals the symmetry class of the target elastic tensor. Second column denotes the designed Sector. Third column depicts the micro-cells taken from the database as initial configurations for the topology optimization algorithm. Fourth column depicts the micro-cells obtained as solution of the topology optimization algorithm.

city tensor are denoted $\mathbf{C}^h_{db}$. Alternatively, the homogenized elasticity tensor computed with the micro-cells being the solution of the TOP are denoted $\mathbf{C}^h_N$.

Note that the micro-architecture configurations remain rather simple and almost similar to the initial configurations gathered from the database. Also, observe that the micro-architectures in all sectors are honeycomb-like structures, but the cell shapes change notably in different sectors.

Even when a given sector of the L-panel has similar elastic properties, in accordance with the criterion adopted to define them, explained in the previous sub-Section, sectors have non-uniform distribution of the normal basis directions. Therefore, the designed representative micro-cell for one sector has to be rotated to the physical directions with the angle $-\theta$ at every point of the structure. We evidence this result in Figure B.14. There, we depict the designed micro-structure for this sector in the physical directions for an identical sector which has been designed with a unique micro-cell.

Table B.2 displays the components of the target elasticity tensor $\mathbf{C}^*$, $\mathbf{C}^h_{db}$ and $\mathbf{C}^h_N$ in the mentioned sectors, respectively.

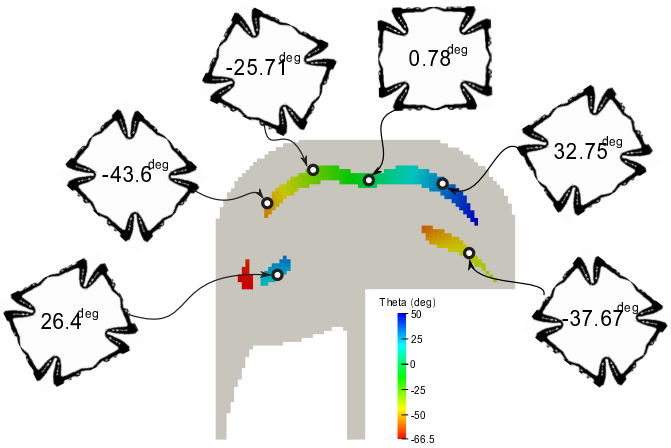

Figura B.14: Resulting micro-structure of Sector 6 rotated to the physical directions. The rotation angle $-\theta$ is shown in accordance with the color scale.

Note that, even when the initial configuration value $\mathbf{C}^h_{db}$ is close to the target one, the optimization algorithm improves notably the results even without changing substantially the material distribution of the initial configuration. The last column in this Table identifies the volume fraction of the gathered and solved micro-cells.

Note also that from Figure B.12 and Table B.2, the Sector 13 requires a material with isotropic symmetry $O(2)$, as well as, an elasticity tensor with zero Poisson ratio and low stiffness. In this case, the re-entrant micro-structure designed with the present procedure facilitates the attainment of effective properties with almost zero Poisson ratio.

Plate subjected to three load systems

Figure B.15 shows the micro-structures computed for two sectors of the plate subjected to three independent load systems.

The optimal structural result is taken from the first FMO problem solution, see Figure B.3, test *iv*. In this case, material with symmetry Z_2 is found in the solution of the FMO problem even without including constraint (B.2). As the most challenging cases, we design the micro-structures of two points where the ratio $|C^*_{1112}/C^*_{1111}|$ is maximum. One case corresponds to a tensor with one null eigenvalue. The other case corresponds to a tensor with three non-null eigenvalues.

Figure B.16 compares the micro-cells taken as initial configurations of the topology optimization algorithm with those obtained as solutions of the TOP. Sectors shown in this Figure are the same as those depicted in Figure B.15.

Table B.3 displays the components of the target elasticity tensor $\mathbf{C}^*$ in the mentioned sectors. They are also compared with the homogenized elasticity tensors gathered from the database, $\mathbf{C}^h_{db}$, and with the homogenized elasticity tensors computed with the topology optimization algorithm $\mathbf{C}^h_N$.

Tabla B.2: L-panel test. Topology optimization algorithm results. $\mathbf{C}^*$ target elasticity tensor, $\mathbf{C}^h_{db}$ homogenized elastic tensor of the initial configuration (taken from the database), $\mathbf{C}^h_N$ homogenized elastic tensor of the converged configuration (values are multiplied by the factor 1000 ($E_0 = 1.MPa$). Last column displays the volume fraction of the stiff phase.

Sector		C_{1111}	C_{2222}	C_{1212}	C_{2212}	C_{1112}	C_{1122}	Vol. Frac.
1	$\mathbf{C}^h_{db}$	7.93	7.93	0.94	0	0	-1.79	0.30
1	$\mathbf{C}^h_N$	7.19	7.19	1.85	0	0	-3.12	0.17
1	$\mathbf{C}^*$	7.07	7.07	2.00	0	0	-3.07	-
6	$\mathbf{C}^h_{db}$	7.54	4.91	0.65	0	0	-1.61	0.28
6	$\mathbf{C}^h_N$	7.93	5.41	1.14	0	0	-2.28	0.21
6	$\mathbf{C}^*$	7.96	5.37	2.00	0	0	-2.27	-
13	$\mathbf{C}^h_{db}$	4.04	4.04	1.90	0	0	0.24	0.35
13	$\mathbf{C}^h_N$	4.04	4.04	2.01	0	0	0.02	0.14
13	$\mathbf{C}^*$	4.04	4.03	2.00	0	0	0.01	-
24	$\mathbf{C}^h_{db}$	13.73	3.09	1.94	0	0	-0.96	0.40
24	$\mathbf{C}^h_N$	13.22	4.29	1.57	0	0	-1.80	0.15
24	$\mathbf{C}^*$	14.03	4.35	2.00	0	0	-1.85	-
70	$\mathbf{C}^h_{db}$	64.21	6.72	0.09	0	0	13.79	0.12
70	$\mathbf{C}^h_N$	60.99	5.93	0.08	0	0	10.16	0.11
70	$\mathbf{C}^*$	60.75	5.90	2.00	0	0	10.14	-
72	$\mathbf{C}^h_{db}$	48.11	15.27	0.12	0	0	18.55	0.12
72	$\mathbf{C}^h_N$	47.35	13.73	0.07	0	0	20.79	0.10
72	$\mathbf{C}^*$	48.38	14.03	2.00	0	0	21.09	-
80	$\mathbf{C}^h_{db}$	82.81	2.08	2.37	0	0	-2.21	0.40
80	$\mathbf{C}^h_N$	80.15	3.43	0.02	0	0	-0.46	0.12
80	$\mathbf{C}^*$	82.43	4.00	2.00	0	0	-0.37	-
84	$\mathbf{C}^h_{db}$	91.52	1.64	2.20	0	0	-2.29	0.40
84	$\mathbf{C}^h_N$	89.69	3.19	0.02	0	0	-0.18	0.12
84	$\mathbf{C}^*$	91.79	4.00	2.00	0	0	-0.14	-
85	$\mathbf{C}^h_{db}$	93.28	5.66	0.83	0	0	2.04	0.23
85	$\mathbf{C}^h_N$	91.05	3.24	0.22	0	0	1.37	0.13
85	$\mathbf{C}^*$	91.91	4.02	2.00	0	0	0.37	-
91	$\mathbf{C}^h_{db}$	57.25	50.52	0.86	0	0	38.57	0.18
91	$\mathbf{C}^h_N$	60.84	36.03	0.76	0	0	40.68	0.17
91	$\mathbf{C}^*$	60.39	35.61	2.00	0	0	42.16	-

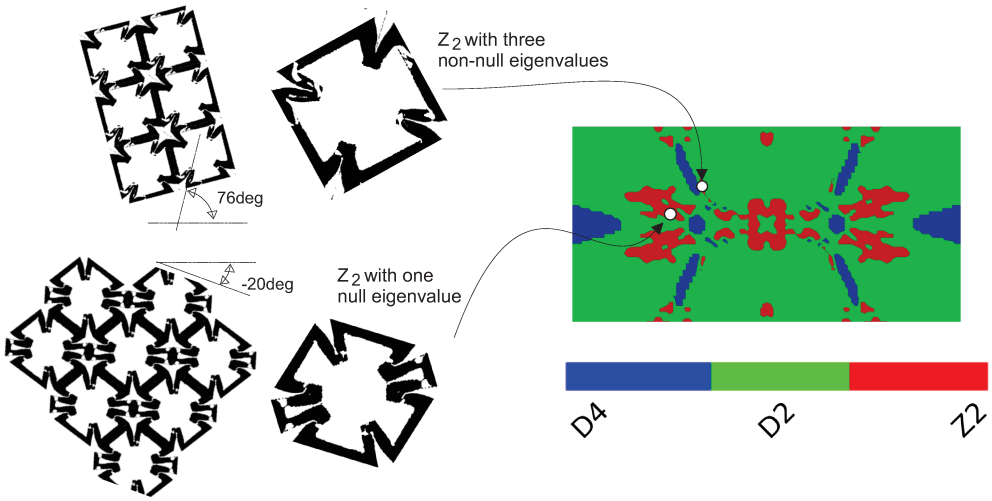

Figura B.15: Computed micro-cells for two sectors of the Plate subjected to three load systems. The right picture depicts the distribution of symmetry classes. Two micro-cells are shown. The sectors with these micro-cells correspond to Z_2 symmetries with one null eigenvalue and three non-null eigenvalues, respectively.

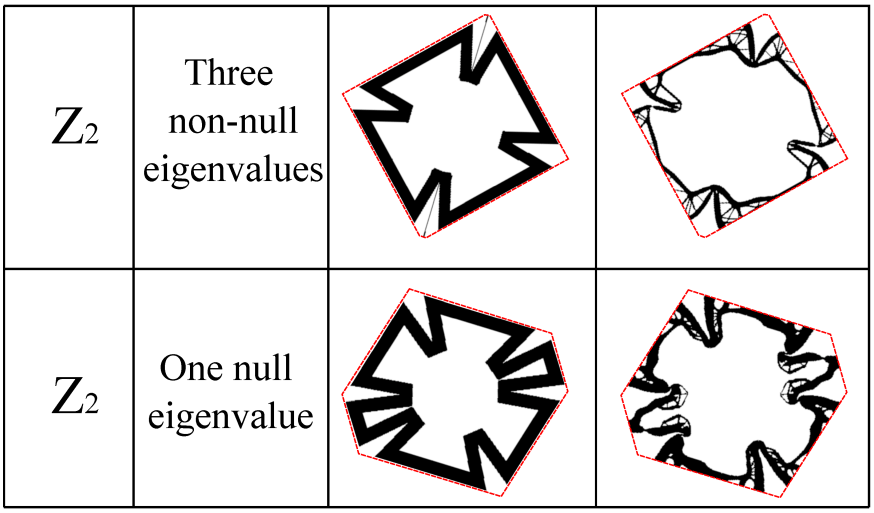

Figura B.16: Plate subjected to three load systems. Configurations taken for initializing the topology optimization algorithm and the obtained solutions.

Tabla B.3: Plate subjected to three load systems. Topology optimization algorithm results for two cases, one of them displays full anisotropic elasticity Z_2. $\mathbf{C}^*$ is the target elasticity tensor, $\mathbf{C}^h_{db}$ is the homogenized elastic tensor of the initial configuration, gathered from the database, and $\mathbf{C}^h_N$ is the homogenized elastic tensor of the topology optimization algorithm converged configuration (values are multiplied by the factor 1000 ($E_0 = 1.MPa$). Last column displays the volume fraction of the stiff phase.

Sector		C_{1111}	C_{2222}	C_{1212}	C_{2212}	C_{1112}	C_{1122}	Vol. Frac.
With one	$\mathbf{C}^h_{db}$	13.00	5.69	4.68	1.62	-1.62	-0.25	0.45
null	$\mathbf{C}^h_N$	15.52	3.56	6.72	4.13	-4.60	-2.58	0.29
eigenvalue	$\mathbf{C}^*$	15.63	3.18	6.79	4.63	-4.63	-2.56	-
With three	$\mathbf{C}^h_{db}$	8.83	8.24	5.35	-2.17	2.17	1.94	0.35
non-null	$\mathbf{C}^h_N$	14.41	2.94	6.65	-3.46	3.68	-0.57	0.17
eigenvalues	$\mathbf{C}^*$	14.38	2.61	6.66	-3.65	3.65	-0.63	-

6. Conclusions

In this paper, a two-scale material design approach, coupled in one-direction, has been explored. The effective elasticity tensors at the macro-scale are computed via a methodology based on a free parametrization of materials. Then, these effective elasticity tensors are used as target tensors for the inverse design of the micro-architectures.

This weakly coupled two-scale approach has been previously reported in the literature. However, the discussions of results obtained with it, and presented in sub-Sections 3.2, provide the necessary ingredients to state the main contributions of the paper.

These contributions focus on studying two new tools for the inverse design of material micro-architectures in optimal structural problems. They are useful procedures for attaining periodic material configurations with simple honeycomb-like micro-architectures whose effective elasticity tensors cover a wide range. The main characteristics of both tools are summarily described as follows:

i) The first tool defines a rule for the cell shape selection. Then, the TOP is solved in the spatial domain limited by the so-chosen cell. These cells are the Voronoi-cells of Bravais lattices having the same kind of symmetry than the one displayed by the target effective elasticity tensors.

ii) The other tool defines an adequate material distribution in the adopted cell. This material distribution is taken as the initial configuration for the iterative topology optimization algorithm.

An additional rule proposed in this paper is the alignment of the Voronoi-cell periodicity directions with the natural coordinate system directions of the target elasticity tensor. This rule simplifies the material distribution configurations within the Voronoi-cells. In this case, it is necessary to compute the natural coordinate system of every target elasticity tensor.

Both tools, when combined with the above-mentioned rule, mitigate the most significant limitation of the two-scale material design methodology described in this paper. This is a remarkable result which is useful for the development of realizable optimal structures using this methodology.

Finally, it is emphasized that the new proposed tools are not only limited to the inverse design of micro-architectures in the context of structural optimization problems, but also they can be usefully applied to other more general types of metamaterial inverse design problems.

Acknowledgments

The authors acknowledge the financial support from CONICET and ANPCyT (grants PIP 2013-2015 631 and PICT 2014-3372) and from the European Research Council under the European Unions Seventh Framework Programme (FP/2007-2013) / ERC Grant Agreement N. 320815 (ERC Advanced Grant Project Advanced tools for computational design of engineering materials COMP-DES-MAT).

Appendix B1: Discretization of the FMO formulation

The finite element method is used to compute the structural response solution and evaluate $\mathbf{u}_k$ as a function of $\hat{\mathbf{C}}(\mathbf{x})$. Conventional bilinear quadrilateral finite elements are used. The elasticity tensor $\hat{\mathbf{C}}_i$ is taken to be constant within every i-th finite element, with the indices: $i = 1, ..., n_{el}$ and n_{el} is the number of finite elements in the mesh. The symmetry of each tensor $\hat{\mathbf{C}}_i$ is enforced by defining only the six independent components, $\hat{C}_{i1111}$, $\hat{C}_{i1122}$, $\hat{C}_{i1112}$, $\hat{C}_{i2222}$, $\hat{C}_{i2212}$, $\hat{C}_{i1212}$, as design variables for the i-th finite element.

Utilizing this approach, the FMO problem can be rewritten as follows [8]:

$$\min_{(\hat{\mathbf{C}}_1,...,\hat{\mathbf{C}}_{n_{el}},\mathbf{u}_1,...,\mathbf{u}_{n_{load}})} \sum_{i=1}^{n_{el}} \operatorname{tr}(\hat{\mathbf{C}}_i)\Omega_i^e \tag{B.24a}$$

$$\text{such that: } \mathbb{K}\mathbf{u}_k - \mathbf{f}_k = \mathbf{0};\ \left(\mathbb{K} = \bigwedge_{j=1}^{n_{el}} \int_{\Omega_j^e} (\mathbf{B}^j)^T \hat{\mathbf{C}}_j \mathbf{B}^j \, dV\right); (k = 1, .., n_{load}) \tag{B.24b}$$

$$\sum_{k=1}^{n_{load}} w_k \langle \mathbf{f}_k \cdot \mathbf{u}_k \rangle \leq \bar{f}; \tag{B.24c}$$

$$\underline{\rho} \leq \operatorname{tr}(\hat{\mathbf{C}}_i) \leq \bar{\rho}; \quad (i = 1, ..., n_{el}) \tag{B.24d}$$

$$\hat{\mathbf{C}}_i \succeq 0; \quad (i = 1, ..., n_{el}) \tag{B.24e}$$

where Ω_i^e is the area of the i-th finite element. Expressions (B.24b) are the n_{load} equilibrium equations, one for each independent load system. The stiffness matrix of the discrete equilibrium equations is denoted $\mathbb{K}$ and is computed with a conventional numerical integration. $\mathbf{B}$ denotes the conventional strain-displacement matrix. Expression (B.24e) imposes the positive semi-definite character on $\hat{\mathbf{C}}_i$.

This FMO problem has $(6 \times n_{el} + n_{load} \times n_{dof})$ design variables, where n_{dof} is the number of degrees of freedom of the finite element mesh (dimension of the interpolated displacement field).

We solve the semi-definite optimization problem (B.24) using the IPOPT primal-dual algo-

[8] Introducing an abuse of notation, discrete and continuous fields in this Section are identified with the same symbols.

rithm, see Wächter y Biegler (2006), with a second-order method. The Hessian matrix is simple to evaluate, but it requires enormous resources of memory. In general, problems presented in this work, up to 10000 quadrilateral finite elements, need 50 to 70 iterations. Here, we do not pursue the objective of evaluating the computational performance of IPOPT for solving very-large-scale problems. For computational benchmarks of structural optimization problems using the IPOPT algorithm, see Rojas-Labanda y Stolpe (2015). Also, additional information about specific algorithms designed for solving FMO problems can be found in the paper of Weldeyesus y Stolpe (2015) and references cited therein.

Appendix B2: Symmetries of the elasticity tensor in plane problems

Let us consider a generic plane elasticity tensor $\mathbf{C}$. In the Cartesian coordinate system, its components are denoted C_{ijkl}, with $i, j, k, l = 1, 2$.

Following the Kelvin's notation, this tensor can be written in the matrix format

$$\mathbf{C} = \begin{bmatrix} C_{1111} & C_{1122} & \sqrt{2}C_{1112} \\ C_{2211} & C_{2222} & \sqrt{2}C_{2212} \\ \sqrt{2}C_{1211} & \sqrt{2}C_{1222} & 2C_{1212} \end{bmatrix} . \tag{B.25}$$

Also, $\mathbf{C}$ can be expressed in the normal coordinate system (normal basis), see Auffray y Ropars (2016) and Cowin y Mehrabadi (1987). The normal coordinate system is rotated an angle θ respect to the Cartesian coordinate system.

In normal coordinates, the tensor (B.25) is represented by the matrix

$$\mathbf{C}_N = \begin{bmatrix} K + G + a_1 + d_1 & K - G - d_1 & \sqrt{2}d_2 \\ K - G - d_1 & K + G - a_1 + d_1 & -\sqrt{2}d_2 \\ \sqrt{2}d_2 & -\sqrt{2}d_2 & 2G - 2d_1 \end{bmatrix} , \tag{B.26}$$

called the normal form of $\mathbf{C}$. In this expression, K, G, a_1, d_1 and d_2 are material parameters. The angle θ should also be considered as an additional material parameter. Note that θ is the rotation angle taking the matrix (B.25) and transforming it to expression (B.26).

According to the symmetry group qualifying $\mathbf{C}_N$, these material parameters K, G, a_1, d_1 and d_2 are:

- Symmetry Z_2 (anisotropic) has six independent elastic coefficients: K, G, a_1, d_1 and d_2 plus the angle θ. The normal form of $\mathbf{C}_N$ results with the components $(C_N)_{1112} = -(C_N)_{2212}$.

- Symmetry D_2 (orthotropic) has five independent elastic coefficients: K, G, a_1 and d_1 plus the angle θ. The normal form of $\mathbf{C}_N$ results with the components $(C_N)_{1112} = (C_N)_{2212} = 0$ ($d_2 = 0$).

- Symmetry D_4 (tetragonal) has four independent elastic coefficients: K, G and d_1 plus the angle θ that should be defined such that $a_1 = d_2 = 0$. The normal form of $\mathbf{C}_N$ results with the components: $(C_N)_{1111} = (C_N)_{2222}$ and $(C_N)_{1112} = (C_N)_{2212} = 0$.

- Symmetry $O(2)$ (isotropic), has two independent elastic coefficients: K, G. The angle θ is arbitrary. Then, The normal form of $\mathbf{C}_N$ results with the components: $(C_N)_{1111} = (C_N)_{2222}$, $(C_N)_{1212} = (C_N)_{1111} - (C_N)_{1112}$ and $(C_N)_{1112} = (C_N)_{2212} = 0$. In this particular case, we identify

$$\kappa = K - \frac{G}{3}, \tag{B.27}$$

  where, κ is the 3-D bulk modulus and G is the shear modulus.

In all cases, except for isotropic symmetry, the angle θ is an additional parameter of the elasticity tensor.

We recall that the normal format (B.26) of $\mathbf{C}$ is not preserved in arbitrary Cartesian bases.

B2.1. Reorientation of the elasticity tensor to the normal basis

The rotation angle θ transforming $\boldsymbol{C}$ to the normal axis is found with the algorithm proposed by Auffray y Ropars (2016), see also Vianello (1997).

Auffray et al. introduce the fourth and second order tensors denoted $\mathbf{D}$, $\mathbf{a}$ and the coefficients λ and μ. All these terms are defined as follows:

$$\begin{aligned}
D_{ijkl} =& C_{ijkl} - \\
&- \frac{1}{6}(\delta_{ij}C_{kplp} + \delta_{kl}C_{ipjp} + \delta_{ik}C_{lpjp} + \delta_{lj}C_{ipkp} + \delta_{il}C_{jpkp} + \delta_{jk}C_{iplp}) \\
&+ \frac{C_{pqpq}}{12}(5\delta_{ij}\delta_{kl} - \delta_{ik}\delta_{jl} - \delta_{il}\delta_{jk}) - \frac{C_{ppqq}}{8}(3\delta_{ij}\delta_{kl} - \delta_{ik}\delta_{jl} - \delta_{il}\delta_{jk}) \,, \\
a_{ij} =& \frac{1}{12}(2C_{ipjp} - C_{pqpq}\delta_{ij}) \,, \\
\lambda =& \frac{1}{8}(3C_{ppqq} - 2C_{pqpq}) \,, \\
\mu =& \frac{1}{8}(2C_{pqpq} - C_{ppqq}) \,.
\end{aligned} \tag{B.28}$$

With these expressions, the invariants of $\mathbf{C}$ are calculated

$$I_1 = \lambda + \mu \quad , \quad J_1 = \mu \quad , \quad I_2 = a_{pq}a_{pq} \quad , \tag{B.29}$$
$$J_2 = D_{pqrs}D_{pqrs} \quad , \quad I_3 = a_{pq}D_{pqrs}a_{rs} \quad , \quad J_3 = R_{pq}a_{qr}D_{prst}a_{st} \; .$$

where the tensor:

$$R = \begin{pmatrix} 0 & 1 \\ -1 & 0 \end{pmatrix} ,$$

These invariants define the symmetry class of $\mathbf{C}$. The procedure is described in Figure B.17. Also, the coefficient determining the normal form of $\mathbf{C}$, equation (B.26), are determined with expressions (B.28) as follows:

$$\begin{aligned} a_1 =& \frac{1}{2}(a_{11} - a_{22}) \; , \\ a_2 =& \frac{1}{2}(a_{12} + a_{21}) \; , \\ d_1 =& \frac{\sqrt{8}}{8}(D_{1111} + D_{2222} - D_{1122} - D_{1212} \\ & - D_{2112} - D_{2121} - D_{1221} - D_{2211}) \; , \\ d_2 =& \frac{\sqrt{8}}{8}(D_{1112} + D_{1121} + D_{1211} + D_{2111} \\ & - D_{2221} - D_{2212} - D_{2122} - D_{1222}) \; , \end{aligned}$$

Also, defining the angles:

$$\theta_\alpha = \frac{1}{2}\tan^{-1}\left(\frac{a_2}{a_1}\right) \quad ; \quad \theta_\beta = \frac{1}{4}\tan^{-1}\left(\frac{d_2}{d_1}\right) \; ,$$

the angle θ is determined with the rule: $\theta = \theta_\alpha$ for the classes Z_2 or D_2; and $\theta = \theta_\beta$ for the class D_4.

Bibliografía

Allaire G. *Shape optimization by the homogenization method*, volumen 146. Springer Science & Business Media, 2012.

Amstutz S. Analysis of a level set method for topology optimization. *Optimization Methods and Software*, 26(4-5):555–573, 2011.

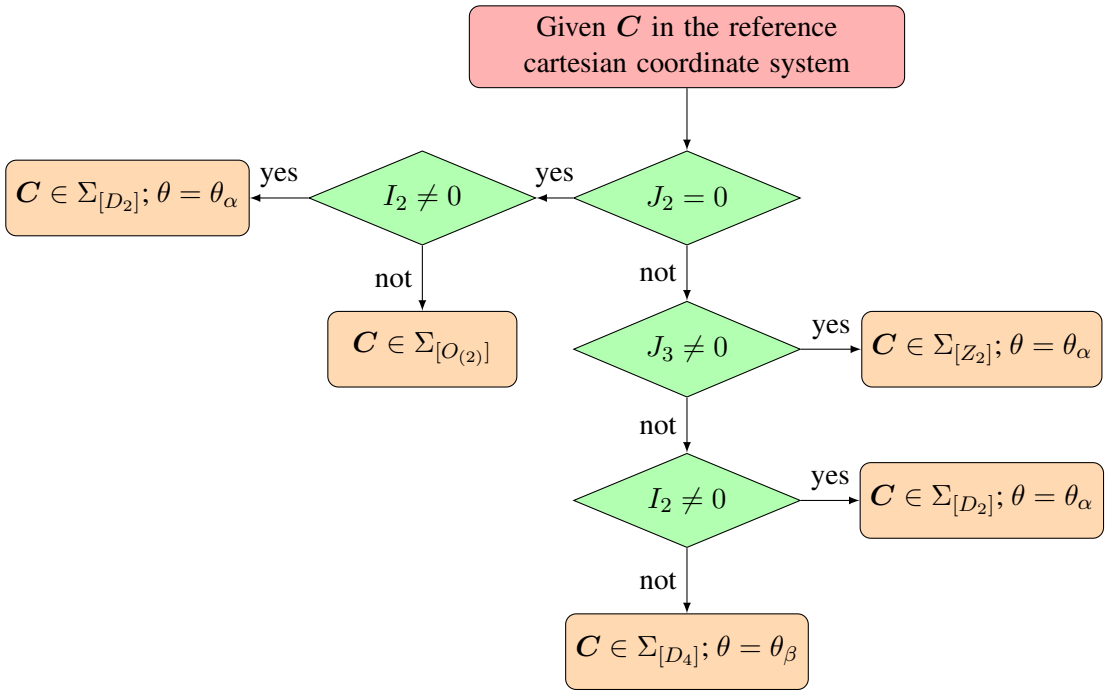

Figura B.17: Classification of $\boldsymbol{C}$-symmetry and angle θ between the normal basis and the Cartesian basis (Auffray y Ropars (2016))

Amstutz S. y Andrä H. A new algorithm for topology optimization using a level-set method. *Journal of Computational Physics*, 216(2):573–588, 2006.

Amstutz S., Giusti S., Novotny A., y de Souza Neto E. Topological derivative for multi-scale linear elasticity models applied to the synthesis of microstructures. *International Journal for Numerical Methods in Engineering*, 84(6):733–756, 2010.

Ashcroft N. y Mermin N. *Solid State Physics*. Harcourt College Publishers, New York), 1976.

Auffray N. y Ropars P. Invariant-based reconstruction of bidimensional elasticity tensors. *International Journal of Solids and Structures*, 87:183–193, 2016.

Bendsøe M. Optimization of structural topology, shape, and material. 1995.

Bendsøe M., Díaz A., Lipton R., y Taylor J. Optimal design of material properties and material distribution for multiple loading conditions. *International Journal for Numerical Methods in Engineering*, 38(7):1149–1170, 1995.

Bendsøe M., Guedes J., Haber R., Pedersen P., y Taylor J. An analytical model to predict optimal material properties in the context of optimal structural design. *Journal of Applied Mechanics*, 61(4):930–937, 1994.

Cherkaev A. *Variational methods for structural optimization*, volumen 140. Springer Science & Business Media, 2012.

Cowin S. y Mehrabadi M. On the identification of material symmetry for anisotropic elastic materials. *Quarterly Journal of Mechanics and Applied Mathematics*, 40(Part 4):451–476, 1987.

Diaz. A. y Benard A. Designing materials with prescribed elastic properties using polygonal cells. *International Journal for Numerical Methods in Engineering*, 57(3):301–314, 2003.

Fu M., Xu O., Hu L., y Yu T. Nonlinear shear modulus of re-entrant hexagonal honeycombs under large deformation. *International Journal of Solids and Structures*, 80:284–296, 2016.

Giusti S., Ferrer A., y Oliver J. Topological sensitivity analysis in heterogeneous anisotropic elasticity problem. theoretical and computational aspects. *Computer Methods in Applied Mechanics and Engineering*, 311:134–150, 2016.

Kittel C. Introduction to solid state physics. *University of Pennsylvania Law Review*, 154(3):477, 2005.

Kočvara M., Stingl M., y Zowe J. Free material optimization: recent progress. *Optimization*, 57(1):79–100, 2008.

Kolken H. y Zadpoor A. Auxetic mechanical metamaterials. *RSC Advances*, 7(9):5111–5129, 2017.

Lopes C., dos Santos R., y Novotny A. Topological derivative-based topology optimization of structures subject to multiple load-cases. *Latin American Journal of Solids and Structures*, 12(5):834–860, 2015.

Méndez C., Podestá J., Lloberas-Valls O., Toro S., Huespe A., y Oliver J. Computational material design for acoustic cloaking. *International Journal for Numerical Methods in Engineering*, 2017.

Milton G. y Cherkaev A. Which elasticity tensors are realizable? *Journal of engineering materials and technology*, 117(4):483–493, 1995.

Milton M. The theory of composites. *The Theory of Composites, by Graeme W. Milton, pp. 748. ISBN 0521781256. Cambridge, UK: Cambridge University Press, May 2002.*, página 748, 2002.

Pedersen P. On optimal orientation of orthotropic materials. *Structural and Multidisciplinary Optimization*, 1(2):101–106, 1989.

Podestá J., Méndez C., Toro S., y Huespe. A. In preparation, 2017.

Ringertz U. On finding the optimal distribution of material properties. *Structural and Multidisciplinary Optimization*, 5(4):265–267, 1993.

Rojas-Labanda S. y Stolpe M. Benchmarking optimization solvers for structural topology optimization. *Structural and Multidisciplinary Optimization*, 52(3):527–547, 2015.

Schury F. Two-scale material design-from theory to practice. 2013. PhD Thesis, Friedrich-Alexander-Universitat Erlangen-Nurnberg.

Schury F., Stingl M., y Wein F. Efficient two-scale optimization of manufacturable graded struc-

tures. *SIAM Journal on Scientific Computing*, 34(6):B711–B733, 2012.

Sigmund O. Design of material structures using topology optimization. 1994a. PhD thesis, Technical University of Denmark.

Sigmund O. Materials with prescribed constitutive parameters: an inverse homogenization problem. *International Journal of Solids and Structures*, 31(17):2313–2329, 1994b.

Sigmund O. A new class of extremal composites. *Journal of the Mechanics and Physics of Solids*, 48(2):397–428, 2000.

Sigmund O. y Maute K. Topology optimization approaches. *Structural and Multidisciplinary Optimization*, 48(6):1031–1055, 2013.

Stingl M., Kočvara M., y Leugering G. A sequential convex semidefinite programming algorithm with an application to multiple-load free material optimization. *SIAM Journal on Optimization*, 20(1):130–155, 2009.

Ting T. *Anisotropic elasticity: theory and applications*. 45. Oxford University Press, 1996.

Vianello M. An integrity basis for plane elasticity tensors. *Archives of Mechanics*, 49(1):197–208, 1997.

Wächter A. y Biegler L. On the implementation of a primal-dual interior point filter line search algorithm for large-scale nonlinear programming. *Mathematical Programming*, 106(1):25–57, 2006.

Weldeyesus A. y Stolpe M. A primal-dual interior point method for large-scale free material optimization. *Computational Optimization and Applications*, 61(2):409–435, 2015.

Zowe J., Kočvara M., y Bendsøe M. Free material optimization via mathematical programming. *Mathematical programming*, 79(1):445–466, 1997.

Anexo C

Computational material design for acoustic cloaking

El artículo presentado a continuación ha sido publicado en la revista **"International Journal for Numerical Methods in Engineering"**.

C. Méndez, J.M. Podestá, O. Lloberas-Valls, S. Toro, A.E. Huespe, J. Oliver, *"Computational material design for acoustic cloaking"*, **"International Journal for Numerical Methods in Engineering"**, DOI: 10.1002/nme.5560.

Computational material design for acoustic cloaking

C. Méndez[1], J.M. Podestá[2], O. Lloberas-Valls[3,4],
S. Toro[2], A.E. Huespe[2,3][1], J. Oliver[3,4]
[1]CIMNE-Latinoamérica, Iturraspe 785, CP 3000, Santa Fe, Argentina
[2]CIMEC-UNL-CONICET, Predio Conicet "Dr Alberto Cassano", CP 3000 Santa Fe, Argentina
[3]Centre Internacional de Metodes Numerics en Enyinyeria (CIMNE),Campus Nord UPC.
[4]E.T.S d'Enginyers de Camins, Canals i Ports, Technical University of Catalonia (Barcelona Tech)
Campus Nord UPC, Mòdul C-1, c/ Jordi Girona 1-3, 08034, Barcelona, Spain

Keywords: transformation acoustic applications; acoustic cloak; pentamode material; topological derivative; topology optimization; extremal material.

Abstract

A topology optimization technique based on the topological derivative and the level set function is utilized to design/synthesize the micro-structure of a pentamode material for an acoustic cloaking device.

The technique provides a micro-structure consisting of a honeycomb lattice composed of needle-like and joint members. The resulting metamaterial shows a highly anisotropic elastic response with effective properties displaying a ratio between bulk and shear moduli of almost 3 orders of magnitude. Furthermore, in accordance with previous works in the literature, it can be asserted that this kind of micro-structure can be realistically fabricated.

The adoption of a topology optimization technique as a tool for the inverse design of metamaterials with applications to acoustic cloaking problems is one contribution of this paper. However, the most important achievement refers to the analysis and discussion revealing the key role of the external shape of the prescribed domain where the optimization problem is posed.

[1]Corresponding author. E-mail address: ahuespe@intec.unl.edu.ar (A.E. Huespe).

The efficiency of the designed micro-structure is measured by comparing the scattering wave fields generated by acoustic plane waves impinging on bare and cloaked bodies.

1. Introduction

New methodologies to fabricate metamaterials open a wide range of interesting applications in engineering and science. In this context, the goal is to design and manipulate architectured micro-structures to develop new materials with exotic mechanical, optical, acoustical or thermal properties (Zheng et al. (2014), Kadic et al. (2013), Narayana y Sato (2012)). These metamaterials are envisaged to satisfy specifically given requirements at the macro-structure scale level.

For example, making an object *invisible* to sound waves can be achieved by covering it with an appropriately designed layer of material having extreme and highly anisotropic elastic properties. Following this kind of approach, one technique to get acoustic cloaking is based on the coordinate transformation method, reported by Norris (2008), whereby the material properties of the cloak copy the geometrical coefficients of an adequate space (singular) transformation. Norris has generalized the key observation of Pendry et al. (2006) to acoustic wave problems. Pendry has shown that metamaterials can be designed at will, by adopting singular coordinate transformations, to redirect electromagnetic waves and, therefore, attaining optical cloaking devices.

According to Norris, metamaterials for cloaking systems based on transformation acoustic can be categorized into two broad classes: materials requiring anisotropic inertial mass densities, identified with inertial cloaking devices (see Cheng et al. (2008) for realizations of this type of metamaterial), and materials requiring anisotropic bulk moduli. Realizations of this last type of metamaterials can be reached through pentamode materials.

Pentamode materials have been initially proposed by Milton and Cherkaev (Milton y Cherkaev (1995)). These materials are usually formed by truncated cones, similar to bars, and joints which are spatially distributed as a Bravais lattice.

Layman et al. (2013) have developed a design methodology for pentamode materials employed in acoustic cloaking devices. In their approach, these authors use a methodology where the micro-structure topology is prescribed beforehand, i.e. the micro-structure has a pre-defined architecture. The dimensions and geometrical position of each member constituting the micro-structure are parametrized. The most convenient set of parameters is then determined through a non-linear programming algorithm, such that the effective elastic properties are adjusted to those values required by Norris's analysis.

Additionally, pentamode materials have been fabricated and reported by Kadic et al. (2014). A number of issues concerning the material processing are addressed in Kadic et al. (2014). An im-

portant conclusion reported in this paper, closely connected with the present work, is that in order to allow genuine pentamode material realizations, the members constituting the micro-structure have to be neither pin-jointed nor rigid-jointed.

The main objective of the present paper is to contribute to computational design/synthesis of pentamode material, constituted by highly heterogeneous microstructures, aiming to built acoustic cloaking devices. The question that has to be solved is how to distribute and combine the material within a prescribed domain to obtain the desired properties of the composite for building the cloaking device.

To solve this inverse design problem, we use a technique based on a topology optimization algorithm. Starting from the seminal paper of Bendsøe y Kikuchi (1988) on topology optimization, there have been a huge number of well-known and established inverse techniques for material micro-structure design based on topology optimization. The book of Bendso y Sigmund (2013) and, more recently, the review paper by Sigmund et al.Sigmund y Maute (2013) give excellent overviews of different approaches that can be found in the literature. Furthermore, a more specific discussion of topics here addressed can be found in the recent review by Osanov y Guest (2016) and the references cited therein. It is important to mention that these kind of techniques provide a detailed description of the material micro-structure without preconceiving beforehand any kind of micro-architecture.

In this work, we adopt the topology optimization algorithm previously presented by Amstutz y Andrä (2006), which uses a level set function and the topological derivative concept. This algorithm has been enhanced in posterior contributions of Amstutz and co-authors and successfully applied to a series of topology optimization problems, such as micro-structure inverse design (Amstutz et al. (2010)), structural design subjected to stress constraints (Amstutz et al. (2012)) and design of piezoelectric actuators (Amigo et al. (2016)). Furthermore, based on the contributions of Novotny y Sokołowski (2012), who have obtained expressions of topological derivatives in the three-dimensional space, this kind of algorithm can be extended to solve 3D topology optimization problems. Synthesis of 3D micro-structures utilizing topological derivatives has been shown by Özdemir (2014).

The Amstutz's algorithm is here adapted to seek the micro-structure topology of a material which effective elasticity tensor is equal to the target tensor given by Norris's analysis. It is shown that the Amstutz's algorithm, with some minor modifications introduced in the present contribution, turns to be an adequate technique for designing pentamode materials for acoustic cloaking.

Also, we analyze an important aspect of topology optimization techniques for designing metamaterials, which has not been particularly discussed in the literature. It refers to the relationship

between the symmetry of the material to be synthesized and the external shape of the prescribed domain where the optimization problem is posed. Our results demonstrate that the external shape plays an important role in obtaining good micro-architecture designs. We propose a procedure to appropriately define this external shape. Conclusions extracted from this discussion can be extended to more general metamaterial inverse design problems using these techniques; provided that the effective properties of the target material satisfy given symmetry requirements. Discussion of this point is one of the main achievements of the present paper.

A brief description of the topics covered in this paper is the following. First, in Section 2, some pentamode material properties are highlighted. These properties are subsequently utilized in the context of Norris's method. A reminder of this method is briefly presented in Appendix 6. Also, in the same Appendix, the elasticity tensors reported by Gokhale et al. (2012) are described and briefly summarized in sub-Section 2.1. They are the target tensors adopted in this work for the pentamode material inverse design.

In Section 3, a sketch of the topology optimization problem utilized for the micro-structure synthesis of the acoustic cloaking device is presented. A more detailed description of this procedure is shown in Appendix 6.

The topology optimization algorithm described in Appendix 6 is validated in sub-Section 3.3. The validation test consists of synthesizing an extremal metamaterial having a high ratio between the bulk and shear moduli.

The procedure for designing the micro-structure of the acoustic device is addressed in Section 4. The so-designed micro-structure is virtually tested through computational simulation of the scattered wave field produced by means of a cloaked object immersed in a fluid. The result is compared with the field produced by the same bare object. This assessment is presented in Section 5.

Finally, in Section 6, some conclusions are addressed.

2. A pentamode material

A Pentamode material is a class of extremal material having five easy (compliant) modes of deformation in a three-dimensional space, and having only one non-easy (hard) mode of deformation. The elasticity tensor of this material has one non-null eigenvalue and five null eigenvalues (hence the name of pentamode given to this class of material). For example, a compressible inviscid fluid (ideal gas) is a pentamode material, where shear strains in any directions represent easy modes of deformations, while volumetric strains represent hard modes of deformation. Milton y Cherkaev (1995) have coined the name of pentamode materials in the context of linear elasticity,

see also Milton (2002) where additional properties of this type of materials are analyzed.

Pentamode materials are a special class of linear anisotropic elastic solids. They can be characterized through elasticity tensors represented by:

$$\hat{\mathbf{C}} = \kappa^\star \mathbf{S} \otimes \mathbf{S} \qquad ; \tag{C.1}$$

where $\kappa^\star$ is a pseudo-bulk modulus with the dimensions of stress and $\mathbf{S}$ is an adimensional symmetric second order tensor with norm not necessarily equal to one. As usual, the symbol $\otimes$ denotes the tensorial product.

Pentamode materials are useful for constructing acoustic cloaking devices. These devices require a particular heterogeneous distribution of properties characterized by $\kappa^\star$ and $\mathbf{S}$. In particular, for cylindrical acoustic cloaking devices, it can be considered a rotationally symmetric pattern of material properties in the plane (X_1, X_2), schematized in Figure C.1-a [2] , where the tensor $\mathbf{S}$ could be defined in a rather general context by:

$$\mathbf{S} = \sqrt{\frac{\kappa_r}{\kappa^\star}}(\mathbf{e}_r \otimes \mathbf{e}_r) + \sqrt{\frac{\kappa_\theta}{\kappa^\star}}(\mathbf{e}_\theta \otimes \mathbf{e}_\theta); \tag{C.2}$$

$\mathbf{e}_r$ and $\mathbf{e}_\theta$ being the radial and circumferential unit vectors related to the polar coordinate system. The material properties, $\kappa_r(\mathbf{X})$ and $\kappa_\theta(\mathbf{X})$ are seen as the radial and circumferential bulk moduli, respectively. Additionally, $\mathbf{S}$ satisfies a self-equilibrium condition: $\mathrm{div}_{\mathbf{X}}\mathbf{S} = \mathbf{0}$ [3] (note, however, that $\mathbf{S}$ is not a stress).

By adopting Voigt [4] notation for describing tensors of second and fourth order in the coordinate system defined by the basis $\{\mathbf{e}_r, \mathbf{e}_\theta\}$, the strain and stress tensors in this case, removing the out-of-plane component, result in $\boldsymbol{\varepsilon} = [\varepsilon_r, \varepsilon_\theta, 2\varepsilon_{r\theta}]^T$ and $\boldsymbol{\sigma} = [\sigma_r, \sigma_\theta, \sigma_{r\theta}]^T$, while the elasticity tensor $\hat{\mathbf{C}}$ defined in equation (C.1) ($\mathbf{S}$ given by equation (C.2)) is represented in the same basis by the matrix:

$$\hat{\mathbf{C}} = \begin{bmatrix} \kappa_r & \sqrt{\kappa_r \kappa_\theta} & 0 \\ \sqrt{\kappa_r \kappa_\theta} & \kappa_\theta & 0 \\ 0 & 0 & 0 \end{bmatrix}. \tag{C.3}$$

[2] In the following, we preserve the name of pentamode material for plane (two-dimensional) problems. Removing the third dimension and the out-of-plane field components, the elasticity tensor has only three eigenvalues. Particularizing the same concept of pentamode material, two of these eigenvalues are related to compliant modes of deformation and only one is related to a hard mode. Strictly, this material should be called bi-mode material.

[3] In this work, the gradient and divergence operators are denoted by $\nabla_{\mathbf{X}}(\cdot)$ and $\mathrm{div}_{\mathbf{X}}(\cdot)$, respectively. Subindex $\mathbf{X}$ emphasizes the coordinate system where they are evaluated.

[4] Voigt or tensorial notation are used indistinctly in this paper. The proper context of every equation determines which specific notation is used.

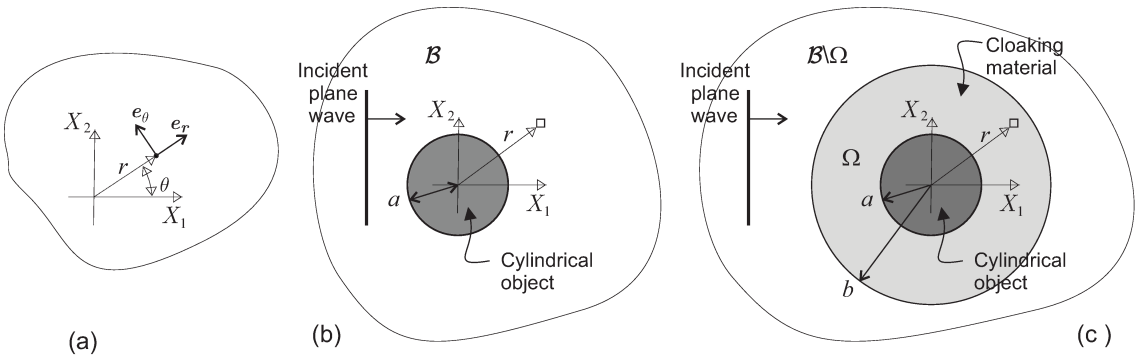

Figura C.1: Acoustic cloaking problem. (a) Polar coordinate system; (b) domain of analysis $\mathcal{B}$ with a cylindrical object immersed in the fluid; and (c) cylindrical object with a cloaking device.

The equation of motion in a solid composed of this particular pentamode material is derived as follows. The constitutive equation and the momentum balance equation for the solid are given by:

$$\boldsymbol{\sigma} = \hat{\mathbf{C}} : \boldsymbol{\varepsilon} = \kappa^{\star}(\mathbf{S} : \boldsymbol{\varepsilon})\mathbf{S} = -\hat{p}\mathbf{S} \, , \tag{C.4}$$

$$\boldsymbol{\rho}^{\star} \cdot \ddot{\mathbf{u}} = \mathrm{div}_{\mathbf{X}}\boldsymbol{\sigma} = -\mathbf{S} \cdot \nabla_{\mathbf{X}}\hat{p} \, , \tag{C.5}$$

where $\mathbf{u}$, $\boldsymbol{\varepsilon}$ and $\boldsymbol{\sigma}$ are the displacements, strain and stress fields, respectively, and

$$\hat{p} = -\kappa^{\star}(\mathbf{S} : \boldsymbol{\varepsilon}) \tag{C.6}$$

is a pseudo-pressure scalar term. In (C.4), the trace of the tensorial product between the two second order tensors is denoted by the symbol $(:)$, while the symbol $(\cdot)$ indicates the contraction of one index of the tensorial product. In accordance with (C.4), only stresses proportional to $\mathbf{S}$, with the proportionality factor given by pseudo-pressures, can be held by this material. The momentum balance equation (C.5) is written assuming that the inertial mass density, $\boldsymbol{\rho}^{\star}$, is a generalized second order tensor, not necessarily a spherical one.

After replacing the conventional kinematical compatibility condition $\boldsymbol{\varepsilon} = \frac{1}{2}(\nabla_{\mathbf{X}}(\mathbf{u}) + \nabla^{T}_{\mathbf{X}}(\mathbf{u}))$ in equation (C.4), deriving in time and replacing (C.5) into (C.4), a wave propagation equation in terms of the pseudo-pressure field $\hat{p}$ can be derived as follows:

$$\ddot{\hat{p}} - \kappa^{\star}\, \mathbf{S} : \nabla_{\mathbf{X}} \left((\boldsymbol{\rho}^{\star})^{-1} \cdot \mathbf{S} \cdot \nabla_{\mathbf{X}}\hat{p} \right) = 0 \, . \tag{C.7}$$

2.1. Pentamode material for acoustic cloaking devices

Next, let us consider a cylindrical object of radius $r = a$ immersed in a fluid occupying the infinite domain $\mathcal{B}$. The object is reached by an incident plane wave propagating from left to right, as sketched in Figure C.1-b. The fluid is characterized by a bulk modulus κ_0 and density ρ_0.

We address the problem of designing the pentamode material placed in the circular ring Ω, with exterior radius $r = b$ and thickness $b - a$, acting as the acoustic cloaking device for the cylindrical object, see Figure C.1-c.

Equation (C.7) is utilized in the transformation acoustic analysis by Norris and co-authors (Norris (2008) and Gokhale et al. (2012)) to define the properties $\kappa^\star$, $\boldsymbol{\rho}^\star$ and $\mathbf{S}$ of a pentamode material which is used to built an acoustic cloaking device adapted for a cylindrical object. Appendix A briefly summarizes Norris's analysis by which the pentamode material parameters for solving this problem are determined. The principal equations being necessary for the following development of the paper are also summarized in Appendix A and have been taken from Gokhale et al. (2012).

Considering the large set of possible maps defining a useful coordinate transformation for this problem, Gokhale et al. (2012) have defined one transformation preserving the isotropy of the inertial mass density, while keeping the elastic anisotropic properties to a bare minimum (see Appendix 6). According to these authors, by adopting this particular transformation map and then copying the elastic coefficients of the pentamode material to the geometrical parameters induced by the transformation, the bulk moduli and the inertial mass density of this material result in:

$$\kappa^\star = \kappa_0 \frac{1}{f'(r)} \left(\frac{r}{f(r)} \right) \quad , \quad \kappa_r = \kappa_o \frac{1}{f'(r)} \left(\frac{f(r)}{r} \right) \quad , \quad \kappa_\theta = \kappa_o f'(r) \left(\frac{r}{f(r)} \right) \tag{C.8}$$

$$\boldsymbol{\rho}^\star = \hat{\rho}\mathbf{1} \qquad , \qquad \hat{\rho} = \rho_o f'(r) \left(\frac{f(r)}{r} \right) , \tag{C.9}$$

where r is the radial coordinate as shown in Figure C.1-b. The function $f(r)$, defining the coordinate transformation map, is given by:

$$f(r) = \begin{cases} \left(\frac{b^2 - a\delta}{b^2 - a^2} r - \frac{a-\delta}{b^2-a^2} b^2 \frac{a}{r} \right); & a \leq r \leq b \\ r; & r \geq b \end{cases} \tag{C.10}$$

with δ being a geometrical parameter whose meaning is discussed in Appendix. Note case that, defining $\mathbf{1}$ as the unit tensor, $\boldsymbol{\rho}^\star$ results in a spherical tensor retrieving the concept of an isotropic inertial mass density. Figure C.2-a plots the function $f(r)$ for $\delta = 0.333a$ and $b = 2a$, while Figure C.2-b plots the corresponding normalized material properties described in equations (C.8) and (C.9) as a function of the radial coordinate.

Then, from expression (C.3), the elasticity tensor of a pentamode material, whose properties

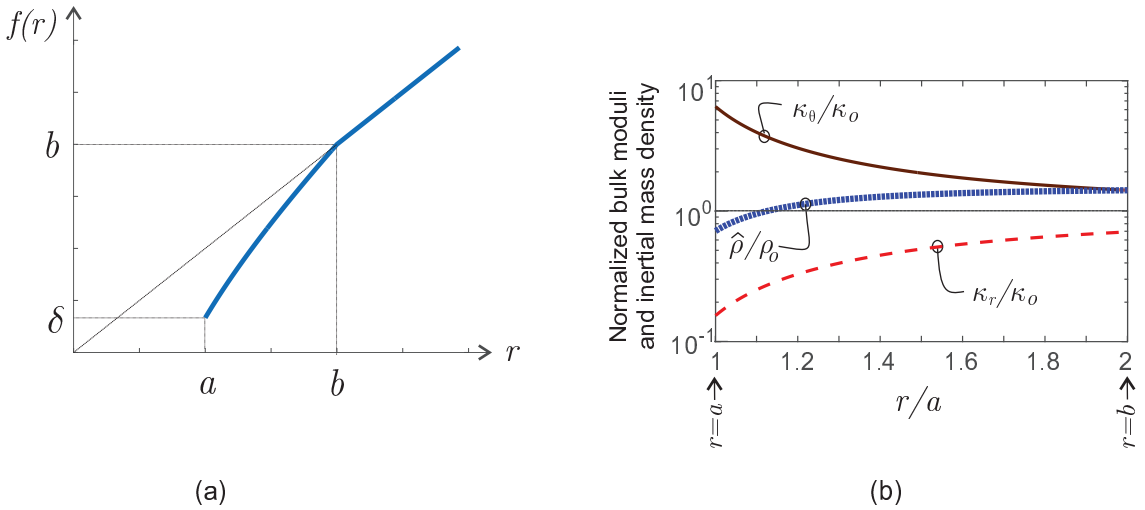

Figura C.2: (a) Plot of the function $f(r)$ taken from Gokhale et al. (2012). This function defines the coordinate transformation which is adequate for designing a cylindrical acoustic cloaking layer with minimal elastic anisotropy. (b) Normalized material properties of expressions (C.8) and (C.9), derived from the coordinate transformations (C.27)-(C.29) (Appendix 6) and the parameter $\delta = 0.333a$. The normalization factors are the fluid properties.

are given by (C.8) and (C.9), is defined by:

$$\hat{\mathbf{C}} = \kappa_o \begin{bmatrix} \frac{1}{f'(r)}\left(\frac{f(r)}{r}\right) & 1 & 0 \\ 1 & f'(r)\left(\frac{r}{f(r)}\right) & 0 \\ 0 & 0 & 0 \end{bmatrix}. \tag{C.11}$$

3. Topology optimization problem

The design of the material micro-structure required by Norris's analysis is carried out by defining an appropriate optimization problem which is described in this Section.

Also in this Section, we study the selection of an adequate external shape of the unit cell in where the topology optimization problem is placed. Finally, in sub-Section 3.3, the whole procedure for solving the topology optimization problem is assessed and validated.

3.1. Synthesis of micro-structures as a topology optimization problem

Let us consider a two-phase composite with a periodic micro-structure occupying the macro-scale domain Ω, such as schematized in Figure C.3. One phase is assumed to be very stiff and is denoted by M1. The other one is assumed to be very compliant and is denoted by M2. It is assumed that the micro-structure characteristic length, ℓ_{UC}, is much smaller than the characteristic length of the body ℓ [5].

[5] In relation to the acoustic cloaking problem here addressed, ℓ can be taken as the cylinder radius.

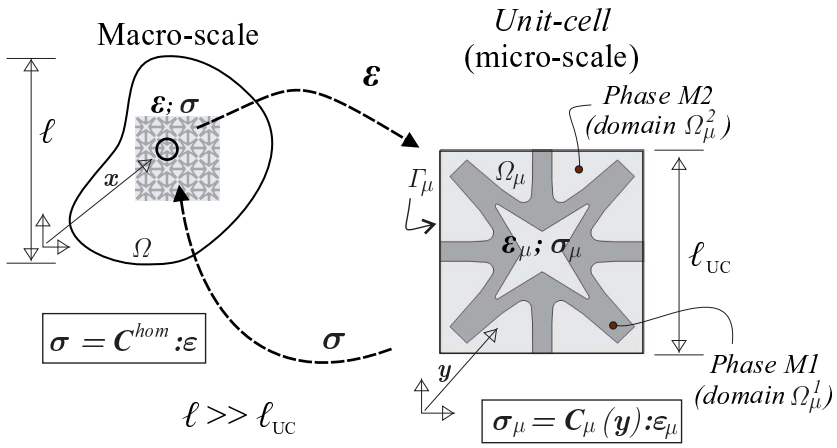

Figura C.3: Multiscale material model of a composite with two phases: M1 and M2. Computational homogenization approach to determine $\boldsymbol{\sigma}(\varepsilon)$.

The effective properties of this composite, subjected to elastic loading regimes, are computed via a conventional homogenization technique from a unit-cell denoted by Ω_μ. This homogenization technique is briefly explained in Appendix 6. The effective elasticity tensor $\mathbf{C}^{hom}$ obtained through this homogenization technique relates the macro-stress field $\boldsymbol{\sigma}(\mathbf{x})$ with the macro-strain field $\varepsilon(\mathbf{x})$, as follows:

$$\boldsymbol{\sigma} = \mathbf{C}^{hom}(\Omega_\mu^1) : \varepsilon \ . \tag{C.12}$$

Denoting Ω_μ^1 and Ω_μ^2 the micro-cell domains occupied by phases M1 and M2, respectively, the argument of $\mathbf{C}^{hom}$ remarks its dependence with the material distribution within the unit cell.

Let us now consider a unit-cell, with domain Ω_μ, defined by its external boundary Γ_μ. The material distribution within this domain is determined by solving the following topology optimization problem:

$$\min_{\Omega_\mu^1} \mathcal{J}(\Omega_\mu^1) = \min_{\Omega_\mu^1}(\|\mathbf{C}^{hom}(\Omega_\mu^1) - \hat{\mathbf{C}}\|^2); \tag{C.13}$$

where the target tensor $\hat{\mathbf{C}}$ is a data of the problem [6], while the conventional Frobenius norm $\|\cdot\|$ computes the distance between $\mathbf{C}^{hom}$ and $\hat{\mathbf{C}}$. In problem (C.13), minimization of the objective function $\mathcal{J}(\Omega_\mu^1)$ is attained by changing the placement of material M1 within the domain delimited by Γ_μ.

The optimal distribution of M1 is found with the topology optimization algorithm proposed by Amstutz y Andrä (2006) and its extended version Amstutz et al. (2010) particularly adapted to solve inverse material design problems.

Here, the Amstutz's algorithm has been slightly modified to solve the specific problem (C.13).

[6] As it is shown in sub-Section 4.2, the target tensor $\hat{\mathbf{C}}$ in the acoustic cloaking design problem is given by equation (C.11)

Some details of this algorithm are presented in Appendix 6, while a more fundamental description of the original version can be found in the mentioned bibliography.

The algorithm is implemented with linear triangular finite elements. Therefore, linear polynomials are used to interpolate the level set functions as well as the topological derivative in Ω_μ.

3.2. Selecting an appropriate shape of the boundary Γ_μ

The mathematical problem associated with the topology optimization algorithm is defined in a two-dimensional domain delimited by an external boundary Γ_μ which has to be known in advance. The selection of an adequate shape of Γ_μ is a particularly important issue whenever composites with periodic micro-structures and showing specific symmetries have to be designed.

In this sub-Section, a guideline for solving this issue is given. The idea is inspired by concepts taken from crystallography, Bravais lattices and elastic properties of crystals and also exploits the symmetry shown by the pentamode material.

In 2D problems, it has been demonstrated that there are only four different symmetry classes for describing any arbitrary elasticity tensors (see Auffray y Ropars (2016) and the references cited therein, as well as Ting (1996)). The elasticity tensor $\hat{\mathbf{C}}$ of a plane pentamode material, defined in equation (C.1), has orthotropic (orthorhombic) symmetry denoted by D_2 in Aufray et al. This kind of symmetry is also a characteristic of the elasticity tensors associated with crystalline structures (Landau y Lifshitz (1959)) that have an atomic distribution placed on the vertices of a (centered rectangular) Bravais lattice having orthogonal primitive vectors $\mathbf{a}_1$ and $\mathbf{a}_2$, such as shown in Figure C.4-a. The lattice parameter $\eta = \|\mathbf{a}_1\|/\|\mathbf{a}_2\|$ governs approximately the ratio between the coefficients C_{11} and C_{22} of the crystal effective elasticity tensor.

We conjecture that the external boundary Γ_μ coincides with the boundary of a unit-cell utilized in crystallography. In the present case, the unit-cell is taken from a Bravais lattice having orthorhombic symmetry. Figure C.4-b shows the Wigner-Seitz unit-cell denoted V-Cell (by Voronoi cell) of a Bravais lattice having this kind of symmetry. It is a non-regular hexagon containing one lattice point (point 0 in Figure C.4-a) in the center. The hexagon is built around this point and its sides are the perpendicular bisectors of the segments joining the central point 0 and every one of the other six closest points in the lattice (A, B, C, D, E and F in Figure C.4-a).

According to this conjecture, we use V-Cells to represent the boundaries Γ_μ of generic unit-cells associated with pentamode materials. The V-Cell external boundary can be described with only one parameter, such as the lattice parameter η. In Figure C.5 are shown several Wigner-Seitz unit-cells for different lattice parameters η, denoted from now on as the shape parameter. For $\eta = \sqrt{3}$, the unit-cell is a regular hexagon, while for $\eta = 1$, it is a square.

From the previous consideration, an isotropic pentamode material should be represented by a regular hexagon defined for the shape parameter $\eta = \sqrt{3}$.

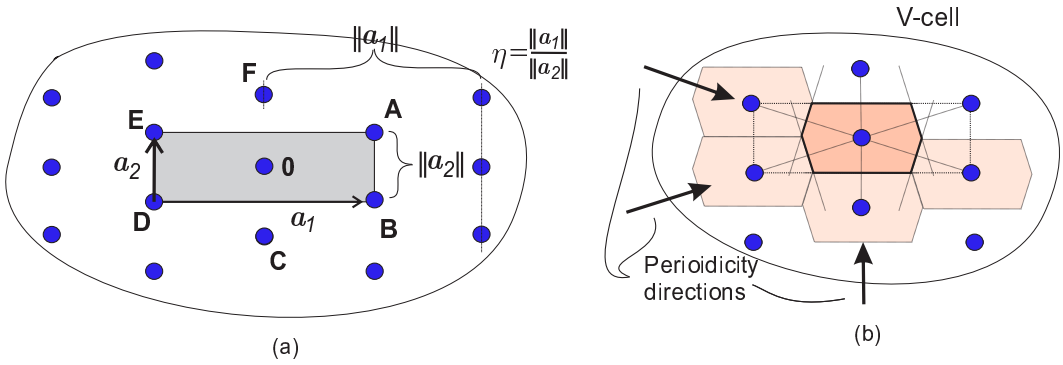

Figura C.4: a) Crystal system with orthorhombic symmetry D_2. The associated centered rectangular Bravais lattice has the primitive orthogonal vectors $\mathbf{a}_1$ and $\mathbf{a}_2$; b) Wigner-Seitz cells (V-Cells) inspiring the selection of the external boundary shape Γ_μ of the unit-cell used for designing the pentamode material. The vectors indicating the periodicity directions are depicted.

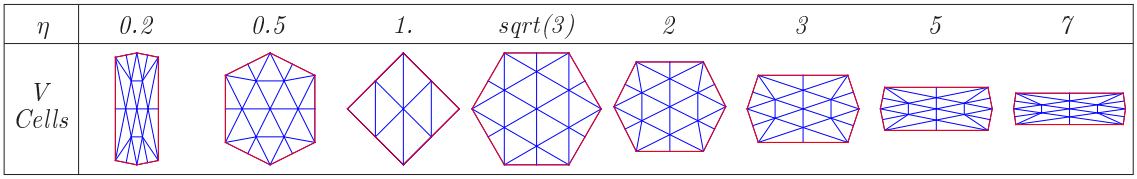

Figura C.5: Wigner-Seitz cell (V-Cell) for different shape parameters η.

3.3. Validation of the design methodology based on topology optimization

The algorithm presented in Appendix 6 is validated and assessed through analytical and numerical solutions taken from Sigmund Sigmund (2000). The proposed problem for this assessment consists in designing the micro-structure topology of an extremal isotropic two-phase material displaying the maximum ratio $\hat{\kappa}/\hat{G}$, where $\hat{\kappa}$ and $\hat{G}$ are the effective bulk and shear moduli of the composite. Sigmund has solved this problem and obtained several micro-structures using a topology optimization tool based on SIMP.

Before presenting the results, a-priori analytical estimations of the bounds for the effective elastic properties of an isotropic composite are discussed. The analyzed composite is constituted by two-phases and bounds, for this kind of composites, have been determined by Hill and successively improved by by Hashin-Shtrikman, Walpole (1966) and Cherkaev y Gibiansky (1993). According to the notation utilized by Cherkaev et al., the effective elasticity tensor of a plane strain

elastic isotropic material (using Voigt notation for tensors) can be written as:

$$\hat{\mathbf{C}}^e = \begin{bmatrix} \hat{K}+\hat{G} & \hat{K}-\hat{G} & 0 \\ \hat{K}-\hat{G} & \hat{K}+\hat{G} & 0 \\ 0 & 0 & \hat{G} \end{bmatrix} \quad , \qquad \hat{K} = \hat{\kappa} + \hat{G}/3 \; , \tag{C.14}$$

where, as indicated above, $\hat{\kappa}$ and $\hat{G}$ are the effective bulk and shear moduli of the material, and $\hat{K}$ is the plane strain effective bulk modulus. The Hashin-Strikman bounds for a plane elastic isotropic composite with two phases, identified in the following with the numbers 1 and 2, having volume fractions f_1, f_2 and being characterized by the bulk moduli κ_1 and κ_2 and shear moduli G_1 and G_2, respectively, satisfying $\kappa_1 > \kappa_2$ and $G_1 > G_2$, are:

$$K_{HS}^{low} = K_2 + \frac{f_1}{\frac{1}{K_1-K_2} + \frac{f_2}{K_2+G_2}} \quad ; \quad K_{HS}^{upp} = K_1 + \frac{f_2}{\frac{1}{K_2-K_1} + \frac{f_1}{K_1+G_1}} \quad ; \tag{C.15}$$

$$G_{HS}^{low} = G_2 + \frac{f_1}{\frac{1}{G_1-G_2} + \frac{f_2(K_2+2G_2)}{2G_2(K_2+G_2)}} \quad ; \quad G_{HS}^{upp} = G_1 + \frac{f_2}{\frac{1}{G_2-G_1} + \frac{f_1(K_1+2G_1)}{2G_1(K_1+G_1)}}. \tag{C.16}$$

Then, the effective plane strain bulk and shear moduli, $\hat{K}$ and $\hat{C}$, of the composite satisfies:

$$K_{HS}^{low} \leq \hat{K} \leq K_{HS}^{upp} \qquad ; \qquad G_{HS}^{low} \leq \hat{G} \leq G_{HS}^{upp}. \tag{C.17}$$

Next, let us consider the case studied by Sigmund consisting in finding the micro-structure that provides the maximum possible ratio $\hat{\kappa}/\hat{G}$, agreeing with the analytical estimations of these bounds. In the analysis of Sigmund, here reproduced, both phases are characterized by $K_1 = 5/7$; $K_2 = K_1/20$; $G_1 = 5/13$; $G_2 = G_1/20$ (units of moduli are given in GPa), with the volume fraction $f_1 = 0.5$. Then, the bounds (C.15)–(C.16) result in $K_{HS}^{low} = 0.0830$, $K_{HS}^{upp} = 0.2235$, $G_{HS}^{low} = 0.0439$, $G_{HS}^{upp} = 0.1157$. These bounds are represented in Figure C.6-a coinciding with the green external box. In the same Figure, the curve corresponding to the improved lower limit bound, found by Cherkaev y Gibiansky (1993) has been plotted. The Walpole point is denoted by W_p and has also been plotted in the same Figure. In accordance with these improved bounds, the W_p point determines the maximum ratio $\hat{\kappa}/\hat{G}$ that can be attained with this type of two-phase composite. For the considered composite, the coordinates of the W_p point are $\hat{K}_{W_p} = \hat{K}_{HS}^{upp} = 0.2235$ and

$$G_{W_p} = G_2 + \frac{f_1}{\frac{1}{G_1-G_2} + \frac{f_2(K_1+2G_2)}{2G_2(K_1+G_2)}} = 0.0503 \; . \tag{C.18}$$

Therefore, from (C.14), the effective elasticity tensor of the two-phase composite associated to the W_p point is:

$$\mathbf{C}_{W_p} = \begin{bmatrix} 0.2738 & 0.1732 & 0 \\ 0.1732 & 0.2738 & 0 \\ 0 & 0 & 0.0503 \end{bmatrix}. \tag{C.19}$$

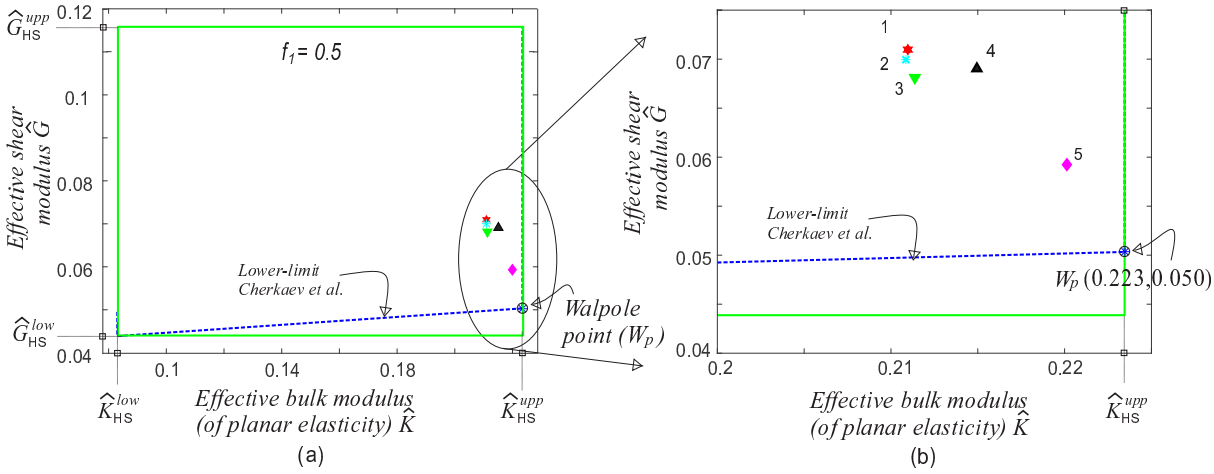

Figura C.6: Bounds of effective properties for a two-phase isotropic composite according to Hashin-Shtrikman and Cherkaev et al. Properties of phases 1 and 2 are $K_1 = 5/7$; $K_2 = K_1/20$; $G_1 = 5/13$; $G_2 = G_1/20$ (units of moduli in GPa). Volume fraction of phase 1 is $f_1 = 0.5$. The Walpole point is denoted by W_p. Symbols indicate the effective properties of five microstructures obtained with the topology optimization algorithm.

Procedure for designing the extremal material

The problem (C.13), constrained by the condition $f_1 = 0.5$, determines the optimal microstructure topology whose homogenized elasticity tensor, $\mathbf{C}^{hom}$, matches the target elasticity tensor: $\hat{\mathbf{C}} = \mathbf{C}_{W_p}$ of expression (C.19). This topology optimization problem is solved with the algorithm described in Boxes 1 and 2 of Appendix 6. The constraint fixing the volume fraction is imposed to the problem (C.48) through an augmented lagrangian technique reported in Ferrer et al. (2016) and Giusti et al. (2016).

Because the target elasticity tensor is isotropic (symmetry $O(2)$ according to Auffray y Ropars (2016)), the original domain where the topology optimization algorithm is computed, is the regular hexagon shown in Figure C.7. Note that the Wigner-Seitz unit-cell of a Bravais lattice with symmetry $O(2)$ is also a regular hexagon. Additionally, symmetry of the material distribution within the hexagonal unit-cell is imposed by forcing a reflection symmetry of the level-set function respect to the symmetry axis 1-1', 2-2' and 3-3' shown in Figure C.7-a. The symmetry is forced in every iteration of the algorithm, after computing (C.49) in Loop A of Box 2 and before the normalization of ψ^{i+1}.

Results and discussion

Figure (C.7) shows the micro-structures 1 to 5 that have been obtained with this methodology, using different initializations procedures.

Let us consider the obtained homogenized elasticity tensor corresponding to structure 5:

$$\mathbf{C}_5^{hom} = \begin{bmatrix} 0.279 & 0.161 & 0.000 \\ 0.161 & 0.279 & 0.000 \\ 0.000 & 0.000 & 0.059 \end{bmatrix}. \tag{C.20}$$

The effective parameters $\tilde{G} = C_{33}$ and $\tilde{K} = C_{11} - \tilde{G}$, computed from (C.20), are plotted in Figure C.6. The present approach gives a relative difference of 17 % between $\mathbf{C}_{W_p}(3,3)$ and $\mathbf{C}_5^{hom}(3,3)$. The micro-structures 5 is notoriously similar to that obtained by Sigmund utilizing the SIMP technique.

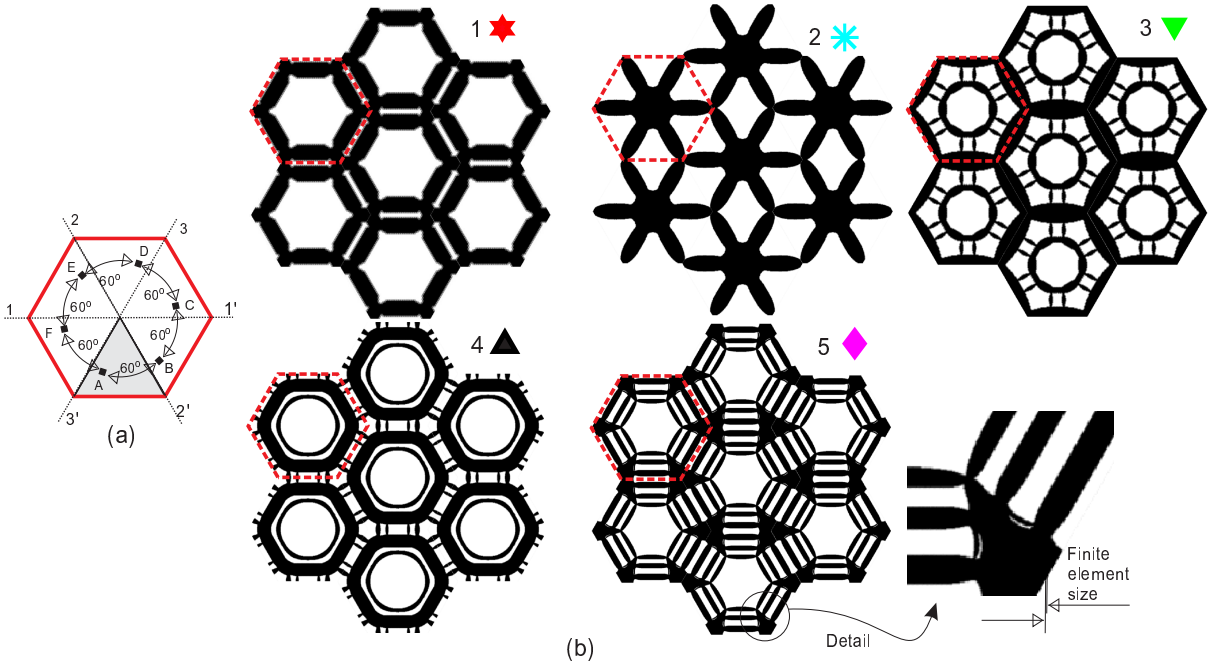

Figura C.7: a) The material distribution within a unit-cell has reflection symmetry with the symmetry axes being 1-1', 2-2' and 3-3'. b) Micro-structures obtained with the algorithm of Boxes 1 and 2 (Appendix 6). Elements with negative values of the level set function are in black and show the position where phase M1 is placed.

4. Design of the pentamode material for acoustic cloaking

By adopting the analytical results of Gokhale et al. (2012), shown in Appendix 6, we design the micro-structure of a highly anisotropic pentamode metamaterial used as a layer for diminishing

the acoustic wave scattering caused by a cylinder immersed in fluids.

4.1. Problem description

A sketch of the addressed problem is shown in Figure C.8. The layer covering the cylinder of radius $r = a$ has a thickness which is identical to the cylinder radius ($b = 2a$). The mapping $f(r)$, defining the coordinate transformation in Norris's analysis, is given by equation (C.10) (see also Appendix 6) with the parameter $\delta = 0.333a$. With this parameter, the effective scattering cross section area of the cloaked object has to be similar to that produced by a bare cylinder of radius $a_r = \delta = 0.333a$.

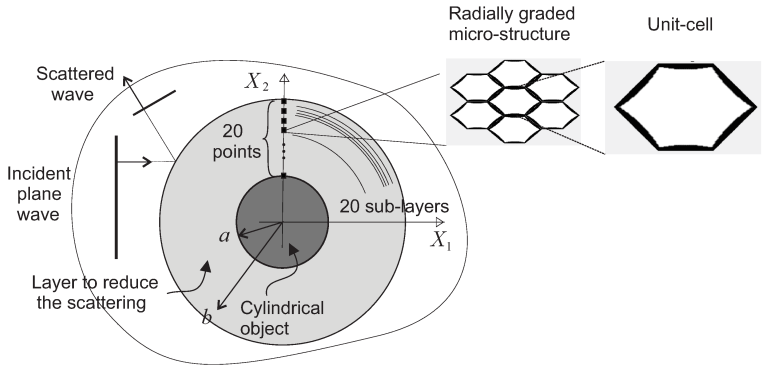

Figura C.8: Scattering reduction layer.

We design 20 unit-cells of the graded layer in correspondence with the same quantity of radial points equally spaced between $r = a$ and $r = b = 2a$. We assume that the graded layer is composed of 20 uniform sub-layers which micro-structures are designed with those 20 cells.

The stiff phase of the synthesized material (material M1) is assumed to be aluminum with properties $\kappa_{Al} = 70.GPa$, $G_{Al} = 25.5GPa$ and $\rho_{Al} = 2700.Kg/m^3$. The soft phase (material $M2$) is assumed to be a flexible polymer foam characterized by an isotropic material whose elastic modulus has a contrast factor $\gamma = 0.00001$ times the elastic modulus of the aluminum (taken from Ashby (2005), pp.51).

4.2. General design procedure

The procedure guiding the design of the micro-structures of each sub-layer aims to satisfy point-wise the following two conditions:

i) The effective elasticity tensor $\mathbf{C}^{hom}$ of the synthesized composite matches the target tensor $\hat{\mathbf{C}}$ defined in (C.11) for the corresponding sub-layer. Note that this tensor is described in the coordinate system whose basis is: ($\mathbf{e}_r$, $\mathbf{e}_\theta$).

ii) The effective inertial mass density ρ^{hom} of the same unit-cell matches the target inertial mass density $\hat{\rho}$ defined by equation (C.9).

Both goals can be attained in two sequential steps. The first step searches the optimal distribution of phase M1 satisfying the objective described in task *i)* without imposing the density constraint. This problem is formulated as a topology optimization problem and solved with the algorithm of Appendix 6. The solution provides a homogenized density ρ^{OT} which is assumed to satisfy $\rho^{OT} < \hat{\rho}$. This is a reasonable assumption which can be satisfied by taking an enough high ratio E_1/ρ_1 of the material M1 (aluminum in this case).

In a second step, the micro-cell density is adjusted to $\hat{\rho}$. This objective is attained by filling the holes (soft phase) with a composite constituted by the phase M1 dispersed in the phase M2. In this case, the disperse dense material does not work as a structural component and the effective elasticity is not substantially modified. We assume that the second step can be easily solved. Therefore, in the following, we only address the topology optimization problem associated with the first step.

A similar design procedure in two sequential steps has been reported by Kadic et al. (2014). To build a pentamode material, these authors have independently adjusted the effective bulk moduli in a first stage, and then, the effective inertial mass density. Additionally, they have proven the fabricability of the so-designed metamaterial by manufacturing small samples.

4.3. Technique for adjusting the anisotropic bulk moduli

The external boundary Γ_μ delimiting the domain Ω_μ, in where the topology optimization problem is posed, has to be known in advance. Due to the symmetry of the target tensor $\hat{\mathbf{C}}$ (orthotropic symmetry D_2), V-Cells with given shape parameters η are chosen. In each case, η is adjusted for each sub-layer of the 20 designed cells.

Influence of the shape parameter η on the resulting micro-structures

To better understand the role played by the selection of Γ_μ and the shape parameter η in the present design technique, we study the influence of this parameter on the obtained micro-structure solution.

Sub-layer number 15 of the acoustic cloaking device is chosen to perform this study. For this

sub-layer, the target elasticity tensor $\hat{\mathbf{C}}$ is given by the expression (see equation (C.11)):

$$\hat{\mathbf{C}} = \begin{bmatrix} 5.893 & 2.250 & 0 \\ 2.250 & 0.859 & 0 \\ 0 & 0 & 0 \end{bmatrix}. \tag{C.21}$$

V-Cell geometries, as shown in Figure C.4, are tested. Then, the optimal solutions of problem (C.13) are sought by varying the parameter η in the range: $1 \leq \eta \leq 8$.

In Figure C.9-a, the optimal value of $\mathcal{J}$ attained for different parameters η are plotted. Two finite element meshes are solved. Results obtained with the coarse mesh (with $m_{max} = 3$ and $h_0^e = \ell_{UC}/32$) are denoted by (CM), while those obtained with the finest one, $m_{max} = 4$, are denoted by (FM). We recall that m_{max} defines the number of mesh refinements and h_0^e is the initial finite element mesh size. Both parameters have been defined in Box 1 (Appendix 6). The finite element size of the finest mesh is half of that of the coarse mesh.

In the same Figure, the effective elasticity tensor component C_{33}^{hom} and the homogenized inertial mass density ρ^{OT} of the designed cell (Figures C.9-b and c, respectively) are also plotted. We recall that the effective densities plotted in Figures C.9-c, are the results of the topology optimization problem (C.13) without imposing a density constraint.

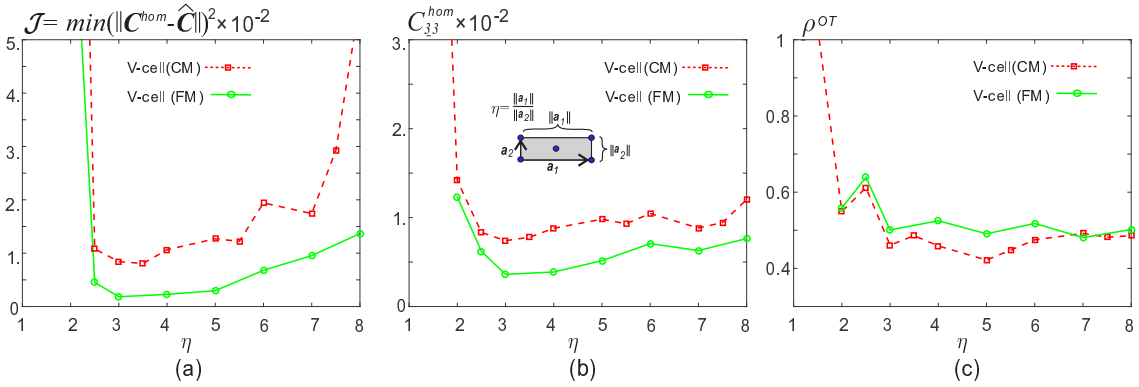

Figura C.9: Two set of solutions attained with finite element mesh refinement, CM and FM denote coarse and fine mesh, respectively. V-Cells are characterized with the shape parameter η: a) optimal attained value of $\mathcal{J}$ defined in problem (C.13); b) Shear stiffness C_{33} of the effective attained elasticity tensor; c) effective attained inertial mass density ρ^{OT}.

Results in Figure C.9 show a rather sensitive response with respect to changes of the shape parameter η. The minimal shear modulus C_{33}^{hom} and the minimal objective function value $\mathcal{J}$ are attained in the range $3 \leq \eta \leq 5$. Also, note that in the same range of η, the effective inertial mass density is almost constant around $\rho^{OT} = 0.5$.

It is noted that the correct capturing of the effective shear modulus of the sub-layer, represented

by the term C_{33}^{hom}, is crucial to get a good response of the cloaking device. According to Norris's analysis, this term has to be zero.

Figure C.10 displays the micro-structures and the corresponding effective elasticity tensors obtained as solution of the topology optimization problem computed with four V-Cell geometries. In all cases, except in the result with $\eta = 2$, we have obtained good agreement between $\mathbf{C}^{hom}$ and the target tensor defined in expression (C.21).

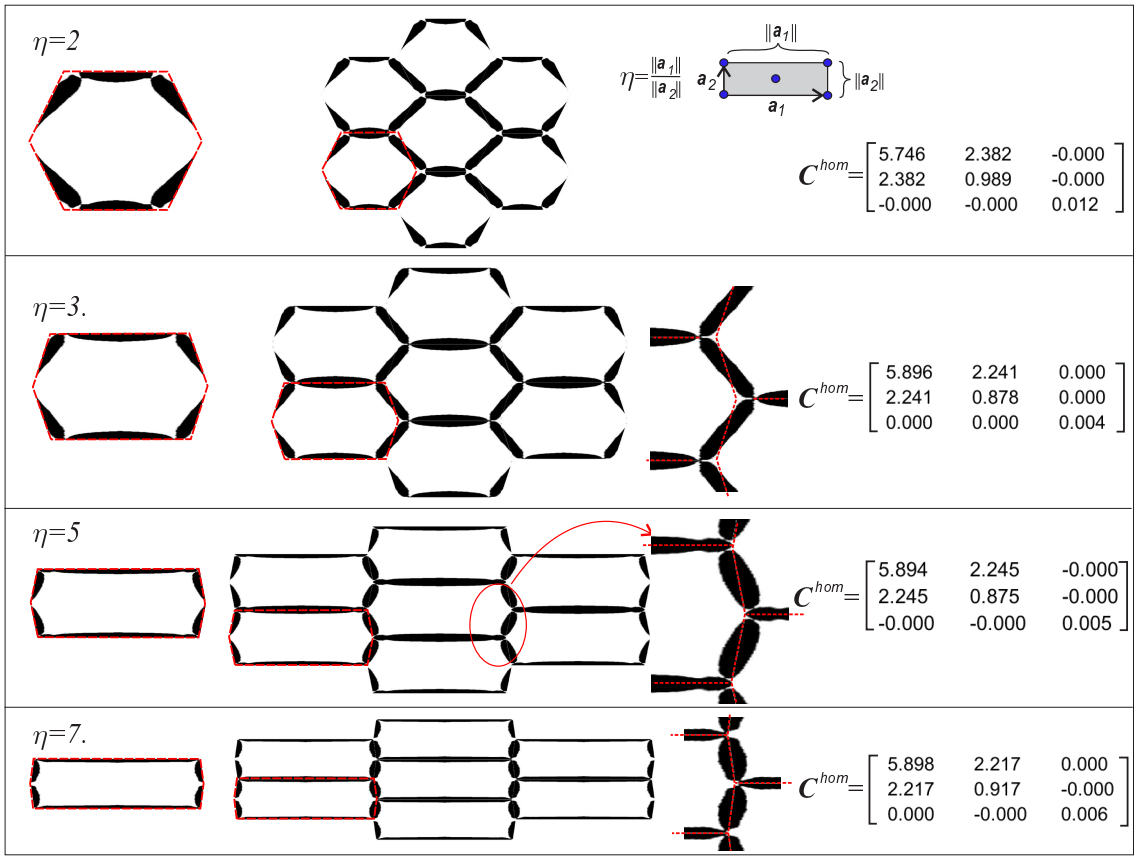

Figura C.10: Microstructures for sub-layer number 15 obtained with V-Cells (FM) and varying the shape parameter η. The first column displays the unit-cells and the solutions provided by the topology optimization algorithm. The second column displays the resulting micro-structures obtained by the spatial repetition of the computed unit-cell. The third column (cases with $\eta = 3, 5$ and 7) displays details of the joints between needle-like members. The last column shows the computed effective elasticity tensors.

Conclusions of the study about the influence of η on the microstructure design are summarized as follows:

- As the finite element mesh is refined (m_{max} is increased), better solutions to problem (C.13) are obtained. However, the crucial conclusion is that the shape of Γ_μ is of paramount importance to obtain good solutions. Tests conducted with rectangular unit-cell shapes, using different slenderness ratios, yield unsatisfactory results.

- From Figure C.9, the range of parameters $3 \leq \eta \leq 5$ provides good approaches to the solution of the topology optimization problem. Notably, however, geometries defined with

$\eta < 2.5$, that correspond to squares or regular hexagons, are excluded from the admissible configurations and must be avoided.

- There are several micro-structure architectures providing effective elasticity tensors $\mathbf{C}^{hom}$ approaching the target one. It is the case of the microstructures depicted in Figure C.11. Then, it can be concluded that the problem (C.13) has not a unique solution and that several material architectures are admissible for the present acoustic cloaking device.

- In most cases observed in Figures C.10, the external boundaries of the V-Cells do not coincide well with the hexagonal cells displayed by the obtained honeycomb-like micro-structures. For example, for the microstructures depicted in Figure C.11, we have detected that for $\eta \approx \hat{C}_{11}/\hat{C}_{22} \approx 7$ (Figure C.11-b), the V-Cell captures almost exactly the geometry of the basic cell. However, this configuration does not lead to the better solution. The best solution is obtained for $\eta \approx 3.75$ (Figure C.11-a).

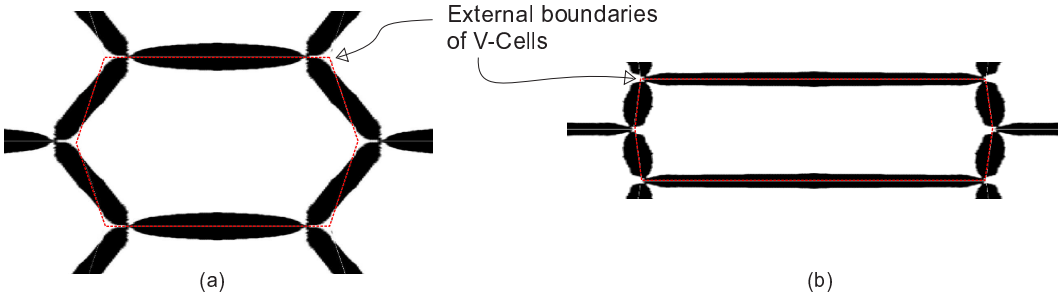

Figura C.11: Two possible micro-structures for sub-layer 15 obtained with V-Cells characterized with the shape parameters: a) $\eta = 3$ and b) $\eta = 7$.

4.4. Results of the designed acoustic cloaking device

From the exposed conclusions in the previous sub-Section and in order to avoid a similar study for the 20 sub-layer designs, we solve these topology optimization problems by adopting V-Cell geometries whose shape parameters are defined through a relation depending on the coefficients of the target elasticity tensor, as follows:

$$\eta = \sqrt{3}\left(1 + 0.2\frac{\hat{C}_{11} - \hat{C}_{22}}{\hat{C}_{22}}\right) .$$

This criterion is taken by considering the following empirical rules: for an isotropic pentamode material, with $\hat{C}_{11}/\hat{C}_{22} = 1$, the V-Cell should be a regular hexagon defined by $\eta = \sqrt{3}$. While for $\hat{C}_{11}/\hat{C}_{22} \approx 6.9$, that corresponds to the sub-layer 15 studied in the previous sub-Section, the V-Cell should be defined by $\eta = 3.75$, which has proven to give the most optimal solution.

Figure C.12 shows the micro-structures of sub-layers 1, 5, 10, 15 and 20, obtained with this procedure. The second column displays details of the synthesized micro-structures such as the needle-like members and joints. The third column shows the effective elasticity tensors $\mathbf{C}^{hom}$ and densities ρ^{OT} compared with the target elasticity tensors $\hat{\mathbf{C}}$ and target densities $\hat{\rho}$ for these sub-layers.

As commented above, the solutions for the 20 cells provide homogenized mass densities which are lower than the ones required by Norris's analysis. Therefore, in the validation test of next Section, we assume that these densities could be exactly adjusted to the target values.

Figure C.13 plots the effective properties κ_r^{hom}, κ_θ^{hom} and C_{33}^{hom} for the synthesized 20 sub-layers.

5. Scattering performance assessment of the designed layer

The performance of the metamaterial designed with the technology of the previous Section, whose properties are plotted in Figure C.13, is next assessed in the following examples.

This performance is evaluated by studying the scattering wave field produced by a plane wave impinging on a cloaked cylindrical object immersed in an infinite fluid medium. The cloaking device being designed with a parameter $\delta = 0.333m$ has to affect the external wave field, outside the cloak region, as much as a bare cylindrical object of radius $a_r = 0.333m$. Then, the goal of the present validation test consists in comparing the scattered wave field for both cases.

Considering the excessively high computational cost required by a detailed DNS simulation (Direct Numerical Simulation) of this problem including the modeling of the material micro-structure and its interaction with the fluid, we simulate a simplified verification test. The acoustic cloaking device is modeled with 20, layers perfectly connected, made of elastic materials whose properties are identical to the effective ones determined with the design methodology of the previous Section.

Figure C.14 displays the pressure maps (real part) for several cases of the mentioned problem computed with an in-house finite element code. This code solves the wave equation problem in the frequency domain and utilizes a Perfectly Matched Layer (PML) technique for modeling the infinite domain of the fluid. Pressure maps in the Figure are the results of an incident plane wave, from the left. The wave frequency is $2.07Khz$ (angular frequency: $\omega = 1.3e4rad/s$) and the medium, across which the wave propagates, is water with a density $\rho_0 = 1000.Kg/m^3$ and a volumetric modulus $\kappa_0 = 2.25GPa$. The wave speed in this medium is $c_0 = 1500.m/seg$ and the wave number for this frequency is $k = \omega/c_0 = 8.67rad/m$ with a wavelentgth $\lambda = 2\pi/k = 0.72m$. The analyzed domain has a size of $10.m \times 10.m$.

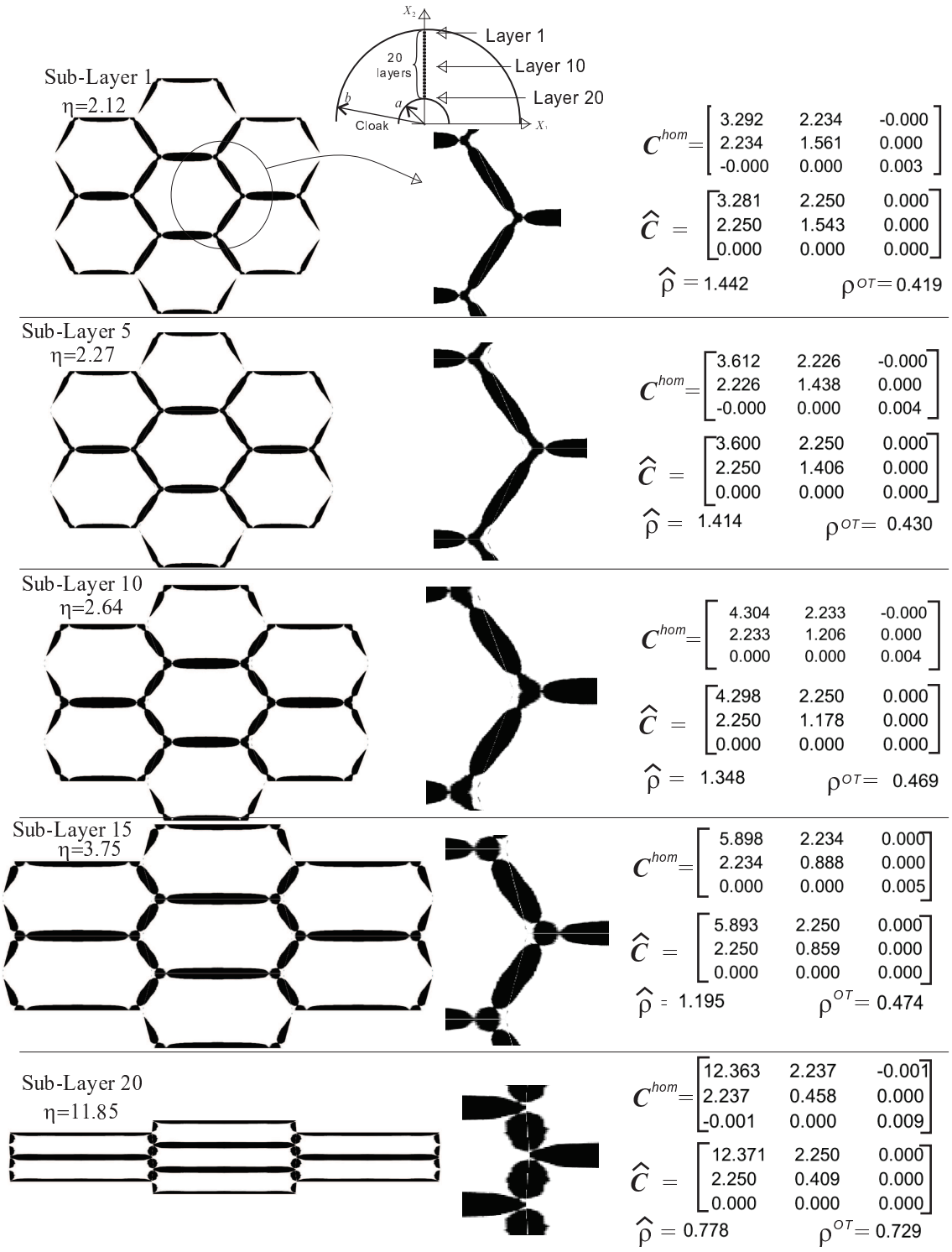

Figura C.12: Solutions obtained with the topology optimization algorithm for several sub-layers of the acoustic cloaking device. $\mathbf{C}^{hom}$ and ρ^{OT} are the effective elasticity tensors and homogenized densities of the micro-cells obtained with the topology optimization algorithm. $\hat{\mathbf{C}}$ and $\hat{\rho}$ are the target effective elasticity tensors and densities according to Norris's analysis.

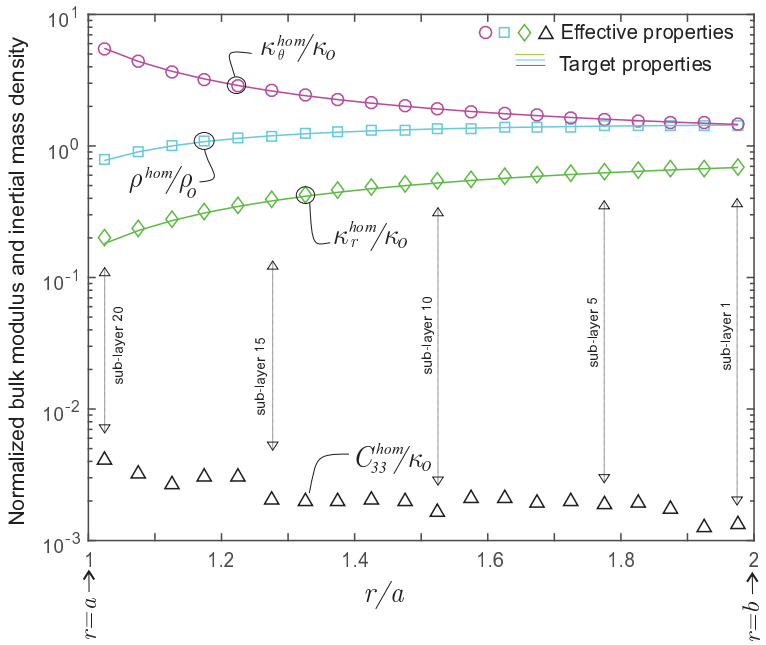

Figura C.13: Normalized effective properties of the 20 sub-layers obtained with the topology optimization algorithm. The bulk moduli κ_r^{hom} and κ_θ^{hom}, the inertial mass densities ρ^{hom} and shear moduli C_{33}^{hom} are shown in symbols. Curves in line are the analytical expression taken from Figure C.2.

Solutions are computed and compared for different cases:

i) object with perfect cloak designed according to analytical results of Norris;

ii) bare object of radius $a = 1.m$;

iii) object of radius $a = 1.m$ with the cloaking device designed in accordance with the topology optimization technique and the parameter $\delta = 0.333m$;

iv) bare object of radius: $a_r = 0.333m$.

We recall that the external domain solution of case *iii)* should mimic the solution of case *iv)*.

In order to quantitatively compare the solutions presented in Figure C.14, the effective cross section areas are computed in the last three cases. Let us consider again a plane wave traveling from left to right in a free infinite medium with a vertical wavefront. The pressure response in the time domain $(\mathbf{X}, t)$ can be expressed by:

$$p^i(\mathbf{x}, t) = p_0 \exp\left(i(\mathbf{k} \cdot \mathbf{X} - \omega t)\right) \tag{C.22}$$

where, recalling that k is the wave number, $\mathbf{k} = k\mathbf{e}_x$ is the wave vector, and $\mathbf{e}_x$ is the unit vector in the horizontal direction. The rigid cylindrical object of radius $a = 1.m$ is placed at $\mathbf{X} = \mathbf{0}$. The cloak occupies the space $\Omega = \{\mathbf{X} \mid 1.m \leq \|\mathbf{X}\| \leq 2.m\}$. The object produces a scattered wave field which, at large distances from the cylinder, can be assumed as spherical wave field centered

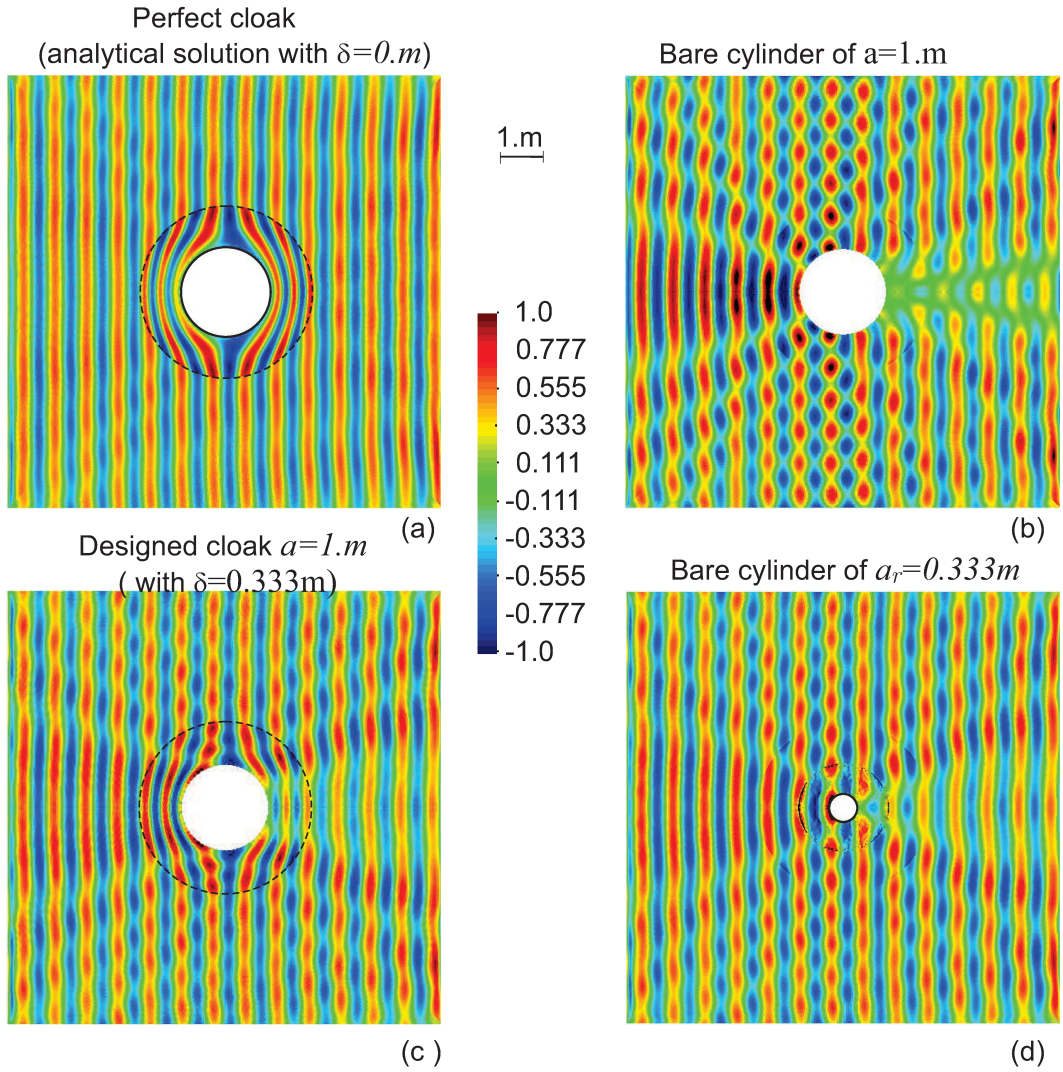

Figura C.14: Pressure maps (real part) of an incident plane wave problem. Domain size: $10.m \times 10.m$, wave angular frequency: $\omega = 1.3e4rad/s$. a) Solution of the cylinder with radius $a = 1m$ and perfect cloaking (parameter $\delta = 0.m$). The material properties of the cloak are given by Norris's analysis in Appendix 6; b) solution with a bare cylinder of radius $a = 1.m$; c) cylinder of radius $a = 1m$ with the designed acoustic cloaking using the parameter $\delta = 0.333m$; d) solution with a bare cylinder of radius $a_r = 0.333m$.

at $\mathbf{X} = \mathbf{0}$. The pressure field, $p(\mathbf{X}, t)$, resulting from the incident and scattered waves is computed in the frequency domain with the finite element code. By considering that $p_w(\mathbf{X})$ denotes the amplitude of the pressure field in the frequency domain, the effective cross section area (per unit of thickness) of the object is evaluated as follows:

$$\sigma^{eff} = \int_{\mathcal{S}} \frac{(\Delta p_w)(\Delta \bar{p}_w)}{p_w^i \bar{p}_w^i} d\mathcal{S} \qquad ; \qquad \Delta p_w(\mathbf{X}) = p_w(\mathbf{X}) - p_w^i(\mathbf{X}) \tag{C.23}$$

where the integration curve $\mathcal{S}$ is a circle of radius $r = 4.5m$ and the symbol $(\bar{\cdot})$, over both terms in the integrand, represents the complex conjugate of the magnitude.

Figure C.15-a depicts, in a polar plot, the integrand value of expression (C.23) along the curve $\mathcal{S}$ as a function of the angular position θ. Three curves corresponding to cases *ii)*, *iii)* and *iv)* are shown. Figure C.15-b depicts a zoom of the polar plot in where only the case *iii)* and *iv)* are shown. Note that the cloaked cylinder of radius $a = 1$ generates a scattered wave field, with notably lower values of the integrand term if compared with the bare cylinder of the identical radius. Furthermore, the integrand value distribution is qualitatively identical to that produced by a significantly smaller object.

Figure C.15-c plots the effective cross-section areas (per unit of thickness of the object) for the three cases: *ii)*, *iii)* and *iv)* and different frequencies of the incident plane wave. These results quantify the capability of the designed cloak at different wave frequencies. They confirm that, in a wide range of frequencies, the cloaking device is almost insensitive to this variable.

5.1. Modal analysis of a micro-cell

Considering that the micro-structure of the designed material consists of slender bars with a filler polymer possessing a very low stiffness and a dense disperse phase, it is necessary to guarantee that the lower eigenfrequencies of the unit-cell are much higher than the frequency of the sound wave. This requirement should be satisfied to guarantee that the static homogenization analysis, implicitly considered in this paper, is a valid assumption of the model and that the natural frequencies of the cloak do not interfere the sound wave.

The unit-cell eigenfrequencies increase with the inverse of the cell size. Therefore, it can be guaranteed that the above requirement is satisfied for small enough cell sizes. The maximum cell size of the designed pentamode material is limited by the acoustic wavelength and by the thickness of the layers in which the cloaking device is divided. The shortest wavelength in the analysis of Figure C.15 is $0.25m$ and the layer thickness, by assuming an identical value for all layers, is $0.05m$.

In view of the above discussion, the modal analysis of the unit-cell of layer 1 is subsequently

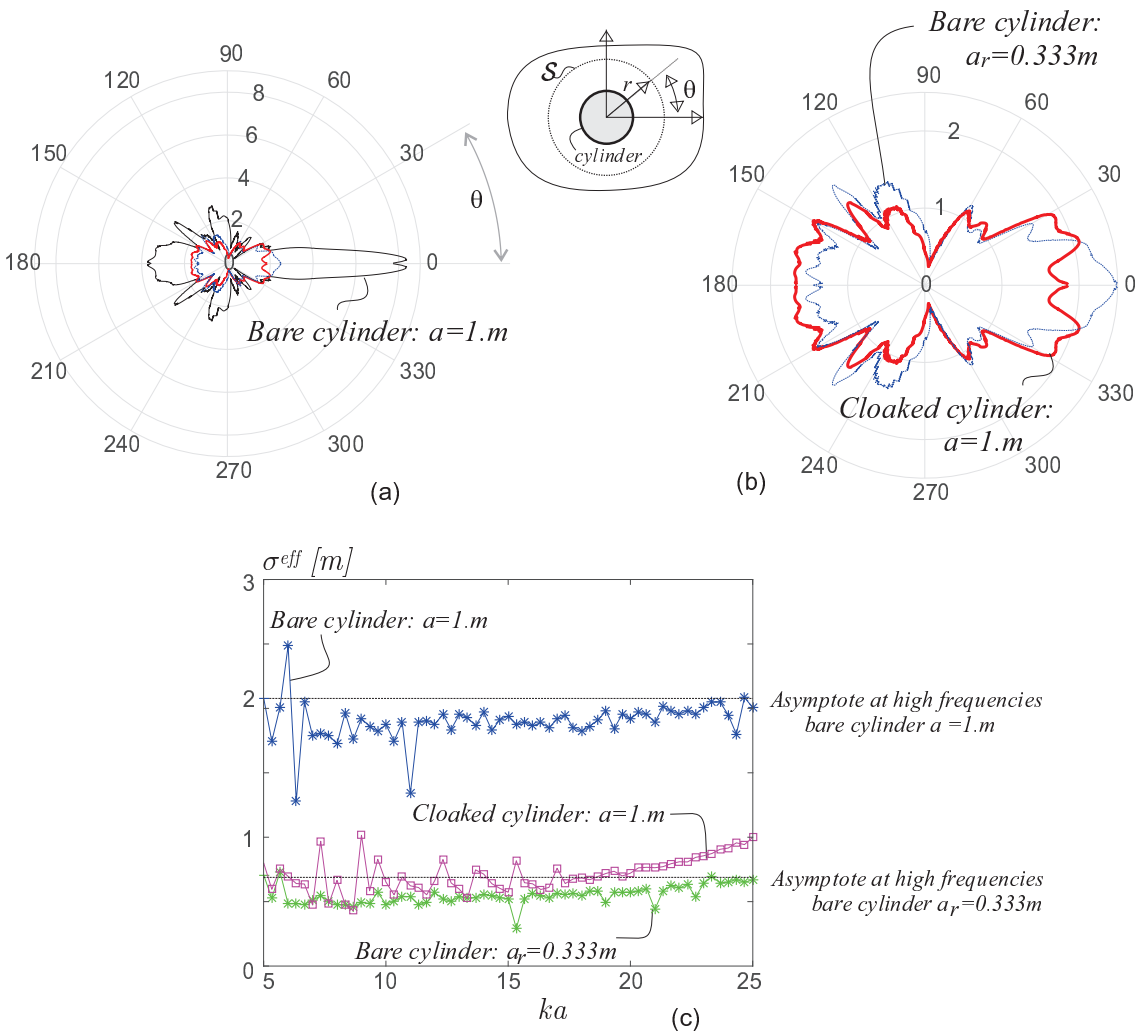

Figura C.15: a) Polar plots of the integrand in (C.23) corresponding to the cases: *ii)*, *iii)* and *iv)*; b) zoom of the polar plot shown in (a) displaying the cases *iii)* and *iv)*; c) Effective cross-section areas (per unit of thickness) for cases *ii)*, *iii)* and *iv)* computed for different wave numbers of the incident wave.

performed. In the context of evaluating minimal eigenfrequencies of the designed micro-structures, this layer is the most compromised one. Figures C.16-a and b show the finite element model of the analyzed cell and the adopted geometrical dimensions. A characteristic cell size of $0.01m$ is arbitrarily chosen. Two cases are solved. In the first one, the polymer, as well as the dynamical effect of the disperse phase are neglected. In the second case, all the components are considered.

In accordance with the cell designed for layer 1, in Figure C.16, the density provided by the solution of the topology optimization algorithm is $\rho^{OT} = 389.kg/m^3$. The target density is $\hat{\rho} = 1442.kg/m^3$. Therefore, by taking a polymer density $\rho_{Pol} = 20.Kg/m^3$ and the aluminum density $\rho_{Al} = 2700.kg/m^3$, the target density $\hat{\rho}$ is get by dispersing a volume fraction $f_{Al} = 0.2642$ of aluminum into the polymer. The disperse aluminum phase is modeled by assigning the aluminum properties to finite elements randomly placed into the space which is originally occupied by the polymer, until the required volume fraction is reached. Therefore, due to the fact that the cell volume is $1.06e-4m^2$ and the number of finite elements is 11911, the mean size of the aluminum particles used in the analysis is $8.9e-09m^2$.

Periodic boundary conditions are imposed to the finite element model of the unit cell Note that the acoustic wavelengths are much larger than the cell size.

The obtained results in both cases are: a) the lower eigenfrequency when the polymer and disperse phase is neglected is $79kHz$. b) the lower eigenfrequency when the polymer and disperse phase is taken into account is $75kHz$. Then, both frequencies result much higher than the sound wave frequencies considered in the analysis of the previous sub-Section.

The eigenmode related to the lower eigenfrequency for the case a) is depicted in Figure C.16-c.

These results confirms that, for cell sizes smaller than $0.01m$, the homogenization static analysis followed in this paper is a valid assumption.

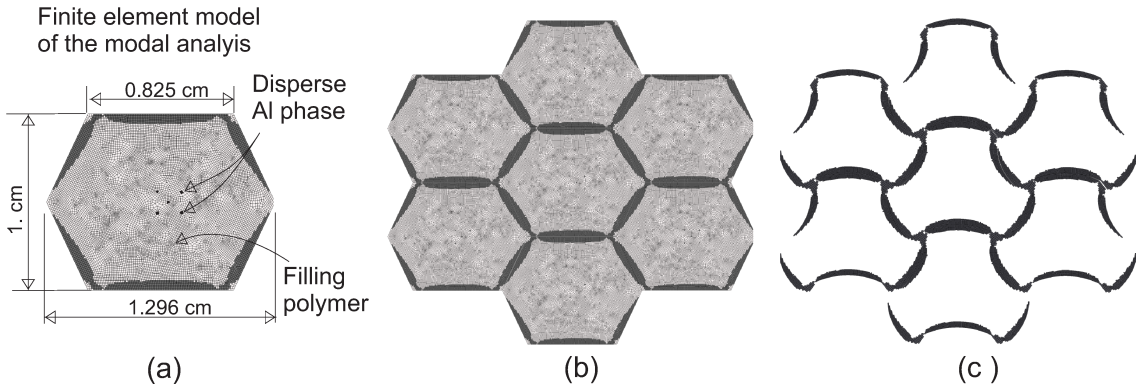

Figura C.16: Modal analysis of the unit cell taken from layer 1 of the cloaking device. a-b) Finite element model. c) Eigenmode corresponding to the lower eigenfrequency when polymer and disperse phase effects are neglected.

6. Conclusions

The results presented in this work show the viability of using topology optimization techniques based on topological derivative to design the micro-structures of a graded layer for acoustic cloaking devices. The manufacturing feasibility of such layers, employing available materials, has been already proven.

To attain such results, it has been imperative to properly select a unit-cell geometry where the topology optimization problem is posed. In this sense, it has been shown that the material symmetry can be properly exploited to solve this issue. The presented study has provided additional ingredients to understand the influence of the unit-cell external shape on the results obtained with the optimization algorithm. From this study, it has been proven that solutions strongly depend on this variable, and that square or regular hexagonal shapes have to be discarded in several cases.

The validation test proves the effectiveness of the synthesized composite for satisfying the target proposed for the cloaking device. This virtual test shows a significant decrease of the scattered wave power produced by the immersed cloaked object. The pattern of the scattered wave agrees acceptably well with the ideal case of an immersed bare object with reduced dimensions.

An additional conclusion refers to the wide range of metamaterial design problems in which this type of framework can be applied. The most promising application field is related to metamaterial design problems whose micro-structure architecture cannot be conjectured beforehand. Typical cases are the design of: *i)* extreme materials with large negative Poisson ratios, *ii)* ultralight and ultra stiff metamaterials, *iii)* material for thermal flux manipulation, between others. Progress in the synthesis of ultralight and ultra stiff structures using this type of computational design tool has been presented by the authors in Podestá et al. (2016).

Finally, a potential improvement of this technology can be identified by introducing the notion of topological derivatives of anisotropic elastic materials. Some of the authors of this paper have recently published a work with contributions in this topic, see Giusti et al. (2016). This derivative, within the context of topology optimization, opens the possibility to design metamaterials through several length scales.

Acknowledgments

The authors acknowledge the financial support from CONICET and ANPCyT (grants PIP 2013-2015 631 and PICT 2014-3372) and from the European Research Council under the European Unions Seventh Framework Programme (FP/2007-2013) / ERC Grant Agreement N. 320815 (ERC Advanced Grant Project Advanced tools for computational design of engineering materials

COMP-DES-MAT). Oriol Lloberas-Valls gratefully acknowledges the funding received from the Spanish Ministry of Economy and Competitiveness through the “Juan de la Cierva” Postdoctoral Junior Grant: JCI-2012-13782 and the National Research Plan 2014: MAT2014- 60919-R.

Appendix C1: Linear acoustic theory and field transformation analysis

Let us consider a conventional acoustic wave problem propagating in a fluid medium at rest and placed in an homogeneous domain $\tilde{\mathcal{B}}$, see Figure C.1. In this medium, κ_0 denotes the time-averaged bulk modulus and ρ_0 denotes the time-averaged density. The disturbance produced by the wave motion superposed to the time-averaged fields are assumed small. Then, the linear acoustic wave equation in terms of the pressure field $P(\tilde{\mathbf{X}}, t)$ can be written as (Banerjee (2011)):

$$\ddot{P} - \kappa_0 \, \mathrm{div}_{\tilde{\mathbf{X}}}(\rho_0^{-1} \nabla_{\tilde{\mathbf{X}}} P) = 0 \, . \tag{C.24}$$

In the present description, $\tilde{\mathcal{B}}$ refers to the homogeneous space because the wave propagate with null scattering strength. $\tilde{\mathcal{B}}$ is also assumed as the reference space for the transformation to be defined in the following.

Following to Norris (2008), the form-invariance property of equation (C.24) is next exploited. Let us consider the physical space $\mathcal{B}$, where some object is immersed in the fluid, and the coordinate system $\mathbf{X}$ in $\mathcal{B}$. The physical space is mapped from the reference space through a coordinate transformation, $\mathbf{X} = \boldsymbol{\phi}(\tilde{\mathbf{X}})$, sketched in Figure C.17. The map $\boldsymbol{\phi}$ is assumed to be one-to-one and invertible, except at possibly one point in the domain $\Omega \subset \tilde{\mathcal{B}}$. The deformation gradient of $\boldsymbol{\phi}$ ($\boldsymbol{\phi} : \tilde{\mathcal{B}} \rightarrow \mathcal{B}$) is: $\mathbf{F} = \nabla_{\tilde{\mathbf{X}}} \boldsymbol{\phi}$.

Then, equation (C.24) can be re-written in the physical frame $\mathbf{X}$ by introducing the tensorial transformations of the differential operators: $\mathrm{div}_{\mathbf{X}}(\cdot)$ and $\nabla_{\mathbf{X}}(\cdot)$, in terms of $\mathrm{div}_{\tilde{\mathbf{X}}}(\cdot)$ and $\nabla_{\tilde{\mathbf{X}}}(\cdot)$. These tensorial transformations can be derived by introducing the deformation analysis, within the context of finite elasticity, described in the book of Ogden Ogden (1997). The resulting wave propagation equation in the physical domain is given as follows:

$$\ddot{p} - \kappa_0 J \, \mathrm{div}_{\mathbf{X}} \left((\rho_0 J)^{-1} \mathbf{V}^2 \cdot \nabla_{\mathbf{X}} p \right) = 0 \tag{C.25}$$

where $\mathbf{V}^2 = \mathbf{F}\mathbf{F}^T$, $J = \det(\mathbf{F})$ and the pressure in the physical space is denoted by $p(\mathbf{X}, t)$.

However, and following to Norris, a more general and adequate expression of the acoustic wave equation (C.24) in the physical space can be defined by introducing a second order symmetric tensor field $\boldsymbol{\Sigma}$, such that: $\mathrm{div}_{\mathbf{X}} \boldsymbol{\Sigma} = \mathbf{0}$. In this case, equation (C.25) can be equivalently rewritten

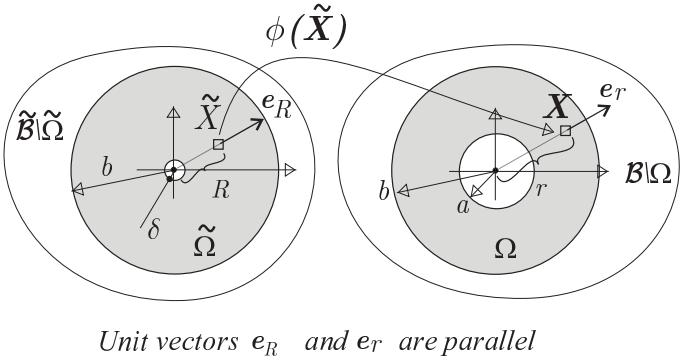

Figura C.17: Radially symmetric deformation map. Homogeneous ($\tilde{\mathcal{B}}$) and physical ($\mathcal{B}$) spaces.

as:

$$\ddot{p} - \kappa_0 J\boldsymbol{\Sigma} : \nabla_{\mathbf{X}} \left((\rho_0 J\boldsymbol{\Sigma})^{-1} \cdot \mathbf{V}^2 \cdot \nabla_{\mathbf{X}} p \right) = 0 \tag{C.26}$$

At every point of $\mathcal{B}$, it can be recognized the similar form displaying the pseudo-pressure wave equation (C.7), which represents an acoustic wave propagating across a pentamode material, and the acoustic wave equation (C.26) in the transformed space. Both equations can be made identical under the condition that the parameter of the geometrical transformations, given by the map ϕ in (C.26), are reinterpreted as being the heterogeneous properties of the pentamode material defined in Section 2. This condition is satisfied if the following constraints on the material properties are imposed point-wise:

i) $\mathbf{S} \equiv \boldsymbol{\Sigma}$,

ii) $\kappa^\star = \kappa_0 J$, and

iii) $\boldsymbol{\rho}^\star = \rho_0 J\boldsymbol{\Sigma} \cdot \mathbf{V}^{-2} \cdot \boldsymbol{\Sigma}$.

With this redefinition of the pentamode material properties in $\mathbf{X}$, the wave equation in $\mathcal{B}\backslash\Omega$ mimics the wave equation in the reference empty space $\tilde{\mathcal{B}}\backslash\tilde{\Omega}$.

C1.1. A radially symmetric deformation map for cylindrical object cloaking

Let us consider an acoustic wave propagating in a medium where a cylindrical object of radius a is immersed, as shown in Figure C.1-b. Our goal is to design the properties of the metamaterial filling the circular ring domain Ω, of thickness $b - a$, around the cylinder such that it acts as a cloaking for the object. In this way, the wave propagating at the exterior domain $\mathcal{B}\backslash\Omega$ is not affected by the object.

This goal can be reached by exploiting the results of the previous sub-Section. Let a radially

symmetric deformation map be given by:

$$\mathbf{X} = \boldsymbol{\phi}(\tilde{\mathbf{X}}) = \frac{r(R)}{R}\tilde{\mathbf{X}} \tag{C.27}$$

where R and r are the radial coordinates of two points: $\tilde{\mathbf{X}}$ and $\mathbf{X}$ ($R = \left\|\tilde{\mathbf{X}}\right\|$ and $r = \|\mathbf{X}\|$) in the reference and physical spaces, respectively, related through the map (C.27). The radial unit vectors in both spaces are defined by:

$$\frac{\mathbf{X}}{r} = \mathbf{e}_r = \mathbf{e}_R = \frac{\tilde{\mathbf{X}}}{R}\,; \tag{C.28}$$

The radial coordinate $r(R)$ is defined by the inverse function:

$$R = f(r) = \begin{cases} \left(\frac{b^2 - a\delta}{b^2 - a^2} r - \frac{a-\delta}{b^2-a^2} b^2 \frac{a}{r}\right); & a \leq r \leq b \\ r; & r \geq b \end{cases} \tag{C.29}$$

The interpretation of this deformation map is sketched in Figure C.17. This function transforms the circular ring domain $\tilde{\Omega}$, of thickness $b - \delta$, in another circular ring Ω, of thickness $b - a$, while the exterior domain $\mathcal{B}\backslash\Omega$ is identically mapped.

By considering a null parameter δ for this transformation, the map (C.27)-(C.29) is singular at the origin and the cylinder acoustic cloaking, associated with this transformation, is perfect. To avoid the singularity, we assume a value: $\delta > 0$. In this case, the effective cross-section of the immersed object is reduced if compared with that of the bare cylinder. Therefore, the device built with the so-idealized pentamode material work as a scattering reduction layer instead of as a perfect cloaking device.

The function (C.29) is taken from Gokhale et al. (2012) and, according to these authors, satisfies the criteria by which the cloaking material properties show minimal elastic anisotropy.

Further identities involving the gradient of deformation of $\boldsymbol{\phi}$ and the associated right stretch tensor are derived from (C.28) and (C.29) as follows:

$$\mathbf{F} = \frac{1}{f'(r)}\mathbf{I}_r + \frac{r}{f(r)}\mathbf{I}_\perp \quad ; \quad \mathbf{I}_r = \mathbf{e}_r \otimes \mathbf{e}_r \quad ; \quad \mathbf{I}_\perp = \mathbf{1} - \mathbf{e}_r \otimes \mathbf{e}_r; \tag{C.30}$$

$$J = \det(\mathbf{F}) = \frac{1}{f'(r)}\left(\frac{r}{f(r)}\right)^{(n_d-1)} \tag{C.31}$$

where we consider a two-dimensional space, with $n_d = 2$.

Furthermore, we choose:

$$\kappa^\star = \kappa_0 J = \kappa_0 \frac{1}{f'(r)}\frac{r}{f(r)}\,, \tag{C.32}$$

and:

$$\mathbf{S} = \left(\frac{f(r)}{r}\right)\left(\mathbf{I}_r + \frac{rf'(r)}{f(r)}\mathbf{I}_\perp\right) . \tag{C.33}$$

Note that the divergence-free condition of the field $\mathbf{S}$ follows from equation (C.33).

From expressions (C.32), (C.33) and (C.1), the moduli of the elastic constitutive tensor κ_r and κ_θ in equation (C.3), result in:

$$\kappa_r = \kappa_o \frac{1}{f'(r)}\left(\frac{f(r)}{r}\right) \qquad ; \qquad \kappa_\theta = \kappa_o f'(r)\left(\frac{r}{f(r)}\right) \tag{C.34}$$

and therefore:

$$\hat{\mathbf{C}} = \begin{bmatrix} \frac{1}{f'(r)}\left(\frac{f(r)}{r}\right) & 1 & 0 \\ 1 & f'(r)\left(\frac{r}{f(r)}\right) & 0 \\ 0 & 0 & 0 \end{bmatrix} . \tag{C.35}$$

Also, the inertial mass density is given by:

$$\boldsymbol{\rho}^\star = \rho_o f'(r)\left(\frac{f(r)}{r}\right)\mathbf{1} \tag{C.36}$$

In this case, $\boldsymbol{\rho}^\star$ results in a spherical tensor, and therefore:

$$\rho_r = \rho_\theta = \rho = \rho_o f'(r)\frac{f(r)}{r} . \tag{C.37}$$

With these definition of the material parameters at the cloak, and the condition: $f(r=b) = b$, the radial impedance and the circumferential wave speed at the interface separating both domains, medium and cloak, are identical:

$$Z_r^{\text{cloack}}(r=b) = \sqrt{\kappa_r \rho} = \sqrt{\kappa_o \rho_o} = Z_r^{\text{medium}}(r=b); \tag{C.38}$$

$$c_\theta^{\text{cloack}}(r=b) = \sqrt{\kappa_\theta/\rho} = \sqrt{\kappa_o/\rho_o} = c_\theta^{\text{medium}}(r=b) . \tag{C.39}$$

Appendix C2: Topology optimization algorithm for inverse design of the micro-structure

In this Appendix, the most salient points of topology optimization algorithm utilized for micro-structure inverse design are discussed. These points include the computational homogenization technique (sub-Section 6), which is used to evaluate the effective properties of the composite, the topological derivative of the homogenized elasticity tensor described in sub-Section 6, and the

optimization algorithm summarized in two Boxes 1 and 2 of sub-Section 6. Also, the modification of some key aspects of the topology optimization algorithm are included in order to adapt this algorithm to the acoustic cloaking design problem.

C2.1. Computational homogenization

Let us consider the two-phase composite schematized in Figure C.3 with a periodic micro-structure represented through a unit cell denoted by Ω_μ.

The macro-strain and macro-stress fields described at Ω are denoted by $\boldsymbol{\varepsilon}$ and $\boldsymbol{\sigma}$, respectively. The same fields observed at the micro-scale Ω_μ are denoted by $\boldsymbol{\varepsilon}_\mu$ and $\boldsymbol{\sigma}_\mu$. These terms are represented in Figure C.3-a, where the homogenization procedure is also sketched.

A linear elastic response for every phase of the composite at the micro-scale is assumed. It is expressed by:

$$\boldsymbol{\sigma}_\mu(\mathbf{y}) = \mathbf{C}_\mu(\mathbf{y}) : \boldsymbol{\varepsilon}_\mu(\mathbf{y}) \ , \tag{C.40}$$

where $\mathbf{C}_\mu(\mathbf{y})$ is the elasticity tensor of the corresponding phase at point $\mathbf{y}$. Then, a macroscopic linear constitutive relation, $\boldsymbol{\sigma} = \mathbf{C}^{hom} : \boldsymbol{\varepsilon}$, is inherited, whose effective elasticity tensor is denoted by $\mathbf{C}^{hom}$. The tensor $\mathbf{C}^{hom}$ is evaluated by following conventional computational homogenization techniques imposing periodic boundary conditions at Γ_μ, see de Souza Neto y Feijóo (2006). Due to the assumed linearity of the relation $\boldsymbol{\sigma}(\boldsymbol{\varepsilon})$, we compute the homogenized constitutive tensor evaluating three homogenized macro-stresses, $\boldsymbol{\sigma}_1$, $\boldsymbol{\sigma}_2$ and $\boldsymbol{\sigma}_3$ for specific macro-strains $\boldsymbol{\varepsilon}_1$, $\boldsymbol{\varepsilon}_2$ and $\boldsymbol{\varepsilon}_3$. The three strains $\{\boldsymbol{\varepsilon}_1, \boldsymbol{\varepsilon}_2, \boldsymbol{\varepsilon}_3\}$, given by: $\boldsymbol{\varepsilon}_1 = \mathbf{e}_r \otimes \mathbf{e}_r$, $\boldsymbol{\varepsilon}_2 = \mathbf{e}_\theta \otimes \mathbf{e}_\theta$ and $\boldsymbol{\varepsilon}_3 = 1/2(\mathbf{e}_r \otimes \mathbf{e}_\theta + \mathbf{e}_\theta \otimes \mathbf{e}_r)$, define a canonical basis of the macro-strain space. In Voigt notation, the j-th basis of these strain tensors can be written as: $\boldsymbol{\varepsilon}_j = [(\varepsilon_j)_{rr}, (\varepsilon_j)_{\theta\theta}, 2(\varepsilon_j)_{r\theta}]^T$.

Then, the matrix of the elasticity tensor is given by:

$$\mathbf{C}^{hom} = [\boldsymbol{\sigma}_1(\boldsymbol{\varepsilon}_1), \boldsymbol{\sigma}_2(\boldsymbol{\varepsilon}_2), \boldsymbol{\sigma}_3(\boldsymbol{\varepsilon}_3)] \ . \tag{C.41}$$

So, the j-th column of $\mathbf{C}^{hom}$ is the macro-stress $\boldsymbol{\sigma}_j(\boldsymbol{\varepsilon}_j)$ computed as the volumetric average of the micro-stress $(\boldsymbol{\sigma}_\mu)_j$:

$$\boldsymbol{\sigma}_j(\boldsymbol{\varepsilon}_j) = \frac{1}{|\Omega_\mu|} \int_{\Omega_\mu} (\boldsymbol{\sigma}_\mu)_j \ d\Omega_\mu \ . \tag{C.42}$$

The micro-stress $(\boldsymbol{\sigma}_\mu)_j$ results from solving the unit-cell boundary value problem briefly defined as follows:

i) the macro-strain $\boldsymbol{\varepsilon}_j$ is uniformly distributed into the unit-cell domain Ω_μ. This term operates as the driving force of the mechanical problem formulated at the unit-cell;

ii) the micro-strain field, $(\boldsymbol{\varepsilon}_\mu)_j$, in Ω_μ is the addition of two terms: $(\boldsymbol{\varepsilon}_\mu)_j = \boldsymbol{\varepsilon}_j + (\tilde{\boldsymbol{\varepsilon}}_\mu)_j$. The last term, $(\tilde{\boldsymbol{\varepsilon}}_\mu)_j$, is a kinematically compatible micro-strain fluctuation field;

iii) micro-stress $(\boldsymbol{\sigma}_\mu)_j$ is a self-equilibrated stress field satisfying anti-periodic traction boundary conditions and the elastic constitutive relation (C.40).

Additional details of this homogenization procedure can be obtained in the reference works de Souza Neto y Feijóo (2006).

The rule of mixtures is the homogenization technique adopted for evaluating the effective inertial mass density ρ^{hom}.

C2.2. Topological derivative of the homogenized elasticity tensor

The unit-cell domain Ω_μ considered in the previous sub-Section is separated in two disjoint domains: Ω_μ^1 and Ω_μ^2, occupied by phase M1 and M2, respectively ($\Omega_\mu = \Omega_\mu^1 \cup \Omega_\mu^2$), see Figure C.18.

Phase M1 is an isotropic elastic material whose elastic modulus and Poisson's ratio are denoted by E_μ^1 and ν_μ^1. Phase M2 is also an isotropic elastic material whose elastic modulus and Poisson's ratio are defined by: $E_\mu^2 = \gamma E_\mu^1$ and $\nu_\mu^2 = \nu_\mu^1$, where the parameter γ is the stiffness contrast ratio between phases M1 and M2.

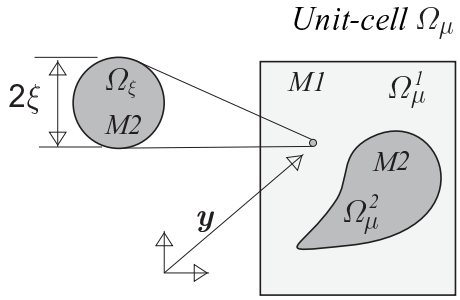

Figura C.18: Multiscale material model of a composite with two phases: M1 and M2. The topological derivative $D_T\mathbf{C}^{hom}(\mathbf{y})$ of the homogenized elasticity tensor $\mathbf{C}^{hom}(\mathbf{y})$ gives its sensitivity to material distribution changes within the micro-cell.

For a given distribution of phases, let us consider the homogenized constitutive tensor $\mathbf{C}^{hom}$. The topological derivative of $\mathbf{C}^{hom}$, denoted by $D_T\mathbf{C}^{hom}$, at point $\mathbf{y}$ occupied by phase M1, is the fourth order tensor representing the sensitivity of $\mathbf{C}^{hom}$ to the nucleation of a circular perturbation around $\mathbf{y}$. The perturbation consists in substituting a ball of material M1 and radius ξ by an identical ball constituted of material M2. The ball area $|\Omega_\xi|$ is the perturbation parameter. Alternatively, if $\mathbf{y}$ refers to a point occupied by phase M2, the topological derivative indicates the sensitivity of nucleating a circular perturbation of material M1.

The mathematical meaning of the topological derivative can be illustrated through the asymptotic expansion of the effective elasticity tensor $\mathbf{C}_{pert}^{hom}$ which is the homogenized tensor after introducing the perturbation. This asymptotic expansion is developed in terms of the area $|\Omega_\xi|$ and is written as follows:

$$\mathbf{C}_{pert}^{hom} = \mathbf{C}^{hom} + \frac{|\Omega_\xi|}{|\Omega_\mu|} D_T\mathbf{C}^{hom}(\mathbf{y}) + \mathcal{O}\left(\frac{|\Omega_\xi|}{|\Omega_\mu|}\right). \tag{C.43}$$

The last term in (C.43) is an infinitesimal of order two in the argument. Further details about the meaning of (C.43) can be found in Amstutz et al. (2010) and Giusti (2009).

Using Voigt notation for fourth order tensors, the (i,j)-th component of the topological derivative matrix $(i,j=1,...,3)$, denoted by $[D_T\mathbf{C}^{hom}]_{ij}$, is computed through the following expression:

$$[D_T\mathbf{C}^{hom}]_{ij} = -\frac{\chi_1}{E_\mu^1}\Big(4(\boldsymbol{\sigma}_\mu)_i : (\boldsymbol{\sigma}_\mu)_j - \chi_2 \text{tr}((\boldsymbol{\sigma}_\mu)_i)\text{tr}((\boldsymbol{\sigma}_\mu)_j)\Big)\,, \tag{C.44}$$

where

$$\chi_1 = \frac{1-\gamma}{1+\tau\gamma}\;\;,\;\; \chi_2 = \frac{1-\gamma(\tau-2\zeta)}{1+\zeta\gamma}\;\;,\;\; \tau = \frac{1-\nu_\mu^1}{1+\nu_\mu^1}\;\;,\;\; \zeta = \frac{3-\nu_\mu^1}{1+\nu_\mu^1}\,,$$

while $(\boldsymbol{\sigma}_\mu)_i$ and $(\boldsymbol{\sigma}_\mu)_j$ are the micro-stress fields utilized in the integrand of equation (C.42). These stresses are the solution of the micro-cell problem defined in the previous sub-Section.

Equation (C.44) has been derived by implicitly assuming that a ball of material M2 is introduced into the domain M1. Alternatively, if the perturbation consist of introducing a small ball of material M1 into the domain M2, the role of E_μ^1, E_μ^2 and γ in equation (C.44) should be exchanged to compute $D_T\mathbf{C}^{hom}$ in that position (E_μ^2 takes the role of E_μ^1 and γ is redefined as: $\gamma = E_\mu^2/E_\mu^1$).

C2.3. Topology optimization algorithm based on the Amstutz's procedure

The algorithm for solving the problem (C.13) relies on two ingredients:

a) A continuous function $\psi(\mathbf{y})$ (with $\psi \in L^2(\Omega_\mu)$) which zero level set represents the geometry of the interface M1-M2. It is called the level set function and is defined by:

$$\psi(\mathbf{y}) := \begin{cases} < 0 \;\;;\;\; \forall \;\; \mathbf{y} \in \Omega_\mu^1 \;; \\ \\ > 0 \;\;;\;\; \forall \;\; \mathbf{y} \in \Omega_\mu^2 \;. \end{cases} \tag{C.45}$$

where sub-domains Ω_μ^1 and Ω_μ^2 have been previously defined.

b) The topological derivative $g(\mathbf{y})$ which is defined as follows:

$$g(\mathbf{y}) := \begin{cases} -D_T\mathcal{J}(\mathbf{y}); & \text{if: } \mathbf{y} \in \Omega_\mu^1 \ ; \\ \\ D_T\mathcal{J}(\mathbf{y}); & \text{if: } \mathbf{y} \in \Omega_\mu^2 \ . \end{cases} \tag{C.46}$$

The topological derivative of the objective function (C.13), considering the Frobenius norm, results in:

$$D_T\mathcal{J}(\mathbf{y}) = 2\left(\mathbf{C}^{hom} - \hat{\mathbf{C}}\right) : D_T\mathbf{C}^{hom}(\mathbf{y}) \ , \tag{C.47}$$

and this functions can be computed after replacing $D_T\mathbf{C}^{hom}$ by the term defined in (C.44).

In the Amstutz's approach, the function ψ of the optimal solution of a topology optimization problem is found through a fixed point iteration and the topological derivative, providing a descent direction of the objective function. This algorithm has been slightly adapted to dealt with the objective function described in the problem (C.13). It is described in the following Boxes 1 and 2.

Box 1: Topology Optimization Algorithm defined in Ω_μ:

Given:

- one initial finite element mesh of size h_0^e,

- a trial level set function $\psi_0(h_0^e)$, and $m = 0$.

Compute $\mathbf{C}^{hom}(\psi_0(h_0^e))$ and the sequence of tensors $\check{\mathbf{C}} = \{\check{\mathbf{C}}_1, ..., \check{\mathbf{C}}_\ell, ...\check{\mathbf{C}}_{n_c}\}$ described by equation (C.50), and then:

DO LOOP 1 (mesh refinement loop): m-index: from 0 to m_{max}

DO LOOP 2 (sequence of $\check{\mathbf{C}}_\ell$ toward $\hat{\mathbf{C}}$): ℓ-index: from 1 to n_c

Evaluates a new ψ_ℓ by solving:

$$\psi_\ell(h_m^e) = arg\{\min_{\psi_\ell} \mathcal{J}(\psi_\ell)\} = arg\{\min_{\psi_\ell}(\|\mathbf{C}^{hom}(\psi_\ell) - \check{\mathbf{C}}_\ell\|)^2\}, \tag{C.48}$$

using the algorithm in BOX 2

END LOOP 2

Performs a finite element mesh refinement, $h_{m+1}^e \leftarrow h_m^e/2$

Project $\psi_{n_c}(h_m^e)$ to the new mesh: $\psi_0(h_{m+1}^e) \leftarrow \psi_{n_c}(h_m^e)$

Compute: $\mathbf{C}^{hom}(\psi_0(h_{m+1}^e))$

Compute a new sequence $\check{\mathbf{C}}$ (equation (C.50))

END LOOP 1

Box 2: Algorithm for solving problem (C.48)

Given a trial level set function: $\psi^i = \psi_{\ell-1}$

DO LOOP A: (i-index increases):

Select a step length ξ (line search), then compute:

$$\hat{\psi}^{i+1} = \psi^i + \xi \, \frac{g(\psi^i)}{\alpha}, \text{ and normalize: } \psi^{i+1} = \frac{\hat{\psi}^{i+1}}{\|\hat{\psi}^{i+1}\|_{L^2}} \tag{C.49}$$

Compute: $\mathcal{J}(\psi^{i+1})$ and $g(\psi^{i+1})$

IF: $\mathcal{J}(\psi^{i+1})$ satisfies the convergence criterion:

STOP: the algorithm converges and the solution is: $\psi_\ell = \psi^{i+1}$

ENDIF

END LOOP A

Description of Box 1: the procedure consists of two nested loops:

1) (LOOP 1) The external loop handles a finite element mesh refinement sequence. The parameter m_{max} identifies the maximum number of times that the mesh is refined during the solution process. Then, each finite element mesh, in the refinement sequence, is identified by a characteristic mesh size: h^e_m where sub-index m denotes the m-th loop. The level set function ψ is defined in each node of the finite element mesh. Then, the dependence of the level set function ψ with the finite element mesh is remarked using the notation $\psi(h^e_m)$, where h^e_m represents the finite element mesh size at loop m.

2) The field $\psi(h^e_m)$ is determined by solving the problem (C.13) with the target elasticity tensor $\hat{\mathbf{C}}$. This field is found through a sequence of n_c sub-problems solved in the inner loop (LOOP 2). The level set function solution of every sub-problem (ψ_ℓ) is identified with a sub-index coinciding with the inner loop index. So, $\psi_0(h^e_m)$ represents the trial level set function for the mesh of size h^e_m, while $\psi_{n_c}(h^e_m)$ is the solution obtained after solving n_c sub-problems.

In the inner loop, each sub-problem is similar to (C.13) but with a redefined target elasticity tensor. For each sub-problem, the target elasticity tensor is taken from a convex combination of $\mathbf{C}^{hom}(\psi_0(h^e_m))$ and $\hat{\mathbf{C}}$ as follows:

$$\check{\mathbf{C}}_\ell = \left(\frac{n_c - \ell}{n_c}\right) \mathbf{C}^{hom}(\psi_0(h^e_m)) + \left(\frac{\ell}{n_c}\right) \hat{\mathbf{C}} \, . \tag{C.50}$$

The notation adopted in this equation emphasizes the fact that $\mathbf{C}^{hom}$ depends on the level set function determining the topology of the cell Ω_μ.

The tensor $\check{\mathbf{C}}_\ell$ is utilized to compute the objective function $\mathcal{J}$, and the corresponding topological derivative, of the ℓ-th sub-problem in the inner loop as follows:

$$\mathcal{J} = (\|\mathbf{C}^{hom}(\psi) - \check{\mathbf{C}}_\ell\|)^2 \,, \tag{C.51}$$

which is solved with the algorithm presented in Box 2. Observe that for $\ell = n_c$ is $\check{\mathbf{C}}_{n_c} = \hat{\mathbf{C}}$. Then, the last internal loop solves the original problem (C.13).

Description of Box 2: the iterative algorithm for solving the level set function $\psi_\ell(h_m^e)$, of the sub-problem (C.48), utilizes a fixed point iteration. The topological derivative $g(\psi)$ is used as a feasible descent direction to optimize $\mathcal{J}(\Omega_\mu^1)$ in problem (C.13) (additional details about this important point can be found in Amstutz y Andrä (2006) and Amstutz et al. (2010)). The normalization factor α is chosen to avoid the ill-conditioning happening in points close to the solution of problem (C.48). Note that $\|g\|_{L^2} \to 0$ as: $\mathbf{C}^{hom}(\psi) \to \check{\mathbf{C}}_\ell$. The value α is selected as the average of $\|g\|_{L^2}$ in the initial iterations of the loop in Box 2.

Step length selection (ξ) **and convergence criterion in Box 2**

The step length ξ is found through a line search defined by:

$$\xi = arg\,(\min_{\tilde{\xi} \in \mathcal{I}_\xi} \mathcal{J}(\psi_{\tilde{\xi}}^{i+1})) \tag{C.52}$$

with

$$\hat{\psi}_{\tilde{\xi}}^{i+1} = \psi^i + \tilde{\xi}\,\frac{g(\psi^i)}{\alpha} \qquad , \qquad \psi_{\tilde{\xi}}^{i+1} = \frac{\hat{\psi}_{\tilde{\xi}}^{i+1}}{\|\hat{\psi}_{\tilde{\xi}}^{i+1}\|_{L^2}}$$

and the parameters $\tilde{\xi}$ are taken from the set of numbers defined by:

$$\mathcal{I}_\xi := [\xi_{min} : \Delta\xi : \xi_{max}] \quad ; \quad \Delta\xi = \frac{\xi_{max} - \xi_{min}}{10}$$

where ξ_{min} and ξ_{max} are the minimum and maximum allowed step lengths which are taken as $\xi_{min} \ll 1$ and $\xi_{max} = 1$, respectively, and $\Delta\xi$ is a pre-defined increment of the step length.

The stop criterion is given by:

$$|\mathcal{J}(\psi^{i+1}) - \mathcal{J}_{10}| < tol \tag{C.53}$$

where $\mathcal{J}_{10}$ is the average of $\mathcal{J}$ in the last 10 iterations and tol is an absolute tolerance.

The initialization of the algorithm is performed through the sequential procedure defined in Box 1. With the internal loop 2, the results gradually change, from the trial solution to the original one, by solving a sequence of closely related optimization problems. Each problem of this sequence is defined by a modified target tensor, which is adjusted till reaching the original target value $\hat{\mathbf{C}}$.

Following the idea introduced by Amstutz y Andrä (2006), the external loop 1 handles a sequence of finite element mesh refinements. The initial loop starts with a rather coarse mesh. After convergence, the mesh is refined and the level set function is projected onto the new mesh. This process is repeated until reaching a given accuracy. According to Amstutz y Andrä (2006), the objective pursued with this mesh mapping strategy is to improve the algorithm response respect to local minimum. In the present version, they are tested with the coarser meshes, by fixing the step length to $\xi = 0.1$ in equation (C.49). Once the finest mesh is solved, the activation of the line search provides a more controlled approach to a specific local minimum.

Bibliografía

Amigo R., Giusti S., Novotny A., Silva E., y Sokolowski J. Optimum design of flextensional piezoelectric actuators into two spatial dimensions. *SIAM Journal on Control and Optimization*, 54(2):760–789, 2016.

Amstutz S. y Andrä H. A new algorithm for topology optimization using a level-set method. *Journal of Computational Physics*, 216(2):573–588, 2006.

Amstutz S., Giusti S., Novotny A., y de Souza Neto E. Topological derivative for multi-scale linear elasticity models applied to the synthesis of microstructures. *International Journal for Numerical Methods in Engineering*, 84(6):733–756, 2010.

Amstutz S., Novotny A., y de Souza Neto E. Topological derivative-based topology optimization of structures subject to drucker–prager stress constraints. *Computer Methods in Applied Mechanics and Engineering*, 233:123–136, 2012.

Ashby M. *Materials selection in mechanical design*. Elsevier, Butterworth-Heinemann, 3rd. edición, 2005.

Auffray N. y Ropars P. Invariant-based reconstruction of bidimensional elasticity tensors. *International Journal of Solids and Structures*, 87:183–193, 2016.

Banerjee B. *An introduction to metamaterials and waves in composites*. CRC Press, 2011.

Bendso M. y Sigmund O. *Topology optimization: theory, methods, and applications*. Springer Science & Business Media, 2013.

Bendsøe M. y Kikuchi N. Generating optimal topologies in structural design using a homogenization method. *Computer methods in applied mechanics and engineering*, 71(2):197–224, 1988.

Cheng Y., Yang F., Xu J., y Liu X. A multilayer structured acoustic cloak with homogeneous isotropic materials. *Applied Physics Letters*, 92(15):151913, 2008.

Cherkaev A. y Gibiansky L. Coupled estimates for the bulk and shear moduli of a two-dimensional isotropic elastic composite. *Journal of the Mechanics and Physics of Solids*, 41(5):937–980, 1993.

de Souza Neto E. y Feijóo R. Variational foundation on multi-scale constitutive models of solids: small and large strain kinematical formulation. *LNCC Research & Development Report No 16*, 16, 2006.

Ferrer A., Oliver J., Cante J., y Lloberas-Valls O. Vademecum-based approach to multi-scale topological material design. *Advanced Modeling and Simulation in Engineering Sciences*, 3(1):23, 2016.

Giusti S. Análise de sensibilidade topológica em modelos constitutivos multi-escalas (ph. d. thesis). *LNCC, Rio de Janeiro, Brasil*, 2009.

Giusti S., Ferrer A., y Oliver J. Topological sensitivity analysis in heterogeneous anisotropic elasticity problem. theoretical and computational aspects. *Computer Methods in Applied Mechanics and Engineering*, 311:134–150, 2016.

Gokhale N., Cipolla J., y Norris A. Special transformations for pentamode acoustic cloaking. *The Journal of the Acoustical Society of America*, 132(4):2932–2941, 2012.

Kadic M., Bückmann T., Schittny R., Gumbsch P., y Wegener M. Pentamode metamaterials with independently tailored bulk modulus and mass density. *Physical Review Applied*, 2(5):054007, 2014.

Kadic M., Bückmann T., Schittny R., y Wegener M. Metamaterials beyond electromagnetism. *Reports on Progress in Physics*, 76(12):126501, 2013.

Landau L. y Lifshitz E. *Course of Theoretical Physics Vol 7: Theory and Elasticity*. Pergamon Press, 1959.

Layman C., Naify C., Martin T., Calvo D., y Orris G. Highly anisotropic elements for acoustic pentamode applications. *Physical review letters*, 111(2):024302, 2013.

Milton G. y Cherkaev A. Which elasticity tensors are realizable? *Journal of engineering materials and technology*, 117(4):483–493, 1995.

Milton M. The theory of composites. *The Theory of Composites, by Graeme W. Milton, pp. 748. ISBN 0521781256. Cambridge, UK: Cambridge University Press, May 2002.*, página 748, 2002.

Narayana S. y Sato Y. Heat flux manipulation with engineered thermal materials. *Physical Review Letters*, 108(21):214303, 2012.

Norris A. Acoustic cloaking theory. En *Proceedings of the Royal Society of London A: Mathematical, Physical and Engineering Sciences*, volumen 464, páginas 2411–2434. 2008.

Novotny A. y Sokołowski J. *Topological derivatives in shape optimization*. Springer Science & Business Media, 2012.

Ogden R. *Non-linear elastic deformations*. Courier Corporation, 1997.

Osanov M. y Guest J. Topology optimization for architected materials design. *Annual Review of Materials Science*, 46:211–233, 2016.

Özdemir İ. Topological derivative based optimization of 3d porous elastic microstructures. *Computational Materials Science*, 81:319–325, 2014.

Pendry J., Schurig D., y Smith D. Controlling electromagnetic fields. *science*, 312(5781):1780–1782, 2006.

Podestá J., Huespe A., Méndez C., y Fachinotti V. Diseño computacional de metamateriales ultrarígidos y ultralivianos. *Mecánica Computacional*, 35, 2016.

Sigmund O. A new class of extremal composites. *Journal of the Mechanics and Physics of Solids*, 48(2):397–428, 2000.

Sigmund O. y Maute K. Topology optimization approaches. *Structural and Multidisciplinary Optimization*, 48(6):1031–1055, 2013.

Ting T. *Anisotropic elasticity: theory and applications*. 45. Oxford University Press, 1996.

Walpole L. On bounds for the overall elastic moduli of inhomogeneous systems. *Journal of the Mechanics and Physics of Solids*, 14(3):151–162, 1966.

Zheng X., Lee H., Weisgraber T., Shusteff M., DeOtte J., Kuntz E.D.J., Biener M., Ge Q., Jackson J., et al. Ultralight, ultrastiff mechanical metamaterials. *Science*, 344(6190):1373–1377, 2014.

Anexo D

Making use of Symmetries in the 3D Elastic Inverse Homogenization Problem

El artículo presentado a continuación ha sido publicado en la revista **"International Journal for Multiscale Computational Engineering"**.

C. Méndez, J.M. Podestá, S. Toro, A.E. Huespe, J. Oliver, *"Making use of Symmetries in the 3D Elastic Inverse Homogenization Problem"*, DOI: 10.1615/IntJMultCompEng.2019029111.

Making use of Symmetries in the 3D Elastic Inverse Homogenization Problem

J.M. Podestá[1], C. Méndez[2], S. Toro[1], A.E. Huespe[1,3][1]

[1]CIMEC-UNL-CONICET, Predio Conicet "Dr Alberto Cassano", CP 3000 Santa Fe, Argentina

[2]CIMNE-Latinoamérica, Iturraspe 785, CP 3000, Santa Fe, Argentina

[3]Centre Internacional de Metodes Numerics en Enyinyeria (CIMNE),Campus Nord UPC.

Keywords: elastic symmetry; 3D topology optimization; Wigner–Seitz 3D cells, elastic inverse homogenization.

Abstract

An analysis of the connection between the symmetry of the material layout at the microscale of 3D periodic composites and the symmetry of the effective elastic properties is performed. We analyze some possible Bravais lattices and space groups, which are typically associated with crystallography, to study the way in which the symmetries of these geometrical objects can be used for the microarchitecture design of 3D elastic metamaterial.

For obtaining the material architecture at the microscale, we follow an inverse design technique jointly with an homogenization-based topology optimization algorithm. In this context, a procedure is proposed for:

i) solving the topology optimization algorithm on a conveniently chosen spatial domain;

ii) identifying the space group symmetry of the periodic material topology, at the microscale, to guarantee the correct symmetry of the homogenized elastic properties of the designed material;

[1]Corresponding author. E-mail address: ahuespe@intec.unl.edu.ar (A.E. Huespe).

iii) building the microcell finite element mesh such that the symmetry of the material layouts, being compatible with different space groups, can be easily implemented and enforced.

Particularly, related to item i), we suggest adopting the Wigner-Seitz cells of specific Bravais lattices having the same point group of the target elasticity tensor.

The numerical assessment of the proposed design procedure is presented. It consists of the searching for a class of extreme materials. The obtained solutions show that different composites architectures emerge depending on the cell shape selection.

1. Introduction

1.1. Problem motivation

In this paper, we present a methodology aiming at the microarchitecture synthesis of three-dimensional periodic composites whose homogenized elastic properties are similar to stipulated effective elasticities. The design of composites satisfying this requirement is a well-known problem in the literature. It has been clearly explained and described in the book by Bendsoe y Sigmund (2003) and references cited therein. A number of contributions addressed to solve this problem have been posteriorly published which should be mentioned in the following. In particular, typical examples where this problem naturally arise, within the context of a larger design problem, can be seen in the papers by Méndez et al. (2017) and Podestá et al. (2018). To reach this objective, we appeal to the symmetries characterizing the material layouts of composites at the microstructural level as well as to the symmetry characterizing the stipulated effective elasticities. The symmetry notion is ubiquitous in the nature. In general, this notion results in an extremely important physical property. Particularly, some features of material responses can be predicted without resorting to experimentation or complicated calculations by only appealing to the geometrical symmetries at different length scales of the material structure.

1.2. Microarchitecture design using symmetric topologies

The microarchitecture synthesis of a periodic composite with prescribed target effective elastic properties can be though as an inverse design problem that is formulated by means of an homogenization-based topology optimization problem, such as proposed in the pioneering work by Sigmund (1994) and widely reported in the posterior literature (Neves et al. (2000), Wang et al. (2014), Coelho et al. (2016), Li et al. (2018), Oliver et al. (2018)).

Nice microstructures have been obtained by Sigmund (2000) with this formulation and more recently by Andreassen et al. (2014) in the context of three-dimensional microstructure designs.

In the present paper, we follow this approach aiming at the three-dimensional microarchitecture design of elastic metamaterials realized as biphasic composites.

A particular issue arising in this type of inverse homogenization-based design approach is the selection of the domain shape where the topology optimization problem is solved. In our opinion, this domain shape would result in a good selection if, as an outcome of the approach, the same domain is also a unit cell of the designed composite.

There are some aspects to be considered for selecting adequate cell shapes. For example, Coelho et al. (2016) reported that the cell size influences the obtained topology solutions. But, which is more important for the approach taken in the present contribution is the fact that a significant number of material layout topologies could be hidden or unreachable for some frequently used cell shapes, typically cubes or right rectangular prisms in 3D (Diaz. y Benard (2003)). Furthermore, It has been shown that the realization of certain classes of composites, such as the Vigdergauz microstructures or the microstructures proposed by Sigmund (2000), could be promoted by enforcing some kind of material layout symmetry. These issues have been particularly studied in the 2D elastic material design context by the authors in previous contributions, see Podestá et al. (2018) and Podesta et al. (2018).

In view of these observations and following similar arguments to the ones given by Podesta et al. (2018), here, we propose to employ concepts taken from crystallography to define the cell shape. These concepts are intimately related to the symmetry properties of the crystal structures and the elastic target tensors. Thus, three-dimensional crystal symmetry properties, defined according to their point groups and space groups, are the primary information guiding the selection of the unit cell shape that is considered for solving the topology optimization algorithm.

Our proposal consists of taking the Wigner-Seits cell of a Bravais lattice that is compatible with the point group of the target elasticity tensor. Also, the material layout at the microcell could be enforced to satisfy the space group symmetry compatible with the same elasticity tensor. By adopting this approach, it can be guarantee that the homogenized elastic properties of the designed composite will have the same, or higher, symmetry than the target ones. This methodology is a generalization to three-dimensional problems of the one reported in Podesta et al. (2018) for two-dimensional cases.

By using this approach in the three-dimensional problems, we notice a challenge that does not exist in the two-dimensional ones; there is not any crystal system space group guaranteeing the realization of a periodic composite with isotropic effective elastic properties. Thus, we test our proposal by designing the microarchitecture of an isotropic extreme material with different Wigner-Seitz cells. In this test, the topology optimization algorithm does not explicitly impose the

isotropy constraint. The obtained microstructure results are evaluated with a criterion measuring the proximity to an effective isotropic response.

A brief description of the paper is next given. Section 2 presents a brief summary of the microarchitecture design methodology that we follow. This methodology can be seen as an inverse homogenization technique formulated as a topology optimization problem. Section 3 and Appendix 6 give a short description of crystal symmetries and their connection with the symmetries of the material elastic properties. Evidently, a full explanation regarding the crystal structure symmetries largely exceed the scope of the present paper; thus, the interested reader should consult the specific literature for additional information on this topic.

Section 4 describes the main contribution of the paper. We explain the proposed procedure guiding the selection of the cell shape and the possible space group symmetry to be imposed in the microarchitecture topology design.

A numerical assessment making use of this procedure is presented in Section 5. We show a three-dimensionl design problem of an extreme isotropic composite material with maximum shear and bulk modulus. We seek the solution by only testing a cubic crystal system and its three related Bravais lattices.

Finally, Section 6 presents the conclusions and final remarks of this paper. The topology optimization algorithm is briefly described in Appendix 6.

2. Homogenization-based topology optimization problem

Material design via inverse homogenization refers to the problem of finding the material configuration at the microscale of a periodic composite whose effective elasticity tensor is identical to a target elasticity tensor. This problem has been formulated as an homogenization-based topology optimization problem in the pioneering works of Sigmund (1994), Sigmund (1995) and Sigmund (2000). In the following years, several works using this approach and emplying a variety of topology optimization algorithms have been reported. Only to mention a few, we cite the works by Neves et al. (2000), Andreassen et al. (2014) who describe three-dimensionl elastic metamaterial designs using the SIMP optimization algorithm, and Huang et al. (2013), who have used the bi-directional evolutionary structural optimization (BESO) algorithm. Two interesting recent reviews about this methodology can be found in Cadman et al. (2013) and Osanov y Guest (2016)).

Here, we follow a similar homogenization-based approach. Let us consider a structure whose material is a periodic composite constituted by two isotropic elastic phases M_1 and M_2. We take a unit cell of this material identified by Ω_μ. In this microcell, phases M_1 and M_2 occupy the domains Ω_μ^1 and Ω_μ^2, respectively, see Figure D.1.

The characteristic function $\chi(\mathbf{y})$ is defined in Ω_μ. It identifies the positions where the phase M_1 is placed and takes the following values:

$$\chi(\mathbf{y}) = \begin{cases} 0 & \forall \mathbf{y} \in \Omega_\mu^2 \\ \\ 1 & \forall \mathbf{y} \in \Omega_\mu^1 \end{cases} . \tag{D.1}$$

Evidently, the homogenized elasticity tensor of the composite, $\mathbf{C}^h$, depends on the geometrical configuration of the phases M_1 and M_2 in Ω_μ. This dependence is made explicit by introducing the notation $\mathbf{C}^h(\chi)$. This tensor can be evaluated in Ω_μ by enforcing periodic boundary conditions in displacements fluctuations. Then, standard computational techniques based on finite elements (Feyel y Chaboche (2000)) or Fast Fourier Transform (Michel et al. (1999)) can be used to get this goal.

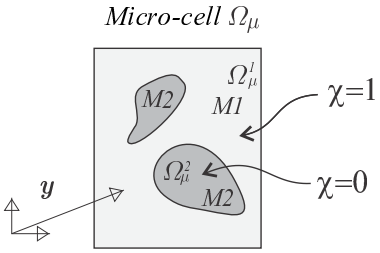

Figura D.1: Microcell used as the design domain for the Topology Optimization Problem. The material layout is defined in Ω_μ. The homogenized elastic properties $\mathbf{C}^h$ of the composites are also computed in Ω_μ

2.1. The topology optimization algorithm

Next, we formulate the microarchitecture inverse design problem as a topology optimization problem. Let be given the design domain Ω_μ and the target effective elasticity tensor $\hat{\mathbf{C}}$. Let also be given the space $\mathcal{V}_\chi$ collecting together all the characteristic functions $\chi(\mathbf{y})$ in Ω_μ where the domains Ω_μ^1 and Ω_μ^2 can be arbitrarily changed. Then, the optimization problem is formulated as follows:

$$\begin{aligned} &\min_{\chi \in \mathcal{V}_\chi} \ \|\mathbf{C}^h(\chi) - \hat{\mathbf{C}}\| \\ &\qquad \text{such that: } V^h(\chi) - V^{obj} = 0 \, . \end{aligned} \tag{D.2}$$

Where $V^h = (\int_{\Omega_\mu} \chi \, d\Omega)/|\Omega_\mu|$, is the volume fraction of the stiff phase M_1 and V^{obj} is the target volume fraction of the same phase.

The problem (D.2) can be reformulated and implemented by defining a continuous function ψ in Ω_μ whose zero level set ($\psi = 0$) identifies the stiff-void material interface. The position of

the zero level set is iteratively updated, using a gradient-like method. The update direction for ψ is defined through the topological derivative of $\mathbf{C}^h$. Hence, the problem (D.2) is rephrased as the optimization problem (D.13), in Appendix 6. The algorithm for solving it has been reported by Amstutz and co-workers, see Amstutz y Andrä (2006) and Amstutz et al. (2010), and a brief summary is presented in Appendix 6.

To facilitate the comparative analysis performed in Section 5, we use a conventional Helmholtz filter forcing the optimization algorithm in Appendix 6 to provide solutions displaying approximately only one length scale of the stiff phase. This filter is implemented using equation (D.25), Appendix 6. Additional details of this filter can be found in Lazarov y Sigmund (2011) and Wang et al. (2011).

2.2. Issues related to the design domain selection

Two implicit variables in the problem (D.13) of Appendix 6 must be defined in advance. Their values result from a decision taken by the designer and play an important role to govern the complexity of the attained microarchitecture topology. They are:

i) the shape of the design domain Ω_μ.

ii) the microstructure periodicity directions. In fact, to find the effective properties of the composite, it is necessary to impose constraints on the displacement fluctuations on the boundary of Ω_μ which are compatible with the characteristic periodicity directions of the composite. The periodic constraints in the inverse homogenization problem result from a decision taken by the designer, by arguing that the microarchitecture is periodic along pre-established directions. Due to this assumption, the full material architecture is a spatial replica, by tessellation, of the cell Ω_μ.

3. Crystal symmetry properties

We start this Section by briefly discussing some crystal symmetry properties. In the present context of the microarchitecture design, crystal symmetries are exploited to guide the designer in making adequate decisions about the design domain selection.

Crystals can be characterized according to their specific symmetry properties. These properties are inherited from the underlying Bravais lattices and from their motifs. Two crystals sharing identical *point group* symmetry elements are said to belong to the same crystal system. Implicit to this classification is considered the translational and glide symmetries of the crystal motif which are taken into account to characterize the crystal symmetry properties, they constitute the *space*

group of the crystal system. We postpone until Appendix 6 the discussion of further details about well-established crystal symmetry properties and the description of the notation adopted to identify point and space groups which are used in this Section[2].

The characteristic feature referred to the crystal structure that is here stressed is the relationship between the crystal symmetry of a given material and the symmetry of its associated effective physical properties. In particular, the elastic symmetry properties. This relationship can be stated in terms of the Neumann's principle which establishes that: *the symmetry elements of any physical property of a crystal must include the symmetry elements of the point group of the crystal.* (see Nye (2006), pp.20).

According to this principle, the relation between crystal systems and elastic symmetry classes is given by their compatibility with similar point group transformations. This fact is summarized in Table D.1 displaying six columns that are explained in the next sub-Sections. Each row, in the first column, describes an elasticity tensor class which is associated with a specific crystal system and to more than one possible point groups and space groups. The fifth column indicates the number of Bravais lattice types that share identical point group symmetries with the elasticity class shown in column 1. They are collected together as a lattice system. These Bravais lattices are depicted in Table D.5, Appendix 6.

3.1. Elastic symmetry classes and crystal systems

The first column in Table D.1 displays the structure of the matrix representation[3] of the elasticity tensor $\mathbf{C}$ and the identities that its coefficients have to satisfy accordingly to the symmetry of the elasticity class to which it belongs to.

The established relations between the first and third columns in Table D.1 are determined with the procedure proposed by Ting (1996). This procedure uses the following sequence of operations. First, a point group is taken. Subsequently, the symmetry conditions being compatible with the point group elements are enforced to the elastic response, and the resulting format of the elasticity matrix is determined. Following this procedure with the 32 point groups, it is possible to collect together the set of point groups rendering identical matrix formats. Thus, it can be concluded that every matrix format is compatible with a specific set of point groups.

The crystal symmetries can be classified by using a similar procedure, but now the cross relationships, i.e. finding common symmetry elements, are performed with the space group transfor-

[2]For a detailed mathematical and physical description of the following concepts: crystal system, Bravais lattice, lattice system, point group, space group, etc., the reader may consult Sólyom (2007) and Souvignier (2016).

[3]Kelvin's notation is assumed for the matrix form of the elasticity tensor

Tabla D.1: Symmetry elements (point and space groups) of Crystal Systems (CS), Elasticity Classes (EC) and Lattice Systems (LS). Each row identifies the triplet (CS-EC-LS) with point group compatibility. First column describes the matrix format of the elasticity tensor class. The symbols in column 1 indicates: "$*$" ^{0}a possibly non-zero component; "$*-*$" two identical component; "$*-\bar{*}$" two equal component with opposite sign; "$\otimes$" the shear moduli is equal to $(C_{11}-C_{12})$ (see Ting (1996)). Fifth columns indicate the number of Bravais lattices constituting the lattice system defined in the sixth column.

Elasticity Tensor	Crystal System	Point Groups	Space Groups	Bravais Lattice	Lattice System
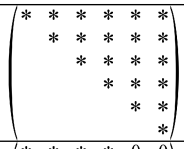	Triclinic	1,$\bar{1}$	2	1	Triclinic
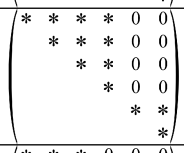	Monoclinic	2,m,2/m	13	2	Monoclinic
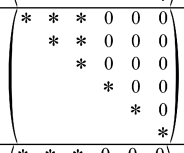	Orthorhombic	222,mm2, mmm	59	4	Orthorhombic
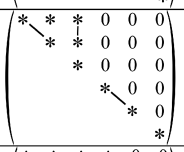	Tetragonal	4,$\bar{4}$,4/m, 442,4mm, $\bar{4}$2m,4/mmm	68	2	Tetragonal
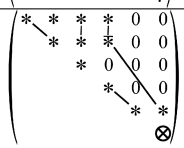	Trigonal	3,$\bar{3}$, 32,3m, $\bar{3}$m	7	1	Rhombohedral
			18	1	Hexagonal
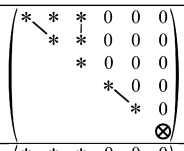	Hexagonal	6,$\bar{6}$, 6/m,622, 6mm,$\bar{6}$m2, 6/mmm	27		
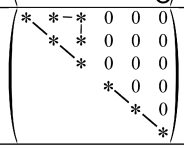	Cubic	23,m$\bar{3}$, 432,$\bar{4}$3m, m$\bar{3}$m	36	3	Cubic
Total	7	32	230	14	7

mations. Using this technique, only seven crystal systems are determined.

Furthermore, as a consequence of the Neumann's principle, crystal systems and elasticity classes are related by sharing similar point groups. This association is evidenced in Table D.1 between the first and second column. Therefore, an elastic class is designed with the name given to the corresponding crystal system. An exception to this rule is the isotropic elastic class which has not associated any crystal system.

The coefficients of the elastic matrices are described in a coordinate system whose coordinate planes coincide with the crystal symmetry planes. We call it the natural coordinate system. Additionally, by appealing to thermodynamic stability arguments, these matrices should be positive definite.

4. Microarchitecture design tools based on the target elastic symmetry

The characteristic symmetries of crystal structures described in Table D.1 and complemented with the information presented in Table D.5, Appendix 6, provide the basis for guiding the selection of the domain shape Ω_μ that is described in Section 2. The information in these Tables is used to define the next procedure.

1) The domain Ω_μ, which is used for solving the topology optimization problem (D.2), is *the Wigner-Seitz cell* of a Bravais lattice that belongs to the lattice system whose point group is compatible with the target elasticity tensor symmetry.

This compatibility relationship between lattice point group and elastic symmetry is implicit in Table D.1 because the elasticity classes and the Bravais lattice systems with compatible point groups are placed in identical rows. Consequently, the Table indicates an automatic procedure to define the cell domain by choosing a Bravais lattice of the corresponding lattice system. Note that the specific descriptions of the 14 three-dimensional lattices that belong to different lattice systems are represented in Table D.5 of Appendix 6.

For example, let us consider a target elasticity tensor with hexagonal symmetry. This elastic symmetry class is classified in the sixth row of Table D.1 and is compatible with only one Bravais lattice having a point group $6/mmm$. This lattice is displayed in the sixth row of Table D.5. According to the present proposal, the design domain Ω_μ for solving the problem (D.2) should be similar to the Wigner-Seitz cell of this compatible lattice. This Wigner-Seitz cell is schematized in Figure D.2.

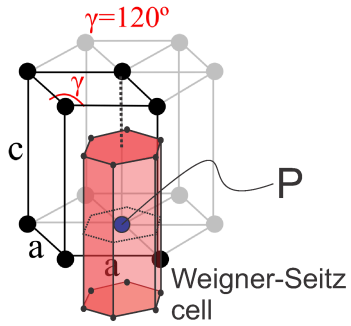

Figura D.2: Wigner-Seitz cell (in red color) of the primitive hexagonal Bravais lattice whose point group is $6/mmm$. Atom P is the Voronaoi cell center.

We remark that the periodicity directions of the microstructure to be designed are implicitly defined once the Wigner-Seitz cell is adopted because they coincide with the Bravais lattice primitive directions.

2) Furthermore, the procedure can guarantee beforehand that the homogenized elasticity tensor of the designed composite will preserve the same symmetry class to that of the target one. This feature is achieved if the solution of the optimization algorithm is constrained to attain a symmetric topology compatible with the space group of the elasticity tensor class. Taken the same example above mentioned, a target tensor with hexagonal symmetry, we can guarantee that the homogenized elasticity of the designed composite will also have hexagonal symmetry if the solved topology is compatible with the space group $P6/mmm$.

4.1. Cubic system

A particular interest in metamaterial design aims at attaining microarchitectures with effective isotropic elastic properties. Such as mentioned above, the isotropic elasticity class is not represented in Table D.1 because there is not a crystal system whose compatible point group determines this class of elastic symmetry.

Due to this feature, we focus our attention in the cubic crystal system to design isotropic metamaterials. This crystal system shows the higher possible symmetry of all crystal structures. Table D.2 describes additional details of the properties associated with the Cubic System which are used in the next numerical assessment. They can be summarized as follows:

i) There are three Bravais lattices compatible with the cubic system: Primitive, Face Centered and Body-Centered, see Table D.5 of Appendix 6. They are denoted SC, FCC, and BCC, respectively.

ii) Five-point groups and 36 spatial groups are compatible with the Cubic system.

Tabla D.2: Cubic System. Compatible point and space groups. Bravais lattices compatible with the cubic systems are: Primitive (SC), Face Centered Cubic (FCC) and Body Centered Cubic (BCC). Weigner-Seitz cells of the three Bravais lattices.

Elasticity Tensor	Crystal System	Point Groups	Space Groups		
$\begin{pmatrix} * & * & * & 0 & 0 & 0 \\ & * & * & 0 & 0 & 0 \\ & & * & 0 & 0 & 0 \\ & & & * & 0 & 0 \\ & & & & * & 0 \\ & & & & & * \end{pmatrix}$	Cubic	23	P23, P$2_1$3	F23	I23, I$2_1$3
		m$\bar{3}$	Pm$\bar{3}$, Pn$\bar{3}$, Pa$\bar{3}$	Fm$\bar{3}$, Fd$\bar{3}$	I$\bar{3}$, Ia$\bar{3}$
		432	P432, P$4_2$32, P$4_3$32, P$4_1$32	F432, F$4_1$32	I432, I$4_1$32
		$\bar{4}$3m	P$\bar{4}$3m, P$\bar{4}$3n	F$\bar{4}$3m, F$\bar{4}$3c	I$\bar{4}$3m, I$\bar{4}$3d
		m$\bar{3}$m	**Pm$\bar{3}$m**, Pn$\bar{3}$n, Pm$\bar{3}$n, Pn$\bar{3}$m	**Fm$\bar{3}$m**, Fm$\bar{3}$c, Fd$\bar{3}$m, Fd$\bar{3}$c	**Im$\bar{3}$m**, Ia$\bar{3}$d
Compatible Bravais lattice					
Wigner-Seitz cell					

Spatial groups of these lattices with high symmetries are $Pm\bar{3}m$, $Fm\bar{3}m$, $Im\bar{3}m$ which share the point group $m\bar{3}m$ guaranteeing the cubic symmetry of the effective crystal elastic properties. These spatial groups are chosen in this paper to define the initial configurations of the iterative algorithm used to solve the numerical test presented in next sub-Section.

Figure D.3-a depicts some of the point group symmetry elements of the cubic system (BCC). A crystal motif is introduced in Figure D.3-b, therefore, the symmetry element $\bar{3}$ belongs to the space group $Pm\bar{3}m$.

Table D.2 additionally depicts the three Wigner-Seitz cells of the three cubic lattices. These unit-cells preserve the point group symmetries of the underlying Bravais lattices.

5. Design of an extremal isotropic material. Numerical application.

We design the three-dimensionl microarchitecture of a metamaterial constituted of void and a stiff phase. The objective is to attain an isotropic composite displaying maximum effective shear and bulk moduli, G^{eff} and K^{eff}, respectively, for a given volume fraction of the stiff phase. A similar topology design problem has been solved and reported in the literature using the SIMP technique by Andreassen et al. (2014) and the BESO technique by Huang et al. (2011). Here, we particularly study the microarchitecture topologies obtained with the present proposal, as well as, the closeness to elastic isotropy of the designed composite overall response.

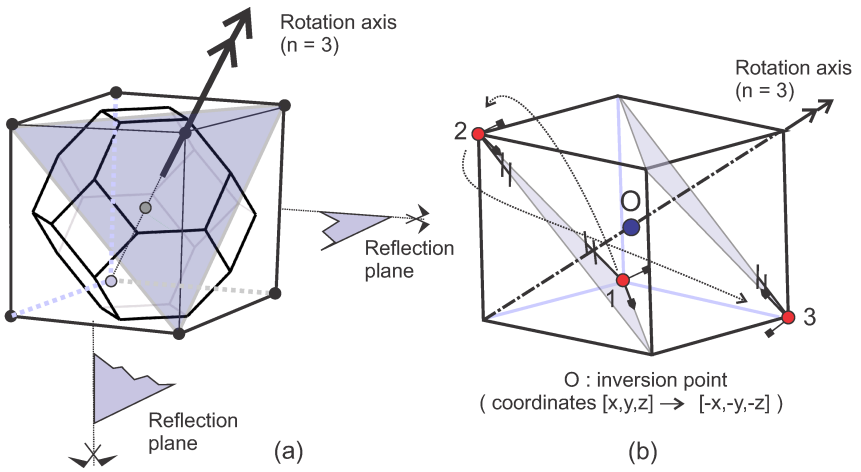

Figura D.3: a) Some point group elements of the BCC system. A threefold rotoinversion and two reflection planes. The Wigner-Seitz cell preserves these point group symmetry elements. b) Representation of the typical cubic system symmetry element $\bar{3}$. The symbol $\bar{3}$ indicates that the crystal pattern will remain identical after a $\pi/3[rad]$ rotation (transformation $1 \rightarrow 2$) followed by an inversion through the atom O (transformation $2 \rightarrow 3$).

Hashin y Shtrikman (1963) have reported bounds for the maximum and minimum effective attainable shear and stiffness moduli of two-phase composites with (quasi-) isotropic overall properties. In particular, for a composite constituted of void and a stiff phase with bulk modulus K, shear modulus G and volume fraction f, K^{eff} and G^{eff} satisfy:

$$K^{eff} \leq \frac{4GKf}{4G + 3K(1-f)} , \tag{D.3}$$

$$G^{ff} \leq G + \frac{1-f}{\frac{6}{5G}\frac{(K+2G)f}{(3K+4G)} - \frac{1}{G}} . \tag{D.4}$$

The right hand part of these expressions are the Hashin and Shtrikman upper-bounds.

Stiff phase material properties. In the present design problem, the values of bulk and shear moduli of the stiff phase are $K = 1.669[GPa]$ and $G = 0.3571[GPa]$. The void is numerically simulated by taking a contrast factor $\gamma = 1e-5$, being γ the ratio between an assumed pseudo-void moduli and the stiff phase moduli. The stiff phase void fraction is $f = 0.338$.

Target elasticity tensor for the inverse design problem: Figure D.4 displays the Hashin-Strikman upper-bounds defined by the right hand terms of the expressions (D.3) and (D.4). These bounds are plotted in the space (K^{eff}, G^{eff}) with green lines. The point with maximum shear and bulk moduli at the top-right vertex of these bounds is shown in the plot with the green point and coordinates $\hat{K} = 0.1699[GPa]$ and $\hat{G} = 0.0789[GPa]$. This point represents the properties of the target extreme metamaterial that is designed in the present assessment. In Kelvin notation, the corresponding target isotropic elastic tensor, $\hat{C}$, of an isotropic material whose bulk and shear modulus are $\hat{K}$ and $\hat{G}$ is given by :

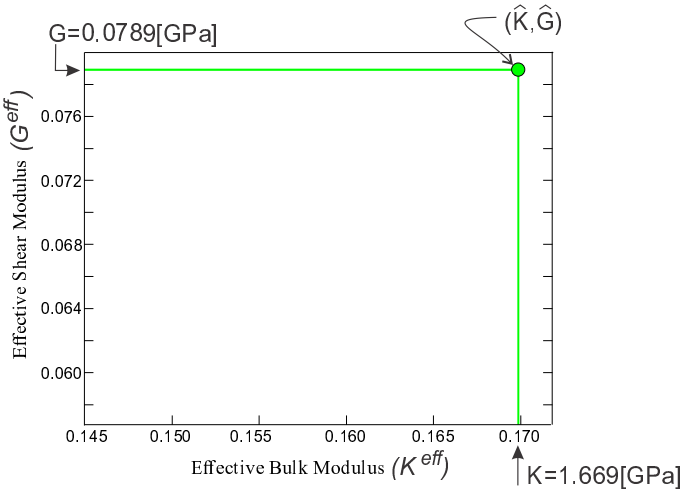

Figura D.4: Hashin-Strikman upper-bounds in the space (K^{eff}, G^{eff}).

$$\hat{C} = \begin{pmatrix} \hat{K}+\frac{4}{3}\hat{G} & \hat{K}-\frac{2}{3}\hat{G} & \hat{K}-\frac{2}{3}\hat{G} & 0 & 0 & 0 \\ & \hat{K}+\frac{4}{3}\hat{G} & \hat{K}-\frac{2}{3}\hat{G} & 0 & 0 & 0 \\ & & \hat{K}+\frac{4}{3}\hat{G} & 0 & 0 & 0 \\ & & & 2\hat{G} & 0 & 0 \\ & sym. & & & 2\hat{G} & 0 \\ & & & & & 2\hat{G} \end{pmatrix} \tag{D.5}$$

Algorithm and cells for solving the optimization problem. The tensor $\hat{C}$ of expression (D.5) and the constraint imposed on the stiff phase volume fraction are the data inputs defining the topology optimization problem (D.13).

The sensitivities of the microarchitecture solutions with the adopted cell shapes are estimated. Thus, we take three different classes of cells which are the Wigner-Setiz cells of the following Bravais lattices that are compatible with the Cubic lattice system:

- Primitive Cubic Bravais Lattice (SC)
- Body Centered Cubic Bravais Lattice (BCC)
- Face Centered Cubic Bravais Lattice (FCC)

These Bravais Lattices and the corresponding Wigner-Seitz cells are shown in Table D.3. Here, we restrict the numerical evaluations to test Cubic system lattices because they have the higher symmetry. The lattice parameter of the three cubic lattices is $a = 1$. To attain comparable results, we define the volumes of the SC, BCC and FCC Wigner-Seitz cells as 1, 0.5 and 0.25, respectively.

Tabla D.3: Cells compatible with the Cubic lattice systems used in the numerical tests

Lattice System	Bravais Lattice	Wigner-Seitz Cell
Primitive SC	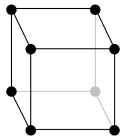	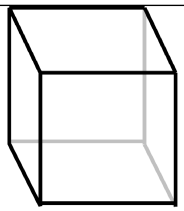
Body centered BCC	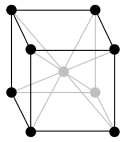	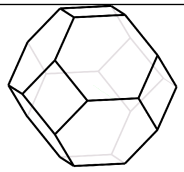
Face centered FCC	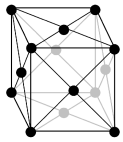	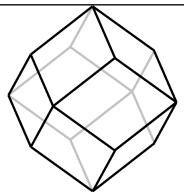

A property of the Wigner-Seitz cells is that their volumes are proportional to the number of atoms per cell in the corresponding lattice systems.

The algorithm does not enforce the microarchitecture topologies to be compatible with a specific space group symmetry. Therefore, the obtained topologies and the overall symmetry properties of the designed composites will be strictly related to the specific cells used in each test.

The optimization algorithm uses a Helmholtz filter with the parameter $r_{ls} = 0.001$, see equation (D.25) of Appendix 6. This filter prescribes a minimum section of the stiff phase that could be achieved in the material layout solutions. Therefore, the microarchitectures will display topologies with approximately one length scale. Additional discussion on this topic can be found in Lazarov y Sigmund (2011).

Finite element models of the cells. The finite elements are linear tetrahedrons. We only mesh a reduced domain of the Wigner-Seitz cells. These reduced zones are depicted in the Figure D.5 for the FCC and BCC cells and are obtained following a similar procedure to get the irreducible Brillouin zones. Subsequently, the mesh of the full Wigner-Seitz cell is generated by applying successive point symmetry operations (reflections and rotations) to the original reduced zone mesh.

This meshing technique provides a symmetric finite element mesh that preserves the higher point group symmetry of the corresponding Wigner-Seitz cell. Thus, using these symmetric meshes, different kind of material distributions, with predetermined space group symmetries, can be

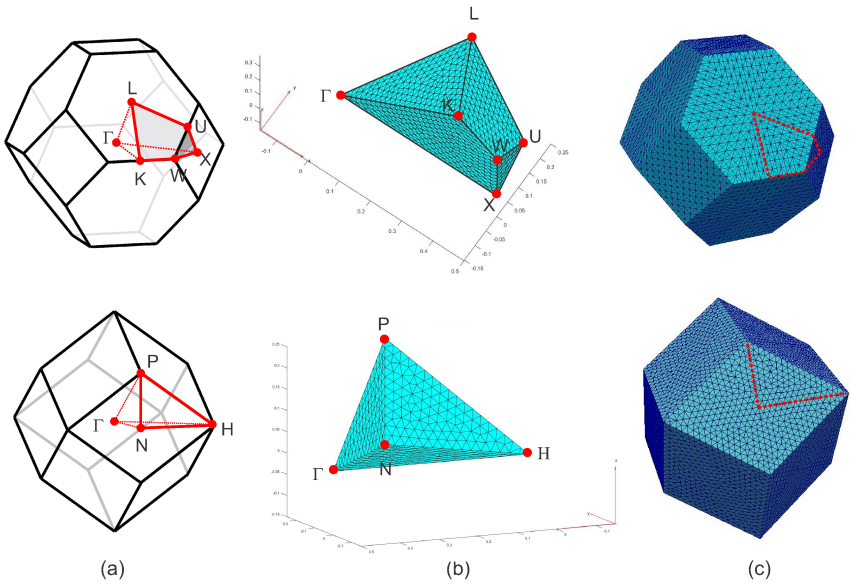

Figura D.5: Finite element meshes of the Wigner-Seitz cells (BCC and FCC cells). a) Reduced domains. Γ is the central point of the Wigner-Seitz cell; *L* the central point of a hexagonal face; X the central point of the contiguous square face; K the middle point of the edge between two hexagonal faces; U the middle point of the edge between the hexagonal and square. a) Meshes of the reduced domains. b) Meshes of the full domains obtained from the meshes of the reduced domains by successive transformations of symmetry (reflections and rotations).

easily implemented in the topology optimization algorithm.

using the so-generated symmetric meshes, different kind of material distributions, with predetermined space group symmetries, are much simpler to implement or impose in the topology optimization algorithm.

The number of finite elements in the three cells are taken such that the volume of the elements is similar in the three cases. Thus, the number of finite element in the SC, BCC and FCC cells are proportional to 1, 0.5 and 0.25, respectively.

Starting configuration of the topology optimization algorithm. Topology optimization problems aiming at microstructure design, in general, contain many local minima. This characteristic induces a strong tendency to attain different solutions, depending on the initial guess configuration (Osanov y Guest (2016)). Consequently, it is important to test several starting configurations to evaluate and compare the so-obtained solutions.

In the present numerical assessment, three initial configurations are tested: a) a spherical void placed around the central point of the cell; b) a cellular-like configuration with closed walls. The walls are coincident with the cell faces and the walls are of uniform thickness; c) a truss-like configuration with bars of identical sections joining the Wigner-Seitz cell vertices.

Assessment of the cell capacity for capturing isotropic responses. As already mentioned above, the isotropic elastic response of the designed composite cannot be guaranteed by only enforcing a stiff phase material layout consistent with the space group of some particular crystal system. This

aspect of the three-dimensionl problem introduces a marked difference with respect to the 2D case which has been analyzed in the previous contribution by the authors, see Podesta et al. (2018).

In consequence, we introduce an indicator to find how close are the homogenized properties of the designed composites to isotropic responses. Based on this indicator and without imposing implicitly the isotropy constraint into the formulation of the optimization algorithm, we assess which cell provides a better response to capture this elastic feature.

This indicator is computed as follows. Given an arbitrary elasticity tensor $\mathbf{C}^h$, we define an isotropic elastic tensor of comparison by following the procedure proposed by Meille y Garboczi (2001). First, using the components of $\mathbf{C}^h$, it is evaluated:

$$C_{11}^{iso} = \frac{1}{5}(C_{11}^h + C_{22}^h + C_{33}^h) + \frac{2}{15}(C_{12}^h + C_{13}^h + C_{23}^h) + \frac{4}{15}(C_{44}^h + C_{55}^h + C_{66}^h) \tag{D.6}$$

$$G^{iso} = \frac{1}{15}(C_{11}^h + C_{22}^h + C_{33}^h) - (C_{12}^h + C_{13}^h + C_{23}^h) + 3(C_{44}^h + C_{55}^h + C_{66}^h) \tag{D.7}$$

$$K^{iso} = C_{11}^{iso} - \frac{4}{3}G^{iso} \tag{D.8}$$

and with the so-determined bulk and shear moduli, K^{iso} and G^{iso}, an isotropic tensor $\mathbf{C}^{iso}$ is computed with expression (D.5). Our assumption is that this is the closer isotropic tensor to the original $\mathbf{C}^h$. It is taken as the reference tensor to perform the following analysis.

Finally, we introduce a coefficient of anisotropy

$$\chi = \|C^h - C^{iso}\| \tag{D.9}$$

which measures the distance between C^h and C^{iso}. A zero value of this coefficient indicates that C^h is isotropic. Contrarily, a large value of χ indicates that C^h is far from being isotropic.

Analysis of results

Figure D.6-a plots the results for the nine different cases in the space K^{eff} vs. G^{eff}. They are compared with the upper Hashin-Strikman bounds, also plotted in the same Figure. The results have been computed using the three Wigner-Seitz cells: Primitive Cubic (SP), Face Centered Cubic (FFC) and Body-Centered Cubic (BCC) and the three initial configurations. The symbols identify the cell types and the colors identify the initial configurations.

The corresponding coefficients of anisotropy, defined by expression (D.9), are plotted in Figure D.6-b. Independently of the adopted initial configurations, we note from this plot that the BCC cell provides microarchitecture topologies whose effective elastic properties tend to be more isotropic respect to the solutions provided by the other two alternative cells.

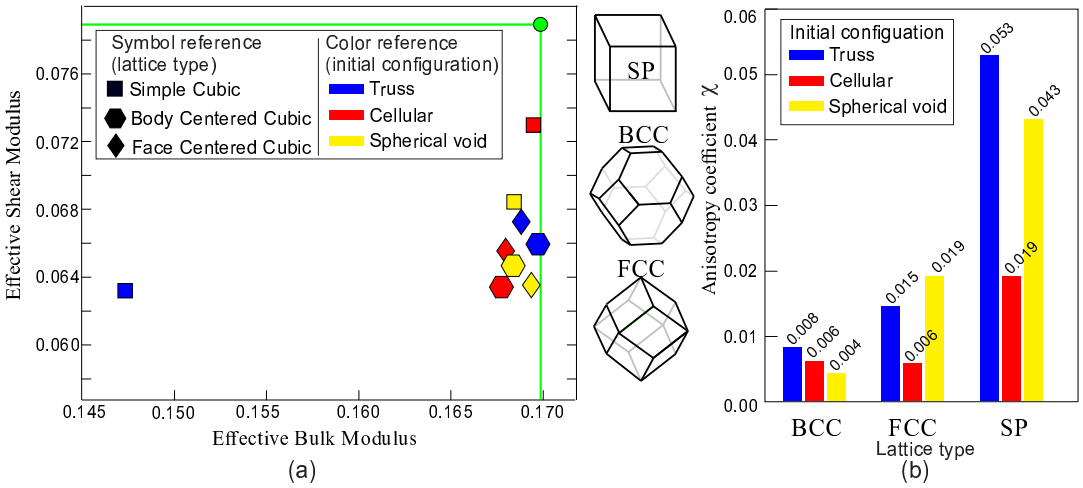

Figura D.6: a) Space K^{eff} vs. G^{eff}: the results obtained with Primitive (SP), Face Centered (FFC) and Body-Centered (BCC) cubic Wigner-Seitz cells are superposed to the Hashin-Strikman upper bounds displayed in green lines. The initial configurations adopted in each case are distinguished with blue, red and yellow colors; b) Anisotropy coefficients χ for the nine tested case.

Figure D.7 depicts the material distributions obtained with these cells and with the spherical void initial configurations. Two views of each solutions are displayed; the full cell solutions are shown in Figures b), d) and f) and the cells cut with middle planes are shown in Figures a), c) and e). Note that the material distributions assimilate to hollow topologies. Also, note the highly symmetric pattern of the material layouts obtained with the algorithm even without imposing any symmetry constraint.

Table D.4 shows the components of the target effective elasticity tensor computed with expression (D.5). These components are compared with the homogenized tensor values obtained with the SP, BCC and FCC cells and cellular-like initial configurations. We observe from Figure D.6-a that, apparently, the SP solution display closer values to the target ones. However, the identity $\hat{C}_{33} = (\hat{C}_{11} - \hat{C}_{12})$, which must be satisfied by isotropic tensors, is more tightly verified with the BCC and FCC solutions if compared with the SP solution. This behavior, which is not transparent from results in Figure D.6-a, is confirmed with those depicted in Figure D.6-b. The stiff phase volume fractions in these solutions are accurate to the third figure ($f = 0.338$).

6. Conclusions

New contributions for synthesizing three-dimensionl microarchitectures of elastic composites are proposed. These contributions are addressed to enlarge the range of attainable microarchitectures in the framework of the inverse design problems formulated as homogenization-based topology optimization algorithms

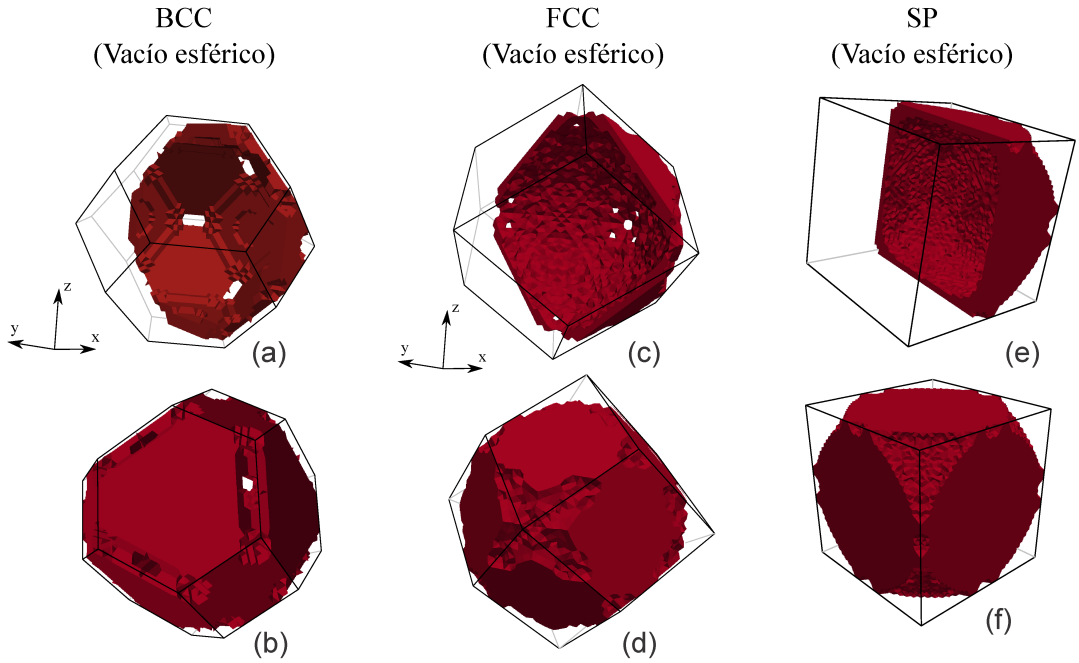

Figura D.7: Microarchitectures with maximun bulk and shear moduli: a) and b) correspond to BCC cells (cutted with a middle plane (a) and full cell solutions (b), respectively); c) and d) correspond to FCC cells (cutted with a middle plane (c) and full cell solutions (d), respectively); e) and f) correspond to SP cells (cutted with a middle plane (e) and full cell solutions (f), respectively).

Tabla D.4: Computed effective elasticity tensors

	C_{11}	C_{22}	C_{33}	C_{44}	C_{55}	C_{66}	C_{12}	C_{13}	C_{23}
Target	0.2750	0.2750	0.2750	0.1578	0.1578	0.1578	0.1172	0.1172	0.1172
SP Cellular	0.2732	0.2732	0.2732	0.1398	0.1394	0.1392	0.1177	0.1177	0.1179
BCC Cellular	0.2559	0.2571	0.2552	0.1272	0.1274	0.1276	0.1246	0.1243	0.1244
FCC cellular	0.2570	0.2572	0.2569	0.1286	0.1274	0.1284	0.1242	0.1239	0.1241

Based on the symmetry of the target elastic properties, we propose a procedure for selecting a spatial three-dimensionl domain where the topology optimization algorithm is solved. Furthermore, this procedure also provides a route to enforce the symmetry of the material layout within this spatial domain compatible with predefined crystal spatial groups. The so-proposed rules are derived from concepts widely developed in crystallography. This contribution is a generalization of a procedure that has been previously presented by the authors in 2D problems.

The procedure has been tested by synthesizing an isotropic elastic material with prescribed maximum effective shear and bulk moduli. The results, which have been obtained without implicitly imposing a constraint of overall isotropic response, show that the BCC cells provide the tighter isotropic solution if compared with alternative cubic cells, no matter the initial configuration adopted for the topology optimization algorithm.

Furthermore, by considering that the volume ratio between the SC and BCC cells is two; then, the size of the problem with the BCC cell is half of the problem size using the SC cell for similar resolutions.

An additional advantage of the proposed methodology is that very simple and precise numerical techniques, widely reported in the literature, can be used to generate the three-dimensionl Wigner-Seitz cells. Algorithms for determining the Wigner-Seitz cells of arbitrary distributions of points in the space, particularly the Bravais lattice atoms, are well developed in Computational Mechanics and can be easily used to determine the Wigner-Seitz cells of the 14 Bravais lattice types. Additionally, the technique based on meshing a reduced domain, and subsequently generate the mesh of the full cell through space group symmetry operations, facilitates the implementation of different types of symmetry constraints on the material layout.

Acknowledgment

The authors acknowledge the financial support from CONICET and ANPCyT (grants PICT 2014-3372 and 2016-2673).

Appendix D1: Structure and Symmetry of Crystals

D1.1. Bravais lattices

Crystals are periodic structures, with periodicity along three linearly independent directions. This property is formalized by introducing the concept of a lattice. Lattices are defined by three vectors $\mathbf{a}$, $\mathbf{b}$ and $\mathbf{c}$, the primitive vectors of the lattice, which form a basis in $\mathbb{R}^3$. The set of abstract

Tabla D.5: Catalog of the 14 Bravais lattices classified according to their lattice system

Lattice System	Point Group	Primitive	Base-Centered	Body-Centered	Face-Centered
Triclinic	$\bar{1}$	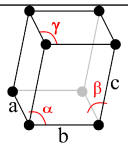 $P\bar{1}$			
Monoclinic	$2/m$	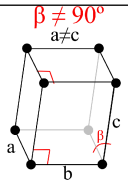 $P2/m$	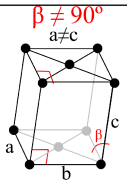 $C2/m$		
Orthorhombic	mmm	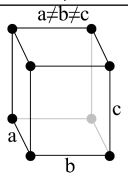 $Pmmm$	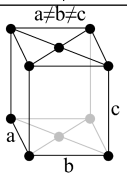 $Cmmm$	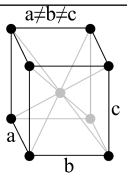 $Immm$	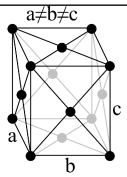 $Fmmm$
Tetragonal	$4/mmm$	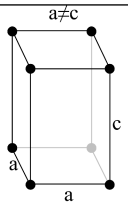 $P4/mmm$		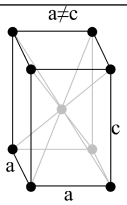 $I4/mmm$	
Rhombohedral	$\bar{3}m$	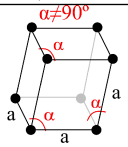 $R\bar{3}m$			
Hexagonal	$6/mmm$	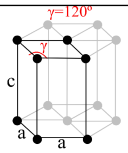 $P6/mmm$			
Cubic	$m\bar{3}m$	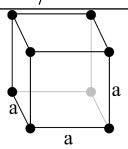 $Pm\bar{3}m$		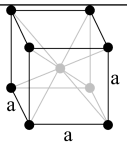 $Im\bar{3}m$	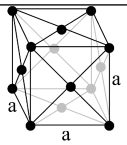 $Fm\bar{3}m$

points, or atoms

$$\mathbf{L} := \{l\mathbf{a} + m\mathbf{a} + n\mathbf{c} \mid l, m, n \in \mathbb{Z}\} \tag{D.10}$$

constitute a *Bravais lattice*. In the three-dimensional space, according to the relationship between the vectors of the basis, we can distinguish 14 types of Bravais lattices which are characterized in Table D.5. Notice that they are collected in a set of lattice systems.

Unit Cell

The space $\mathbb{R}^3$ can be subdivided into cells of finite volume having all the same shape. They are called *unit cells* if these volumes cover all the space without overlapping when are translated by the vectors of the lattice $\mathbf{L}$.

The *primitive unit cell* is a standard cell that consists of the parallelepiped generated by the primitive vectors of the lattice (third column in Table D.5). Although all the 14 Bravais lattices have a primitive unit cell constructed in this way, in many cases, it is more convenient to use a *conventional cell* in order to better visualize the structure of the lattices (columns 4 to 6 in Table D.5). These conventional cells are not necessarily unit cell because they could contain more than one lattice point and consequently their volumes are larger than the volumes of the primitive unit cell.

Another standard construction for the unit cells is the Wigner-Seitz cell. This cell consists of those points of $\mathbb{R}^3$ that are closer to a given lattice point than to any other point of $\mathbf{L}$ (see Table D.3 for cubic lattices).

Two remarkable features of the Wigner-Seitz cells are noted: *i)* its volume is the minimum one that a unit cell can have since, by construction, this cell contains only one lattice atom; *ii)* it preserves the same point group symmetry of the corresponding Bravais lattice. Primitive unit cells, in general, do not have this property.

D1.2. Crystallographic point groups

Point symmetries are symmetry operations that leave at least one point fixed. There are five types of point symmetries in 3D. They are the inversion ($\bar{1}$), rotations (2, 3, 4 or 6), reflection (m), rotation-inversion ($\bar{2} = m$, $\bar{3}$, $\bar{4}$ or $\bar{6}$) and the identity (1). Not all rotations are allowed because they must be compatible with the discrete translation symmetry of the crystals, that is the reason because they are called *crystallographic point groups*.

After applying the crystallographic restriction theorem, a total of 32 point groups are all the possible symmetries that a given crystal in 3D can have. They are enumerated in the third column of Table D.1. By *"crystal"* we mean a lattice with a base or motif. Not all the point groups are compatible with all lattices, but many of them are compatible with the same group of lattices. This

fact allows a classification of point groups in *crystal systems*, which can be seen in the second column of Table D.1.

The lattices themselves (or crystals without a base) have their own point group, which can be seen in the second column of Table D.5. Lattices with the same point group are grouped in *lattice systems* and are shown in the first column of the table.

Unit cells are not unequivocally defined and they can have practically any symmetry. However, as we mentioned above, Wigner-Seitz cells preserve the same symmetry as the associated Bravais lattices, and therefore, they have the same point groups shown in Table D.5. As with the lattice, we are considering here Wigner-Seitz cells without a motif in its interior.

D1.3. Space groups

On one hand, the discrete translation symmetry of the crystal restricts the infinite possible point groups to only 32, but, on the other hand, it adds two new kind of symmetries. One type corresponds to the glide planes (denoted by a, b, c, n or d), which consist of a reflection followed by a translation. The other type corresponds to the screw axis (e.g., 3_2, 4_1, 6_3), which represent a rotation followed by a translation.

Combining these two symmetry types with the 32 point groups, 270 space groups can be classified. In the forth column of Table D.1, we can see the amount of them compatible with each crystal and lattice system.

Besides the letters and numbers corresponding to the symmetries, in the nomenclature of space groups also appear a capital letter that helps to identify the compatible Bravais lattice (e.g., P for principal, F for face centered, I for body centered). In Table D.5, the space groups of the 14 Bravais lattices can be seen below the images, and in Table D.2, the 36 space groups compatible with the 3 cubic lattices are enumerated.

Appendix D2: Solving the topology optimization problem with Topological Derivative Algorithm

We summarize in this Appendix the topology optimization algorithm that is used for solving the numerical test here presented. The algorithm is a well-established technique reported in the papers Amstutz y Andrä (2006), Amstutz et al. (2010). It is a level-set method (LSM) with sensitivity computed through the topological derivative, see Novotny y Sokołowski (2012) and Ammari et al. (2008). This technique has been implemented in a 3D code using an Augmented-Lagrangian scheme proposed by Lopes et al. (2015).

Let us introduce a smooth level set-funtion defined in the microcell Ω_μ, $\psi \in C^0(\Omega_\mu)$, satisfying

$$\psi(\mathbf{y}) = \begin{cases} < 0 & \forall \mathbf{y} \in \Omega_\mu^2 \\ > 0 & \forall \mathbf{y} \in \Omega_\mu^1 \\ 0 & \text{in the interfaces} \end{cases} , \tag{D.11}$$

then, the characteristic functions $\chi(\mathbf{y})$ in Ω_μ, given by expression (D.1), can be redefined as follows:

$$\chi(\psi) = \begin{cases} 0 & \forall \psi \leq 0 \\ 1 & \forall \psi > 0 \end{cases} . \tag{D.12}$$

and the problem (D.2) is rephrased as:

$$\begin{aligned} &\min_{\psi \in C^0} \ \|\mathbf{C}^h(\psi) - \hat{\mathbf{C}}\| \\ &\text{such that: } V^h(\psi) - V^{obj} = 0 \ . \end{aligned} \tag{D.13}$$

By making use of an augmented Lagrangian technique, see Lopes et al. (2015), the problem (D.13) is rewritten as follows:

$$\max_{\lambda} \min_{\psi} \mathcal{T}(\psi, \lambda), \tag{D.14}$$

with:

$$\mathcal{T}(\psi, \lambda) = \|\mathbf{C}^h(\psi) - \hat{\mathbf{C}}\| + \lambda V_1 + \frac{\alpha}{2} (V_1)^2 \tag{D.15}$$

where $V_1 = \int_{\Omega_\mu} \chi(\psi) \ d\Omega$ is the volume fraction of the hard phase, λ is the Lagrange multiplier and α is the penalty parameter of the augmented term.

The algorithm for solving the problem (D.14) has one loop, where α is hold fixed and λ is modified iteratively.

The minimum of $\mathcal{T}$ is searched with a descent direction algorithm. For problem (D.14), the topological derivative used to estimate the descent direction is given by

$$D_\psi \mathcal{T}(\psi, \lambda) = \frac{(\mathbf{C}^h - \hat{\mathbf{C}}) : D_\psi \mathbf{C}^h}{\|\mathbf{C}^h - \hat{\mathbf{C}}\|} + \lambda \mathbf{1} + \alpha V_1 \mathbf{1} \tag{D.16}$$

where $D_\psi \mathbf{C}^h$ is the topological derivative of the homogenized elasticity tensor and is given by the expressions:

$$D_\psi \mathbf{C}^h = m_1 \left(m_2 (\mathbf{1} \otimes \mathbf{1}) + 2\mathbb{I} \right) \ ; \tag{D.17}$$

the symbols $\mathbf{1}$ and $\mathbb{I}$ represent the second and fourth order unit tensor, respectively, and the coefficient m_1 and m_2 are:

$$\begin{aligned} m_1 &= \frac{15\mu\delta_\mu(\nu-1)}{15\mu(1-\nu)+2\delta_\mu(5\nu-4)}; \\ m_2 &= \frac{\delta_\lambda\left[15\mu\lambda(1-\nu)+2\lambda\delta_\mu(5\nu-4)\right]-2\delta_\mu(\lambda\delta_\mu-5\mu\nu\delta_\lambda)}{5\delta_\mu\left[3\mu\lambda(1-\nu)-3\mu\nu\delta_\lambda-\lambda\delta_\mu(1-2\nu)\right]}; \end{aligned} \tag{D.18}$$

with $\delta_\lambda = \lambda - \lambda_0$; $\delta_\mu = \mu - \mu_0$ and $(\lambda;\mu)$ being the Lamè parameters of the base material and $(\lambda_0;\mu_0)$ being the Lamè parameters of the material introduced as a spherical perturbation. The Poisson ratio of the base material is ν. Additional description and properties of this tensor can be found in Ammari et al. (2008), where it is called the Elastic Moment Tensor (EMT).

Then, we define the function :

$$g(\mathbf{y}) = \begin{cases} -(D_\psi \mathcal{T}) & if : \psi < 0 \\ \\ +(D_\psi \mathcal{T}) & if : \psi > 0 \end{cases}, \tag{D.19}$$

The updating formula for ψ is defined by

$$\psi^{k+1} = \psi^k + \tau g, \tag{D.20}$$

with the scaling factor τ being determined by means of a line search technique.

The Lagrange multiplier λ is updated using the Uzawa algorithm

$$\lambda^{l+1} = \text{máx}(0, \lambda^l + \alpha \int_{\Omega_\mu} \chi(\psi)\, d\Omega). \tag{D.21}$$

The penalty parameter α is hold fixed during the full process.

A local optimality criterion of problem (D.14), see Amstutz (2011), is given by the condition

$$D_\psi \mathcal{T} > 0 \quad ; \quad \forall \mathbf{y} \in \Omega_\mu \tag{D.22}$$

which can be implemented by verifying the inequality

$$\left[\frac{\int_{\Omega_\mu} g\psi \, dV}{\|g\|_{L^2}\|\psi\|_{L^2}}\right] > (1 - tol_\psi) \; ; \tag{D.23}$$

combined with

$$\|\mathbf{C}^h - \hat{\mathbf{C}}\| < tol_C \; ; \tag{D.24}$$

he terms $to\psi$ and tol_C are tolerances to zero.

Additionally, a Helmholtz-type filter taken from Lazarov y Sigmund (2011) is implemented. The smooth level set function $\tilde{\psi}$ in each iteration $(k+1)$-iteration is computed by solving the field equation:

$$r_{ls}^2 \nabla^2 \tilde{\psi}^{k+1} + \tilde{\psi}^{k+1} = \psi^{k+1} \tag{D.25}$$

with homogeneous boundary conditions $d(\tilde{\psi}^{k+1})/d\mathbf{n} = 0$ on the boundary of Ω_μ. The filter characteristic size r_{ls} determines the minimum length scale in the topology optimization problem.

Bibliografía

Ammari H., Calmon P., y Iakovleva E. Direct elastic imaging of a small inclusion. *SIAM Journal on Imaging Sciences*, 1(2):169–187, 2008.

Amstutz S. Analysis of a level set method for topology optimization. *Optimization Methods and Software*, 26(4-5):555–573, 2011.

Amstutz S. y Andrä H. A new algorithm for topology optimization using a level-set method. *Journal of Computational Physics*, 216(2):573–588, 2006.

Amstutz S., Giusti S., Novotny A., y de Souza Neto E. Topological derivative for multi-scale linear elasticity models applied to the synthesis of microstructures. *International Journal for Numerical Methods in Engineering*, 84(6):733–756, 2010.

Andreassen E., Lazarov B., y Sigmund O. Design of manufacturable 3d extremal elastic microstructure. *Mechanics of Materials*, 69(1):1–10, 2014.

Bendsoe M. y Sigmund O. *Topology optimization: theory, methods, and applications*. Springer Science & Business Media, 2003.

Cadman J., Zhou S., Chen Y., y Li Q. On design of multi-functional microstructural materials. *Journal of Materials Science*, 48(1):51–66, 2013.

Coelho P., Amiano L., Guedes J., y Rodrigues H. Scale-size effects analysis of optimal periodic material microstructures designed by the inverse homogenization method. *Computers & Structures*, 174:21–32, 2016.

Diaz. A. y Benard A. Designing materials with prescribed elastic properties using polygonal cells. *International Journal for Numerical Methods in Engineering*, 57(3):301–314, 2003.

Feyel F. y Chaboche J. Fe2 multiscale approach for modelling the elastoviscoplastic behaviour of long fibre sic/ti composite materials. *Computer methods in applied mechanics and engineering*, 183(3-4):309–330, 2000.

Hashin Z. y Shtrikman S. A variational approach to the theory of the elastic behaviour of multiphase materials. *Journal of the Mechanics and Physics of Solids*, 11(2):127–140, 1963.

Huang X., Radman A., y Xie Y. Topological design of microstructures of cellular materials for maximum bulk or shear modulus. *Computational Materials Science*, 50(6):1861–1870, 2011.

Huang X., Zhou S., Xie Y., y Li Q. Topology optimization of microstructures of cellular materials and composites for macrostructures. *Computational Materials Science*, 67:397–407, 2013.

Lazarov B. y Sigmund O. Filters in topology optimization based on helmholtz-type differential equations. *Int. J. Numer. Meth. Engng*, 86:765–781, 2011.

Li H., Luo Z., Gao L., y Walker P. Topology optimization for functionally graded cellular composites with metamaterials by level sets. *Computer Methods in Applied Mechanics and Engineering*, 328:340–364, 2018.

Lopes C., dos Santos R., y Novotny A. Topological derivative-based topology optimization of structures subject to multiple load-cases. *Latin American Journal of Solids and Structures*, 12(5):834–860, 2015.

Meille S. y Garboczi E. Linear elastic properties of 2d and 3d models of porous materials made from elongated objects. *Modelling and Simulation in Materials Science and Engineering*, 9(5):371, 2001.

Méndez C., Podestá J., Lloberas-Valls O., Toro S., Huespe A., y Oliver J. Computational material design for acoustic cloaking. *International Journal for Numerical Methods in Engineering*, 112(10):1353–1380, 2017.

Michel J., Moulinec H., y Suquet P. Effective properties of composite materials with periodic microstructure: a computational approach. *Computer methods in applied mechanics and engineering*, 172(1-4):109–143, 1999.

Neves M., Rodrigues H., y Guedes J.M. Optimal design of periodic linear elastic microstructures. *Computers & Structures*, 76(1-3):421–429, 2000.

Novotny A. y Sokołowski J. *Topological derivatives in shape optimization*. Springer Science & Business Media, 2012.

Nye J. *Physical Properties of Crystals: Theri representation be tensors and matrices*, volumen 146. Clarendon Press- Oxford, 2006.

Oliver J., Ferrer A., Cante J., Giusti S., y Lloberas-Valls O. On multi-scale computational design of structural materials using the topological derivative. En *Advances in Computational Plasticity*, páginas 289–308. 2018.

Osanov M. y Guest J. Topology optimization for architected materials design. *Annual Review of Materials Science*, 46:211–233, 2016.

Podesta J., Mendez C., Toro S., y Huespe A. Symmetry considerations for topology design in the elastic inverse homogenization problem. *submitted*, páginas 1–43, 2018.

Podestá J., Méndez C., Toro S., Huespe A., y Oliver J. Material design of elastic structures using voronoi cells. *International Journal for Numerical Methods in Engineering*, 2018.

Sigmund O. Materials with prescribed constitutive parameters: an inverse homogenization problem. *International Journal of Solids and Structures*, 31(17):2313–2329, 1994.

Sigmund O. Tailoring materials with prescribed elastic properties. *Mechanics of Materials*, 20(4):351–368, 1995.

Sigmund O. A new class of extremal composites. *Journal of the Mechanics and Physics of Solids*, 48(2):397–428, 2000.

Sólyom J. *Fundamentals of the Physics of Solids: Volume 1: Structure and Dynamics*, volumen 1. Springer Science & Business Media, 2007.

Souvignier B. A general introduction to space groups. *International Tables for Crystallography*, A:22–41, 2016. Chapter:1.3.

Ting T. *Anisotropic elasticity: theory and applications*. 45. Oxford University Press, 1996.

Wang F., Lazarov B., y Sigmund O. On projection methods, convergence and robust formulations in topology optimization. *Structural and Multidisciplinary Optimization*, 43(6):767–784, 2011.

Wang Y., Luo Z., Zhang N., y Kang Z. Topological shape optimization of microstructural metamaterials using a level set method. *Computational Materials Science*, 87:178–186, 2014.

Anexo E

Homogenized elasticity tensor database of periodic composites with microarchitectures displaying symmetric topologies

A continuación se presenta la documentación para el uso de las herramientas computacionales producidas en el contexto de esta tesis. Dichas herramientas se encuentran disponibles en un repositorio de acceso público y tienen como fin proveer al usuario de:

- Algoritmo de obtención de la clase de simetría y expresión en coordenadas naturales de un tensor elástico arbitrario de estado plano.
- Base de datos de tensores homogeneizados para problemas en estado plano.
- Algoritmo de generación de base de datos para geometrías parametrizadas para el usuario.

J.M. Podestá, C. Méndez, S. Toro, A.E. Huespe, *"Homogenized elasticity tensor database of periodic composites with microarchitectures displaying symmetric topologies"*, **Mendeley Data repositories.** DOI: 10.17632/7kgf9xnrhb.1

Homogenized elasticity tensor database of periodic composites with microarchitectures displaying symmetric topologies

J.M. Podestá[1], S. Toro[1], C. Méndez[1], A.E. Huespe[1,2,3][1]

[1]CIMEC-UNL-CONICET, Predio Conicet "Dr Alberto Cassano", CP 3000 Santa Fe, Argentina

[2]Centre Internacional de Metodes Numerics en Enyinyeria (CIMNE),Campus Nord UPC.

[3]E.T.S d'Enginyers de Camins, Canals i Ports, Technical University of Catalonia (Barcelona Tech)

Campus Nord UPC, Mòdul C-1, c/ Jordi Girona 1-3, 08034, Barcelona, Spain

Keywords: database of homogenized elasticity tensors; metamaterial design; elastic symmetry; topology optimization; inverse homogenization; tailored elastic properties.

Information contained in the DataSet

A database containing homogenized plane elasticity tensors that correspond to periodic biphasic composites with parameterized microstructure is stored in this DataSet. The code used to build this database is also included in the DataSet.

Details of the database construction have been described in the papers Podestá et al. (2018) and Podesta et al. (2018). In those papers, this database is used as a tool for the microarchitecture topology design of elastic metamaterials. The relevant theory and formulation supporting the information stored in the database have been described in both referenced works. The users of the present DataSet are addressed to the mentioned papers for consulting additional details.

[1]Corresponding author. E-mail address: storo@cimec.unl.edu.ar (S. Toro).

1. Data structure, Files and Folders

The files included in the present DataSet are stored in two folders and correspond to the following items:

i) A database of the homogenized elasticity tensors constituted by a set of Matlab files, with extension `mat`. They are stored in the folder "`Homogenized Elastic Tensor Database`". The data in these files can be loaded and worked out with Matlab.

ii) The code to generate or to modify the database of item *i)* above are stored in the folder called "`Database generation code`".
This code has been tested in MATLAB 2017a with OS: Windows 10 64 bits, Linux Fedora 64 bits and Ubuntu 14 64 bits.

Both items are additionally explained in the following part of this document.

1.1. Database of the homogenized plane elasticity tensors

The database stores the homogenized plane elasticity tensors resulting from periodic biphasic (a stiff phase and a void phase) composites having parameterized microstructures. The homogenized tensors stored in the present database correspond to plane stress hypothesis.

Four parameters characterize the microstructure of the composite.

This parametrization is based on the underline Bravais lattice which is related to the microstructure (see Podesta et al. (2018)). The five Bravais lattices in plane problems are depicted in Figure E.1. A coordinate system (x, y) shown in Figure E.2-a is introduced to determine the directions along which the Bravais lattice atoms are distributed. The adopted x-axis is the bisector of the segments parallel to the primitive lattice vectors $\mathbf{a}_1$ and $\mathbf{a}_2$. The unit cell of the microstructure is defined in this coordinate system and coincides with the Wigner-Seitz cell (Voronoi cell) of the lattice.

The four parameters characterizing the composite microstructure are next described. The notation adopted is defined in Figures E.2a, b, c and e.

i) Two parameters identify the types of Bravais lattice and the Voronoi cell geometry associated with the periodic microarchitecture. They are (see Figure E.2-a): `m_angle` which is the angle α formed between the two primitive lattice vectors $\mathbf{a}_1$ and $\mathbf{a}_2$ and `m_relVec` which is the ratio $\|\mathbf{a}_2\|/\|\mathbf{a}_1\|$.

Discret sets of values `m_alpha` and `m_relVec` are taken to generate different microstructures. These values conform a nun-uniform grid in the $\mathbf{R}^2$ space (`m_alpha, m_relVec`).

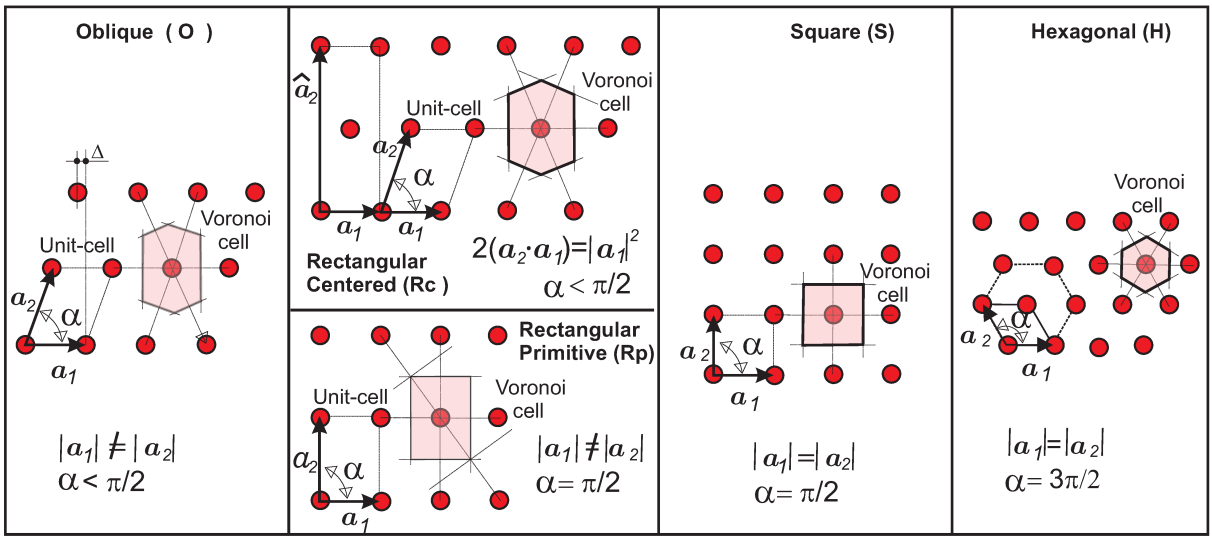

Figura E.1: The five types of Bravais lattices in plane problems. They are characterized by the two primitive vectors $\mathbf{a}_1$ and $\mathbf{a}_2$.

The grid cover the reduced space depicted in grey in the Figure E.2-b and c. Every grid point in this space is taken to compute the corresponding microstructure, associated with such a point, and its homogenized elasticity tensors. The density of points in the grid is defined with the variables `nDivAng` and `nDivGama` governing the number of divisions in the axis `m_angle` and `m_relVec`, respectively. The database files in the present DataSet have been computed with a 6283 grid points covering the reduced space.

ii) One parameter identifies the void fraction of the stiff phase. Implicitly, this parameter defines the thickness "e" of the bars constituting the microarchitectures, see Figure E.2-d and e. The name given to each file in the database, stored in the folder "`Homogenized Elastic Tensor Database`", identify the volume fraction with the characters: `_SolFrac`. For example: `_SolFrac070000` identify the solution with a volume fraction of value $f = 0.7$.

iii) A fourth parameter identifies the layout, or pattern, of the stiff material distribution within the micro-cell. The database is built using two patterns shown in Figure E.2-d and e, and therefore, there are two values of this parameter. They are identified in the computed homogenized tensors through the file name characters `PoisPos` and `PoisNeg` that are stored in the database and agree with material layout denominations given in Figure E.2-d and e. Several solutions have been computed with the material layout denoted `PoisNeg` by changing the reentrant factor r, shown in Figure E.2-e. The value of the reentrant factor can be identified in the database files with extension `mat` using the characters `fE` followed by the reentrant factor.

The Young's modulus and Poisson's ratio of the stiff phase are $E = 1.GPa$ and 0.3, respec-

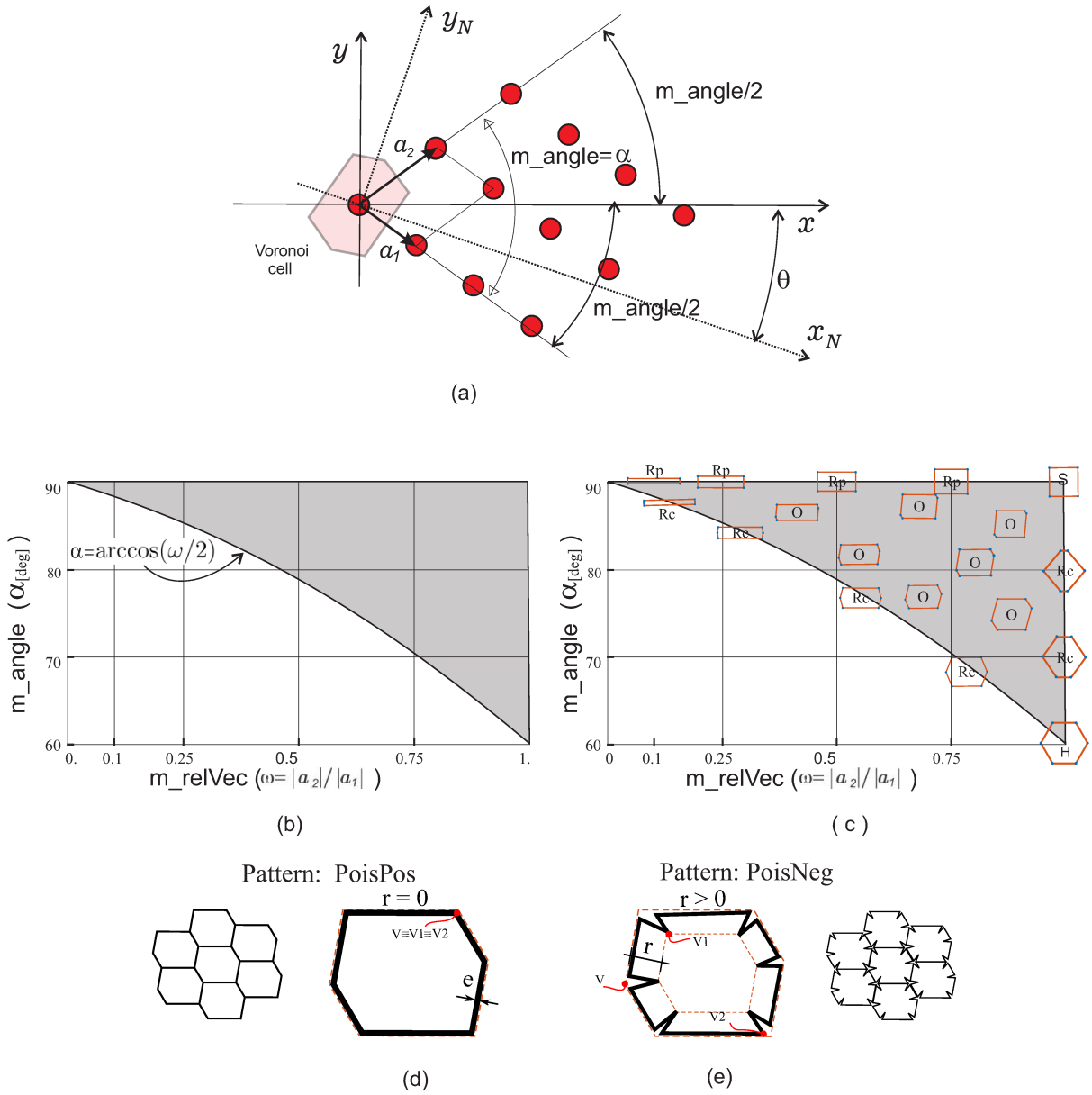

Figura E.2: Microarchitecture parametrization of the composites: a) Two parameters, `m_alpha` ($= \alpha$) and `m_relVec` ($= \|\mathbf{a}_2\|/\|\mathbf{a}_1\|$), identify the different types of Bravais lattices characterizing the periodic microarchitecture. b-c) Reduced region of the plane (`m_alpha, m_relVec`) defining all the possible Bravais lattices. d-e) One parameter identifies the pattern of the stiff material distribution within the micro-cell (`PoisPos, PoisNeg`), the void fraction parameter, f, is defined through the thickness e of the bars.

tively. For the particular kind of composites here assumed, the homogenized elasticity tensors is a homogeneous function of degree 1 respect to the stiff phase elasticity tensor, it scales proportionaly with the Young's modulus of the stiff phase. This is useful for adjusting the use of the homogenized tensors stored in the database to a wider range of composites.

Every file with extension `mat` of the database is denoted with initial characters identifying the stiff phase layout and final characters identifying the stiff phase volume fraction. The stored data in those files are described in Table E.1. The main parameter stored in those files is the homogenized elasticity tensors (`m_CHsSim`) which, for every grid point, is a vector of dimension 6 (Voigt notation). The stored components are organized as follows: $[C_{11}, C_{12}, C_{22}, C_{13}, C_{23}, C_{33}]$. The components of the tensor (`m_CHsSim`) are given in the coordinate system (x, y), see Figure E.2-a.

Variable name	Size	Type	Description
`E`	1x1	double	Young's modulus stiff phase
`a`	1x1	double	modulus of the primitive vector $\mathbf{a}_1$
`e_Tol`	1x1	struct	several tolerances, micro-cell geometry
`m_AreaMC`	6283x1	double	micro-cell area
`m_CHsSim`	6283x6	double	homogenized elasticity tensor (Voigt notation)
`m_ContrMallador`	6283x1	double	meshing error message number
`m_ContrPeriod`	6283x1	double	periodic boundary condition error message number
`m_EspPar`	6283x1	double	bar thickness- pattern geometry
`m_EspParErrRV`	6283x1	double	error of the thickness computation
`m_RelSol`	6283x1	double	computed stiff phase volume fraction
`m_angle`	6283x1	double	angle α of the Bravais lattice
`m_facInt`	6283x1	double	reentrant factor for layout `PoisNeg`
`m_facLad`	6283x1	double	side factor for layout `PoisNeg`
`m_hMaxEF`	6283x1	double	maximum finite element size of the cell mesh
`m_nEl`	6283x1	double	number of finite elements of the cell mesh
`m_nPolInt`	6283x1	double	
`m_relVec`	6283x1	double	ratio $\|\mathbf{a}_2\|/\|\mathbf{a}_1\|$ of the Bravais lattice
`nDivAng`	1x1	double	number of division of `m_angle`-axis
`nDivGamma`	1x1	double	number of division of `m_relVect`-axis
`nTens`	1x1	double	number of stress vector components
`po`	1x1	double	stiff phase Poisson's ratio
`strHyp`	1x1	double	plane strain =1, or plane stress =2
`tipoGeom`	1x1	double	
`tipoGrilla`	1x1	double	

Tabla E.1: Data stored in files with extension `mat`

2. The code to generate or to modify the database

The name of the code main file is "`MainDBGenerator.m`".

Some variables can be modified by editing this file and the first level subroutines. Typical variables which can be modified are the following.

a) The stiff phase volume fractions used to computed the database whcih are defined with the vector `m_fracSolVarCorridas`. In the database, it is defined as follows:

```
m_fracSolVarCorridas = [0.00625, 0.0125, 0.025, 0.05, 0.075, 0.1,
0.125, 0.15, 0.175, 0.2, 0.225, 0.25, 0.275, 0.3, 0.325, 0.35,
 0.4, 0.45, 0.5, 0.6, 0.7, 0.8].
```

b) The variable `s_NomScript` may call two possible scripts:

```
s_NomScript = 'TCH_MCBarrasPoisNegClipper'; or alternatively
s_NomScript = 'TCH_MCBarrasPerimetrales';
```

The first script computes the reentrant layout denoted `PoisNeg`. The second script computes the layout denoted `PoisPos`, see Figure E.2-d and e.

c) In the subroutine at the first level, the following variables can be defined:

- `isPlot= 'true'` to plot the micro-cell geometry. This variable set to: `isPlot= 'false'` increases the computational speed-up.
- `strHyp = 1` → Plane Strain ; `strHyp = 2` → Plane Stress ;
- the main loop of the subroutine can be computed by using parallel computation after changing the statement `for iC = iCIn:nC` by the statement : `parfor iC = iCIn:nC`;
- To generate the cell geometry, it is used a third party codes, the Matlab functions `geom2d` and the mex wrappers `Clipper2` which calls the open source "Clipper" library. The mex file must be generated by re-compiling it if a different OS is used.

3. A procedure to use the database

One possible use of the database may consist of finding the parametrized microstructure providing the most closest homogenized elasticity tensor to a target given one $\mathbf{C}$. The procedure to use the database for obtaining this result has been described in the paper Podesta et al. (2018) and is summarized as follows.

1) The first step consists on normalizing $\mathbf{C}$ with the Young's modulus of the target stiff phase (for plan stress a beter factor may be: $E/(1-po^2)$). The resulting normalized tensor is denoted $\hat{\mathbf{C}}$.

2) Rotate the normalized tensor $\hat{\mathbf{C}}$ and the homogenized tensors `m_CHsSim` stored in the database and here denoted $\mathbf{C}^h$ to the normal base (x_N, y_N). In normal coordinates, these tensors are denoted $\hat{\mathbf{C}}_N$ and $\mathbf{C}^h_N$. This transformation can be performed using the algorith described in Auffray y Ropars (2016) and Podestá et al. (2018) that is implemented in the routine `Auffray_invariants_Cnorm_2`. This routine is used to rotate both tensors $\hat{\mathbf{C}}$ and $\mathbf{C}^h$ to natural coordinates. For example, `m_CHsSim` can be rotated with the following code lines:

```
m_CHMandel = m_ConvVoigtToMandel .* m_CHsSim;
[ m_C_result,v_Elem_class ] = Auffray_invariants_Cnorm_2(m_CHMandel);
theta = v_Elem_class.real_theta_map;
v_ClaseSim = v_Elem_class.v_FESymClass;
```

In the first line of this code, it is transformed the elasticity tensor `m_CHsSim` from Voigt to Mandel notation (`m_ConvVoigtToMandel` is a transformation matrix). In the second line, the elasticity tensor in cartesian coordinates (x, y) is rotated to natural coordinates (x_N, y_N). The elasticity tensor in natural coordinates $\mathbf{C}^h_N$ is called `m_C_result`. In the third line, the variable `theta` is the angle between the x-axis and the normal x_N-axis (see Figure E.2-a). The variable `v_ClaseSim`, in the fourth line, defines the symmetry class to which the $\mathbf{C}^h_N$ tensor belongs to.

3) Once both tensors, $\mathbf{C}^h_N$ and $\hat{\mathbf{C}}_N$, are expressed in the normal basis, the distance: $\|\mathbf{C}^h_N(\boldsymbol{\xi}) - \hat{\mathbf{C}}_N\|$ can be computed for all the elasticity tensors stored in the database. Each database entry is here identified with the four parameter vector $(\boldsymbol{\xi})$. Then, the set of parameter $(\boldsymbol{\xi})$ making minimal this distance provides the optimal microstructure stored in the database for the problem defined in this Section.

Bibliografía

Auffray N. y Ropars P. Invariant-based reconstruction of bidimensional elasticity tensors. *International Journal of Solids and Structures*, 87:183–193, 2016.

Podesta J., Mendez C., Toro S., y Huespe A. Symmetry considerations for topology design in the elastic inverse homogenization problem. *submitted*, páginas 1–43, 2018.

Podestá J., Méndez C., Toro S., Huespe A., y Oliver J. Material design of elastic structures using voronoi cells. *International Journal for Numerical Methods in Engineering*, 2018.

Doctorado en Ingeniería

mención mecánica computacional

Título de la obra:

Marco conceptual para el diseño inverso de metamateriales elásticos

Autor: Juan Manuel Podestá

Lugar: Santa Fe, Argentina

Palabras Claves:

Metamateriales, optimización topológica,
diseño inverso de materiales, derivada topológica,
homogenización computacional, camuflaje acústico,
diseño de materiales en dos escalas, simetría elástica.